

Micro-acoustics in marine and medical research

Edited by

Dr. Spiros Kotopoulos

National Centre for Ultrasound in Gastroenterology
Haukeland University Hospital

Dr. Anthony Delalande

Institute of Medicine, Haematology Section
University of Bergen

Dr. Olav Rune Godø

Institute of Marine Research

Prof. Dr. Michiel Postema

Department of Physics and Technology
University of Bergen

Micro-acoustics in marine and medical research

Edited by
Spiros Kotopoulos
Anthony Delalande
Olav Rune Godø
Michiel Postema

Copyright © 2012
Each chapter is under copyright of its corresponding authors.

All rights reserved. No part of this publication may be reproduced, distributed, or transmitted in any form or by any means, including photocopying, recording, or other electronic or mechanical methods, without the prior written permission of the publisher and authors, except in the case of brief quotations embodied in critical reviews and certain other noncommercial uses permitted by copyright law.

Publisher Information
Kotopoulos
Institutt for fysikk og teknologi
Universitetet i Bergen
Allégaten 55
5007 Bergen
Norway

Visit our website at <http://org.uib.no/micro-acoustics/>

ISBN 978-82-303-1945-1

Limit of Liability/Disclaimer of Warranty: While the publisher and author have used their best efforts in preparing this book, they make no representations or warranties with respect to the accuracy or completeness of the contents of this book and specifically disclaim any implied warranties or merchantability or fitness for a particular purpose. No warranty may be created or extended by sales representatives or written sales materials. The advice and strategies contained herein may not be suitable for your situation. You should consult with a professional where appropriate. Neither the publisher nor author shall be liable for any loss or profit or any other commercial damages, including but not limited to special, incidental, consequential, or other damages.

The information contained in this book is not intended to serve as a replacement for professional medical advice. Any use of the information in this book is at the reader's discretion. The author and publisher specifically disclaim any and all liability arising directly or indirectly from the use or application of any information contained in this book. A health care professional should be consulted regarding your specific situation.

Printed in The Netherlands by UNIVERSAL PRESS

First Printing, August 2012

Sponsors

Bergen universitetsfond



Department of Physics and Technology



Table of contents

Preface	6
1. Northern krill swimming orientation as measured by stereo camera	7
<i>Rokas Kubilius, Lucio Calise, Egil Ona</i>	
2. Acoustic equipped platforms	15
<i>Terje Torkelsen</i>	
3. Ultrasound Standing Wave Device for Particle Manipulation	29
<i>Yongqiang Qiu, Christine Démoré, Sandy Cochran</i>	
4. A new device for fabrication of lipid-shelled microbubbles	41
<i>Joe Fiabane, Ritu Malik, John Steel, Sandy Cochran, Paul Prentice, Ketan Pancholi</i>	
5. Hybrid laser-ultrasound cavitation for cloud evolution studies	51
<i>Bjoern Gerold, Spiros Kotopoulos, Sandy Cochran, Michiel Postema, Paul Prentice</i>	
6. Ultrasound induced mechanical stress: cellular and molecular responses	61
<i>Annemieke van Wamel</i>	
7. Biological and medical applications of low-intensity ultrasound	67
<i>Spiros Kotopoulos, Anthony Delalande, Chantal Pichon, Michiel Postema</i>	

8. Influence of ultrasonic waveforms upon microbubble suspensions	107
<i>Timur Saliev, Loreto Feril, Katsuro Tachibana, Paul Campbell</i>	
9. Ultrasound and microbubble-assisted gene delivery: insights for intracellular mechanism	119
<i>Anthony Delalande, Spiros Kotopoulis, Patrick Midoux, Michiel Postema, Chantal Pichon</i>	
10. The effect of low intensity ultrasound on adhesion molecules, actin monomers and membrane permeability in endothelial cells	131
<i>Chen Geffen, Eitan Kimmel</i>	
11. Flow cytometric characterization and sorting of ultrasound contrast agents	171
<i>Maja Mujić, Spiros Kotopoulis, Anthony Delalande, Marianne Enger, Odd Helge Gilja, Emmet Mc Cormack, Michiel Postema, Bjørn Tore Gjertsen</i>	
12. Funding your research from the European Framework Programs for Research and Innovation	185
<i>Anja Hegen</i>	
Photographs from the workshop	189
Author Index	194

Preface

Acoustic imaging has existed for almost 100 years. It is the most popular imaging modality in earth science, biomedicine, and fisheries. In living organisms, sound fields interact with microstructures, creating typical acoustic responses. These so-called acoustic fingerprints enable the identification, characterisation, discrimination and quantification of, *e.g.*, species, tissue types, and diseases. Under specific conditions, acoustic signals can be used to manipulate or even disrupt microstructures and to impact natural vocalisation in terrestrial and marine animals.

Yet, despite our vast knowledge on the propagation of sound, little is understood about the interactions of sound with microstructures in biomaterials or how sound effects an animal response.

The 1st workshop on micro-acoustics in marine and medical research brought together research professionals with particular expertise on this topic and with diverse backgrounds including agricultural engineering, cell biology, marine biology electrical engineering, gastroenterology, and astrophysics. The workshop was organised by the University of Bergen and the Institute of Marine Research (IMR). It took place at the IMR and the research vessel G.O. Sars, located in Bergen, Norway, on the 7th and the 8th of December, 2011. The outcomes are presented in this book. Each chapter treats a marine or medical application of the evolving field that we dubbed micro-acoustics. To prevent confusion with surface-acoustic-waves research (microacoustics), we added a dash.

Although the workshop had been initiated to exchange ideas and to define future perspectives, the most important finding was that marine and medical acoustics research communities can mutually benefit from close collaborations.

We are grateful to Bergen universitetsfond for granting the financial support for organising the workshop and to the medical imaging research & development cluster MedViz for enabling the printing of this book.

But most of all we thank *you* for opening this book to learn more about the exciting field of micro-acoustics in marine and medical research!

Bergen, 12th of February, 2012

Dr. Spiros Kotopoulos

Dr. Anthony Delalande

Dr. Olav Rune Godø

Prof. Dr. Michiel Postema

1

Northern krill swimming orientation as measured by stereo camera

Rokas Kubilius^{1,2,3}, Lucio Calise³, Egil Ona³

¹University of Bergen, Norway

²Marine Ecosystem Technologies AS, Nedre Åstveit 12, 5106, Bergen, Norway

³Institute of Marine Research, P.O. Box 1870 Nordnes, NO-5817 Bergen, Norway

Abstract

The Northern krill (*Meganicthiphenes norvegica*) swimming orientation and body length was nocturnally measured *ex situ* (mesocosm) and *in situ* in the fjords of western Norway. These were obtained by stereo photo cameras deployed and triggered manually from the onshore cabin and research vessel platform respectively. Slightly positive (*ex situ*) and negative (*in situ*) average krill body tilts were obtained from two datasets. Relatively large spread of individual krill swimming tilts is reported. The good correspondence in krill length measurements by stereo camera and trawl sampling is shown suggesting possible use of the stereogrametry method in krill sizing

Introduction

Euphausiids (broadly referred as krill) are among the key species in many ocean ecosystems [1]. The most abundant krill species in the North Atlantic's and associated seas is *Meganictiphenes norvegica* (Sars, 1857) or Northern krill [2-6]. It is known as important food source for many fish species, as well as some whales and seabirds with some estimates of total consumption to be over 200–400 Mt y⁻¹ [7, 8]. Subsequently Northern krill is an important component of many marine ecosystems and so is desirable to be monitored.

Active acoustics is currently the most promising observation tool in respect to rapid and cost effective sampling of large water bodies for monitoring of pelagic biological resources [9]. In order to convert the backscattered acoustic energy into krill biomass, so-called acoustic target strength (quantified ability to reflect sound) of unit krill mass has to be known. The elongated body shape causes directional sound wave scattering from krill. Therefore, one of the most important factors affecting krill acoustic target strength is incidence angle or body tilt angle in respect to acoustic wave front [10, 11]. The extreme body orientations can reduce acoustic backscattering from same krill animal by several orders of magnitude if compared with the maximum at broad side incidence [10]. Therefore information about average krill swimming orientation is extremely important for accurate scaling of the acoustic data.

The single camera based measurements of euphausiid swimming orientation have been reported before (see e.g. [11-16]), but mostly with few data on each different species. There are only few imagery-based data on particularly *Meganictiphenes norvegica* swimming orientation (*ex situ* [12] and *in situ* [11]). Aquarium based measurements by Kils *et al.* [12] revealed high positive average swimming tilt of Northern krill with large standard deviation of measurements *in situ* observations in Gulf of St. Lawrence have yielded lower in magnitude, but also positive average estimate of Northern krill swimming orientation with quite large spread of measurements and diel variation [11]. There is very little published data available on Northern krill in this respect from Norwegian fjords (see e.g. [13]). Also we are not aware of any stereo camera based investigations of euphausiid swimming orientation.

Methodology

Free-swimming krill was observed nocturnally *ex situ* and *in situ* as two separate measurement experiments. The photo imagery was collected in Nov. 2010 with animals investigated in fjords close to Bergen, Norway: first, in sheltered enclosure (mesocosm) close to the coast (henceforth "Data A"), later by lowering camera system from stationary research vessel in the middle of the fjord (henceforth "Data B"). Both photo data sets were collected along with krill acoustic echo backscattering measurements by new wideband system (not reported here).

Stereo camera setup, calibration and measurement accuracy

Stereo camera system consisted of two identical 12.1 Mpx Imenco SDS 1210 underwater photo cameras, firmly mounted on the specially designed stainless steel

platform providing stable mounting geometry. Two Imenco Flash 110 were attached above the photo cameras. Use of two flashes was necessary due to up to 0.1 sec (measured) variability in camera triggering synchronisation. Both cameras were triggered by single manual switch with communication and imagery obtained via underwater cables. Camera triggering frequency varied depending on krill occurrence, but in general was one to few minutes and no less than 30 sec in-between subsequent stereo picture pairs.

Stereo camera calibration and measurements were done using purpose-built SeaGis products: calibration cube, known length "length bar", calibration software CAL (ver. 2.00) and measurement software PhotoMeasure (ver. 1.86) [17]. The internal camera parameters and relative orientation (Table 1) were determined from >35 stereo pairs of calibration cube pictures processed with CAL. Stereo camera calibrations were performed at the measurement sites at 3-4 m water depth, just before (Data A) or after (Data B) the data collection. Plumb line pictures were taken periodically to confirm vertical reference in krill tilt measurements.

Table 1 - Critical stereo camera system parameters, as calibration output.

Parameter	Camera	
	Left	Right
Calibration for data A measurements		
Focal length (mm)	10.914	10.899
Convergence angle (°)	-6.041	4.283
Distance between cameras (mm)	628.71	
Calibration for data B measurements		
Focal length (mm)	10.901	10.897
Convergence angle (°)	-5.650	5.446
Distance between cameras (mm)	635.15	

Collected imagery was analysed and encountered krill measured on such basic selection criteria: animal is seen on both pictures of stereo pair, in reasonable picture quality and with small enough off-plane angle for reliable measurement (<50-60°, visual evaluation) [18] have shown that, for maximum stereoscopic fish length measurement accuracy and precision, the target should be orientated at 60° or less relative to the stereo camera platform. As our target animal was much smaller and observed nocturnally with sometimes less than ideal light and background contrast conditions, the need for more conservative data filtering was likely [18] also suggested upper limit of distance to the measured object to be 85% of the maximum visibility range. Following this most krill was measured at 1.0-2.5 m range and not accepted for analysis if at over 3 m distance.

Krill orientation and length measurements were done by identifying two points, the anterior edge of eye and tip of telson (length "AT" as in Morris *et al.*, [19]), on krill body seen in full length. Due to sometimes less than ideal picture sharpness part of animals

were measured for tilt only, as krill orientation was often clear, but less frequently the exact position of the eye front edge and tip of telson. The precision estimate was also available for each tilt and length measurement as computed by PhotoMeasure software using the intersection geometry of two 3-dimensional points identified on the krill body. The length measurement precision was confirmed empirically by measuring known length object (in water); measured length accuracy was of average 1.7 mm within both Data A and Data B experiments ($N_A=N_B=12$).

The accuracy of tilt measurements and bearing cut-off angle for reliable tilt/length measurements was more difficult to obtain; small experiment was designed and performed in air. A test object, framed matchstick, of known tilt horizontal (15°) was placed on the flat table surface at multiple positions and distances (1 m, 1.5 m, 2.5 m) from the cameras and with known bearing angle in horizontal plane in respect to the stereo camera system. Tilt measurements were done on test object first positioned broadside to the camera system (0° bearing angle), and then with increasing, less favourable bearing angles up to plus or minus 70° with 5° steps (see Fig. 1, Right). This had to simulate krill swimming towards or away from the camera. Average measured test object tilt from horizontal was 15.4° ($SD=0.3^\circ$, $N=242$). Considering the accuracy of 1° , to which the test object tilt was known here, there was no evidence of tilt measurements being affected by increasing bearing angle (within $\pm 0-70^\circ$) of the test object, as long as animal contour is clearly seen. Only data from krill measured to swim no more than 40° towards or away from the stereo camera system were used to generate results of this study, because only these were considered to be seen clear enough for reliable measurement by the operator.

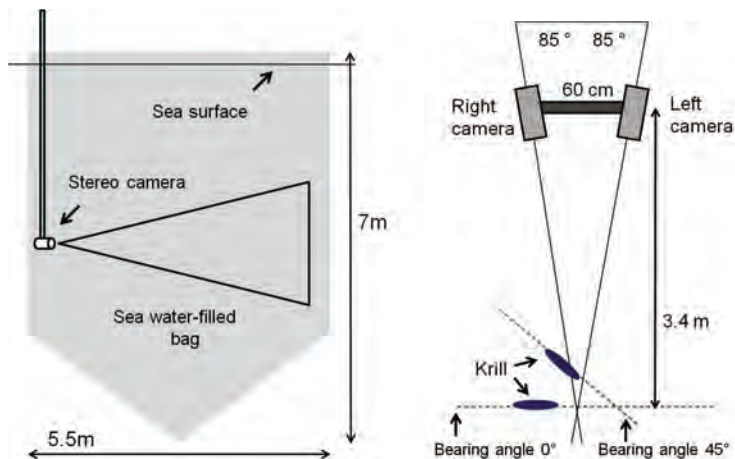


Figure 1 - Basic setup of the mesocosm used to collect Data A (Left) and dorsal view of stereo camera setup, as used in both Data A and B experiments (Right).

Data A

Data A photo material was collected over a 4 nights period at Austevoll Research Station (Norway). A specially designed, deep-water filled bag was installed on a floating well-moored raft 30 m offshore, where the bottom depth was 15 m. The bag of black light-impenetrable plastic was 5.5 m in diameter and 7 m deep with conical lower 1m section (Fig. 1, Left). Seawater was pumped from 160 m depth site in the nearby fjord, sand filtered, monitored for oxygen concentration, temperature, salinity and supplied through a spreader at the centre bottom part of the bag at the rate of 14 L/min (>10% water exchange per 24 h). The outlet was installed into bag wall ~20 cm below water surface. The installation was further covered with black plastic cloak to shelter from direct day light.

Wild krill was caught in Raunefjorden (60°16'N; 5°09'E) over two nights by RV Hans Brattstrøm and transported to the experiment site within one hour following the last catch. The 2 m diameter Methot Isaac-Kidd ring trawl was used to collect live and intact krill (total of 4 hauls at ~20 m depth and 2.5 kn vessel speed). Animals were transported in large buckets then carefully transferred into two 500 L storage tanks installed on the raft next to the bag. The plastic light impenetrable, lid covered storage tanks were equipped with constant supply of fresh sea water (same source as water for bag; inflow of 4 L/min). The krill were stored in the tanks for period of 7 days before being transferred into the experiment bag.

Stereo camera platform was attached to a 40 mm diameter steel pipe lowered 4m into the bag next to its wall and firmly mounted to the raft, looking horizontally towards the center of the mesocosm (Fig.1. Left). A light-sensitive video camera (Kongsberg OE15-100C-0005) was also mounted above the stereo system to provide additional information on krill behaviour during the experiment. Photo and video imagery were obtained and viewed live via Ethernet cable connection to an onshore office.

Data B

This photo dataset was obtained in Osterfjorden over 3 subsequent nights as a part of in-fjord experimental acoustic survey by RV G.O. Sars. Stereo camera system was mounted in horizontally sideways looking position on an acoustic probe platform (1.8 m high, Ø1.3 m, 500 kg). Probe was deployed on steel cable by ship crane; optical cable was used for live communication and triggering of the cameras. Plumb line pictures for camera system pitch and roll reference were taken in subsurface with fully submerged and free-hanging probe. It was assumed to be representative for pictures taken at larger depths. Photo material was collected between 9 p.m. and 5 a.m. (local time) at 10-30 m water depths at 60°34'35"N 5°25'40"E in all three nights (bottom depth ~260 m). The vessel was unanchored, but running on so-called "dynamic positioning" mode, cancelling any drift.

The characteristic euphausiid body shape was easily identifiable in the photographs, still species identification was impossible. The Krill Net trawl hauls were taken in the vicinity of site where imagery material was collected, once a night at about 12 a.m. to 3 a.m. (local time). The ~25 min duration trawl samples were taken at 2.7 kn vessel speed and at 10-21 m water depth to coincide with stereo camera sampling depth.

Results

The raw data analyzed consisted of >3600 stereo photo pairs with about equal contribution from both field experiments. Over 1000 individual krill were identified in Data A and over 600 in Data B. About 20% of these animals were measured. The krill body orientation and length measurement results are shown in Fig. 2.

The krill trawl samples collected in the vicinity of the imagery data collection site in Ostfjorden (Data B) were almost exclusively consisting of *Meganictiphenes norvegica*.

The quite large difference in krill size distribution between subsample measurements and stereo camera measurement results is evident as seen from Figs.2 A2 and A3. This was expected, as krill was released in size-sorted batches over the Data A experiment period, as was needed for echo sounder measurement experiment run in parallel. Therefore, krill size distributions shown in Figs.2 A2 and A3 cannot be directly compared. Length measurements from trawl samples in the vicinity of imagery data collection site in Ostfjorden (Data B) corresponds closely (Figs.2 B2 and B3). Most of the Data B imagery material was collected in the second half of the three measurement nights. No polarized krill schools were observed.

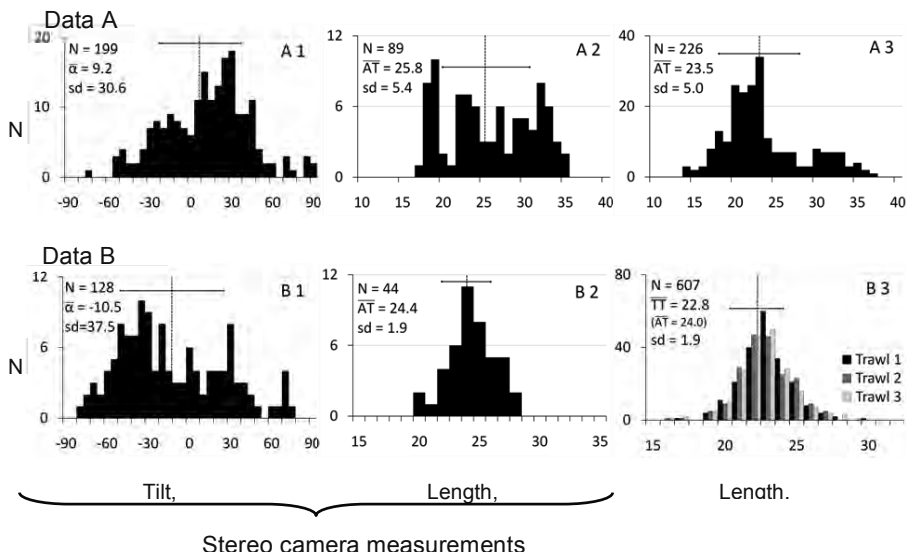


Figure 2 - Northern krill swimming orientation (A1 and B1) and body length distributions (A2 and B2) as measured by stereo camera system in experiments Data A and B. A3 and B3 are krill size distribution obtained from the subsample of krill released into mesocosm of Data A and from trawl samples in the vicinity of the stereo camera measurement site in Ostfjorden respectively. AT refers to krill length from anterior edge of the eye to tip of telson, TT – krill length from tip of rostrum to the tip of telson (as in [19]). Standard deviation of the measurements (sd) and average value are indicated by solid horizontal and dashed vertical lines respectively.

Discussion

The Northern krill swimming orientation measurement results from *in situ* and *ex situ* experiments utilizing stereogrametry methods were presented.

There was substantial difference in average krill body tilt as obtained from Data A and B. Most of the stereo photo data in Ostfjorden (Data B) was collected in the second half of the night (after 00.00 hour local time). The krill diel vertical migration in respect to the surface water light conditions is thought to be feasible explanation for this disparity. Similar euphausiid orientation observations were reported by Dalen *et al.*, [13] in Norwegian fjords at 02.00 hours local time ($\bar{\alpha} = -9.8^\circ$, $sd = 34.1$), though very limited material available [12], on the other hand, reported quite different swimming orientation of krill with average tilt of 53.8° and standard deviation of measurements 64.2° . However, these were made in small aquarium (63 L) what could have altered the natural swimming behaviour of the animals. From our data it is evident that Northern krill has quite variable swimming orientation as evident from large spread of measurements around the mean value. This corresponds quite well with most of euphausiid swimming orientation measurement reports (e.g. [11-15]).

There was good correspondence in size distributions of Northern krill in the open waters of Ostfjorden as measured by two different methods, stereogrametry and trawl sampling (Fig. 2 B2, B3). The stereo camera could be suggested for potential use as alternative to or supplement krill trawl sampling. However, more data should be collected still.

References

1. Mauchline, J., *The biology of mysids and euphausiids*. Advances in marine biology, 1980. **18**: p. 1-681.
2. Mauchline, J. and Fisher, L. R., *Distribution of the euphausiid crustacean Meganyctiphanes norvegica* (M Sars). Limnology and Oceanography, 1968. **13**(4): p. 727-728.
3. Dalpadado, P., *Distribution and reproduction strategies of krill (Euphausiacea) on the Norwegian shelf*. Polar Biology, 2006. **29**(10): p. 849-859.
4. Labat, J.P. and Cuzin-Roudy, J., *Population dynamics of the krill Meganyctiphanes norvegica* (M. Sars, 1857) (Crustacea: Euphausiacea) in the Ligurian Sea (NW Mediterranean Sea). *Size structure, growth and mortality modelling*. Journal of Plankton Research, 1996. **18**(12): p. 2295-2312.
5. Boysen, E. and Buchholz, F., *Meganyctiphanes norvegica in the Kattegat. Studies on the annual development of a pelagic population*. Marine Biology, 1984. **79**(2): p. 195-207.
6. Tarling, G. (ed), *Biology of Northern Krill*. 2010: Elsevier Science & Technology.
7. Simard, Y. and Harvey, M., *Predation on Northern krill (Meganyctiphanes norvegica Sars)*, in *The biology of Northern Krill*, G. Tarling, Editor 2010. p. 277-306.
8. Tarling, G.A. et al., *An introduction to the biology of Northern krill (Meganyctiphanes norvegica Sars)*, in *The biology of Northern Krill*, G. Tarling, Editor 2010. p. 1-40.
9. Simmonds, J. and MacLennan, D., *Fisheries Acoustics: Theory and Practice*. Second edition ed. Fish and Aquatic Resources Series, ed. T.J. Pitcher 2005: Blackwell Science. 437.
10. Greenlaw, C.F., *Backscattering spectra of preserved zooplankton*. Journal of Acoustical Society of America, 1977. **62**(1): p. 44-52.

11. Sameoto, D.D., *Quantitative Measurements of Euphausiids Using a 120-kHz Sounder and Their in situ Orientation*. Canadian Journal of Fisheries and Aquatic Sciences, 1979. **37**: p. 693-702.
12. Kils, U., *The swimming behaviour, swimming performance and energy balance of Antarctic krill, Euphausia superba*. BIOMASS Scientific Series, 1981. **3**: p. 122.
13. Dalen, J. and A. Kristensen, *Measurements of target strength and spatial orientation of euphausiids (krill)*. ICES CM 1981/B: 17, 1981: p. 14.
14. Endo, Y., *Orientation of Antarctic Krill in an aquarium*. Nippon Suisan Gakkaishi, 1993. **59**(3): p. 465-468.
15. Miyashita, K. et al., *Swimming behaviour and target strength of isada krill (Euphausia pacifica)*. ICES Journal of Marine Science, 1996. **53**: p. 303-308.
16. Lawson, G.L. et al., *Improved parameterization of Antarctic krill target strength models*. Journal of Acoustical Society of America, 2006. **119**(1): p. 232-242.
17. SeaGis, *CAL and PhotoMeasure - stereo camera calibration and stereophotogrammetric measurement software packages*. Available at: <http://www.seagis.com.au/index.html>, 2011.
18. Harvey, E. et al., *A Comparison of the Accuracy and Precision of Measurements from Single and Stereo-Video Systems*. Marine Technology Society Journal, 2002. **36**(2): p. 38-49.
19. Morris, D.J. et al., *An assessment of the merits of length and weight measurements of Antarctic krill Euphausia superba*. British Antarctic Survey Bulletin, 1988. **79**: p. 27-50.

2

Acoustic equipped platforms

Terje Torkelsen

Marine Ecosystem Technologies AS - METAS

Abstract

Acoustic is a very applicable technology used in very wide variety of different applications, from detection of the smallest to the biggest. To illustrate the wide span: Medical acoustics are able to monitor micro size particles at a few centimetres range, while marine acoustics are able to monitor shoals of herring up to a distance of 25 km, and detect a few centimetres fish at a range of 1000 meters. In marine acoustics a lot of applications are developed during the last decades. Some of the applications where acoustics are used is described in this chapter.

Introduction to Fishery Acoustics

History

Dolphins and whales have used sound for communication and object detection for millions of years. The science of underwater acoustics started in 1490, when Leonardo da Vinci wrote "If you cause your ship to stop and place the head of a long tube in the water and place the outer extremity to your ear, you will hear ships at a great distance from you." [1].

When Lord Rayleigh wrote the Theory of Sounds in 1877, modern acoustic theory was established. The Titanic disaster of 1912, and start of World War I provided the impetus for the next wave of progress in underwater acoustics. The world's first patent for an underwater echo ranging device was filed by Levis Richardson one month after the sinking of the Titanic, and a German physicist: Alexander Behm obtained a patent for an echo sounder in 1913. In the beginning of 1912, Reginald Fessenden built an experimental system, while he was working for the Submarine Signal Company in Boston. The system was first tested in Boston Harbour, and finally in 1914 from a ship on the Grand Banks of Newfoundland, where Fessenden demonstrated depth sounding and echo ranging, when the system detected an iceberg at 3 km range. Because he was using low frequency, and a small transducer face compared to the frequency, the system was unable to determine the bearing of the iceberg. In 1915, Paul Langevin, together with Constantin Chilowski, developed an active sound device for detecting of submarines, using quartz.

Under the British Board of Invention and Research, the Canadian physicist Robert William Boyle took on the active sound detection project with A.B. Wood. They produced a prototype of ASDIC for testing in mid 1917. This work was carried out for the Anti-Submarine Division of the British Naval Staff, and was undertaken in utmost secrecy, because they was using quartz piezoelectric crystals to produce the world's first practical underwater active sound detection apparatus. In 1939, the Admiralty made up a story that the acronym stood for "**Allied Submarine Detection Investigation Committee**", and this is still widely believed, though no committee with this name has been found in the Admiralty archives.

By the end of 1918, both France and Britain had built prototypes of active sound systems. The British tested their ASDIC in 1920, and started production in 1922. The developments during the war resulted in ASDIC sets which used several different shapes of beam. In 1919, the first scientific paper on underwater acoustics was published describing theoretically the refraction of sound waves produced by temperature and salinity gradients in the ocean.

At the start of World War II, British ASDIC technology was transferred for free to the United States. Research on ASDIC and underwater sound was expanded in the UK and in the US. Germany had also carried out work on the technology in this period. Since then the development has been continued by many countries, including Russia, for both military and civil uses.

SONAR was originally an acronym for **SO**und **N**avigation **A**nd **R**anging. This is a technique that uses sound propagation to navigate, communicate with or detect other vessels in the water. Two types of technology share the name **sonar**: *passive* sonar is essentially listening for the sound made by vessels, while *active* sonar is emitting pulses of sounds and listening for returning echoes. Sonar may be used as a means of acoustic location and of measurement of the echo characteristics of "targets" in the water. The term *sonar* is also used for the actual equipment used to generate and receive the sound. The acoustic frequencies used in sonar systems vary from a very few Hz (infrasonic) to several tenth of MHz (ultrasonic). The study of underwater sound is known as underwater acoustics.

Fisheries Acoustics

The primary tool in fisheries acoustics is the scientific echosounder [2]. Echosounding became developed for fisheries and research purposes during the 1930ies [3]. Scientific and commercial echosounders operate by the same technical principles, but the scientific instrument has a far better accuracy and precision, allowing quantitative assessment of abundance and biomass of fish and plankton.

In an echosounder, a transceiver generates a short pulse with a well defined pulse length (typically 1 ms), which is transmitted into the water by the transducer. The transducer is an array of piezoelectric elements arranged to produce a focused beam of sound. In order to be used for quantitative work, the echosounder must be calibrated in the same environment, and in the same configuration which it will be used. This is typically done by lowering a copper (or other metal) sphere with known acoustic properties into the transducer beam. The calibration sphere is moved through the whole beam while examining the changes in echoes [4]. When done, the sensitivity of the receiver and the angle of the transducer beam are calibrated.

Early echosounders only received sound from a single beam. Because of the acoustic beam pattern, identical targets at different azimuth angles will return different echo levels. If the beam pattern and angle to the target are known, this directivity can be compensated for. Calibration of single beam transducers is a tedious task due to the need of precision in the navigation of the sphere in the beam. With the **split-beam echosounder** this has become far easier. This technology divides the transducer face into four quadrants and compares the phase difference of the same echo in the four beams. The angle off-axis can be fairly precisely estimated, allowing the location of targets in three dimensions. Single-frequency, split-beam echosounders are now the standard instrument of scientific sounders. Horizontal pointing sonar systems are another avenue of development in fisheries acoustics that is not covered here.

Methodology

Biomass estimation is a method of detecting and quantifying fish and other marine organisms by converting the sonar backscattered signal to biomass [2]. An acoustic transducer emits a brief, focused pulse of sound into the water. If the sound encounters objects, such as fish, that are of different density than the surrounding medium, they return some sound energy back toward the source. These echoes provide information

on fish size, location, and abundance. The basic components of the scientific echo sounder hardware function is to transmit the sound, receive, filter and amplify, record, and analyze the echoes. While there are many manufacturers of commercially available echosounders, or fish-finders, quantitative analysis requires that measurements be made with echo sounder equipment having high signal-to-noise ratios and that is calibrated. Further, biomass estimation requires thorough knowledge of the backscattering properties (acoustic target strength) of the target species [5, 6].

In traditional acoustic surveys vessel mounted echosounders are operated along predetermined survey grid according to standardised routines to record fish abundance and biomass comparable to those recorded in previous surveys of the time series. Such assessments form the basis of present state of the art analytical stock assessment [2]. Due to the extended requirement of data needed to support the ecosystem based fisheries management, new methods have emerged during the last decades [7]. These include using scientific sounders on different platforms, enabling observations of marine organisms and key ecosystem processes with true spatial and temporal scaling [8, 9].

Two main categories of such observation platforms have been in use for this purpose: Mobile and Stationary platforms. Mobile platforms collect data in the same manner as a ship, - in spatial, but they observe the target species much closer and with much better resolution. Thus single individual can be resolved from a school including recordings of their acoustic properties [10]. Further, reduced distance to target permit use of the full range of higher frequencies that only cover surface layers from a research vessel. Stationary platforms positioned in a fixed location give acoustic information in true spatial and in time scale although the observed space is limited to the volume covered by the acoustic beam.

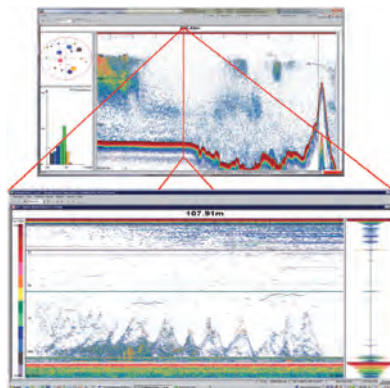


Figure 1 - Two approaches to the same area (Courtesy IMR). The two pictures are showing EK60 echograms from the same area from two different platforms. The upper echogram is recorded from a ship moving. Fish is detected in the water column above the seabed in the exact time when the ship was passing along a transect. The lower echogram shows behaviour of biomass in the exact point over time, recorded by an acoustic buoy. This echogram shows the behaviour pattern of feeding saithe (Courtesy IMR).

Mobile platforms

Ships

The most common acoustic platform is ships. Research vessels of today are designed to be as quiet as possible, with a minimum of noise to interfere with the acoustic signal from the echosounders. Some ships have installed the echosounder transducers in a drop keel to avoid reflections of bubbles, created by waves in bad weather. When the drop keel is in outer position, the transducers are located up to four meters below the ships keel. Scientific ships are equipped with a wide range of acoustic equipment. Echosounders with different frequencies in single beam, split beam and wide band. Sonars of different types, Omni scan, sector scan and single beam. Multibeam hydrographic echo sounder is used for bottom mapping, and parametric sounders used for sub bottom profiling. Automatic Doppler Current Profiler (ADCP) shows the profile of the current between the surface and the seabed continuously. On a cruise, several trawl samples are taken during the day to verify the biomass recorded at the sounders.



Figure 2 - Research Vessel G.O Sars (IMR) on cruise.

Photo : T. Torkelsen

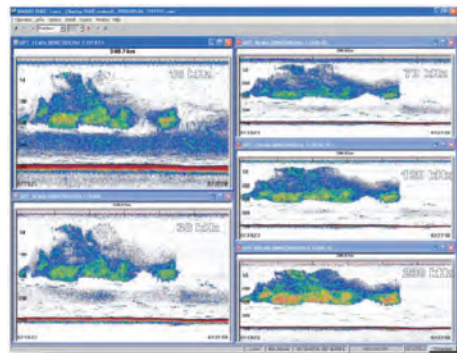


Figure 3 - SIMRAD EK60 with five frequenc (Courtesy Simrad).

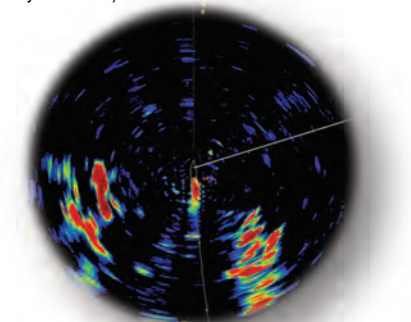


Figure 4 - A Simrad SP90 sonar showing shoal fish on both side of the ship.

AUV's

An **Autonomous Underwater Vehicle** is a free swimming robot that can travel underwater at a pre-planned mission plan without any required input from a operator. The first AUV was developed at the Applied Physics Laboratory at the University of Washington. Scientists have used AUV's to study the ocean and the seafloor. AUV's are also used for detailed seafloor mapping, and for military use. The unit have battery capacity to operate for a long time at depths down to several thousand meters.



Figure 5 - A Kongsberg AUV in operation.

The acoustic equipment used on an AUV spans from Multibeam hydrographic echo sounders and side scan sonars for seabed mapping, to scientific splitbeam echosounders for biomass estimation. Some AUV's have acoustic link installed, giving an operator the possibility to change the plan during the voyage. As payload, an AUV can carry a variety of sensors to measure the concentration of various elements or compounds, such as microscopic life.

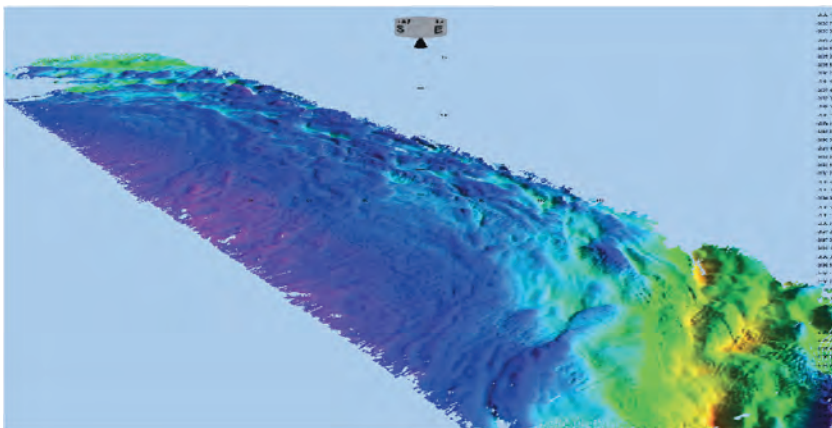


Figure 6 - High resolution 3D bathymetry map recorder by AUV (Source: Marum, Bremen).

Towed vehicles

A towed vehicle is a platform towed by a ship. Such unit can give the scientists opportunity to use higher frequency acoustics, in deeper volumes, out of range for high frequency sounders installed on a ship. MUST (Multi Use System for Towed vehicle) is an example of a towed vehicle, designed for detection, characterization and measurement of biomass and gas in the water column. This unit is designed as a depressor that can be towed down to 1,000 meters depth at up to 8 knot speed. Many different sensors can be installed, giving the scientists a much better basis for interpretation of the signals from the acoustic equipment. The unit was originally designed by IMR for fine scale resource mapping of plankton in deeper layers, but can also be used for seabed mapping, pipeline inspection, and monitoring of natural gas seeps of methane and CO₂. The towing cable also serves as umbilical, providing power to the sensors and communication between the sensors and the operator. The combination of acoustic and sensors is varying, depending on the mission. The controllable transducer platform inside is levelling the transducers regardless of the movements of the vehicle. The operator can manoeuvre the unit to the side of the ships track using the two rudders in the back of the unit. The angle of attack of the depressor is also controlled by the rudders.

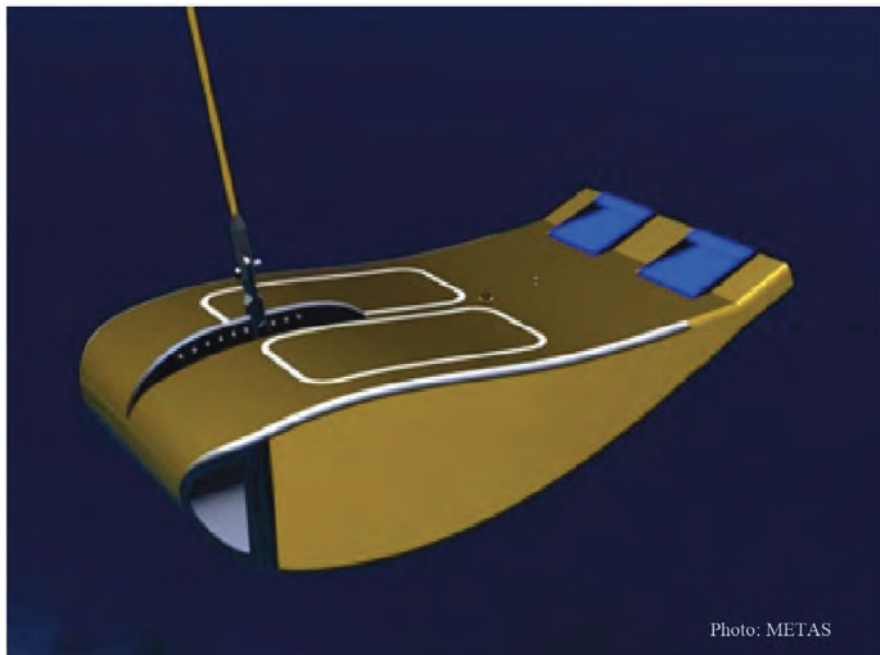


Figure 7 - MUST towed vehicle (METAS).

A typical composition of acoustics and sensors in MUST for monitoring of plankton layers can be like this:

Acoustics:

Simrad EK60 Scientific Sounders::

38, 70, 120, 200 and 333 kHz Splitbeam

670 and 1.200 kHz Single beam

Optional: Acoustic Doppler Current Profiler (ADCP) and Side Scan Sonar

Sensors:

- Laser Optical Plankton Counter (LOPC)
- Video Plankton Recorder (VPR)
- Conductivity sensor
- Temperature sensor
- Depth sensor
- Light sensor
- Chlorophyll sensor
- Turbidity sensor
- Flow meter
- Compass
- Pitch/Roll sensors

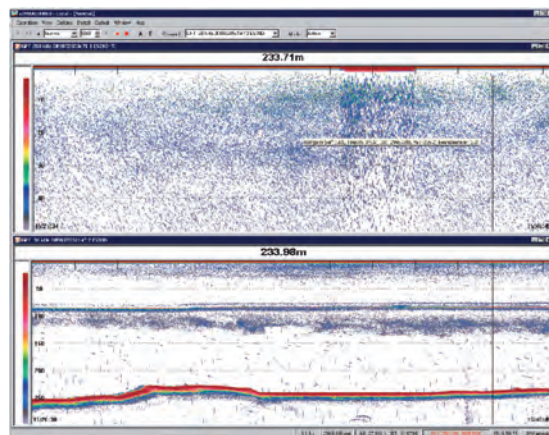


Figure 8 - Plankton layer detected by EK60 installed in MUST (Courtesy IMR).

Stationary Platform

Sometimes it is necessary to monitor in an area over a longer period of time. It could be environmental monitoring in connection with industrial exploration, or monitoring of biomass in a limited area [8]. If the monitoring are to take place over years, than an acoustic Lander platform would be selected. If monitoring are to take place over shorter periods such as months, than an acoustic buoy would be preferred. The great benefit of a stationary platform is that the present of a unit is not disturbing the natural behaviour of the biomass in the sea.

Landers

An acoustic Lander can work in three different modes: autonomous, connected to a communication buoy or connected to a cabled infrastructure. In the two first cases, batteries have to be installed, running the equipment for the deployed time. In case of connection to infrastructure, power to the Lander is supplied from there. When it comes to communication with sensors installed on a Lander, real time communication can be obtained via the communication buoy or via optical fibre in the infrastructure. In autonomous mode, there will be no communication during the deployment time: all data has to be downloaded when the Lander is retrieved.

On the Searching Lander, the transducers can be trained and tilted, monitoring the whole water column with scientific sounders as searchlight sonar. In environmental monitoring, searchlight sonars with different transducer beams suitable for the application can be used. Different types of sensors are often installed on a Acoustic Lander :



Figure 9 - Acoustic Searching Lander.

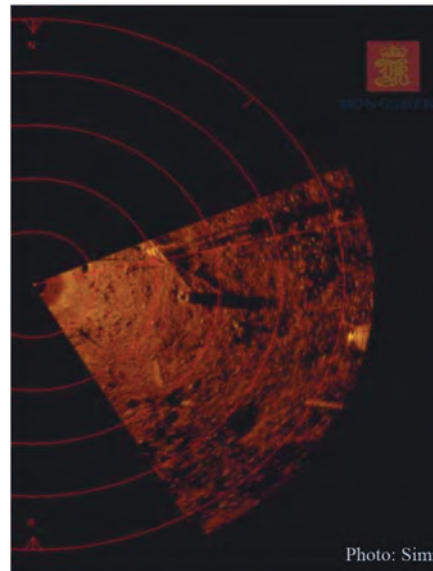


Figure 10 - Picture from a Simrad Mesote searchlight sonar.

Acoustics:

- Simrad EK60 Scientific Sounders: 38, 70, 120, and 200 kHz Splitbeam
- Acoustic Doppler Current Profiler (ADCP) and Hydrophones

Sensors:

- Video camera
- Still camera
- 3D Still camera
- Conductivity sensor
- Temperature sensor
- Depth sensor
- Light sensor
- Chlorophyll sensor
- Turbidity sensor
- Compass
- Tilt sensor Pitch/Roll sensors

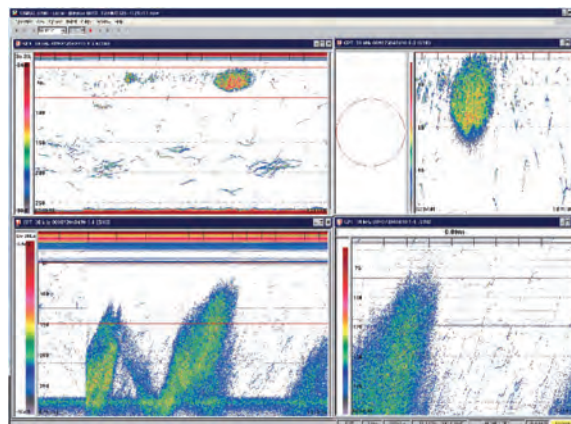


Figure 11 - EK60 echogram from a Searching Lander in vertical and horizontal plan (Courtesy IMR).

Acoustic Buoys

Sometimes it can be of great interest to study behaviour of biomass in an area. An Acoustic buoy is very well suited for such task [11]. The buoy contains different types of sensors in addition to the acoustics. An internal controller is collecting data according to a pre-programmed mission plan. Power is supplied from internal batteries. The buoy have positive buoyancies and are deployed with a weight connected to an acoustic release. When the unit are to be retrieved, an acoustic signal is transmitted from the collecting ship, activating the acoustic release which drops the weight, and the unit will float up to the surface for retrieval.

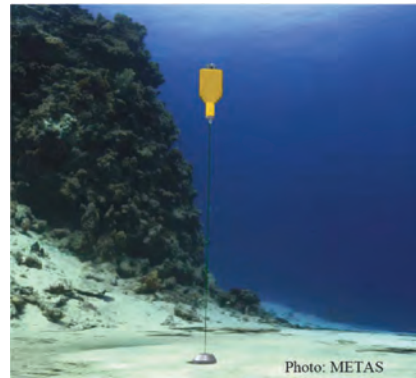


Figure 12 - COMPEC Acoustic buoy (METAS).

Sensors in addition to Scientific sounders

- Recording Doppler Current Profiler (RDCP)
- Compass
- Tilt/Roll
- Oxygen sensor
- Conductivity sensor
- Temperature sensor
- Depth sensor
- Light sensor
- Chlorophyll sensor
- Turbidity sensor

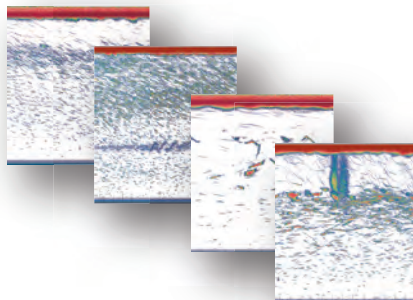


Figure 13 - EK60 echograms from the same area at different time of the day (Courtesy IMR, see also [11]).

Fixed Installations

In connection with environmental monitoring of subsea installations for the offshore industry, a fixed installation is more suitable. This unit is designed to take impact from heavy fishing gear such as a trawl. The unit is connected to a cable infrastructure, giving power to and communication with the unit. The unit is designed to be deployed in 10+ years. The payload for such platform is the same as for a searching Lander, with scientific echosounders where the transducers can be tilted and trained for coverage of the whole water column above the unit. An ADCP is monitoring the current between the seabed and the surface, and oceanographic sensors are monitoring changes in the environments.

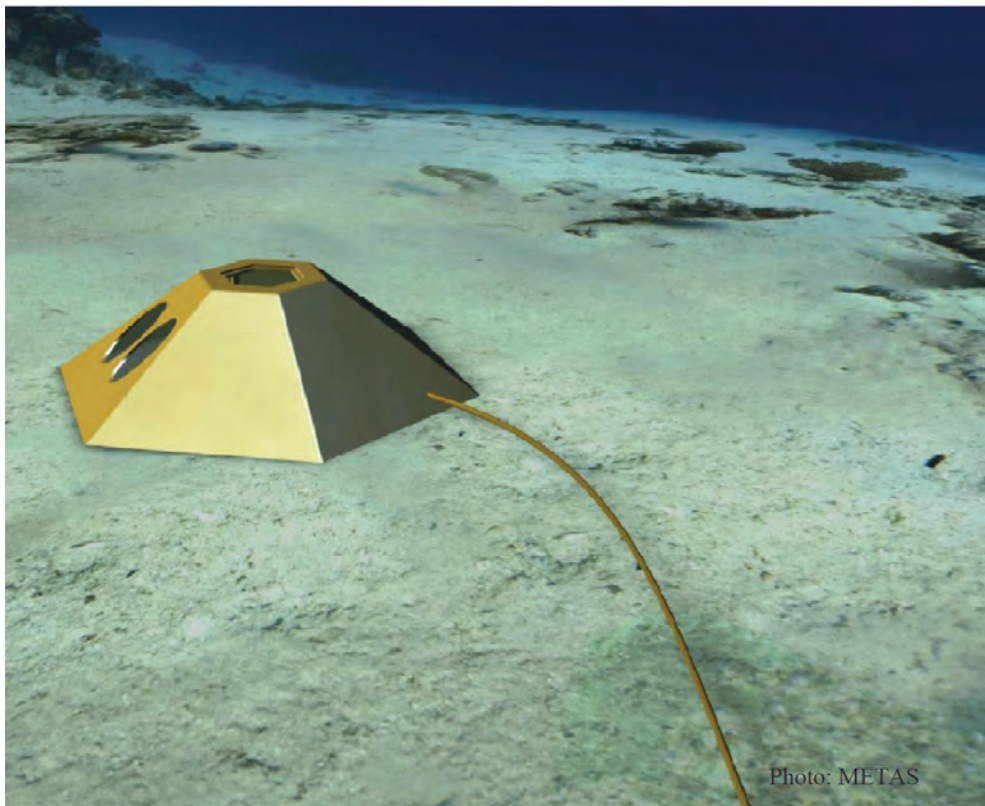


Figure 14 - Fixed Lander (METAS).

Probes

When using acoustics for abundance estimations, it is important to have good knowledge of the target strength (TS) each individual is representing. IMR has developed different TS probes for this purpose, using 38, 70 120, 200 and 333 kHz splitbeam scientific echosounders.

The transducers are arranged on a horizontal stabilized transducer platform in such way that the same echo from a single fish can be monitored on all frequencies at the same time. In this way the frequency response from a fish, or a plankton can be established.

The unit is lowered down to the depth where the biomass to be monitored are present. In that way the targets can be monitored undisturbed, on the higher as well as the lower frequencies in the right elements. Several oceanographic sensors are used to monitor different parameters around the TS probe, and ADCP is monitoring the current present at the measuring point. Krill has a very directive TS, so to confirm the actual swimming behaviour a 3D camera is used to take pictures of the krill.

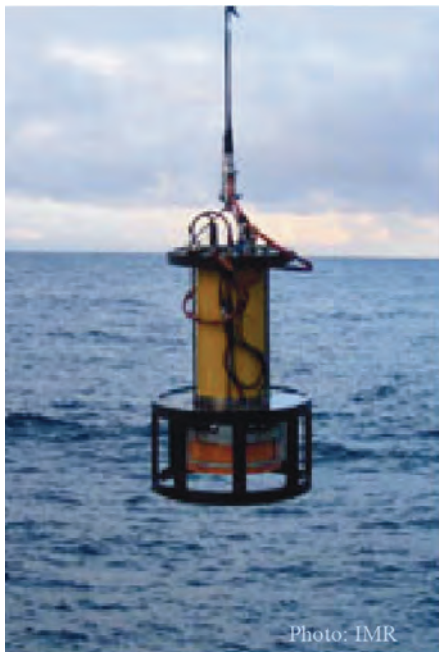


Figure 15 - TS Probe from IMR.

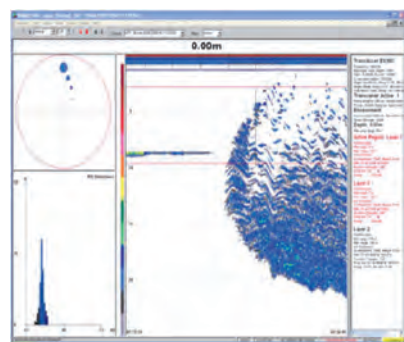


Figure 16 - Single targets from capelin (*Mallotus villosus*) (Courtesy IMR).

Acknowledgements

To the Observation Methodology Group at Havforskningsinstituttet (Institute of Marine Research) in Bergen for outstanding cooperation in the projects where most of our acoustic sensor platforms are developed.

References

1. Urick, R. J. (1983). *Principles of Underwater Sound, 3rd Edition*.
2. Simmonds, J., MacLennan, D.N., 2005. Fisheries acoustics : theory and practice.
3. Sund, O., 1935. Echo Sounding in Fisheries Research. *Nature* 135, 953.
4. Foote, K.G., Knudsen, H.P., Vestnes, G., MacLennan, D.N., Simmonds, E.J., 1987. Calibration of acoustic instruments for fish density estimation: a practical guide. *ICES Coop. Res. Rep.* 144.
5. Foote, K.G., 1987. Fish target strengths for use in echo integrator surveys. pp. 981- 987.
6. Ona, E., 2003. An expanded target-strength relationship for herring. *ICES J. Mar. Sci.* 60, 493-499.
7. Godø, O.R., 2009. Technology answers to the requirements set by the ecosystem approach. In: Beamish, R.J., Rothschild, B.J. (Eds.), *The Future of Fisheries Science in North America*. Springer, p. 736.
8. Godø, O.R., Patel, R., Torkelsen, T., Vagle, S., 2005. Observatory Technology In Fish Resources Monitoring. *Proceedings of the International Conference. International Conference "Underwater Acoustic Measurements: Technologies & Results"* Heraklion, Crete, Greece.
9. Kaartvedt, S., Rostad, A., Klevjer, T.A., Staby, A., 2009. Use of bottom-mounted echo sounders in exploring behavior of mesopelagic fishes. *Mar Ecol-Prog Ser* 395, 109-118.
10. Patel, R., Handegard, N.O., Godø, O.R., 2004. Behaviour of herring (*Clupea harengus* L.) towards an approaching autonomous underwater vehicle. *ICES J. Mar. Sci.* 61, 1044-1049. Blackwell Science, Oxford.
11. Johansen, G., Godø, O., Skogen, M., & Torkelsen, T. (2009). Using acoustic technology to improve the modelling of transportation and distribution of juvenile gadoids in the Barents Sea *ICES Journal of Marine Science* , pp. 1048 - 1054.

3

Ultrasound Standing Wave Device for Particle Manipulation

Yongqiang Qiu, Christine Démoré, Sandy Cochran

Institute for Medical Science and Technology, University of Dundee, UK

Abstract

Using ultrasonic standing waves for noncontact manipulation of microparticles or cells has raised many possible applications in life sciences and medicine. This paper introduces the basic concept and methods of applying ultrasound to manipulate the microparticles in fluids, and also gives two practical examples of trapping and manipulating microparticles with ultrasound standing waves. The design, simulation, fabrication and testing of these two resonant-mode ultrasonic manipulation devices are presented, and some practical issues are discussed, such as temperature changes and streaming. The first device uses a bespoke high frequency (up to 25 MHz) lithium niobate transducer coupled to a fabricated precision reflector and spacers to form a multiple of half-wavelength ultrasound standing waves ($30\text{ }\mu\text{m}$) across a macroscale fluid chamber ($2 \times 5\text{ mm}^2$) in which the microparticles are distributed and trapped by ultrasonic radiation forces. The second device has a 12-element kerfless ultrasonic linear array (2.5 MHz) coupled to a disposable rectangular capillary to trap and manipulate microparticles along the capillary by controlling the active elements of the

array. The experimental results of both devices with 10 μm polystyrene beads show correspondence with pressure distributions simulated with the finite element method and demonstrate the feasibility for potential applications in life sciences.

Introduction

In recent years, precise manipulation of bioparticles, biomolecules and cells has become increasingly important in the life sciences and medicine, with emerging applications such as biological and chemical analysis, cell separation and sorting, the measurement and characterization of cell forces, and tissue engineering. Generally, noncontact microparticle manipulation techniques utilise the forces created to cause migration of microparticles towards equilibrium states at the local potential energy minima. Over these existing techniques, such as magnetic manipulation, dielectrophoresis trapping and optical tweezing, ultrasonic standing wave manipulation offers several potential advantages when employed in tissue or cell studies, such as the ease with which it can be integrated with microfluidic systems [1], maintenance of cell viability [2], and achievement of forces necessary to handle cells with dimensions up to tens of microns, or cell agglomerates of hundreds or thousands of cells [3].

In this paper we summarise the recent development of two resonant-mode ultrasonic devices for microparticle manipulation. The basic concept and methods of ultrasonic standing wave manipulation in fluids are introduced, and some practical issues and challenges are discussed. The first device is a bespoke 23.5 MHz lithium niobate (LiNbO_3) transducer coupled to a reflector for trapping 10 μm polystyrene beads in multiple pressure nodal planes across a millimeter-scale chamber. Because of the high frequency, the distance between trapping sites is of the same order as the cell diameter (tens of microns). In addition, the potential advantage of generating high acoustic pressure gradients and large radiation forces is emerging for some applications in cell biology. The second device is an electronically-controlled ultrasound linear array in a planar half-wavelength resonator device for axial trapping and lateral manipulation of 10 μm fluorescent polystyrene beads, which demonstrates the feasibility of controlling the position of particles along the length of a channel by shifting the active array elements to overcome the dominant effect of chamber geometry on resonant modes.

Methodology

(1) Multilayer Resonators

Ultrasonic standing waves can be formed by two major structures, as shown in Fig. 1. One is a resonant structure, where an incident ultrasonic wave from a single ultrasonic transducer combines with its reflection from a dimensionally-stable, and high acoustic impedance reflector. The other one is a counter-propagating wave structure, where two incoming waves generated from two opposing paired ultrasonic transducers form the ultrasound standing wave by their interference. Besides these methods, the Lund method can also form an ultrasonic standing wave between two sidewalls of a channel by placing an ultrasound source underneath the half-wavelength width channel, where

the standing wave is orthogonal to the incident ultrasound wave [4]. Generally, the resonant structure can generate significantly higher standing wave pressure gradients with lower driven power than the counter-propagating structure and the Lund method [5].

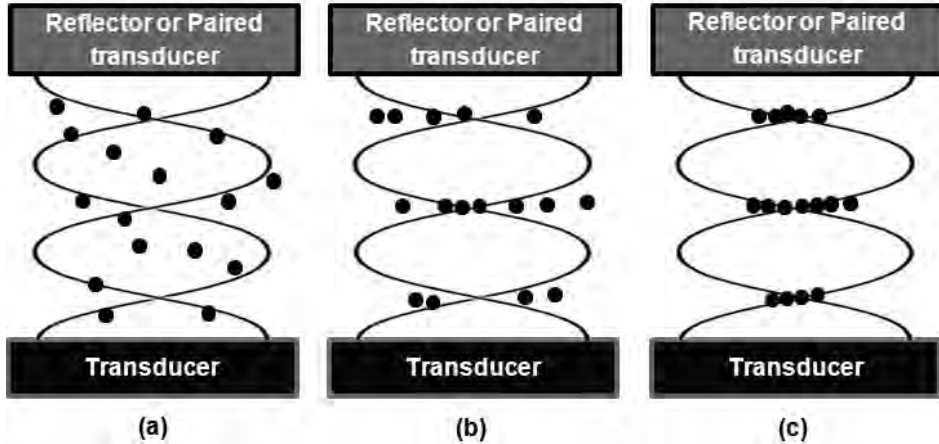


Figure 1 - Particle motion within an ultrasonic standing wave [5]. (a) A standing wave is formed in a fluid, (b) particles move to pressure nodal planes due to the axial radiation force, (c) particles aggregate within the nodal planes because of the lateral radiation forces and Bjerknes forces.

In the multilayer resonator structure, the ultrasound standing wave is formed and the pressure nodal planes are created to trap the microparticles within a fluid layer between the transducer and its parallel reflector. The locations of those pressure nodal planes depend on the transducer driving frequency, the layer thicknesses and boundary materials. The distance between two adjacent pressure nodal planes is a half-wavelength at the transducer driving frequency. Thus the thickness of the fluid layer is usually one or several half-wavelengths.

(2) Acoustic Radiation Forces

For particles immersed in a fluid medium and subjected to an ultrasonic field, ultrasonic radiation forces are generated because of the scattering of the ultrasonic field. This phenomenon occurs for both standing waves and progressive waves; however, the radiation forces are generally larger in the standing wave than in the progressive wave [5]. In an ideal plane standing wave, only an axial radiation force is generated to move the particles to the pressure nodal planes, Fig. 1(b). However, in a practical standing wave field, lateral radiation forces are also generated, which will aggregate the particles within the nodal planes, Fig. 1(c).

Gor'kov [6] reported the theory relating to the acoustic radiation force on a small particle within an ideal fluid subject to an ultrasonic standing wave. He derived a formulation based on the time-average of the kinetic and potential energies, with energy gradients arising from the spatial variation in the ultrasonic pressure field and particle velocity field respectively:

$$F = -\nabla \left(\left(1 - \frac{\rho_f c_f^2}{\rho_p c_p^2} \right) \langle E_{pot} \rangle - \left(\frac{3(\rho_p - \rho_f)}{(2\rho_p + \rho_f)} \right) \langle E_{kin} \rangle \right) V \quad (1)$$

$$\langle E_{pot} \rangle = \frac{1}{2\rho_f c_f^2} \langle p^2 \rangle \quad (2)$$

$$\langle E_{kin} \rangle = \frac{1}{2} \rho_f \langle u^2 \rangle \quad (3)$$

where V is the particle volume, the subscripts f and p relate to the fluid and particle respectively, ρ is the density and c is the speed of sound. E with angle brackets and the subscripts pot and kin indicate the time-averaged potential and kinetic energy densities respectively, which are related to the ultrasonic pressure field, p , and the particle velocity magnitude, u . Because of the 180° phase difference between the pressure field and the particle velocity, the pressure minima are located in the same places as the velocity maxima. Thus the radiation force acting on the particles is always directed towards the pressure nodal planes, i.e. the potential energy minima, and the velocity maxima, i.e. the kinetic energy maxima [7, 8].

Generally, the axial radiation forces most significantly affect the motion of most particles and once these particles are manipulated in pressure nodal planes, they will be drawn to the kinetic energy maximum within local pressure nodal planes by lateral radiation forces, as in Fig. 1. In addition to the axial and lateral radiation forces, when more than one particle is suspended in the standing wave field, each particle will produce a scattered acoustic field which will influence the other particles, leading to the generation of Bjerknes forces between proximal particles. These particle - particle interaction forces also contribute to the formation of aggregates in the ultrasonic standing wave field.

Device I – High Frequency Single Element Trapping Device

According to Gor'kov, radiation force is related to ultrasonic pressure gradient and particle velocity magnitude for given particles and fluid. If a larger radiation force is required for specific applications, it can be generated by raising the ultrasound frequency and thus the pressure amplitude and energy gradients [8]. A simple

multilayer resonator has been developed to exploit this, as shown in Fig. 2. The resonator, which is designed to sit on a petri dish or microscope slide and to be compatible with optical microscopes, has three parts: a LiNbO₃ ultrasonic transducer of about 25 MHz with a low acoustic impedance mounting; a polished reflector made from machinable ceramic (MACOR); and a pair of precision spacers separating the reflector and transducer.

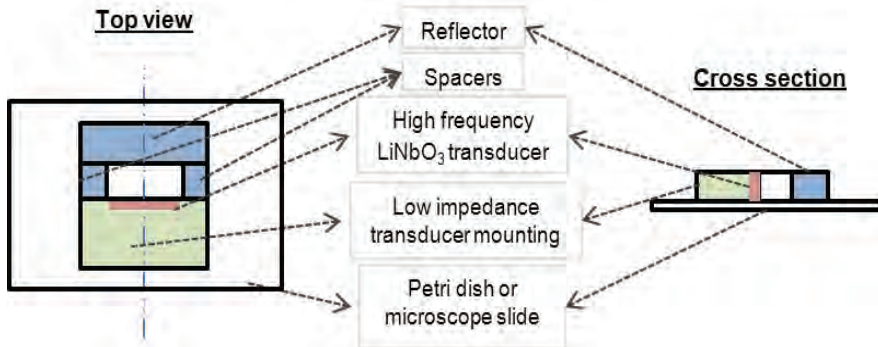


Figure 2 - Schematic of high frequency single element resonator

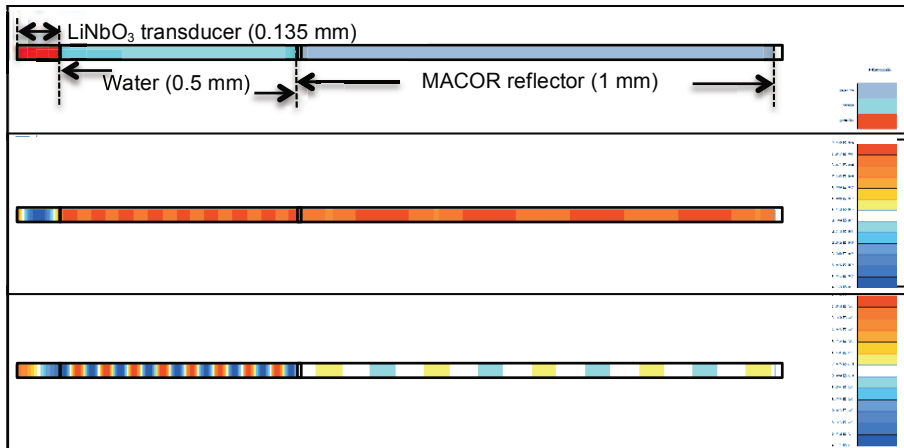


Figure 3 - PZFlex models and simulations of device [8]. (a) model structure and layer dimensions, (b) pressure distribution at 23.3 MHz, (c) X-velocity field at 23.3 MHz.

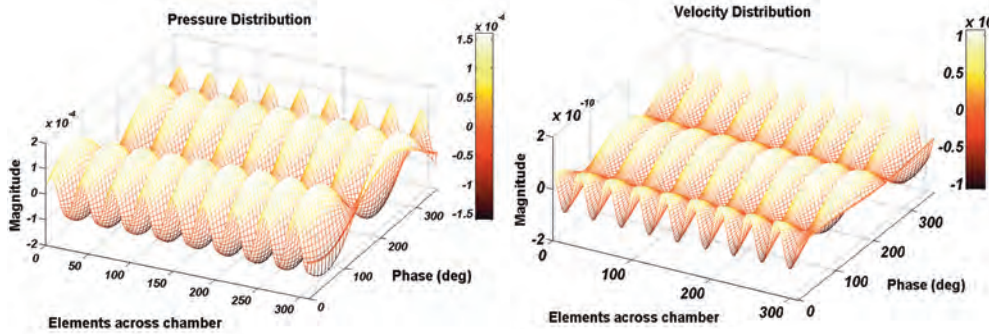


Figure 4 - Pressure (left) and velocity (right) distribution across water chamber with different phase.

Finite element analysis (FEA) has been used to simulate the device. A 2D model of the planar resonator structure was created with PZFlex virtual prototyping (Weidlinger Associates Ltd, Glasgow, UK). The structure of the model and the layer dimensions are illustrated in Fig. 3(a), along with the pressure and x-velocity field distribution at 23.3 MHz (Fig. 3(b, c)). The boundary conditions that were applied were symmetry on the top and bottom of the model and an acoustic absorbing boundary on the right. The transducer mounting, on the left, is set as void because the mixture of glass microballoons and epoxy that was used in the experimental devices inhibits ultrasonic wave propagation because of its high acoustic scattering and low density, $\rho < 0.5 \text{ g}\cdot\text{cm}^{-3}$. The pressure and velocity distributions across the chamber at the resonant frequency were calculated and output into MATLAB (MathWorks, MA, USA) for analysis, as shown in Fig. 4.

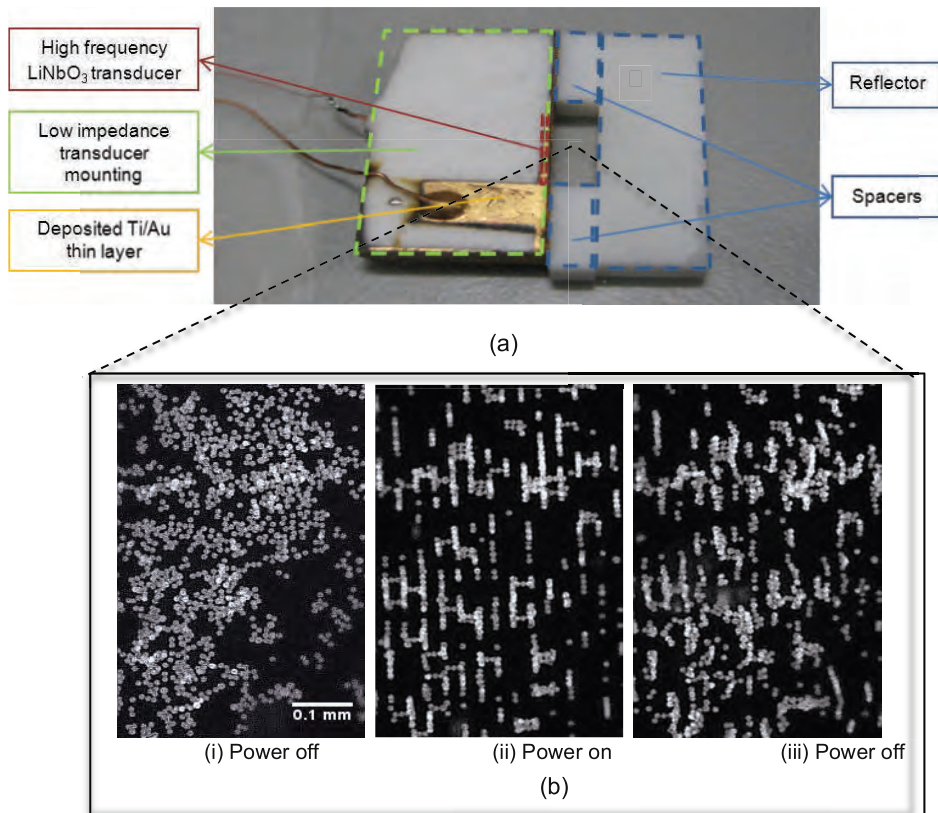


Figure 5 - (a) Manufactured and assembled prototype device, (b) 10 μm polystyrene beads trapped in an ultrasonic standing wave field [8].

A prototype device was fabricated (Fig. 5(a)) with an ultrasonic transducer made with Y-36° LiNbO₃ (Roditi International Corporation Ltd, London, UK) which was lapped and diced to a $0.135 \times 2 \times 5 \text{ mm}^3$ plate. A thin layer of Ag-paint electrode (Electrodag 1415, Acheson Colloids BV, Scheemda, Netherlands) was applied on one side of the LiNbO₃ plate, and a thin Cu wire was attached as the rear connector with a small drop of conductive epoxy (Silver Epoxy Kit, Agar Scientific, UK). The transducer was completed with glass microballoons (Lawrence Industries, Tamworth, UK) filled epoxy (Epofix, Struers A/S, Ballerup, Denmark) with a mass ratio of 1:6 in a PTFE mould ($2 \times 15 \text{ mm}^2$). It was demoulded after 14 hours of curing at room temperature. A Ti/Au thin film electrode with layer thicknesses of 50 and 200 nm respectively was deposited on the front face and connected to an electrical ground wire to obtain good conductivity and

uniformity. The reflector and spacers were fabricated from MACOR (Corning Incorporated, NY, USA) and lapped and polished to obtain a good surface finish. The transducer and reflector were then bonded together with quartz wax (0CON-20, Logitech Ltd, Glasgow, UK) with the spacers in between to allow accurate assembly and easy disassembly and reassembly of the device with other spacers.

To evaluate device performance, a 20 ml of degassed water with a high concentration of 10 μm polystyrene beads (Thermo Fisher Scientific, USA) was injected into the chamber. When the transducer was excited, the beads moved quickly to the nearest pressure nodal planes, forming a band structure with a spacing of $\sim 30 \mu\text{m}$, as shown in Fig. 5(b). It was also noticed that in some positions, 2 or 3 beads were trapped between adjacent band structures; this is thought to be caused by strong particle-particle interaction because of the short distance between particles in the highly concentrated mixture. Moreover, when the power was turned off, the beads started to agglomerate at those positions, as shown in Fig. 5(b-iii), confirming this analysis.

Because of energy dissipation as the transducer is operated, the temperature rises and heat is transmitted into other parts of the system. A thermal imaging camera (JADE, Cedip Infrared Systems, France) was used to investigate this. The device was driven at its resonant frequency, $f = 23.38 \text{ MHz}$, with a continuous sinusoidal wave at different voltages, $v = 6, 8$ and $10 V_{pp}$ for 10 min in each case. It was also driven by a burst wave with different duty cycles, $\delta = 25\%, 50\%$ and 100% , at $10 V_{pp}$ for 5 min in each case. The results in Fig. 6 show that the temperature rise closely correlates with input power. As thermal conduction will also reinforce the streaming effects, driving power and cooling methods need to be considered in an effort to maintain viable environmental conditions for temperature sensitive cells.

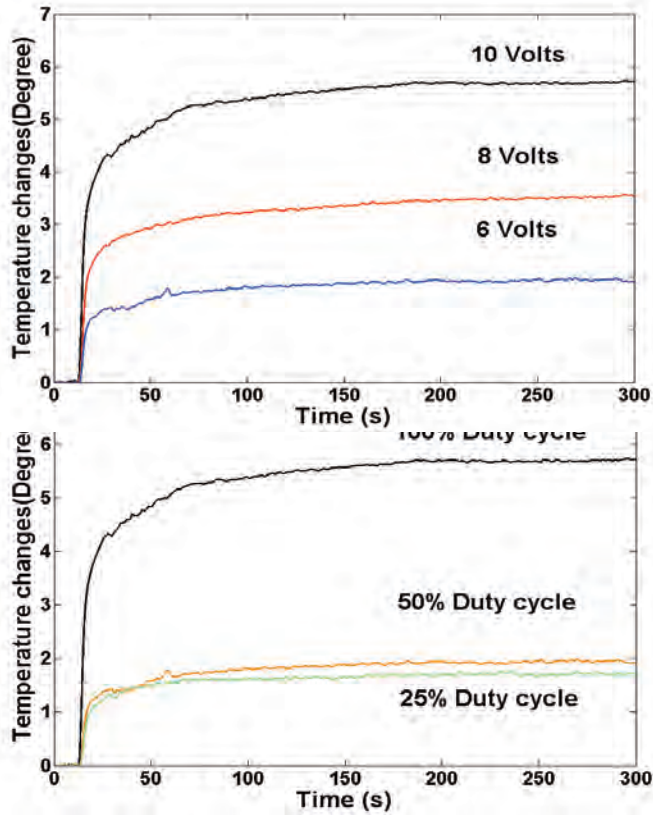


Figure 6 - Temperature changes with different driving voltages (top) and duty cycles (bottom).

Device II – 1D Linear Array Lateral Manipulation Device

Because of the dominant effect of chamber geometry on resonant structure, ultrasonic standing wave manipulation is usually limited to a single dimension in the same direction of wave propagation, so that when an ultrasonic manipulation resonator is integrated in a microfluidic system, the microparticles are trapped in pressure nodal planes of the ultrasound standing waves, and translated through the system by motion of the fluidic medium. To overcome this limitation, a 1D linear ultrasonic array manipulation device (Fig. 7 (a)) was developed, introducing the concept of lateral manipulation of particles without the assistance of fluidic motion.

In this device, lateral trapping is achieved with an array instead of a single element transducer (Fig. 7(b)). A rectangular glass capillary (VitriCom, Ilkley, UK), with $6 \times 0.3 \text{ mm}^2$ internal cross section and 0.3 mm wall thickness, was coupled to the array. The particles were trapped above the centre of the active elements in the middle of capillary. The active subset of array elements was then alternately switched to move the active region along the device, moving the trapping location and the particles along the capillary. Device operation by lateral manipulation of particles has been modelled with COMSOL Multiphysics (Comsol Ltd., Hertfordshire, UK) with the results predicts the effects of lateral ultrasonic field gradients relative to active array elements (Fig. 7(c)).

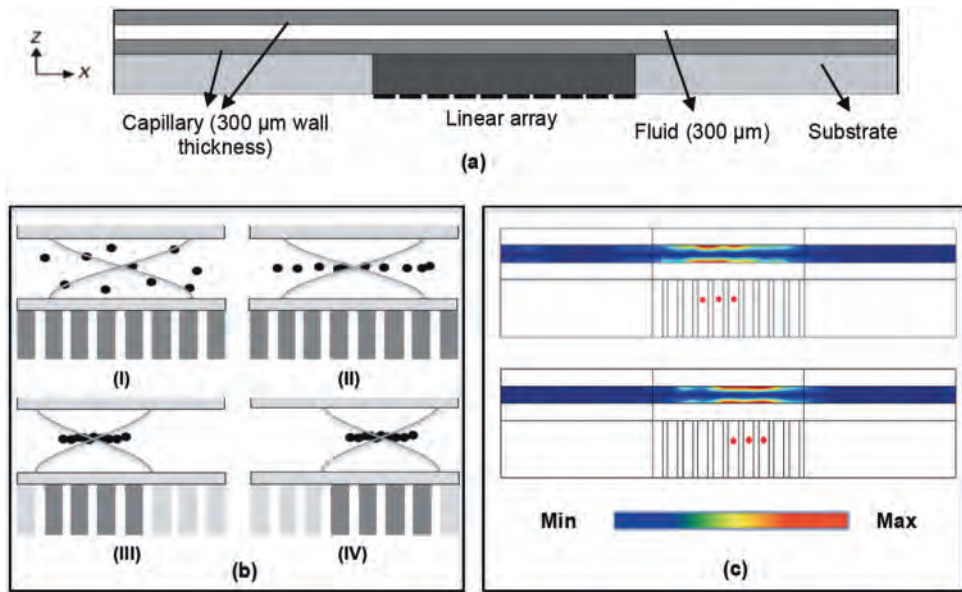


Figure 7 - (a) Cross-section of 1D array manipulation device with capillary; (b) particle lateral manipulation with shifting active array elements; (c) Finite element simulation of shifting the position of potential energy density.

A planar resonator with a 12-element 1D linear array coupled to a capillary was fabricated to assess lateral trapping and manipulation, as shown in Fig. 8(a). A $6 \times 4 \times 2 \text{ mm}^3$ piece of piezoceramic (PZ26, Ferroperm Piezoceramics, Denmark) was embedded in a substrate, which was made from epoxy (Epofix, Struers A/S, Ballerup, Denmark) filled with glass microballoons (Lawrence Industries, Tamworth, UK) as before, to prevent the coupling of ultrasonic energy into the substrate. The PZ26-epoxy wafer was lapped to the specified thickness of 1.0 mm before Ag-paint electrodes were applied to each face. Signal tracks on a printed circuit board (PCB) fixed to the back surface of the PZ26 were connected electrically to the transducer electrodes with silver epoxy. The 12 array elements were defined by scratch-dicing the electrodes, silver epoxy and the PCB together with a high precision dicing saw, as shown in Fig. 8(b).

The ground electrode on the front face was connected to the PCB as well. The other end of PCB was soldered with a 13-pin connector to connect to an external electronic controller. The array was then placed in a housing and coupled to the capillary.

An experiment with 10 μm diameter fluorescent beads was carried out to evaluate device performance. When array elements were active, the beads moved quickly to the pressure nodal plane in the middle of the capillary because of the axial radiation forces, and formed an agglomeration above the active elements because of the lateral radiation forces. Once the particles were agglomerated, they were moved along the channel by selecting other active elements. The result in Fig. 8(c) shows motion of an agglomeration approximately 500 μm long along the channel. Very little leakage of particles from the agglomeration was observed, indicated that the beads were strongly trapped.

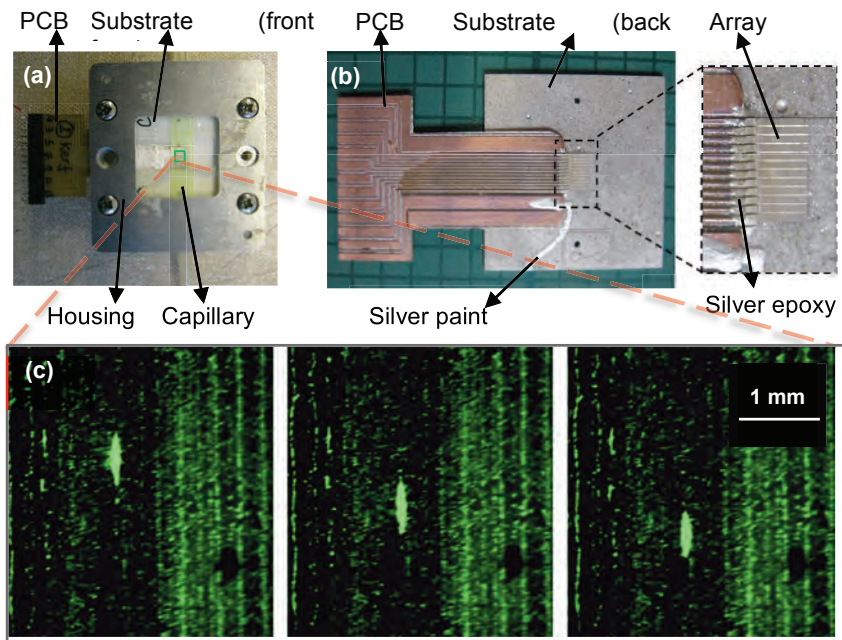


Figure 8 - (a) fabricated array with PCB connection; (b) assembled device; (c) successive microscope images of fluorescent polystyrene bead agglomerates moving along fluid channel [7].

Conclusion

The high frequency single element resonator demonstrates how a high frequency ultrasound transducer can be coupled with a reflector to trap particles in multiple trapping sites with a short standing wavelength of the same order as the cell diameter. Issues such as temperature changes and reinforced streaming require further attention, but the results to date are encouraging. The device based on the 1D array shows the feasibility of manipulating particles laterally along a channel by selecting alternate sets of active array elements. In this case, further exploration is required with arrays with more elements. The structure also has the potential of expansion into 2D, very significantly increasing its flexibility and functionality.

Acknowledgements

The authors would like to thank Keith Mayne, PCT Ltd. (Aberdeen, UK), Jim McAneny, Logitech Ltd. (Glasgow, UK), and the partners of the Sonotweezers project at the Universities of Bristol, Dundee, Glasgow and Southampton, particularly Kees Weijer, Dave Hughes, Martyn Hill and Peter Glynne-Jones, for their contributions, support and assistance in this research.

References

1. T. Laurell, F. Petersson, A. Nilsson, *Chip integrated strategies for acoustic separation and manipulation of cells and particles*. Chem. Soc. Rev., 2007. **36**: p. 492-506.
2. H. Böhm et al., *Viability of plant cell suspensions exposed to homogeneous ultrasonic fields of different energy density and wave type*. Ultrasonics, 2000. **38**(1-8): p. 629-632.
3. J. Hultstrom et al., *Proliferation and viability of adherent cells manipulated by standing-wave ultrasound in a microfluidic chip*. Ultrasound Med Biol, 2007. **33**: p. 145-51.
4. A. Nilsson, F. Petersson, H. Jonsson and T. Laurell, *Acoustic control of suspended particles in micro fluidic chips*. Lab Chip, 2004. **4**: p.131-135.
5. M. Hill and N. Harris, *Ultrasonic Particle Manipulation, Microfluidic Technologies for Miniaturized Analysis Systems*. S. Hardt and F. Schonfeld, Eds., New York, Springer, 2007, p. 357-353.
6. L. P. Gor'kov, *On the forces acting on a small particle in an acoustical field in an ideal fluid*. Sov. Phys. Dokl., 1962. **6**: p.773-775.
7. C. Demore et al., *Transducer Arrays for Ultrasonic Particle Manipulation*. IEEE International Ultrasonics Symposium, 2010.
8. Y. Qiu et al., *Multi-wavelength Ultrasonic Standing Wave Device for Non-invasive Cell Manipulation and Characterisation*. IEEE International Ultrasonics Symposium, 2011.

4

A new device for fabrication of lipid-shelled microbubbles

Joe Fiabane¹, Ritu Malik², John Steel¹, Sandy Cochran²,
Paul Prentice², Ketan Pancholi¹

¹The Robert Gordon University, Aberdeen, UK

²Institute of Medical Science and Technology, Dundee, UK

Abstract

Targeted delivery of therapeutic agents using ultrasound in combination with microbubbles has significant potential for the treatment of genetic conditions and for anti-cancer applications. The role of the microbubble in the approach is to act as both a drug-vehicle, and to be responsive to the application of focused ultrasound, generally administered extra-corporeally. These functions are highly sensitive to the size, and size distribution, of the microbubble population. Improved fabrication techniques are therefore critical to realizing the potential of drug delivery via this modality. Specifically, generating microbubbles small enough to pass through the vasculature, of a narrow size distribution to homogenize insonation response, and enabling the encapsulation of viscous drugs into the microbubble architecture, are crucial factors. Previously reported approaches to generating monodisperse microbubbles typically rely on small internal structures and geometries, which are very susceptible to becoming congested and blocked. Here, we report on the development of a new device with components on the order of 100 μm , capable of producing stable microbubbles below 5 μm in diameter.

Introduction

Microbubbles in medicine

Microbubble suspensions are well established in medicine through their use as contrast agents during diagnostic imaging procedures. Recently research has extended to developing the potential microbubbles have exhibited in a therapeutic context, as carriers for targeted drug delivery. This potential application brings with it new demands for specific microbubble characteristics, requiring more advanced manufacturing methods. The ultrasound-mediated dynamics of a microbubble adjacent to a cell can result in transient permeabilisation of the cell membrane (often referred to as 'sonoporation'), sufficient to allow the delivery of drug molecules to the cytosol. This approach, together with the use of focused ultrasound, constitutes a highly localised and minimally invasive modality for drug delivery, whereby surrounding healthy tissue and cells are virtually unaffected [8-10]. However the response of a microbubble to a given ultrasound exposure is highly dependent on the microbubble diameter, and insonation frequency [3], hence the need for a monodisperse population with strict control over size.

Microbubble fabrication

Existing commercially available microbubble agents typically consist of high molecular weight gas cores, encapsulated by a stabilizing shell of lipids, polymers, proteins or surfactants [1-5]. These bubbles are produced either by sonication [6] or mechanical agitation of a suspension of the shell material in water, in the presence of the core gas. This process is simple and inexpensive but results in microbubbles of a broad size distribution. While larger bubbles ($>10\text{ }\mu\text{m}$) can be removed to reduce the risk of embolism, the final product remains highly polydisperse [7]. This is acceptable for diagnostic imaging contrast agents, however for drug delivery applications, microbubbles of average size $<10\text{ }\mu\text{m}$ and of a narrow size distribution are highly desirable.

Microfluidic techniques

Microfluidics-based methods of microbubble production are capable of producing highly monodisperse populations, and are adaptable to commercial-scale operations due to ease of manufacturing [11]. The two main types of microfluidic device used are T-junctions [12] and flow-focusing devices. T-junction devices (Fig. 1a), as the name suggests, consist of a straight channel (x, typical cross-section $100 \times 33\text{ }\mu\text{m}$) etched into a polymer block, or formed using capillaries, with a second channel (y) incident to it orthogonally. The liquid phase can be introduced via the x channel and the gas via the y (Fig. 1(a)(i)), or vice versa (Fig. 1(a)(ii)). The mechanism of bubble formation varies depending on the configuration. When the gas enters via the x channel, it first flows across the front of the y channel, at which point the liquid flow impinges upon it, squeezing it against the opposite wall, forming a neck and pinching off a bubble, which flows through the exit channel before the process repeats [13]. In the alternative

configuration, the gas emerges from the y channel into the liquid stream, the pressure of which forces the protruding gas downstream. The liquid pressure at the interface increases until a neck forms against the downstream edge of the y channel and a bubble is sheared off [14]. Both mechanisms involve laminar flows. T-junctions produce bubbles with very narrow size distribution (Table 1). Flow-focusing devices (Fig. 1b) consist of three converging channels, the central channel carrying the gas phase and the two outer channels carrying liquid. The flows meet and exit through a narrow aperture. The action of the outer liquid focuses the gas flow into a cone, passing through the aperture as a narrow thread which is broken up into small and uniform-sized bubbles by a sudden increase in liquid pressure at the gas-liquid interface, caused by the syringe pump trying to establish constant flow [15, 16]. The flow in this breakup mechanism is also laminar.

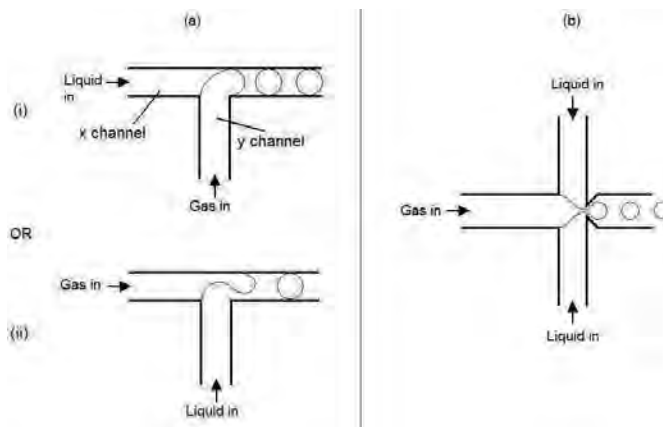


Figure 1 – (a) Possible T-junction microfluidic device configurations, (b) Flow-focusing device.

Therapeutic Microbubbles fabrication

Before microfluidic methods of microbubble production can be adopted commercially, a number of production criteria should be demonstrated. Specifically, (i) a microbubble concentration of $10^6/\text{ml}$ is desirable for drug delivery applications [17], (ii) the system must be capable of operating with viscous fluids [18] such as the drug doxorubicin in aqueous solution, whose viscosity is dependent on concentration but can be as high as 9 cSt [19], (iii) must demonstrate the facility of encapsulating a drug within the microbubble structure [20] and finally (iv) must be practical to operate. The problem with the practicality of existing methods lies in the requirement for high operating pressures and very small geometry. Flow-focusing devices and T-junctions produce microbubbles of similar diameter to the channel or aperture. The geometries necessary to produce bubbles below $10\text{ }\mu\text{m}$ are thus highly susceptible to blockage.

	Sonication [7]	T-junction [7]	Flow focusing [21]
Mean diameter	10.5 μm	30 μm	5 μm
Standard deviation	18.5 μm	0.3 μm	0.1 μm
Typical yield per ml	1×10^7	2×10^8	1×10^5

Table 1: Microbubble population size characteristics for various fabrication techniques.

In this paper we present recent work on the development of a novel microfluidic device which utilizes breakup of the composite gas-in-liquid jet in a turbulent regime. We demonstrate the production of stable suspensions of microbubbles, of diameter $< 5 \mu\text{m}$, using relatively low pressures and an aperture with diameter $100 \mu\text{m}$. The fabrication process bears similarities to the flow-focusing method in that a cone is formed, breaking up as it passes through an aperture. However a second gas phase, air, is added outside the liquid, and can be used to precisely control the diameter of the cone. Utada *et al.* reported a three-phase system involving three immiscible liquids using laminar breakup to form a double emulsion [22]. Our approach is a three fluid system capable of producing microbubbles. However, unlike their method, the outermost fluid (air) in our system acts to induce turbulent break-up. The significant difference in viscosity between the liquid and the core gas causes problems in encapsulating the gas inside the liquid. In contrast with the oil used as the central fluid in [22], our core gas has a tendency to escape from the surrounding liquid phase resulting in failed microbubble formation. Regulating the interfacial tension between air, liquid and aperture material is important in overcoming this difficulty and achieving successful encapsulation.

Methodology

The Virtual Aperture Dynamic Control (VADC) Device

The device consists of a pair of concentric capillaries within a pressurised acrylic chamber (Fig. 2). The outer capillary carries the liquid phase and the inner carries the core gas. The fluids emerge from the capillaries into the pressurised chamber, forming a two-phase flow towards the adjacent $100 \mu\text{m}$ aperture. The flow of the outer air exiting the chamber draws the two-phase flow through the aperture, forming a characteristic “cone” shape (Figs. 2(inset) & 3) ending in a narrow thread much smaller than the aperture itself. The precise diameter of the liquid and core gas streams are dependent on the pressure of the surrounding air. In this way, surrounding air controls the diameter of the effective aperture through which liquid-air jet is passing, or acts as a virtual aperture. This effect is termed “Virtual Aperture Dynamic Control” (VADC). As

this flow exits the device alongside the surrounding air flow, the sharp pressure drop causes turbulent behaviour, breaking the core gas stream into microbubbles.

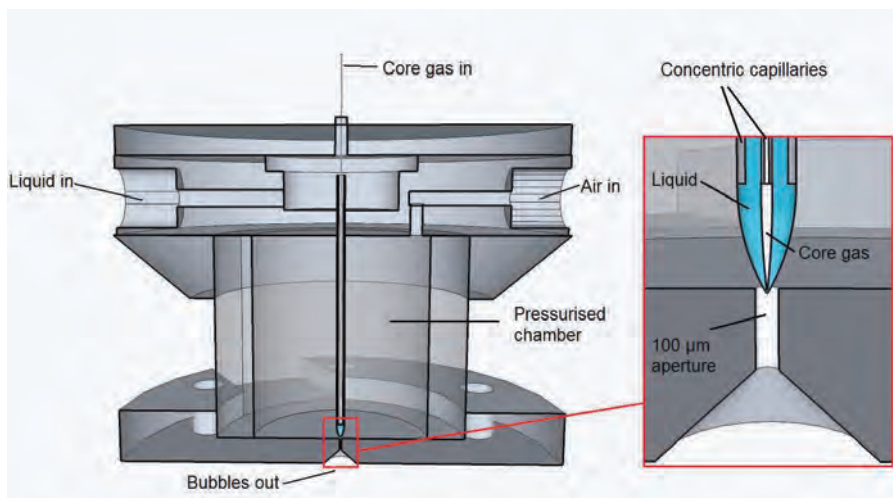


Figure 2 – VADC device (not to scale).

Microbubble chemistry

The liquid phase consists of a suspension of phospholipid and surfactant at a ratio of 9:1 mol/mol in water. The lipid used is 1,2-distearoyl-*sn*-glycero-3-phosphocholine (DSPC) (Avanti Polar Lipids, Alabaster, AL) and the surfactant polyethyleneglycol-40-stearate (Sigma-Aldrich, St. Louis, MO). These form a stabilising monolayer around the microbubbles, extending their shelf life [1]. Experiments have been carried out using air nitrogen and perfluorobutane (F2 Chemicals, Preston, UK) as the core gas.

The lipid DSPC and PEG-40-stearate are dissolved in chloroform, vacuum dried to form a thin film and resuspended in distilled water. The lipid suspension is sonicated in an ultrasonic cleaning bath for efficient and complete dispersion of the solids. The lipid suspension is subsequently stirred overnight in 1 atmospheric pressure air surroundings to achieve air saturation for preparing air-surrounded PFB microbubbles. The lipid suspension is introduced in the device via flexible tubing using a syringe pump to control flow rate. The core gas and air are supplied from cylinders using two-stage regulators. A camera (pco.1600, PCO AG, Kelheim, Germany) attached to a PC is used to monitor and record the formation and behaviour of the fluid cone. Bubbles are collected on a glass slide for examination and measurement by optical microscope. Image processing software Infinity Analyze (Lumenera Corporation, Ottawa, Canada) facilitates manual measurement of bubbles on saved images.

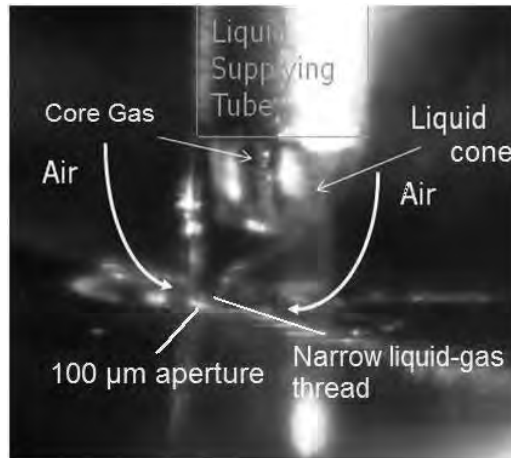


Figure 3 - Cone formation between capillaries and 100 µm aperture (see also Fig.2 inset). Here the capillaries are slightly misaligned to the right of the aperture, hence the cone twists to the left to pass through.

Results

Microbubble sizes were analysed for various input parameters. It was found that the size and yield of bubbles can be closely controlled by varying the inner gas (P_g, Q_g) and outer air (P_a, Q_a) pressures and flow rates, and the liquid flow rate (F_l). Microbubble diameter (D_b) tends to decrease with increasing outer air pressure, or increasing liquid

flow rate, but increase slightly with increasing inner gas pressure. The flow ratio $\frac{Q_g}{Q_a}$, is directly proportional to microbubble diameter (Fig. 4). The most notable effect of increasing the inner gas pressure, however, is to increase the number of bubbles produced.

The yields were assessed by placing a sample in a haemocytometer slide of volume $4 \times 0.1 \mu\text{m}$ and counting manually. At optimal operation the device is capable of producing around 30 million bubbles/ml, of median size $< 5 \mu\text{m}$. Samples were examined at regular intervals for various microbubble compositions in order to determine the effect on bubble stability. Lipid monolayer-stabilised air bubbles disappeared within one hour. When the core gas was changed to nitrogen, stability increased to around 17 hours, with some bubbles remaining after up to 66 hours. Perfluorobutane bubbles (Fig. 5) lasted up to two weeks when refrigerated, due to its slower dissolution.

Discussion

Influence of outer air pressure

The outer air pressure P_o represents the principal means of controlling the size of microbubbles fabricated using this device. This is due to the pressure acting on the outer surface of the liquid flow which compresses the enclosed air stream such that the 2-phase flow becomes a fine thread. Analysis of images captured using the camera indicate that as outer air pressure increases, the diameter of the inner air flow decreases. Secondly, the sudden drop in pressure as the two-phase thread exits the device causes a significant increase in velocity. This leads to turbulent behaviour, resulting in air velocity fluctuations at the liquid surface, and hence pressure fluctuations causing stresses which finally break the two-phase flow into droplets containing microbubbles. Therefore the size of microbubbles is also dependent on the velocity at exit, thereby providing an alternative mechanism by which the air pressure within the chamber affects microbubble diameter. There is a minimum value of outer gas pressure which will result in cone formation and compress the two-phase thread sufficiently for it to pass through the aperture without contacting the sides. At pressures below this threshold the output degrades from a microbubble spray to drip formation at the aperture. This critical pressure value is also strongly dependent on liquid flow rate. For example, when liquid flow rate is set at 0.2 ml/min the threshold pressure is 2.5 bar, whilst increasing the flow rate to 0.4 ml/min causes the threshold pressure to increase to 3.5 bar.

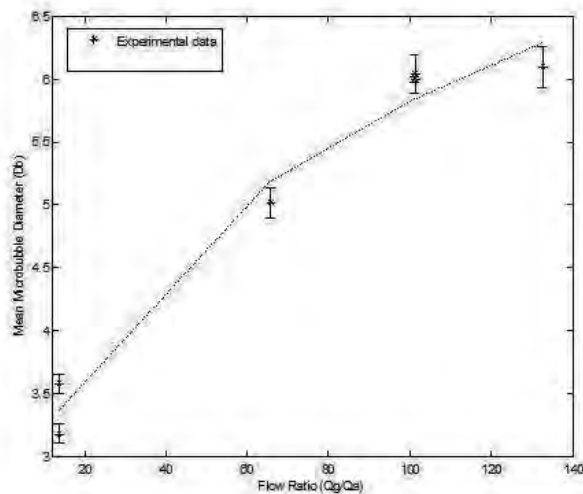


Figure 4 – graph showing flow ratio vs microbubble diameter.

Core gas pressure

Increasing the core gas pressure P_i tends to increase the microbubble size. However, adjustment of this value is restricted as liquid is forced up the inner gas capillary if the core gas pressure is too low for a given outer air pressure, and flow of the inner gas becomes impeded. Conversely, if the inner gas pressure is too high then the gas bursts out from within the cone and controlled microbubble production is impossible. For a given liquid flow rate there is a restricted range for the ratio of $P_o:P_i$ that will give a steady cone in the microbubble-producing regime. For a liquid flow rate of 0.4 ml/min, for example, this ratio is limited to 1.5 – 1.7. Increasing the liquid flow rate tends to decrease the available $P_o:P_i$ values.

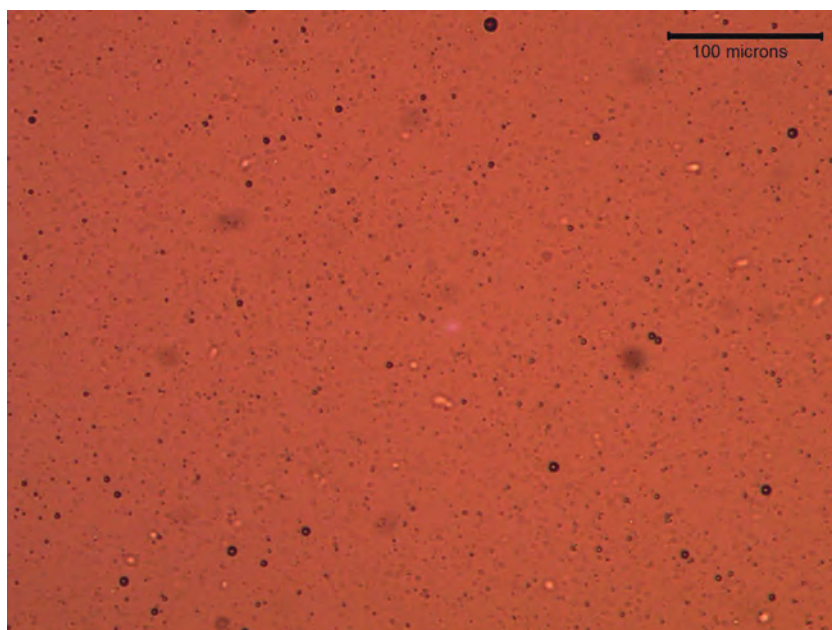


Figure 5 – Lipid-stabilised perfluorobutane bubbles. Scale bar represents 100 μm .

Conclusion

The VADC device is capable of producing microbubbles as small as one-twentieth the diameter of the exit aperture. To our knowledge, this is the lowest value for ratio of bubble diameter to aperture diameter achieved so far. This has a distinct advantage over existing microfluidic technologies as the relatively large internal geometry is much less susceptible to congestion and blockages. Moreover, it is capable of operating with more viscous fluids and particulate suspensions than existing techniques, and can produce yields of at least 30×10^6 microbubbles/ml. Current work is being undertaken to determine the theoretical relationship between input parameters and microbubble

size, and incorporating additional capillaries to the device to facilitate multi-layer shells and drug encapsulation.

Acknowledgements

Joe Fiabane acknowledges support from the Northern Research Partnership. Paul Prentice acknowledges the Norwegian Research Council for an Yggdrasil mobility grant. This research was funded by The Robert Gordon University and EU FP7 grant 'Nanoporation' at IMSaT, University of Dundee.

References

1. Sirsi, S.R. and M.A. Borden, *Microbubble compositions, properties and biomedical applications*. Bubble Science, Engineering and Technology, 2009. **1**: p. 3-17.
2. Calliada, F. et al., *Ultrasound contrast agents Basic principles*. European Journal of Radiology, 1998. **27**: p. S157-S160.
3. Liu, Y., H. Miyoshi and M. Nakamura, *Encapsulated ultrasound microbubbles: Therapeutic application in drug/gene delivery*. J. Control Release, 2006. **114**: p. 89-99.
4. Bjerknes, K. et al., *Preparation of polymeric microbubbles: formulation studies and product characterisation*. International Journal of Pharmaceutics, 1997. **158**, p. 129-136.
5. Yang, F. et al., *Superparamagnetic iron oxide nanoparticle-embedded encapsulated microbubbles as dual contrast agents of magnetic resonance and ultrasound imaging*. Biomaterials, 2009. **30**: p. 3882-3890.
6. Feshitan, J.A., C.C. Chen, J.J. Kwan and M.A. Borden, *Microbubble size isolation by differential centrifugation*. Journal of Colloid and Interface Science, 2009. **329**: p. 316-324.
7. Stride, E. and M. Edirisinghe, *Novel preparation techniques for controlling microbubble uniformity: a comparison*. Med Biol Eng Comput, 2009. **47**: p. 883-892.
8. Van Wamel, A. et al., *Vibrating microbubbles poking individual cells: Drug transfer into cells via sonoporation*. J. Control Release, 2006. **112**: p. 149-155.
9. Qin, S., C.F. Caskey and K.W. Ferrara, *Ultrasound contrast microbubbles in imaging and therapy: physical principles and engineering*. Phys. Med. Biol., 2009. **54**: p. R27-R57.
10. Postema, M., A. van Wamel, C.T. Lancee and N. de Jong, *Ultrasound-induced encapsulated microbubble phenomena*. Ultrasound in medicine and biology, 2004. **30**: p. 827-840.
11. Martinez, C.J., *Bubble generation in microfluidic devices*. Bubble Science, Engineering & Technology, 2009. **1**: p. 40-52.
12. Garstecki, P., M.J. Fuerstman, H.A. Stone and G.M. Whitesides, *Formation of droplets and bubbles in a microfluidic T-junction - scaling and mechanism of break-up*. Lab Chip, 2006. **6**: p. 437-446.
13. Xiong, R. and J.N. Chung, *Bubble generation and transport in a microfluidic device with high aspect ratio*. Experimental Thermal and Fluid Science, 2009. **33**: p. 1156-1162.
14. Zhao, C.-X., and A.P.J. Middelberg, *Two-phase microfluidic flows*. Chemical Engineering Science, 2011. **66**: p. 1394-1411.
15. Gañán-Calvo, A.M., *Generation of Steady Liquid Microthreads and Micron-Sized Monodisperse Sprays in Gas Streams*. Phys. Rev. Lett., 1998. **80**: p. 285-288.
16. Gañán-Calvo, A.M., and J.M. Gordillo, *Perfectly Monodisperse Microbubbling by Capillary Flow Focusing*. Phys. Rev. Lett., 2001. **87**: p. 274501.
17. Van Wamel, A. et al., *Radionuclide tumour therapy with ultrasound contrast microbubbles*. Ultrasonics, 2004. **42**: p. 903-906.

18. Judy, J., D. Maynes and B.W. Webb, *Characterization of frictional pressure drop for liquid flows through microchannels*. International Journal of Heat and Mass Transfer, 2002. **45**: p. 3477-3489.
19. Hayakawa, E. et al., *Studies on the Dissolution Behavior of Doxorubicin Hydrochloride Freeze-Dried Product*. Chem. Pharm. Bull., 1990. **38**: p. 3434-3439.
20. Castro-Hernández, E., W. van Hoeve, D. Lohse, and J.M. Gordillo, *Microbubble generation in a co-flow device operated in a new regime*. Lab Chip, 2011. **11**: p. 2023-2029.
21. Hettiarachchi, K. et al., *On-chip generation of microbubbles as a practical technology for manufacturing contrast agents for ultrasonic imaging*. Lab Chip, 2007. **7**: p. 463-468.
22. Utada, A.S. et al., *Monodisperse Double Emulsions Generated from a Microcapillary Device*. Science, 2005. **308**: p. 537-541.

5

Hybrid laser-ultrasound cavitation for cloud evolution studies

Bjoern Gerold¹, Spiros Kotopoulis², Sandy Cochran¹,
Michiel Postema², Paul Prentice¹

¹Institute of Medical Science and Technology (IMSaT), University of Dundee, Dundee DD2
1FD, UK

²Department of Physics and Technology, University of Bergen, Allégaten 55, 5007 Bergen,
Norway

Abstract

We report on the development of an instrument for hybrid ‘sonoptic’ cavitation studies. A focused ultrasound transducer is housed in a custom-built chamber, which permits optical access to the focal volume, without perturbing the propagating acoustic waves. This configuration allows pulsed-laser irradiation of the liquid at the focus, and simultaneous high-speed observation of cavitation activity in this region. In this paper we provide a brief description of the apparatus and present preliminary data on the distinct cavitation regimes we have observed; specifically, laser-induced cavitation in an established field, and a new phenomenon that we refer to as *laser-nucleated acoustic cavitation*. The former involves a laser-pulse of energy above the threshold value for optical breakdown for the medium, in a pre-established ultrasound field. Here, a cavity rapidly expands to a maximum diameter of a few 100 μms , from the plasma generated on absorption of the optical energy, and collapses to form debris that is subsequently driven by the ultrasound radiation. By contrast, laser-nucleated acoustic cavitation is initiated by a pulse of *energy below the breakdown threshold*, in a pre-established field. For this regime, either form of radiation does not result in cavitation activity without the

other. In combination, the role of the laser-pulse is to initiate activity which is dominated by the ultrasound exposure from the outset. Crucially, the spatial and temporal precision afforded to the occurrence of cavitation by laser-nucleation, allows us to consolidate our assertion of acoustic cavitation. With observations at unprecedented resolutions, we compare the size of constituent cavities *within a single acoustical cycle* to theoretical predictions, based on the frequency of the ultrasound driving the activity. It is expected that such observations will contribute to a greater understanding of cavitation in focused ultrasound, including for potential future therapeutic applications.

Introduction

Acoustic cavitation

Acoustic cavitation refers specifically to the formation and subsequent activity of bubbles, or cavities in the pressure fluctuations of an acoustic field, to distinguish from its mechanical or hydro-dynamical counterparts. The phenomenon is a common occurrence in the application of high intensity focused ultrasound (HIFU) fields to the ablation of diseased tissue, known as focused ultrasound surgery (FUS). In this emerging technique, ultrasound is focused transcutaneously to the site of pathology, thus alleviating the need for conventional surgical intervention, and associated risk of infection and extended patient recovery times. In current clinical procedure, the heating is achieved via viscous absorption of the mechanical energy [1], which is most intense at the focus, where the pressure amplitudes are the largest within the field. Heating also occurs in surrounding healthy tissue, such as in the near-field, but at levels that are not harmful, provided the exposure is not prolonged.

Acoustic cavitation occurs in FUS when the rarefactional tension imposed on the tissue during a negative pressure phase, is sufficient to form microscopic cavities, which fill with gas and vapour extracted from the host tissue. The occurrence of the phenomenon depends on a complex mix of the physical properties of the tissue, and the ultrasonic exposure parameters [1]. Continued HIFU excitation acts to further drive the bubble dynamics with a wide range of subsequent physical activity possible, including net growth through rectified diffusion, repulsion due to radiation forces, cloud formation via bubble-bubble interactions (fragmentation and coalescence), and free-radical production or sonochemistry (to mention but a few). It is generally recognized that cavitation in FUS has significant potential to mediate enhanced therapy, such as rapid tissue heating by 'trapping' of the acoustic energy at the focus, or promoting drug delivery via tissue extravasation and microstreaming/pumping [2]. Translation of the phenomenon into medical practice is hampered, in part, by a fundamental lack of understanding of the rapid development of cavitation under HIFU exposure, and parallel development of acoustical detection techniques for monitoring and control purposes. Nonetheless, a growing body of literature demonstrates both active and passive methods of acoustical cavitation detection, and correlation to cavitation related bio-effects in tissue [3], and tissue-mimicking materials [4]. The deficit in understanding cavitation evolution, particularly over the first few hundred acoustic cycles, stem from

several inherent difficulties in studying the phenomenon *in vitro*, including: (1) uncertainty in predicting the exact location within the field, and moment, of cavitation inception, (2) ultra-fast dynamics, driven at the MHz frequencies typical for FUS applications, and (3) cavities in MHz fields tend to be of the order of a few microns. This may be theoretically inferred with the 'rule-of-thumb' simplified *Minnaert's equation* [5], for bubble radius, R_f resonant to a central ultrasound frequency, f_c , given by;

$$R_f f_c \approx 3 \text{ ms}^{-1}$$

It may be appreciated that direct observational verification of bubble size is challenging for these reasons. Several studies have attempted to observe and characterize cloud evolution in HIFU fields with high-speed cameras, for example [6]. The best high-speed photography devices available are certainly capable of framing at the Nyquist sampling rate for MHz ultrasound, necessary to fully resolve dynamics. Microscopy objective lenses are also well capable of resolving objects on the micron scale. The researchers were, however, forced to image at spatial and temporal resolutions far below those necessary to make any meaningful observations of cavitation clouds, simply to guarantee the imaging of something! As such, they were restricted to presenting images of 'established' clouds on the millimetre scale, at 10 kHz sampling rates, with little impact on the understanding of the dynamical evolution.

Other researchers have resorted to less direct means for studying cavity sizes in acoustic fields. One such technique relies on sonoluminescence observations in pulsed ultrasound of varying inter-burst durations [7, 8], assuming quiescent bubbles dissolve over a period determined by the initial size. Brothie *et al* [8] developed the technique to report that resonant bubble radii in a 1056 kHz field increase with acoustic power, up to some threshold intensity, at which stage R_f stabilizes at $\sim 5 \mu\text{m}$.

Another approach, based on a similar principle, employed active pulse-receive acoustic detection of bubbles, nucleated via HIFU induced destruction of ultrasound contrast agents (UCAs) [9]. The authors used acoustic scattering to measure resonant dissolution times for 'freed bubbles' in a 1.1 MHz field - at pressure amplitudes similar to those of the present work - by comparing scattering patterns to models adjusted to account for the diffusivities of UCA core gases. Although they had to assume multiple size distributions to fit the data, features from the scattering amplitudes corresponded to R_f 's $\approx 0.45, 1.2$ and $1.56 \mu\text{m}$.

Laser-induced cavitation

In contrast to its acoustic counterpart LIC is a very well characterized and understood phenomenon [10], with interest driven largely by ophthalmology applications. This owes to the reliability and reproducibility of employing laser-pulses to generate a cavity at a location, pre-defined by the focal point of a lens, used to concentrate the optical energy into the host medium. LIC studies have contributed greatly to the understanding of

especially single cavity activity, such as jet-formation in the presence of a boundary, and its dependence on the cavity-boundary distance [11]. Although the laser-medium interaction (and to an extent the resulting cavity, such as the degree of asymmetry that evolves) depends somewhat on parameters such as the pulse duration [12], it is well known that the process is plasma-mediated. Absorption of the optical energy at the focus causes localized weak breakdown to form a plasma, which rapidly expands to form a 'hot' cavity of vapour and gas. The requirement for plasma formation imposes an energy threshold on the pulse, below which breakdown does not occur, and a cavity does not form. These factors also translate to a typical lower bound for the maximum diameter LIC bubbles can have, following the initial inflation stage – generally a few 100 μm , with millimetre-sized bubbles being commonly investigated.

In this paper we describe a sonoptic chamber for hybrid laser-acoustic cavitation studies. We use a propagating HIFU field, and introduce cavitation activity by optically focusing a nanosecond laser-pulse into the US focal volume. We have found that reducing the pulse energy to below the breakdown threshold for the system, allows *cavitation nucleation*, without the characteristically large (relative to R_f determined by the field frequency f_c) bubble formation associated with conventional LIC.

Methodology

The hybrid laser-ultrasound experimental platform has been described in detail elsewhere [13], but a short overview is given here for background. The key feature is the sonoptic chamber that accommodates a HIFU field, the focal region of which can be irradiated with a laser-pulse and observed through a microscope objective lens. We employ a 3 nanosecond frequency-doubled neodymium-doped yttrium aluminium garnet (Nd:YAG) laser-pulse for cavitation induction and nucleation. The pulse is steered into the back aperture of a long working distance objective lens (Mitutoyo 50 \times 0.42 NA MPlan NIR ∞ -corrected), from a dichroic mirror reflective to the laser wavelength, 532 nm. The sonoptic chamber is custom-built to 'fit' the HIFU field of a 1.47 MHz focused-bowl transducer, such that the field propagates unhindered by reflection or scattering – other than from cavitation intentionally introduced to the focal region. In this way unwanted interference effects are avoided, and the focused ultrasound may be expected to propagate as it would in an idealised FUS procedure. Fig. 1 (a) depicts the dual focus (optic and ultrasonic) region of the apparatus, schematically. The central glass box is the 'confocal chamber' and contains the liquid which hosts the cavitation activity reported below. The objective lens configuration of fig 1 (a) is that used for the observations reported, whereby one lens focuses the laser and a second orthogonally orientated lens (Mitutoyo 5 \times 0.14 NA MPlan APO ∞ -corrected) is used for imaging purposes. This configuration decouples the laser axis from the imaging and allows the laser spot to be translated independently (as distinct from imaging through the focusing lens as described previously [13]). Fig. 1 (b) and (c) depicts the US focus within the confocal chamber, where cavitation is instigated. The transducer is driven by a sinusoid signal from a function generator (Tektronix) passed through an RF power amplifier (Electronics and Innovation) and impedance matching

network. Alignment of the ultrasonic and laser foci is critical to reproducibility, and is achieved through Schlieren imaging to visualise the ultrasound focus, and translation of the chamber to coincide to the laser spot, inset Fig. 1 (a), [14]. Two high-speed cameras were used for the collection of the data presented below, courtesy of the EPSRC instrument loan pool, the Shimadzu HPV-1 and Cordin 550-62. The former is capable of 100 frames at up to 1 Mfps, the latter 62 frames at up to 4 Mfps. The Cordin is a compressed gas-driven rotating drum device, with a formidable reputation. The sensitive optics of the cameras are protected from scattered laser radiation with a green optical filter.

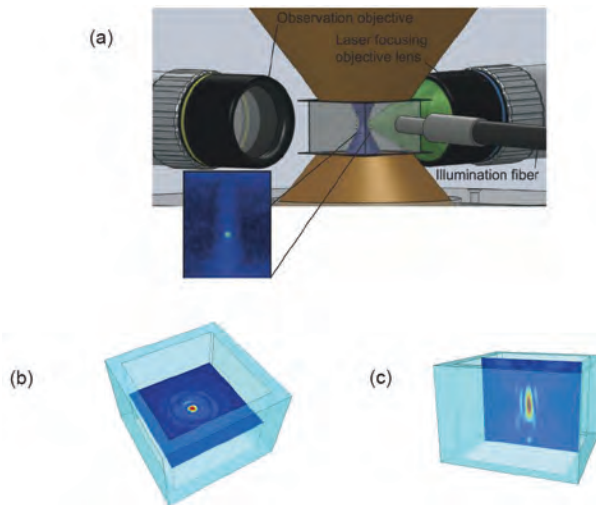


Figure 1. Schematic representation of the sonoptic chamber, housing the ultrasound focal volume, and the optical focus of a laser pulse passed through a long working distance microscope objective lens. Inset is a schlieren image of the focal volume (lighter blue) used to align the optical focus (green spot). Simulated, and to-scale representation of the (a) transverse, and (b) axial focus of the HIFU field, within the confocal region of the sonoptic chamber, which has dimensions: 20x20x14mm. Higher peak pressures are indicated red, with ambient atmospheric pressure represented as deeper blue. It can be seen that the chamber housing does not interfere with the propagating pressure field.

Quoted laser-pulse energies are measured at the back aperture of the objective lens with a power meter (ThorLabs), and HIFU peak negative pressure (PNP) amplitudes with a fibre-optic hydrophone (Precision Acoustics). Spatial scales for the high-speed images presented were determined by imaging flow cytometry beads of diameters 10 and 50 μm , *in situ*. For an experiment, the laser is switched to single pulse mode and triggered from the high-speed camera, with an appropriate delay for the Q-switch. The HIFU field is pre-established (turned on) 5-10 seconds before the laser-pulse is generated, and high-speed photography initiated. All the results presented below use degassed (to $< 4 \text{ mgL}^{-1}$ of dissolved oxygen) tap water as the host medium. The optical breakdown threshold for the system, defined as the pulse energy below which no LIC was observed, was determined to be $1.10 \pm 0.02 \text{ mJ}$, where the error is attributed to

instrumental fluctuations in the pulse energies generated, according to the user manual and consistent with our own power meter measurements.

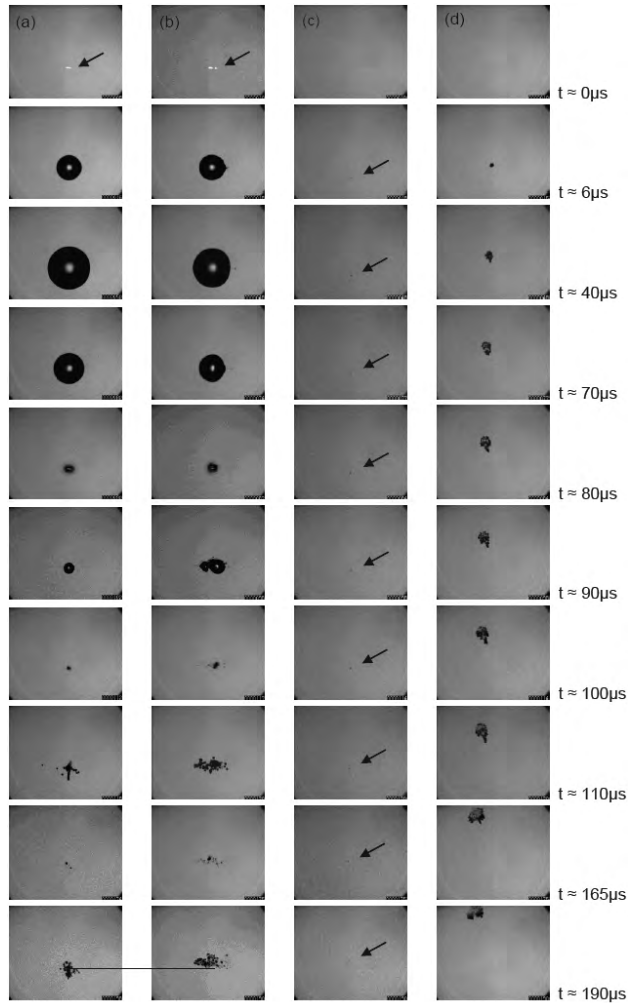


Figure 2 - Selected individual frames extracted from high speed sequences recorded with the Shimadzu HPV-1 camera operating at 0.5 Mfps ($\times 10^6$ frames per second), depicting the various regimes of laser-ultrasound cavitation that may be studied with the apparatus: (a) Laser-induced cavitation (LIC) formed with a laser pulse of above the breakdown threshold, (b) LIC in a low intensity ultrasound field. The line across the 190 μ s images serves to indicate the upwards translation of the debris cloud in the presence of ultrasound. (c) Laser nucleated acoustic cavitation (LNAC) with a laser-pulse below the breakdown threshold, in a low intensity, pre-established ultrasound field, and (d) LNAC in a high intensity, pre-established field. Each frame is 1.2 mm in width.

Results and Discussion

Fig. 2 (a)-(d) represents the various forms of laser-acoustic cavitation that may be studied with the experimental architecture described. Sequence 2 (a) is representative of conventional LIC, as described in the introductory section above. A 1.20 ± 0.02 mJ pulse is focused into the water, of sufficient energy to cause optical breakdown and plasma formation. A spherical cavity of gas and vapour subsequently expands over ~ 40 μ s to a maximum radius, $R_{\max} \approx 300$ μ m. The inertia of the liquid acts to collapse the cavity over the next ~ 40 μ s, which then oscillates through a series of rebounds, with a period of ~ 20 μ s.

The cavitation debris in the aftermath of the primary LIC is subject to two further stimulations, at ~ 110 and ~ 190 μ s. It is well known that plasma formation through the absorption of a laser pulse generates a spherically radiating acoustic transient, as does the collapse of an LIC [10,12]. As the absorption occurs at ~ 0 μ s and the collapse at ~ 80 μ s, this would imply a propagation time ≈ 110 μ s, for the each of the transients to return to the site of cavitation. Taking the speed of sound in water as 1500 ms^{-1} , this translates to a total propagation distance of ≈ 16 cm. We thereby infer that the transients are reflected, and effectively re-focused, from the spherically curved transducer (of geometric focus 80 mm, see above), as opposed to the walls of the confocal chamber.

Sequence 2 (b) is a recording of the cavitation activity that resulted from a 1.20 ± 0.02 mJ laser-pulse focused into the HIFU field with measured PNP = 1.3 ± 0.15 MPa. The early stages of the dynamics are clearly dominated by LIC, with rapid bubble expansion to an $R_{\max} \approx 300$ μ m, i.e. comparable to that of 2 (a); LIC without ultrasound radiation. The collapse time is also seemingly unaffected by the ultrasound. The only notable differences are the larger volume of cavitation debris and a slight upwards translation (~ 50 μ m at 190 μ s, indicated by a line drawn across the images in question, fig. 2) in the centroid of the cloud, in the case of ultrasound radiation being present. We attribute these effects to bubble fragmentation events under the added acoustic energy available to the system, and the action of the primary radiation force [5, 14] (buoyancy is negligible over these timescales, and in any case would act equally in both scenarios).

Sequence 2 (c) captures the cavitation activity resulting from a laser-pulse of 0.95 ± 0.02 mJ incident to the same location as in 2 (b), and in an equivalent field. Such a low energy laser-pulse *does not produce any cavitation activity, without the pre-established US field*. More than fifty tests were undertaken to confirm this. This sequence is representative of the minimal amount of cavitation activity we observed, which consists of a single small nucleus of <10 μ m (arrowed black throughout sequence), which proceeds to translate upwards. We term this activity *laser-nucleated acoustic cavitation* (LNAC), to distinguish it from LIC in an established US field, 2 (b).

Note that the translation speed is approximately constant throughout the sequence and commences from the moment of nucleation. This is in contrast to the LIC in the pre-established field, the centroid of which does not notably translate for the first ~ 100 μ s. However, the translations speed of the debris cloud of 2 (b) and the LNAC of 2 (c) are comparable, as one would expect in an ultrasound field of equivalent intensity.

Fig. 2 (d) depicts LNAC, again with a laser pulse energy of 0.95 ± 0.02 mJ, incident to the focal volume of a much higher intensity field, of $\text{PNP} = 4.1 \pm 0.5$ MPa. As for sequence 2 (c), absorption results in a small cavity nucleus that rapidly develops into a cloud of interacting cavities, which translate as a single entity away from the HIFU source. Although the drag may be expected to be greater for this cloud, than for the cavitation of 2 (c), the translation speed is much higher due to the dependence of the radiation force on the square of the pressure amplitude [5,15].

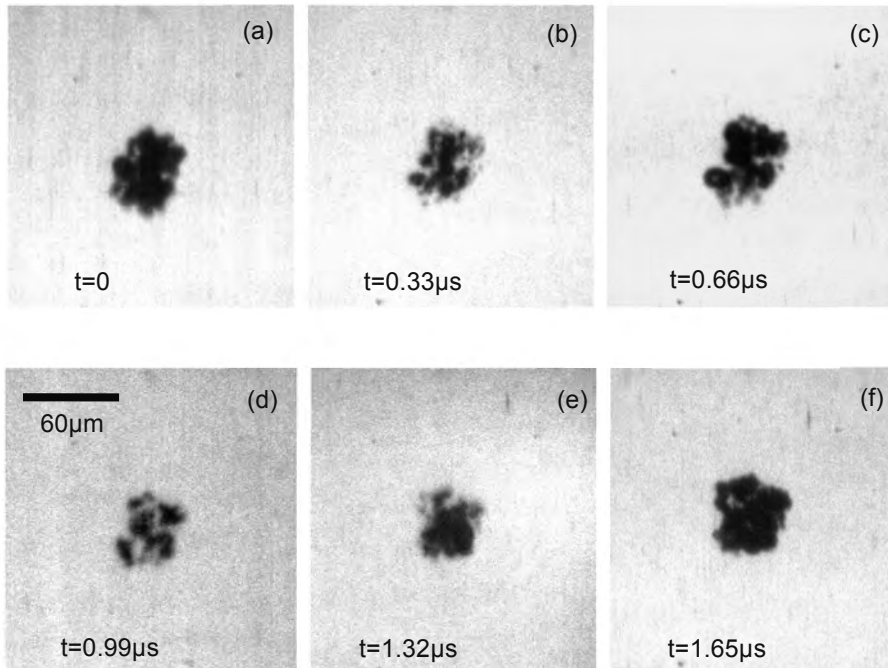


Figure 3. Consecutive frames extracted from an ultra high-speed sequence of a LNAC cloud in the early stages of development in an intermediate intensity field. This sequence was recorded at 3.05 Mfps, with timings of each image acquisition as indicated. (a) A cloud of expanded cavities (alternatively, of high 'void fraction', defined as the ratio of gas phase volume to liquid phase volume) indicates a rarefactional negative pressure amplitude phase of the propagating ultrasound in the locale of the cloud. (b) At $\sim 0.33 \mu\text{s}$ later the cloud appears to be composed of compressed cavities (or is of a lower void fraction) thereby indicating a positive pressure compressional phase of the ultrasound is acting at the time of image acquisition. Note, an f_c of 1.47 MHz used for this work equates to a pressure phase oscillation period of $\approx 0.7 \mu\text{s}$. (c) – (f) Continued cycling under the propagating HIFU pressure fluctuations. Image acquisition was through the 5x objective lens in the orthogonal configuration.

To consolidate our assertion that fig. 2 (c and d) is cavitation that is acoustic in nature, we now consider the size of the component structures within the cloud. In fig. 2 the imaging rate is less than the HIFU frequency, which is adequate to image cloud morphology evolution and translation, but insufficient to resolve component cavity dynamics. The relatively long exposure times used to capture these images result in 'objects' becoming smeared over a region of pixels, as they oscillate under the influence of the incident US. As such, the best we can expect to infer is an upper bound on the maximum diameter during the oscillation. Moreover, this assumes no translation, coalescence, non-symmetrical dynamics etc., which is evidently not the case, and could lead to erroneous measurements.

Fig. 3 (a-f) are close-ups of six consecutive frames extracted from a sequence recorded at 3.05 Mfps, at an 'advanced' stage of LNAC cloud evolution, some 15.8 μs following laser-pulse absorption and initial recorded cavitation activity. This sampling rate satisfies the Nyquist criterion for the 1.47 MHz HIFU frequency used, and as such allows quasi-resolved observation within a single acoustical cycle. Each frame represents an integration of the cavity dynamic over an exposure time significantly less than the inter-frame time of 0.33 μs , compared to the duration of a negative or positive phase of the ultrasound, which at half the period $\approx 0.34 \mu\text{s}$. The HIFU driving this cavitation was of $\text{PNP} = 2.20 \pm 0.26 \text{ MPa}$. This 'mini-sequence' records the cloud through just more than 2 cycles of US propagation. Intuitively, 3 (a)-(c) was recorded during a negative-positive-negative cycle, with (d)-(f) capturing an expansion phase during a negative-positive transition. Fig. 3 (b and d) in particular, allow us to put an upper limit on the minimum radius, R_{\min} , of some of the cavities within the cloud, of the order of a few μms . We estimate that equivalent features in the negative pressure phases of the incident US have R_{\max} 's in the range of $\sim 10 \mu\text{ms}$. This would put many of the observable cavities at around the resonant size for the frequency used, in accordance with published literature. We also note that although the apparent translation under the action of the primary radiation force is much reduced from that observed in fig. 2 (d) - due to both reduced US intensity and increased frame rate for sequence acquisition - this might still result in a slight overestimate to the feature dimensions.

Conclusions

In conclusion, we present preliminary observations on a new technique that allows what appears to be predominantly acoustic cavitation to be nucleated, or seeded, by a nanosecond laser-pulse in an acoustic field. Crucially, the dominance of a large laser-induced bubble is avoided by reducing the pulse energy. The key advantage is the spatial and temporal precision the technique affords, which allows the incorporation of ultra-high speed micro-photography, at the resolutions required to observe cloud formation and evolution.

Acknowledgements

The research leading to these results has received funding from the European Community's Seventh Framework Programme (FP7/2007-2013) under grant agreement n° 230674 (Nanoporation project).

Paul Prentice acknowledges the Norwegian Research Council for Yggdrasil mobility award no. 210949/F11.

We are particularly grateful to Mr Adrain Walker of the EPSRC instrument loan pool, for continued access to various high-speed imaging devices.

References

1. ter Haar, G., *Ultrasound focal beam surgery*. Ultrasound Med Biol, 1995. **21**(9): p. 1089-1100.
2. Coussios, C. et al., *Role of acoustic cavitation in the delivery and monitoring of cancer treatment by high-intensity focused ultrasound*. Int J Hyperthermia, 2007. **23**(2): p. 105-120.
3. M^cGlaughlin, J. et al., *A study of bubble activity generated in ex-vivo tissue by high intensity focused ultrasound*. Ultrasound Med Biol, 2010. **36**(8): p. 1327-1344.
4. Holt, R. and R., Roy, *Measurements of bubble-enhanced heating from focused MHz-frequency ultrasound in a tissue-mimicking material*. Ultrasound Med Biol, 2001. **27**(10): p. 1399-1412.
5. Leighton, T., *Acoustic Bubble*. Academic Press, 1994, London.
6. Chen, H. et al., *High-speed observation of cavitation bubble cloud structures in the focal region of a 1.2 MHz high-intensity focused ultrasound transducer*. Ultrasonics, 2006. **14**: p. 291-297.
7. Lee, J. et al., *Determination of the size distribution of sonoluminescence bubbles in a pulsed acoustic field*. J Am Chem Soc, 2005. **127**: p. 16810-16811.
8. Brothie, A. et al., *Effect of power and frequency on bubble-size distributions in acoustic cavitation*. Phys Rev Lett, 2009. **102**: p. 084302.
9. Chen, W. et al., *The disappearance of ultrasound contrast microbubbles: observation of bubble dissolution and cavitation nucleation*. Ultrasound Med Biol, 2002. **28**(6): p. 798-803.
10. Fujimoto, J. et al., *Time-resolved studies of Nd:YAG laser-induced breakdown*. Invest. Ophthalmol. Vis. Sci., 1985. **26**: p. 1771-1777.
11. Brujan E. et al., *Dynamics of laser-induced cavitation bubbles near an elastic boundary*. J Fluid Mech, 2001. **433**: p. 251-281.
12. Vogel, A. et al., *Shock wave emission and cavitation bubble formation by picoseconds and nanosecond optical breakdown in water*. J Acoust Soc Am, 1996. **100**(1): p. 148-165.
13. Gerold, B. et al., *Laser-nucleated acoustic cavitation in focused ultrasound*. Rev Sci Inst, 2011. **82**(4): p. 044902.
14. Palanchon, P. et al., *Optical observations of acoustical radiation force effects on individual air bubbles*. IEEE UFFC, 2005. **52**(1): p. 104-110.

6

Ultrasound induced mechanical stress: cellular and molecular responses

Annemieke van Wamel

Abstract

Over the last 15 years ultrasound contrast agents mediated local drug delivery became more and more popular to investigate. In that respect it can be foreseen that it will be clinically used in the near future. The response of cells to mechanical forces induced by oscillating ultrasound contrast agent induced deformation of cells is discussed. Emphasis is placed on the awareness of the possible local effects and the need for extensive research in order to make this potentially Nobel-prize winning technique a smashing success. The biology of cells is discussed in relation to the current knowledge of mechanical stress related molecular and cellular responses. We don't know much about the relation between these responses and microbubble oscillation behaviour. It is possible to control microbubble behaviour thus it is also possible to control mechanical-stress-induced cell-responses. If we can trigger one specific response, we can use ultrasound contrast agents for the benefit of local drug delivery for any type of drug and for any type of treatment.

Ultrasound contrast agents

Ultrasound contrast imaging is used to visualize the blood pool in order to determine the existent of circulation and to quantify the amount of perfusion of organs and big vessels. Some acute site-effects are reported but no long-term negative effects are reported. Ultrasound is a cheap and above all not a radiating technique, which makes it a favorable imaging technique. Over the last 15 years ultrasound contrast agents mediated local drug delivery became more and more popular to investigate. In that respect it can be foreseen that it will be clinically used in the near future. Not surprisingly, all basic research is focused on the benefits and good use of ultrasound contrast. Reports of any negative effects have been ignored or just wavered, because the conclusions were drawn from cell culture or animal models. The fact that all positive results come from similar research experiments seems something that's easy to forget. Don't get me wrong, I do believe in the potential benefits of ultrasound mediated local drug delivery. I just believe that we know too little about the physical and cellular mechanisms involved to make it a safe technique that can be used within the next 10 years. Because of its great potential, when it works it is Nobel price worthy, it is necessary to investigate the boundaries and limitation of its medical use.

This paper does not cover all of the new developments in ultrasound contrast mediated responses; rather, it focuses on the response of cells to mechanical forces from a biological standpoint and the oscillating contrast agent induced deformation of cells. Emphasis is placed on the awareness of the possible local effects of oscillating ultrasound contrast agents next to cells which undoubtedly will result in systemic effects

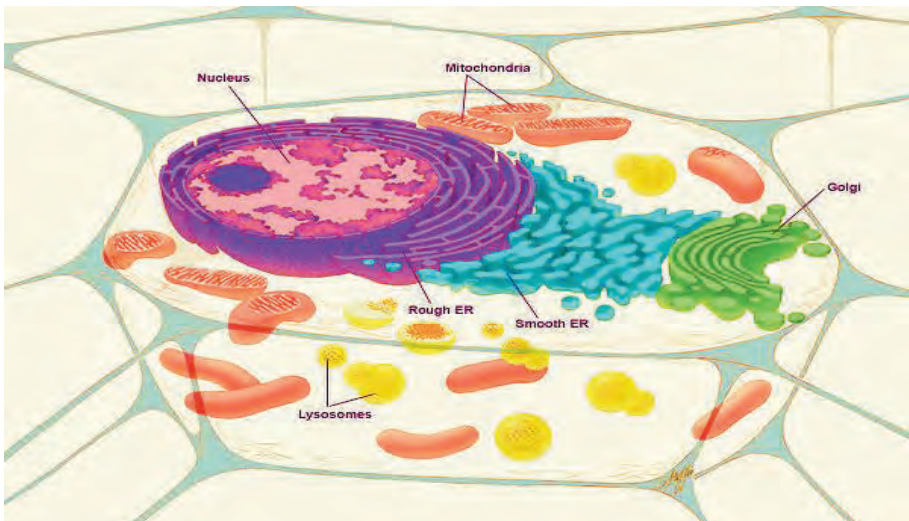


Figure 1 - Schematic cell: cell organelles include the nucleus, mitochondria, rough and smooth endoplasmic reticulum, Golgi bodies, and lysosomes. [adapted from NIH Publication No. 05-1051 National Institutes of Health Revised September 2005 National Institute of General Medical Sciences <http://www.nigms.nih.gov>].

Biologics

Cells are the basic structural and functional units of life. Cells contain cell organelles that interact to exchange information within the cell. Like the internal organs in your body, organelles in the cell each have a unique biological role to play (Figure 1). Constant exchange and processing of information from their surroundings is necessary at molecular and cellular level.

Cells use the information in genes (DNA) to organize assimilated resources into all the structures that make up living organisms and the systems that guide their activities. The majority of the organic components of cells are proteins. Some proteins form the physical structures of cells and organisms. For example, proteins are integral parts of cell membranes, muscle fibers, connective tissues, and body coverings. Other proteins function as chemical messengers, such as hormones, or as enzymes, which regulate all the biochemical reactions that maintain life. The genes store detailed instructions for how to assemble protein molecules and use them in the activities of life. One tiny mistake can mean the difference between life and death.

To perform their specialized functions, cells must use genetic information; synthesize, sort, store, and transport biomolecules, convert different forms of energy, transduce signals, maintain internal structures, and respond to external environments. But merely sending and receiving information is not enough. Living systems must also respond to information they receive. In responding to information, they undergo changes or adjustments that enable the systems to continue functioning. Exchanging and responding to information is a continual process that involves interactions among living systems at all levels of biological organization. Each level of biological organization responds to information in a variety of ways. What kinds of interactions occur at the molecular, cellular, and organism levels of organization?

Much of the information from the environment is received in as energy and chemical substances. This information enters cell at the molecular level and acts as the stimulus for many fundamental life processes, such as metabolism and proliferation. At the molecular level of life, organic molecules (including carbohydrates, lipids, proteins, and nucleic acids) and inorganic molecules (including water, oxygen gas, and carbon dioxide gas) interact in a variety of chemical reactions. A chemical reaction involves the making and breaking of chemical bonds between atoms and groups of atoms. Step-by-step chemical reactions, organized in pathways and controlled by regulatory molecules, transfer energy, build structural parts of cells, and carry out cell functions. When an ultrasound contrast microbubble rubes (oscillates) against a cell, it transfers energy, deforms the cell, and exchanges lipids which the cell membrane, resulting in changes cell morphology and energy levels.

Cell signaling is a molecular process that allows cells to receive, process, transmit, and respond to information. The signals sent by cells are either chemical or electrical. Some chemical signals act locally or at very short distances, other chemical signals, such as hormones, travel throughout the bodies of animals over very long distances. Multicellular organisms contain interacting subsystems — including cells, organs, and

organ systems — that must constantly exchange and respond to information to maintain homeostasis.

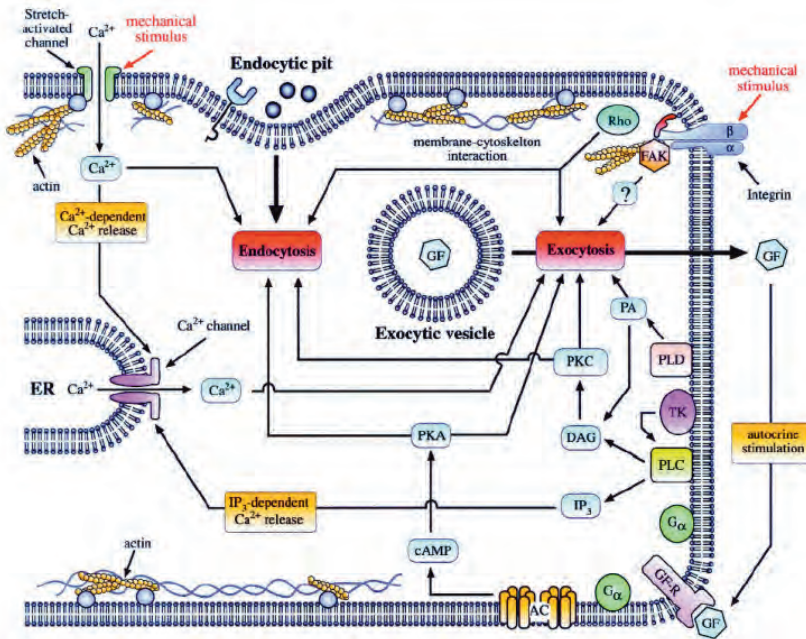


Figure 2 - Possible mechanisms on how cells sense mechanical perturbation. Adapted from Apodaca *et al.* [11].

This constant flow of and response to information occurs primarily at the cellular level through cell signalling. It enables cells to organize into more complex structures that also receive, process, and respond to information within an organism.

At the cellular level, information flows between subsystems within cells, between individual cells, and between cells and their environment. For example, the DNA in a nucleus or an organelle, such as a mitochondrion, responds to other molecules from within the same organelle or from the environment. It may respond by replicating DNA or making the RNA molecules needed for assembling amino acids into proteins. Some of these proteins form the chemical receptors and channels embedded in the external and internal membranes of cells and their organelles. Other molecules made by cells transport signals to other parts of the same cell, to other cells within the same organism or to other organisms in the environment.

The cytoskeleton is an organized structural system consisting of actine filaments (6-10 nm in diameter), intermediated filaments (7-11 nm), and microtubules (25 nm). These structures are the roads and high ways within cells on which transportation of all molecules takes place. This intracellular “distribution system” is a complex system which consists of widespread networks within cells and manages proper execution of

totally balanced transport. We still do not understand very well the mechanism involved. We do not yet fully know how transport-molecules recognize and bind to their cargoes, how they choose a particular transport route, or how they identify the destinations for their cargoes. As for a supervision mechanism to coordinate transport by multiple transport-molecules, we have no knowledge at all. But it is evident that disruption of the cytoskeleton will influence the intracellular transport [1].

Effects of vibrating microbubbles on cells

When ultrasound contrast agents are exposed to ultrasound, microbubbles oscillate. When close or in contact with cells, vibrating microbubbles deform the cells. In a study that investigated the interact between lipid shelled microbubbles and endothelial cell in vitro it was found that, microbubbles can push the cellular membrane inward up to 15% of the cell size and pull the cell membrane outward up to 7.5% of the cell size [2]. Cells experience and respond to mechanical forces. Ultrasound microbubble mediated mechanical stress induces, among others, gene expression changes, cell membrane disruption, DNA-strand breaks, internalization of external molecules, cytoskeleton remodeling and even cell death [3-6].

How do cells sense mechanical perturbation?

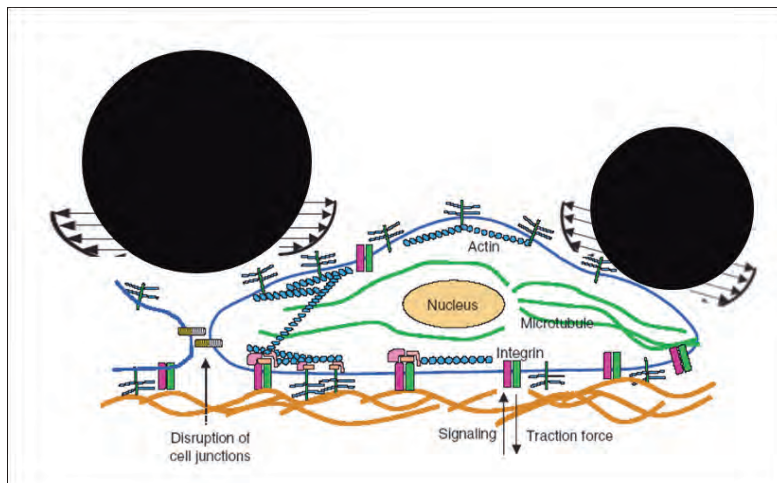


Figure 3 - schematic representation of vibrating microbubbles rubbing against cells. Adapted from Li *et al.* [13].

A straightforward way of transducing mechanical signals might be via the deformation of lipid membrane [8]. Furthermore, it has been proposed that such deformation may result in activation of cytoplasmic molecules such as G proteins, which can triggers a cascade of biochemical events. Mechanosensitive ion channels have also been suggested by many studies. Certain cell membrane receptors have been shown to transmit forces from the cell surface to the cytoskeleton and may serve as mechanosensing molecules. Perhaps the candidate that has received most attention is

the integrin adhesion receptors. A role for integrins has been suggested even when other mechanisms are proposed. For example, the activation of ion channels may be tightly controlled by the underlying cytoskeleton [3, 7-10].

Conclusion

Ultrasound drug delivery or the sonoporation processes involve biochemical and mechanical aspects. We don't know enough to utilize it to its full potential. To understand the organizational principles, structure-function relationships, and regulatory mechanisms in cells requires a combination of biological, biophysical, and biochemical approaches. Ultrasound mediated drug delivery field of research, which is an interdisciplinary endeavour, concerns how cells resist force, deform, and interact, as well as how they sense, generate, and respond to mechanical forces. How do forces applied to the cell membrane and cytoskeleton induce its reorganization? How do the resulting molecular and cellular dynamics regulate cell properties and the shape of a cell? Tension and compression are two different phenomena which will result in two different cell responses. Using ultrasound, it is possible to use an ultrasound sequence that results in a predominantly expanding microbubble or compressing bubbles resulting in a pushing or pulling sensation of the cell [12]. Both cellular responses can therefore be exploited in order to manipulate cells, organs and whole organisms in a beneficial way to tackle the current problems of failing drug delivery and subsequent treatments.

References

1. Hirokawa, N. and Y. Noda, *Intracellular transport and kinesin superfamily proteins, KIFs: structure, function, and dynamics*. *Physiol Rev*, 2008. **88**(3): p. 1089-118.
2. van Wamel, A. et al., *Vibrating microbubbles poking individual cells: drug transfer into cells via sonoporation*. *J Control Release*, 2006. **112**(2): p. 149-55.
3. Davies, P.F., J. Zilberberg, and B.P. Helmke, *Spatial microstimuli in endothelial mechanosignaling*. *Circ Res*, 2003. **92**(4): p. 359-70.
4. Furusawa, Y. et al., *DNA double-strand breaks induced by cavitational mechanical effects of ultrasound in cancer cell lines*. *PLoS One*. **7**(1): p. e29012.
5. Krasovitski, B. et al., *Intramembrane cavitation as a unifying mechanism for ultrasound-induced bioeffects*. *Proc Natl Acad Sci U S A*, 2011. **108**(8): p. 3258-63.
6. Meijering, B.D. et al., *Ultrasound and microbubble-targeted delivery of macromolecules is regulated by induction of endocytosis and pore formation*. *Circ Res*, 2009. **104**(5): p. 679-87.
7. Chien, S., *Mechanotransduction and endothelial cell homeostasis: the wisdom of the cell*. *Am J Physiol Heart Circ Physiol*, 2007. **292**(3): p. H1209-24.
8. Farsad, K. and P. De Camilli, *Mechanisms of membrane deformation*. *Curr Opin Cell Biol*, 2003. **15**(4): p. 372-81.
9. Huang, H., R.D. Kamm, and R.T. Lee, *Cell mechanics and mechanotransduction: pathways, probes, and physiology*. *Am J Physiol Cell Physiol*, 2004. **287**(1): p. C1-11.
10. Zhu, C., G. Bao, and N. Wang, *Cell mechanics: mechanical response, cell adhesion, and molecular deformation*. *Annu Rev Biomed Eng*, 2000. **2**: p. 189-226.
11. Apodaca, G., *Modulation of membrane traffic by mechanical stimuli*. *Am J Physiol Renal Physiol*, 2002. **282**(2): p. F179-90.
12. Postema, M. et al., *High-speed photography during ultrasound illustrates potential therapeutic applications of microbubbles*. *Med Phys*, 2005. **32**(12): p. 3707-11.

7

Biological and medical applications of low-intensity ultrasound*

Spiros Kotopoulos^{1,4}, Anthony Delalande^{2,4}, Chantal
Pichon³, Michiel Postema⁴

¹National Centre for Ultrasound in Gastroenterology, Haukeland University Hospital,
Bergen, Norway

²Department of Haematology, Haukeland University Hospital, Bergen, Norway

³Centre de Biophysique moléculaire, CNRS, Orléans, France

⁴Department of Physics and Technology, University of Bergen, Bergen, Norway

Abstract

Ultrasound is currently used for a vast range of non-destructive testing, evaluation and diagnostics in both industry and medicine. Here we present some results indicating possible uses of low-intensity ultrasound in biology, specifically in the control of blue-green algal growth, and in the medical field to facilitate targeted increased drug uptake. Our results showed that pulsed ultrasound well within the clinical diagnostic range could be used to control algal blooms by bursting the gas-vesicles, forcing the algae to sink. Using continuous wave ultrasound we showed that it is possible to force ultrasound contrast agents to form clusters at a quarter-wavelength of the sonication frequency. Furthermore, using low-intensity pulsed ultrasound we showed that it was possible to force an ultrasound contrast agent, coated with a fluorescent dye, into cancerous cells.

Ultrasound-induced cracking of *Anabaena sphaerica*

Introduction

Algae are aquatic, eukaryotic, photosynthetic organisms, ranging in size from single-celled forms to large kelps. Algae are classified separately from plants since they lack true roots, stems, leaves and embryos. Blue-green algae are known to cause many health hazards to humans including skin rashes, gastrointestinal, respiratory [1], allergic reactions [2] and liver cancer [3]. In addition, blue-green algae may have implications on aquatic and semi-aquatic animals [4].

Eutrophication is the increase in chemical nutrients within the ecosystem, causing blooms of algae and plant life and the subsequent decomposition of blue-green algae by bacteria; an oxygen-consuming process [5]. When billions of such bacterial cells die simultaneously after a bloom, the water becomes oxygen-depleted, killing off oxygen-dependent organisms [6]. The main factors that influence algae growth are temperature and light [7, 8]. At low temperatures and low light conditions, the algae do not photosynthesise and therefore do not bloom. Blue-green algae strands contain nitrogen-producing cells (heterocysts) shown in Fig. 1, these cells have a diameter between 5 and 7 μm . These store the necessary nitrogen and distribute it to other cells [9].

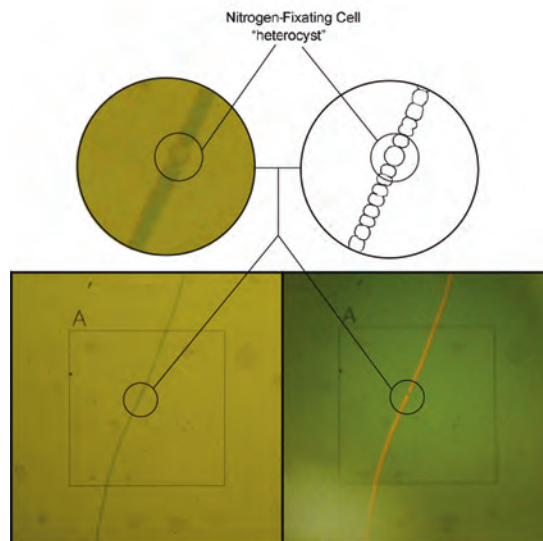


Figure 1 - Nitrogen-fixing body in *Anabaena sphaerica* algae. Under fluorescent light the body does not illuminate red, proving there is no chlorophyll in the body. Each frame corresponds to $565 \times 565 \text{ } (\mu\text{m})^2$.

It is hypothesised that if the membranes of the gas vesicles are disrupted by means of ultrasound, the gas may be released analogous to sonic cracking [10], causing the gas to diffuse and have no means to replenish, thus forcing the strands to sink. At the lakebed, illumination is lower, thus reducing blue-green algae growth. This is a desirable ecological effect, because of resulting suppressed release of toxins into the water.

There are chemical methods to control certain species of blue-green algae but these have side effects such as promotion and growth of other species of algae [11] whilst also affecting aquatic life in fresh water ponds and lakes. Therefore, ultrasonic algae control has been under investigation [12-17]. In [12-17] ultrasonic sonication of different species of algae led to a decrease in algae concentration in the frequency range 20 kHz–1.7 MHz, which is in contrast with [18], where ultrasound was observed to strengthen the cell membranes of red algae. In these studies the exact acoustic conditions have not been specified other than the frequency and power input. Hence, from the acoustics point of view, they are not repeatable. More importantly, the mechanism causing algae eradication or membrane disruption had not been investigated.

Most commercially available equipment works in the lower ultrasonic range [19]. There have been speculations about the physical mechanism behind the algae eradication, specifically about the role of cavitation. In this study, the effectiveness of ultrasonic sonication in the clinical diagnostic range on *Anabaena sphaerica* was investigated.

In this chapter, acoustic fields in the lower clinical diagnostic range were used, taking into account the MI and NURC guidelines.

Materials and Methods

To investigate the effect of diagnostic ultrasound on blue-green algae eradication, three ultrasound transducers were used. A 200-kHz, single element transducer containing a PIC155 piezo crystal (PI Ceramics, Lederhose, Germany), a PA188 (Precision Acoustics Ltd., Dorchester, UK) 1-MHz, single element transducer, and a 2.2-MHz, single element transducer containing a Pz37 piezo crystal (Ferroperm Piezoceramics A/S, Kvistgård, Denmark). The focal distance of the 2.2-MHz transducer was 73mm. The design of two transducers is shown in Fig. 2. The transducers were subjected to 260-Vpp sinusoidal pulses at a 11.8-kHz pulse repetition rate transmitted by a V1.0 pulser-receiver (Sonemat, Coventry, UK). Low acoustic amplitudes were used in order to comply with $MI < 0.3$ [20]. The acoustic amplitudes were measured in a separate water tank in the acoustic foci of the transducers with a 0.2-mm needle hydrophone (Precision Acoustics Ltd.) connected to a TDS 420A digitising oscilloscope (Tektronix Inc, Beaverton). The peak-negative acoustic pressures were 40 kPa for the 1-MHz transducer and 68 kPa for the 2.2-MHz transducer, *i.e.*, $MI \ll 0.1$.

The blue-green algae used were of the *Anabaena* species. The *Anabaena* were obtained from a natural lake and cultured in 2 L of Jaworski's medium [21] at room temperature near a South-facing window in an Erlenmeyer flask for 11 days. Prior to

adding the blue-green algae the Jaworski's medium was put in a Swirtlock 2000 autoclave (Astell Scientific, Kent, UK) at 15-lb pressure for 15 minutes.

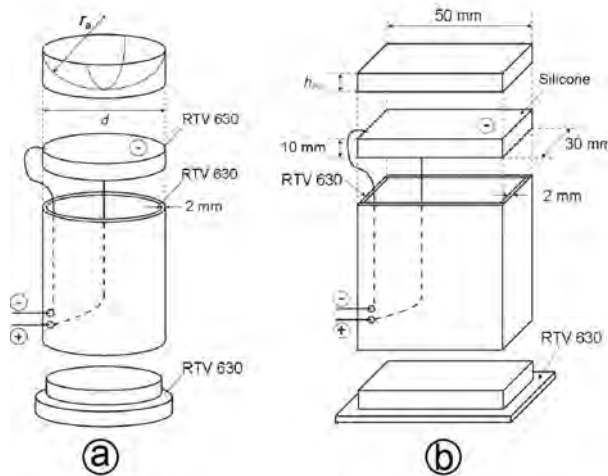


Figure 2 - (a) 2.2-MHz ultrasound transducer with $d = 1''$ diameter and $r_a = 35$ mm acoustic lens. (b) 200-kHz ultrasound transducer with $h_{PG} = 10$ mm matching layer.

Brightness measurements

To measure the time-dependent change in brightness of water containing blue-green algae, the culture was split equally into four 250-mL Perspex beakers: one beaker for each transducer and one control beaker. The transducers were inserted separately in each beaker with the acoustic focus within the sample. Each transducer was turned on for 1 hour. The experimental setup is shown in Fig. 3. A digital photograph of the solution was taken every five minutes using an EOS 350D digital photo camera (Canon Inc, Tokyo, Japan). The lighting and exposure settings were controlled and maintained throughout the sonication. Full manual settings were used: 100 ISO, shutter speed of 1/50 s, f 3.50, focal length of 18mm, no flash, centre weighted metering mode, custom white balance with a B4,0 shift. The digital photographs were converted to 8-bit grey scale. On the photographs of the sonicated solution and control solution, a square area of 160×160 pixels (A1 and B1) in the middle of the beaker, and an area of 160×50 pixels (A2 and B2), at the base of the beaker, was selected, whose average grey-scale depth was calculated using Matlab® (TheMathworks™, Natick, MA). The change in shade between the first image, taken just before sonication and each sequential image after sonication was calculated and graphed for all 18 sonicated and control samples. A white sheet was placed behind the beakers to maintain a constant background. The grey scale of the sheet was also measured and used to calibrate the results. In total, 575 measurements were analysed from 122 photographs.

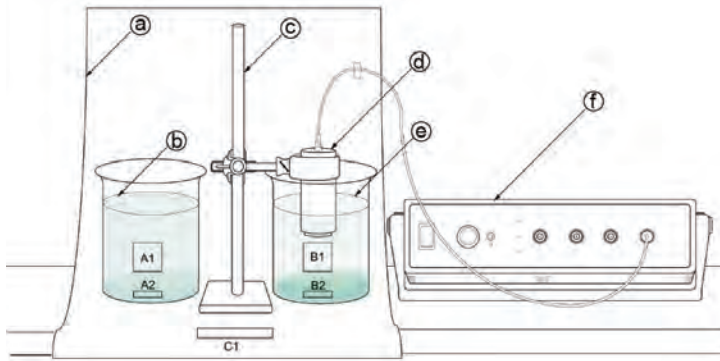


Figure 3 – Experimental setup: (a) white paper sheet; (b) control sample; (c) clamp stand; (d) transducer; (e) sonicated sample; (f) pulser-receiver. Areas A1-B2 represent brightness measurement areas, C1 represents the calibration area.

Viability measurements

Every 10 minutes, a 20- μ L sample was taken from the sonicated solution. Samples were put on a test slide and observed through a CHA microscope (Olympus Corporation, Tokyo, Japan) with an MPlan 10 \times 0.30 NA objective lens (Olympus Corporation) *cf.* Fig. 4. Digital photographs were captured from the microscope's eyepiece using an FE-230 digital camera (Olympus Corporation). Automatic settings were used with Super Macro mode and a -1.0 exposure adjustment. From these digital images deterioration in chlorophyll activity and cell damage was determined. To investigate the effect of ultrasound on the viability of the cells, fluorescent light was used. When fluorescent light is projected onto chlorophyll, it is absorbed and re-emitted as a red glow. The red glow denotes that the chlorophyll is still active and can photosynthesise, thus the blue-green algae strands are still alive.

Fluorescent light was used as the method to check the viability of the chlorophyll, since it is a standardised and accepted method in detecting chlorophyll activity in plants [83, 138]. Fluorescent light was projected onto these samples for no more than 10 seconds in order to capture the digital image. It may assume that there are no disadvantageous effects of the fluorescent light on the blue-green algae [65, 95].

The samples were discarded after being exposed to fluorescent light. Three trials of each frequency were performed. One hundred and thirty-one photographs were taken of the microscopic cell structure.

Post-sonication growth measurements

To measure the effect of ultrasound on blue-green algae growth post-sonication, twenty-four 1-mL samples were removed from three solutions that had been subjected to 1-hour sonication with 200-kHz, 1.0-MHz and 2.2-MHz ultrasound and put into a

culture tray with 96 compartments. Twenty-four control samples were taken. The culture tray was left in sunlight for 30 days. The grey scale value was measured for each compartment.

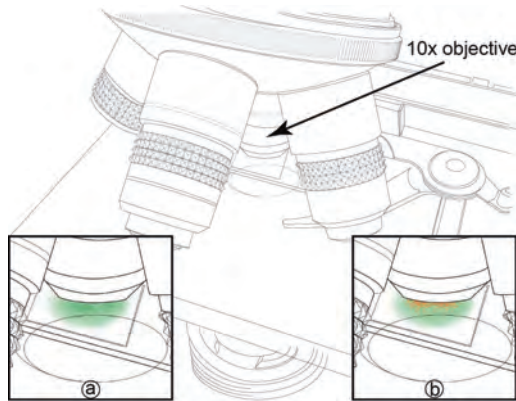


Figure 4 - Schematic showing use of the fluorescence microscope. A 10× objective lens was used. (a) Blue-green algae under tungsten lighting; (b) Blue-green algae under fluorescent lighting.

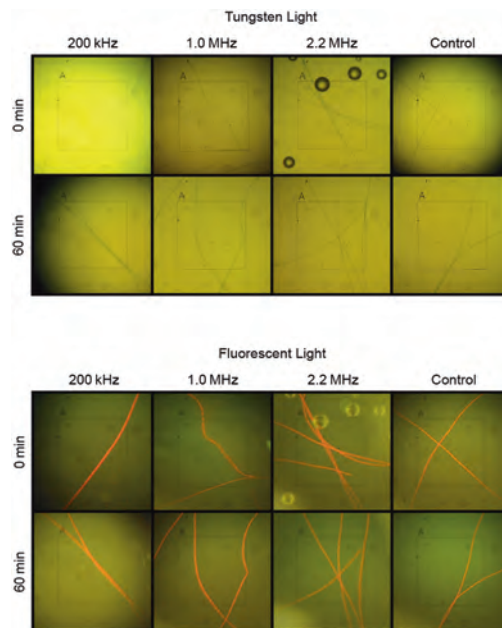


Figure 5 – Microscopic image sequence showing the effect of 200 kHz–2.2 MHz ultrasound on the floating bodies of blue-green algae. Each frame corresponds to $565 \times 565 \text{ } (\mu\text{m})^2$.

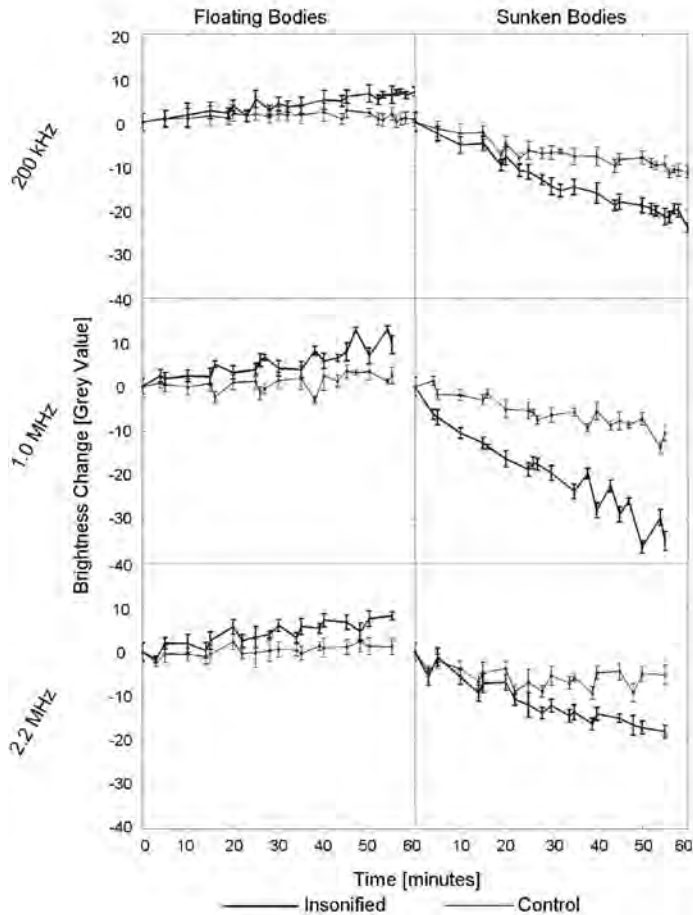


Figure 6 - Water brightness as a function of ultrasonic exposure time for samples containing floating blue-green algae or sunken blue-green algae.

Results and discussion

Figure 5 shows the microscopic effect of ultrasound on floating bodies in the blue-green algae solution. From 0 minutes to 60 minutes of sonication, no change was seen in the physical structure of the blue-green algae for all three frequencies. Fluorescent illumination showed that the ultrasound had no effect on the chlorophyll activity for the all frequencies tested. The active chlorophyll shows that the blue-green algae strands are still alive and able to photosynthesise after 60 minutes sonication. This indicates

that the ultrasound transmitted does not affect the chlorophyll in the cells.

However, Fig. 6 shows that at all frequencies, for the floating bodies, the sonicated samples showed greater brightness than the control samples. For the sunken bodies, all sonicated samples showed reduced clarity when compared to the control samples. Thus, the ultrasound has caused the algae to sink. For example, after 60 minutes, the beakers subjected to 200-kHz sonication were $92 \pm 12\%$ brighter than the control samples, contrasted by the beaker bottoms, which were $53 \pm 27\%$ darker than the control samples.

Clearly, the blue-green algae that were floating in the beaker dropped to the bottom at a faster rate than the control sample. This has been attributed to the disruption of the floating bodies by the ultrasound. This is supported by Fig. 7, which shows that the sunken bodies still have active chlorophyll but less dense kelps were found.

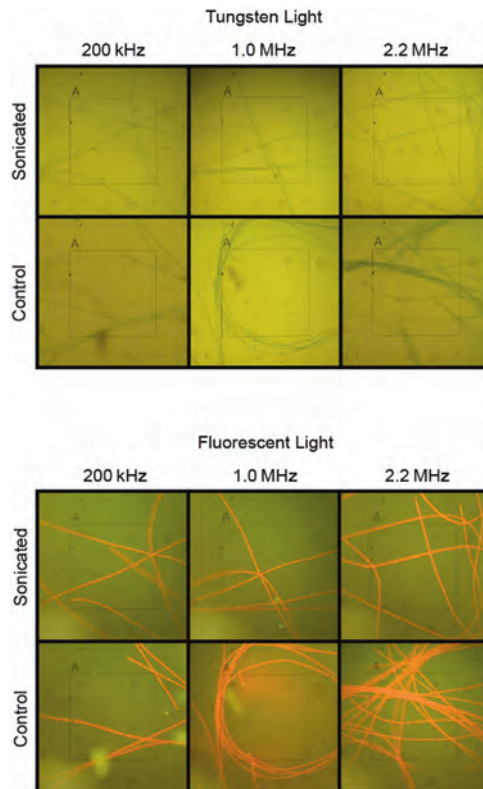


Figure 7 – Microscopic image sequence showing the effect of 200 kHz–2.2 MHz ultrasound on sunken blue-green algae. Each frame corresponds to $565 \times 565 \text{ } (\mu\text{m})^2$.

Figure 8 shows the viability of the culture 30 days after sonication in terms of sample brightness. At 200 kHz, 1.0 MHz, and 2.2 MHz, the samples were $39\pm14\%$, $45\pm17\%$, and $46\pm17\%$ brighter than the control samples, respectively. All samples were significantly brighter than the control samples, even at the lower boundaries of the standard deviation. Thus, these results support the hypothesis that the blue-green algae that have sunk are less capable of multiplying. Hence, sonication may prevent blue-green algae bloom.

The results can be interpreted as follows. When a gas vesicle is subjected to an ultrasound pulse it expands during the rarefaction phase [22]. If the acoustic amplitude is sufficiently high, the encapsulating membrane cannot withhold the bubble from further expanding, resulting in its rupture. This phenomenon is similar to the sonic cracking of micrometre-sized membrane-encapsulated bubbles observed in [10]. Sonic cracking exclusively occurs during the expansion phase of a bubble [23].

The resonance frequency f_0 of an encapsulated microbubble is given by [24]:

$$f_0 = \frac{1}{2\pi} \sqrt{\left(\frac{3\Gamma}{R_0^2 \rho}\right) \left(p_0 + \frac{2\sigma}{R_0} + \frac{2\chi}{R_0}\right) - \left(\frac{2\sigma + 6\chi}{R_0^3 \rho}\right)}, \quad (1)$$

where p_0 is the ambient pressure, R_0 is the bubble radius, Γ is the polytropic exponent of the gas, ρ is the liquid density, σ is the surface tension, and χ is the elasticity of the encapsulation [110]. Using $p_0 = 1.013 \times 10^5$ Pa, $R_0 = 3 \mu\text{m}$, $\Gamma = 1.4$, ρ is 998 kg m^{-3} , $\sigma = 0.072 \text{ N m}^{-1}$, and assuming that the membrane elasticity is similar to that of a lipid encapsulation, $\chi = 0.044 \text{ N m}^{-1}$ [25], it can be estimated $f_0 \approx 1 \text{ MHz}$ for *Anabaena* cells used in these experiments. Since the greatest change in clarity was seen at this particular frequency, it can safely be stated that ultrasound sonication close to gas vesicle resonance frequency leads to a more effective eradication.

The quick decrease in live blue-green algae is similar to that in previous studies [12-17]. It can be assumed that the correlation between (high) frequency and algae eradication in these studies is related to the ultrasound proximity to gas vesicle resonance as well.

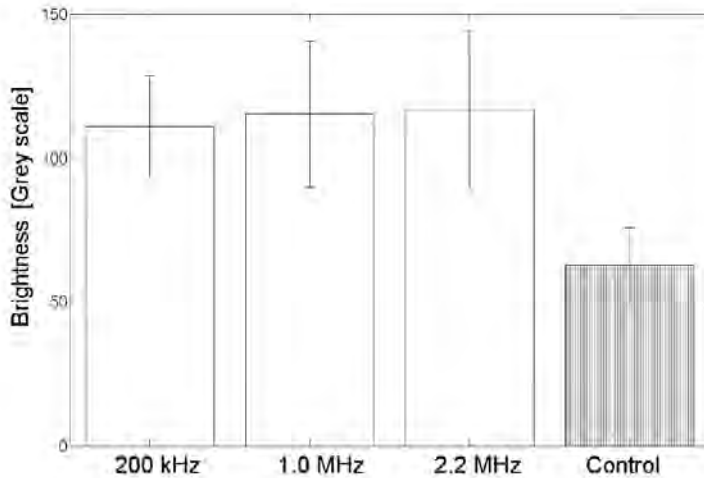


Figure 8 – Water clarity 30 days after sonication.

According to the NURC Rules and Procedures [20], the maximum acoustic pressure to which mammals can be exposed is 708 Pa at frequencies up to 250 kHz.

The transducers used had acoustic pressures of 40 kPa and 68 kPa at driving frequencies 1.0 MHz and 2.2 MHz, respectively. These pressures surpass the NURC Rules and Procedures by over 35 dB.

Conclusion

At any ultrasonic frequency studied, blue-green algae were forced to sink. This supports the hypothesis that the gas vesicles release their gas under ultrasound sonication in the clinical diagnostic range. As supported by previous studies, under identical pulse length and pulse repetition, eradication is most effective close to gas vesicle resonance, at a driving frequency of roughly 1 MHz.

Although the acoustic fields used to eradicate blue-green algae are safe in terms of mechanical index, the acoustic pressures surpass the NURC Rules and Procedures by over 35 dB. Therefore, caution should be taken when using these techniques in a surrounding where aquatic or semi-aquatic animals are present.

Microfoam formation in capillaries

Introduction

Ultrasound contrast agents are used in diagnostic imaging. They consist of microscopically small bubbles containing slowly diffusing gas encapsulated by biodegradable shells. When inserted in the blood stream, these bubbles oscillate upon ultrasonic sonication, thereby creating detectable ultrasound themselves. A brief overview of the most common ultrasound contrast agents has been presented in [26]. It follows that albumin and lipids are currently the most common bubble encapsulation materials. Because of the proven feasibility to attach therapeutic compounds to albumin and lipids, therapeutic application of contrast agents have become of interest [1, 27-29]. It is desirable that the therapeutic load of any such contrast agent is released close to the vessel wall. Therefore, pushing bubbles towards boundaries by means of primary radiation forces has been studied [30].

Both primary and secondary radiation forces resulting from oscillating bubbles, may cause the repulsion or mutual attraction, and eventual collision and coalescence, of contrast agent bubbles. This phenomenon has been less studied.

From the therapeutic point of view, the formation of bubble clusters may be of interest. If the clusters behave as one entity, *i.e.*, one mega-bubble, its ultrasonic manipulation towards a boundary is fairly straightforward and quick. If the clusters can be forced to accumulate to a microfoam, entire vessels might be blocked on purpose using an ultrasound contrast agent and a sound source.

In this chapter, how ultrasound contrast agent clusters are formed and what happens to the clusters if sonication is continued is analysed. Furthermore, high-speed camera footage of microbubble clustering phenomena is shown and the therapeutic consequences of these findings is discussed.

Theory

A brief overview of theory on radiation forces and ultrasound contrast agent has been given in [109]. Bubble translation in the direction of the sound field is caused by a primary radiation force resulting from a pressure gradient across the bubble surface. The translation is maximal during the contraction phase. The velocity v of a bubble in a steady fluid subjected to an ultrasound field can be calculated using [31]:

$$F_r + F_d - \frac{d(mv)}{dt} \approx 0, \quad (2)$$

where F_r is the primary radiation force, F_d is the drag force, $m = \frac{2}{3}\pi\rho R_0^3$ is the added mass of the translating bubble, equivalent to half the mass of the displaced surrounding fluid, in which R_0 is the equilibrium bubble radius and ρ is the density of the surrounding fluid. Averaging over one acoustic cycle, the primary radiation force is given by [31-33]:

$$F_r = \frac{p_a^2 R_0}{\rho c f} \frac{\delta \left(\frac{f_0}{f} \right)}{\left[\left(\frac{f_0}{f} \right)^2 - 1 \right]^2 + \left[\delta \frac{f_0}{f} \right]^2}, \quad (3)$$

where c is the speed of sound, p_a is the peak rarefactional acoustic pressure, δ is the dimensionless total damping coefficient [34], f is the driving frequency, and f_0 is the bubble resonance frequency [34]. The drag force is given by [33, 34]:

$$F_d = -\frac{\pi \eta}{4} C_d Re R_0 v(t), \quad (4)$$

where η is the shear (dynamic) viscosity of the fluid, $Re = \frac{2\rho R_0}{\eta} |v(t)|$ is the Reynolds number, and

$$C_d = -\frac{24}{Re} (1 + 0.15 Re^{0.687}), \quad (5)$$

is the drag coefficient of a contaminated system [35], such as a contrast agent.

Combining Eqns. 2 – 4 and integrating over dt gives the following expression for the average velocity of a bubble:

$$v = \frac{4p_a^2}{\rho c f \eta C_d Re} \frac{\delta \left(\frac{f_0}{f} \right)}{\left[\left(\frac{f_0}{f} \right)^2 - 1 \right]^2 + \left[\delta \left(\frac{f_0}{f} \right) \right]^2} \left[1 - e^{\left(-\frac{3 \eta C_d R_0}{8 \rho R_0^2} t \right)} \right]. \quad (6)$$

Secondary radiation forces, resulting from oscillating bubbles under sonication, may cause the mutual attraction and subsequent coalescence of contrast microbubbles. Two bubbles that oscillate in phase approach each other, whereas two bubbles that oscillate out of phase recede from each other [22, 36]. At low acoustic amplitudes, the phase angle difference ϕ between excursion of the oscillating bubble and the incident sound field is given by [22, 32, 36]:

$$\phi = \pi + \arctan \left(\frac{\delta \left(\frac{f}{f_0} \right)}{1 - \left(\frac{f}{f_0} \right)^2} \right). \quad (7)$$

The presence of an encapsulating shell increases the damping coefficient by a term δ_s [37].

$$\delta_s = \frac{S_f}{2\pi m f_0}, \quad (8)$$

and increases the squared resonance frequency f_0^2 by a term f_s^2 [37]

$$f_s^2 = \frac{\chi}{2\pi R_0^3 \rho}, \quad (9)$$

where S_f is the shell friction [37] and χ is the shell stiffness parameter [22, 37]

$$\chi = \frac{E\epsilon}{1-\nu}, \quad (10)$$

where E is Young's modulus, ϵ is the shell thickness, and ν is Poisson's ratio.

The mean approach velocity v of two identical bubbles is given by [31]:

$$v = \frac{dd}{dt} = -\frac{(2\pi f p_a)^2}{27\eta} \rho \kappa^2 \frac{R_0^5}{d^2}, \quad (11)$$

where d is the distance between the centres of the two bubbles and κ is the compressibility of the bubble. Integrating from the initial distance between the bubbles d_0 to 0 yields the collision time (Eqn. 12) shown in Fig. 9.

$$t_c = -\int_{d_0}^0 \frac{27\eta}{(2\pi f p_a)^2 \rho \kappa^2 R_0^5} d^2 dd = \frac{9\eta}{(2\pi f p_a)^2 \rho \kappa^2 R_0^5} \frac{d_0^3}{3}, \quad (11)$$

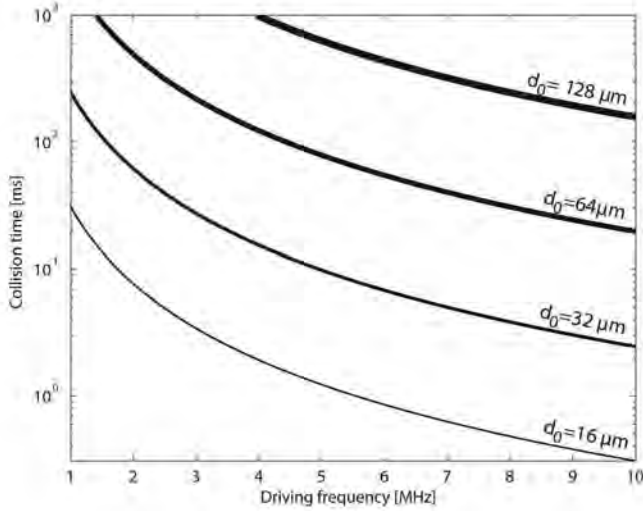


Figure 9 – Collision times of individual encapsulated microbubbles as a function of driving frequency at given distances d_0 , using $p_a = 20$ kPa, $R_0 = 1.25 \mu\text{m}$, $\kappa = 5 \times 10^{-6} \text{ m}^2 \text{ N}^{-1}$ and $\rho = 998 \text{ kg m}^{-3}$.

In a standing wave field, bubbles with resonance frequencies higher than the transmitted sound field aggregate at the pressure antinodes, whereas bubbles with resonance frequencies lower than the transmitted sound field aggregate at the pressure nodes [36]. Hence, the ultimate distance d_∞ between clusters must be a quarter of the wavelength, *i.e.*,

$$d_\infty = \frac{\lambda}{4} = \frac{c}{4f}, \quad (12)$$

Both processes of bubble clusters aggregating and the movement of clusters in the direction of the sound field can be described by a simplified version of Eqn. 6.

$$v = \frac{dh}{dt} \approx \frac{p_a^2}{6\rho c f \eta} \frac{\delta\left(\frac{f_c}{f}\right)}{\left[\left(\frac{f_c}{f}\right)^2 - 1\right]^2 + \left[\delta\left(\frac{f_c}{f}\right)\right]^2}, \quad (13)$$

where h is the distance travelled by the cluster and f_c is the cluster resonance frequency, for which $f_c < f_0$ must hold, since the bubble cluster radius $R_c > R_0$.

For the bubble cluster compressibility κ_c , $\kappa \leq \kappa_c < \kappa_f$ must hold, in which κ_f is the compressibility of a free (unencapsulated) gas bubble.

Bubble coalescence is the fusion of two or more bubbles. As adjacent bubbles collide or expand, the pressure in the film between them increases, resulting in a deformation (flattening) of the bubble surfaces. The continuing bubble expansion causes drainage of the interposed film. This thinning continues until a critical thickness around 0.1 μm is reached, at which the Van der Waals attractive forces result in film rupture and bubble coalescence [38]. Film drainage is generally much faster for free (unencapsulated) bubbles than for encapsulated bubbles, as a result of the flow pattern in the draining film [39].

The coalescence mechanism of lipid-encapsulated microbubbles was investigated, based on high-speed optical observations of sonicated ultrasound contrast agent microbubbles [39]. It was found that, when sonicated at high acoustic amplitudes, lipid-encapsulated microbubbles expose free surfaces during the expansion phase, speeding up the coalescence process dramatically. Hence, for the formation of bubble clouds or microfoams, the use of low acoustic amplitudes is desirable.

Materials and methods

A schematic overview of the experimental setup for simultaneous optical observation during sonication is shown in Fig. 10.

A polycarbonate container was built with internal dimensions of 24×18×15 (cm)³. To give access to a microscope objective lens and reduce optic aberrations, a 11-mm diameter hole was drilled in the base, covered with a 2-mm thick test slide (Jencons (Scientific) Ltd., Leighton Buzzard, Bedfordshire, UK). The container was filled with 2.6 L tap water. The container was locked in place on an $x - y$ translation stage of a DM IRM inverted microscope (Leica Microsystems GmbH, Wetzlar, Germany) with two objective lenses: a 506075 C-Plan 10×/0.22 NA objective lens (Leica Microsystems GmbH), and a 506236 N-Plan 50×/0.50 NA (Leica Microsystems GmbH) objective lens. A Mille Luce™ Fibre Optic Illuminator Model M1000 (StockerYale, Inc., Salem, NH) was connected to an optic fibre with a 7-mm diameter leading into the water of the container. It was placed in line with the objective lens, as shown in Fig. 11.

The charge coupled device (CCD) of a FASTCAM MC-1 high-speed camera (Photron (Europe) Limited, West Wycombe, Bucks, United Kingdom) was mounted to the C-Mount of the microscope and connected to its processing unit, which was capable of recording images up to 10,000 frames per second. The camera was controlled by a laptop computer.

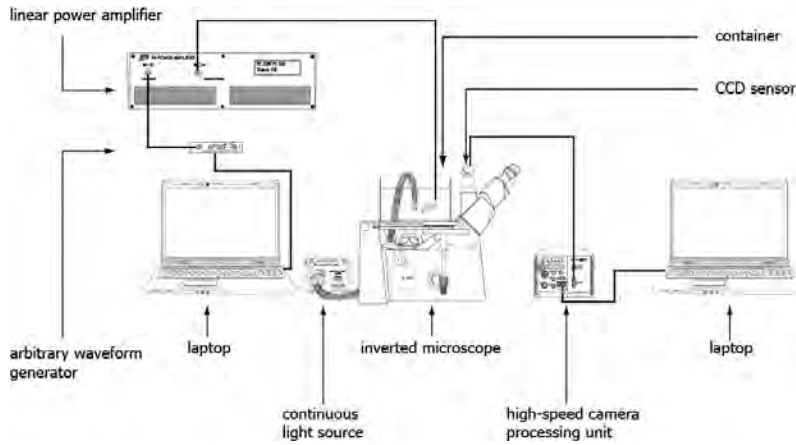


Figure 10 – Schematic overview of the experimental setup.

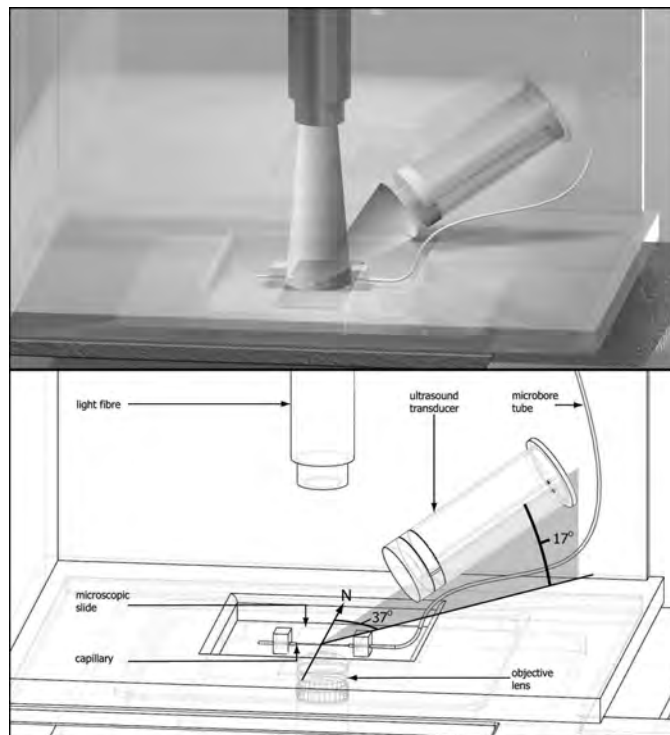


Figure 11 – Close-up of the sonication tank coinciding sound, light beam and objective focus (top) and definitions of the azimuth and elevation of the transducer relative to the North of the container (bottom).

Ultrasound

A laptop computer triggered a DATAMAN-530 arbitrary waveform generator (Dataman Programmers Ltd., Maiden Newton, Dorset, UK), which was connected to a 2100L, 50-dB RF power amplifier (Electronics & Innovation Ltd., Rochester, NY). The power amplifier was connected to a single element transducer containing a Pz37 Piezoelectric ceramic (Ferropem Piezoceramic A/S, Kvistgård, Denmark) with a centre frequency of 2.2MHz. The design of the transducer is shown in Fig. 2. Transmitted signals were continuous waves with frequencies in the range 1–10MHz. The peak-negative acoustic pressures were determined using a PVDF needle hydrophone system with a 0.2-mm active element (Precision Acoustics Ltd., Dorchester, Dorset, UK) connected to a TDS 420A digitising oscilloscope (Tektronix, Inc., Beaverton, OR).

The ultrasound transducer was positioned in the container using a clamp stand, at a focal distance of 38mm from the region of interest to be studied. The azimuth of the length axis of the transducer to the relative North of the container was 37° and the elevation of the length axis of the transducer relative to the base of the container was 17°, as shown in Fig. 11.

Ultrasound contrast agent

Definity® (Lantheus Medical Imaging, North Billerica, MA) consists of C₃F₈ gas microbubbles with mean diameter between 1.1 and 3.3 µm, encapsulated by a lipid/surfactant shell. Its resonance frequency has been measured to be 2.7MHz [61]. The 1.5-ml vials used in these experiments were stored at 9°C. Each vial was shaken for 15 s using a Vialmix® device (Lantheus Medical Imaging, North Billerica, MA). Before introducing the ultrasound contrast agent, it was further diluted using a 0.9% saline solution.

The diluted ultrasound contrast agent was inserted using a syringe into a micro-bore tube with a 0.51-mm inner diameter. The tube led to a CUPROPHAN® RC55 cellulose capillary (Membrana GmbH, Wuppertal, Germany) with a 200-µm inner diameter and 8-µm wall thickness. The middle of the capillary coincided with the optical focus of the objective lens and with the acoustic focus of the ultrasound transducer, as shown in Fig 11. The typical field of view using the 10× objective lens was 500×500 (µm)², whereas the diameter of the acoustic focus was greater than 5mm. Hence, the whole field of view could be considered in acoustic focus.

The capillary was positioned 2 mm above base of the container. The flow speed of the ultrasound contrast agent through the capillary was manually controlled.

In total, 48 experiments were performed. Bubble and cluster sizes were measured and tracked using Image-Pro Plus (Media Cybernetics, Inc., Bethesda, MD). Further analysis was done using Matlab® (The Mathworks™, Natick, MA).

Results and discussion

At the high concentration used, clustering started instantaneously after the ultrasound source activated. Fig. 12 illustrates the speed of cluster formation of DEFINITY[®] ultrasound contrast agent that had been further diluted to 1:20 v/v.

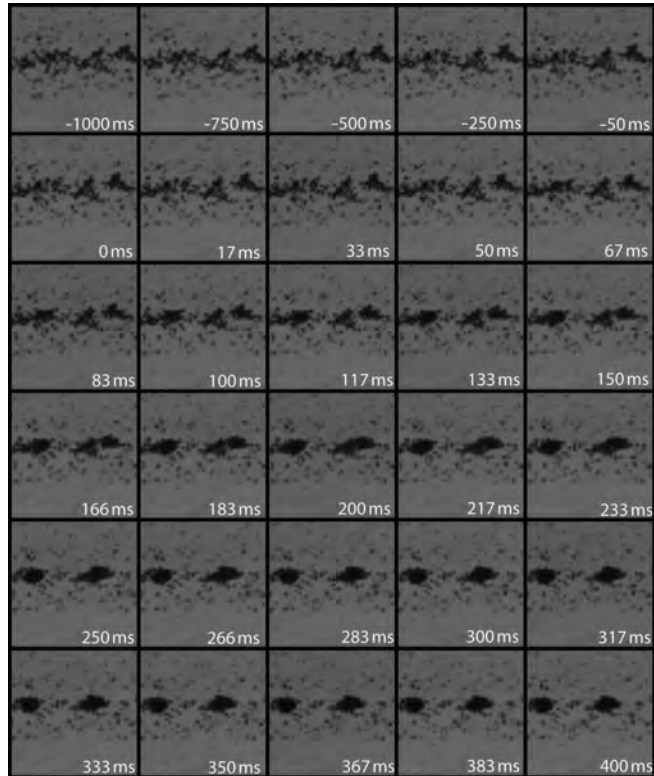


Figure 12 – Microfoam formation during continuous sonication at 2 MHz and 20-kPa peak-negative acoustic pressure. Each frame corresponds to a $120 \times 120 \text{ } (\mu\text{m})^2$ area. Time $t = 0$ was defined by the start of the sonication.

With distances between microbubbles of only few micrometres, collision times from Eqn 11 should be within a second, as shown in Fig. 9. Also from Eqn. 11 and Fig. 9 it is explained why cluster formation must be faster at higher frequencies, if the other acoustic parameters and the concentration are not changed, or, after a fixed duration, larger clusters must have formed using higher frequencies, since bubbles can approach from larger d_0 at higher f . These deductions are confirmed by the following experimental observations. In Fig. 12, after 233 ms two clusters have been formed of approximately $15 \text{ } \mu\text{m}$ diameter each. These started to approach in the subsequent frames. Overall, newly formed clusters collided to form larger clusters. This is illustrated in figures 13 and 14.

Each branch represents a cluster. The branches coming together represent the collision and coalescence of clusters into larger clusters. The velocities of clusters are on the order of tens of micrometres per second. Although increasing the acoustic pressure would increase the cluster velocities dramatically, as evident from Eqn. 13, they would also lead to microbubble disruption [22]. At the frame rates used phenomena associated with microbubble disruption were not observed.

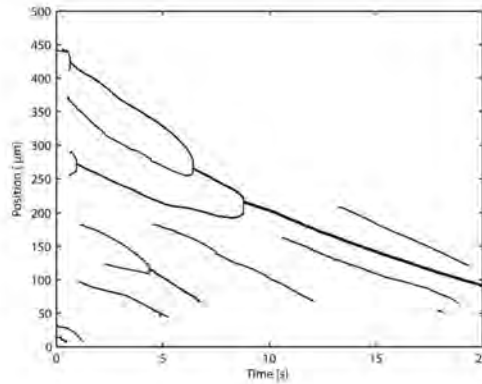


Figure 13 - Cluster positions as a function of time, during continuous sonication at 2 MHz and 20-kPa peak-negative acoustic pressure. Position in the capillary is defined from East (0 μm) to West (500 μm). Bold lines indicate merged clusters. The beginning (left) of a line indicates the formation of a cluster of diameter $> 6.8 \mu\text{m}$. The end (right) of a line indicated the disintegration or contraction of a cluster to a diameter $< 6.8 \mu\text{m}$.

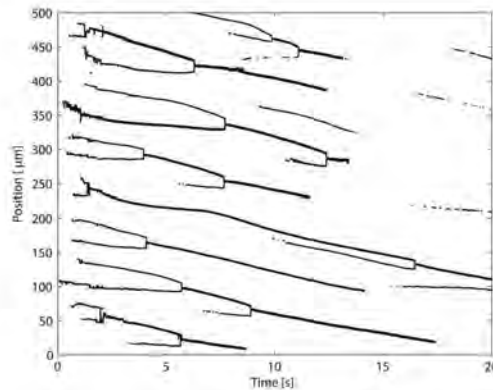


Figure 14 - Cluster positions as a function of time, during continuous sonication at 7 MHz and 22-kPa peak-negative acoustic pressure. Position in the capillary is defined from East (0 μm) to West (500 μm). Bold lines indicate merged clusters. The beginning (left) of a line indicates the formation of a cluster of diameter $> 6.8 \mu\text{m}$. The end (right) of a line indicated the disintegration or contraction of a cluster to a diameter $< 6.8 \mu\text{m}$.

The larger a cluster grows, the lower its resonance frequency becomes. Hence, the velocity of a cluster in the direction of the sound field, defined by Eqn. 13, should decrease in time. If two identical clusters with resonance frequency f_0 merge, the resulting resonance frequency is $f'_c \approx \left(2^{-\frac{1}{3}}\right)f_0 = 0.79f_0$ [110]. Assuming that the compressibility and damping coefficient do not substantially change, a similar decrease in cluster velocity is expected. However, the decrease in slope magnitude of the main branch in Fig. 13 is negligible. This might be explained if the resulting cluster is much stiffer than the original clusters, increasing the damping coefficient.

Also, 7 MHz must be further off the cluster resonance frequency than 2 MHz. Hence; the magnitudes of the slopes in Fig. 14 are lower than those in Fig. 13.

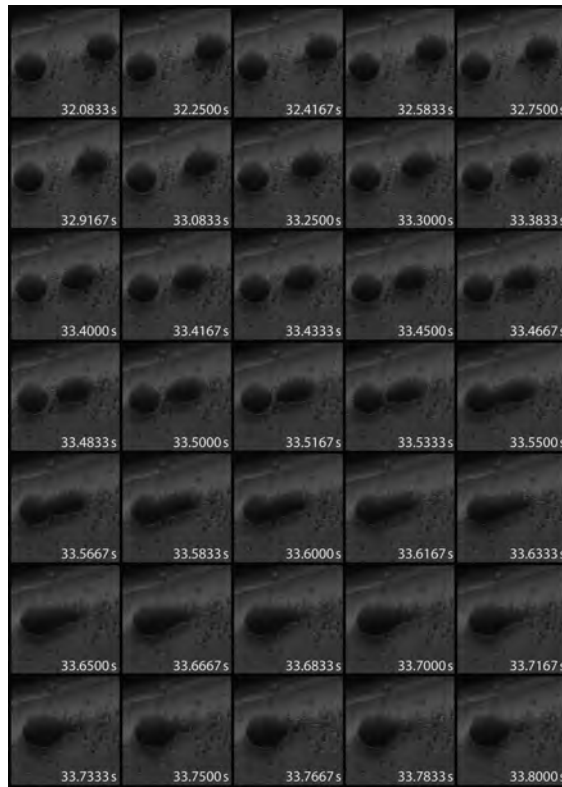


Figure 15 – Two clusters, with 22- μm diameters and an initial distance of 55- μm , colliding and merging during continuous sonication at a 2-MHz driving frequency and a 20-kPa peak-negative pressure. The frame size corresponds to 81×81 (μm)². Times are relative to the start of the sonication ($t = 0$).

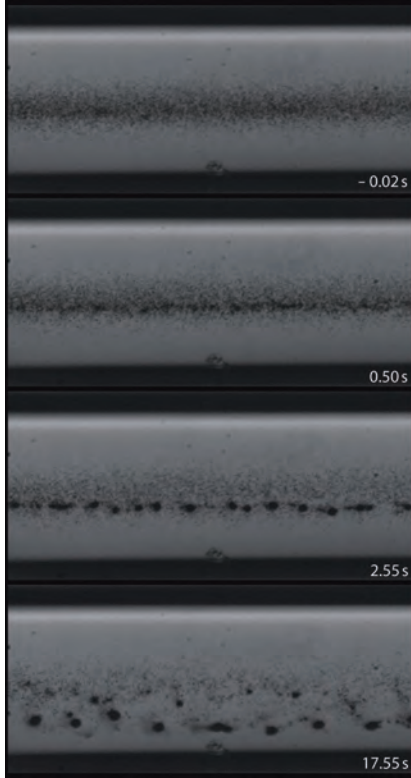


Figure 16 – Clusters forming during sonication at 7 MHz and 22-kPa peak negative pressure. The frame size corresponds to $560 \times 264 \text{ } (\mu\text{m})^2$. Time $t = 0$ was defined by the start of the sonication.

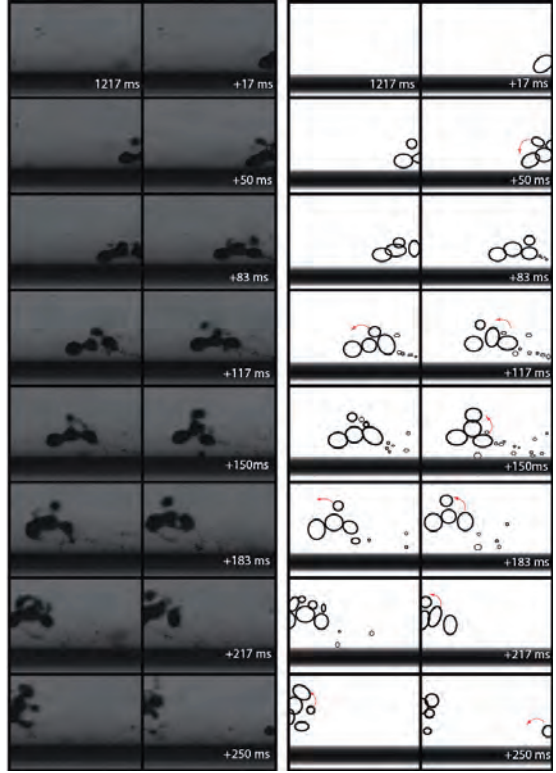


Figure 17 – Morphing microfoam during sonication at 7 MHz and 86 kPa peak-negative pressure and a schematic representation of the event. The frame size corresponds to $274 \times 198 \text{ } (\mu\text{m})^2$. Time $t = 0$ was defined by the start of the sonication.

Secondary radiation forces of clusters onto each other do not explain the cluster colliding times observed. Even if the compressibility of the clusters would be equal to that of a single ultrasound contrast agent microbubble, under the acoustic conditions used the collision times from Eqn. 11 would be just milliseconds.

Hence, the bubble clusters cannot be regarded as identical monopoles in this setting.

A close-up of two colliding clusters with 22- μm diameters forming a 25- μm cluster is shown in Fig. 15. The total time spanning this process is slightly less than 1.8 s.

The clusters were initially formed in the middle of the capillary. These clusters were located at distances $d_0 < \frac{1}{4}\lambda$, as demonstrated in Fig. 16. However, following further cluster coalescence during 17.55 s of sonication, the final distance between the larger

clusters corresponded to $\frac{1}{4}\lambda = 54 \text{ } \mu\text{m}$. These had been pushed towards the lower capillary wall, owing to primary radiation forces.

The clusters velocities towards the capillary wall were between $5 \text{ } \mu\text{m s}^{-1}$ at 7 MHz and 22-kPa peak-negative pressure and $15 \text{ } \mu\text{m s}^{-1}$ at 2 MHz and 20 kPa peak-negative pressure sonication. These are of the same order as the left hand side term in Eqn.13. The magnitudes of the slopes in Fig. 14 did not change close to the capillary wall. Hence, in this experimental setup, any effect of the capillary wall on cluster translation was neglected.

At these bulk concentrations, clusters were formed within seconds with diameters $25 \pm 2 \text{ } \mu\text{m}$. Taking into account the diameters and assuming a spherical shape, it can be estimated that the clusters contain 2,000 microbubbles each.

The clusters interact, owing to primary and secondary Bjerknes forces, creating morphing microfoams. Figure 17 shows four interacting clusters in steady liquid.

Primary Bjerknes forces push the clusters in the direction of the sound field at an average speed of 4 mm s^{-1} . The shear of the capillary wall caused a rotation of the interacting clusters.

Figure 18 shows at least eight interacting clusters. Again, a rotation motion can be observed. Also, individual ultrasound contrast agent microbubbles can be seen to hop from cluster to cluster. This microscopic scale behaviour can be attributed to very subtle changes in the acoustic field, causing ever-changing local nodes and antinodes. With cluster diameters less than $30 \text{ } \mu\text{m}$, buoyancy effects may be neglected at these timescales as well.

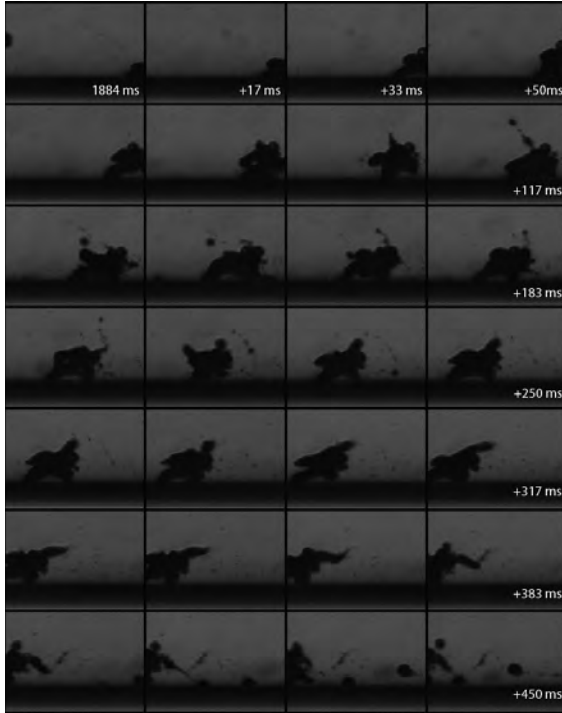


Figure 18 - Morphing microfoam during sonication at 7 MHz and 86 kPa peak-negative pressure and a schematic representation of the event. The frame size corresponds to $274 \times 198 \text{ } (\mu\text{m})^2$. Time $t = 0$ was defined by the start of the sonication.

In summary, the following stages of microfoam formation, illustrated in Fig. 19 were observed. The initial situation was a dense, random bubble distribution before ultrasound arrival. After sonication started, contrast microbubbles collided, owing to secondary radiation forces. Subsequently, these clusters merged within the space of a quarter of the wavelength, owing to primary radiation forces. The resulting microfoams translated in the direction of the ultrasound field, owing to primary radiation forces.

Small deviations in microbubble sizes or shell properties lead to deviations in individual bubbles' resonance frequencies, as expressed in Eqn. 8. These in turn cause oscillation phase differences, as expressed in Eqn. 6, big enough to be observed [40]. Therefore, predicting and manipulating individual microbubbles is technically challenging. It has been demonstrated that as soon as the bubble clusters were formed and as long as they were in the sound field, they behaved as one entity. At the acoustic settings used, it took seconds to force the bubble clusters to positions approximately $\frac{1}{4}\lambda$ apart. It also just took seconds to drive the clusters towards a boundary.

It may assume that vessel blocking can only be successful if a microfoam is created with a diameter equal to or greater than the vessel diameter d_v . From this study it follows that in order to create such a foam, $\frac{1}{4}\lambda > d_v$, or, $f < \frac{c}{4d_v}$.

For therapeutic purposes, it would be of great interest to induce microjetting on entire clusters towards a vessel wall, presumably causing sonoporation or sonolysis.

Although ultrasound-induced microjetting has been observed with ultrasound contrast agents, its occurrence in *in vivo* situations is hard to control [41, 42].

Predictable sonic manipulation would be better feasible if the microbubbles would be forced to cluster to known size and position first.

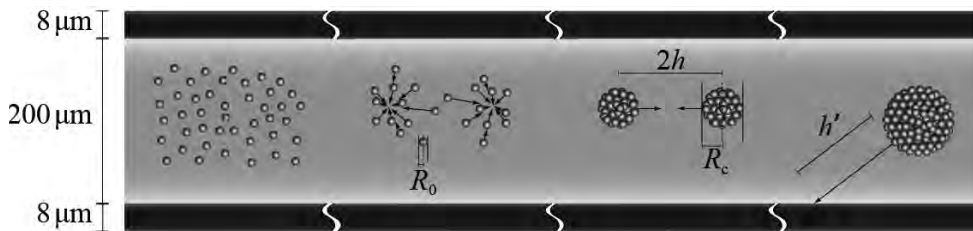


Figure 19 – Schematic representation of the four stages of microfoam formation in a capillary: (left-right) random bubble distribution before ultrasound arrival, bubble colliding during sonication, cluster merger within the space of a quarter of the wavelength, microfoam translation.

Conclusions

The following stages of microfoam formation within a densely populated concentration of microbubbles were observed. After the sonication started, contrast microbubbles collided, forming small clusters, owing to secondary radiation forces.

These clusters coalesced within the space of a quarter of the ultrasonic wavelength, owing to primary radiation forces. The resulting microfoams translated in the direction of the ultrasound field, hitting the capillary wall, also owing to primary radiation forces.

It has been demonstrated that as soon as the bubble clusters were formed and as long as they were in the sound field, they behaved as one entity. At the acoustic settings used, it took seconds to force the bubble clusters to positions approximately a quarter wavelength apart. It also just took seconds to drive the clusters towards the capillary wall.

Subjecting ultrasound contrast agent microbubbles to a continuous low-amplitude signal makes them cluster to known positions and known microfoam sizes, allowing for straightforward sonic manipulation.

Sonoporation at a low MI

Introduction

Sonoporation is the transient permeabilisation and resealing of a cell membrane with the help of ultrasound and/or an ultrasound contrast agent, allowing for the trans-membrane delivery and cellular uptake of macromolecules between 10 kDa and 3 MDa [29]. Many studies have demonstrated increased drug and gene uptake of sites under sonication [28, 43-49]. These studies presumed, that a physical membrane disruption mechanism, *i.e.*, sonoporation, caused the increased uptake, as opposed to naturally occurring active uptake processes, such as endocytosis, that are controlled by the system biology [28, 43-49].

Although mechanical disruption with the aid of ultrasound has been attributed to violent side effects of inertial cavitation and microbubble fragmentation, most notably, the increased uptake has also been observed at low acoustic amplitudes, *i.e.*, in acoustic regimes where inertial cavitation and microbubble fragmentation are not to be expected [50]. An ultrasound contrast agent microbubble might act as a vehicle to carry a drug or gene load to a perfused region of interest. If the same ultrasound field that has been implicated in the sonoporation process can cause release of the therapeutic load, this load could be delivered into cells. Apart from plainly mixing ultrasound contrast agents with therapeutic agents, several schemes have been proposed to incorporate therapeutic loads to microbubbles. These include loads to the microbubble shell [51], therapeutic gases inside the microbubble [52], gas-filled lipospheres containing drugs [53], and drug-filled antibubbles [54]. To understand and ameliorate ultrasound-assisted drug and gene delivery, the physics of controlled release and of sonoporation have been under investigation. That objective also forms the focus for this chapter. Moreover the behaviour of ultrasound contrast agent microbubbles near cancer cells deliberately at low acoustic amplitudes in order to probe whether sonoporation in this regime was possible was studied; and if so, to ascertain what the microscopic mechanism might entail; and finally, to assess and scrutinise the safety aspects of ultrasound exposure in this regime.

Mechanical index

On commercial scanners, the MI has been limited to 1.9 for medical imaging [55]. At low MI, microbubbles pulsate linearly, whereas at high MI, their greater expansion phase is followed by a violent collapse. During the collapse phase, when the kinetic energy of the bubble surpasses its surface energy, a bubble may fragment into a number of smaller bubbles. Fragmentation has been exclusively observed with contrast agents with thin, elastic shells. Fragmentation is the dominant disruption mechanism for these bubbles [22]. Although the fragmentation of therapeutic load-bearing microbubbles must release their loads, the actual drug or gene delivery is in this case a passive process, dependent on diffusion rate and proximity to the target cells. Fragmenting microbubbles may not create pores in cells, since fragmentation costs energy. However, if a microbubble collapses near a free or a solid boundary, the retardation of the liquid near the boundary may cause an asymmetry. This asymmetry

causes differences in acceleration on the bubble surface. During further collapse, a funnel-shaped jet may protrude through the microbubble, shooting liquid to the boundary [56]. The pore size created by a jet has been empirically related to the microbubble expansion [57]. If jets could be directed to cell layers, in case of a microbubble carrying a therapeutic load, the load could be delivered into cells. The jet formation is affected by the cavitation topology, synergistically interacting with local fluid dynamics arising through the bubble's expansion and contraction due to the ultrasound field. However, as the fluid forming the microjet is just the bulk fluid that carries no therapeutic agent, then there is no guarantee that, even with the formation of a sonopore due to jet impact with the cell membrane, therapeutic agent will enter the cell. It needs to be dislodged and mobilised from the bubble first. Furthermore, jetting has not been observed at low or moderate MI [41], so that fragmentation is likely to occur before any delivery takes place. By pushing the loaded microbubbles towards the vessel all using primary radiation forces [30], release can take place closer to target vessels. In a recent study, Caskey *et al.* pushed bubbles into tissue-mimicking gels at $MI=1.5$ [58]. It was previously studied how microclusters consisting of lipid-encapsulated microbubbles can be formed using primary and secondary radiation forces, and how these clusters can be pushed towards vessel walls [59]. It was found that, even at $MI<0.15$, microbubble clusters can be formed and pushed towards a boundary within seconds.

Sonoporation

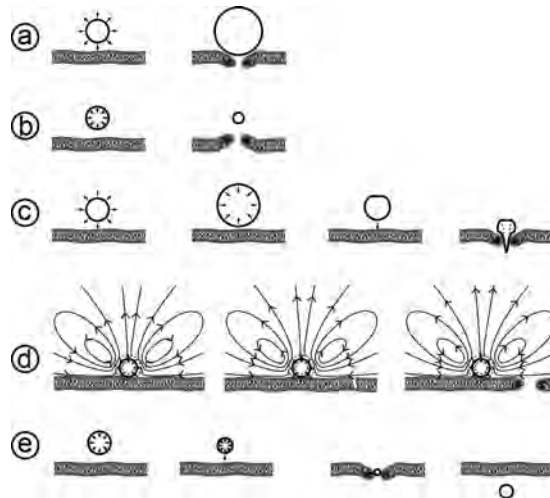


Figure 20 – Possible mechanisms of sonoporation: (a) push, (b) pull, (c) jetting, (d) shear, (e) translation.

There are five non-exclusive hypotheses for explaining the sonoporation phenomenon. These have been summarised in Figure 20: push, pull, jetting, shear, and translation [60]. It has been hypothesised that expanding microbubbles might push the cell membrane inward, and that collapsing bubbles might pull cell membranes outward [61]. These mechanisms require microbubbles to be present in the close vicinity of cells. A separate release mechanism should then ensure localised delivery. Although jetting only occurs in a high-MI regime, it is very effective in puncturing cell membranes. Jetting has been observed through cells using ultrasound contrast agent microbubbles. However, the acoustic impedance of the solid cell substratum formed the boundary to which the jetting took place, not the cell itself [42]. Also, there has not been any proof yet of cell survival after jetting. In a separate study, the role of jetting as a dominant mechanism in sonoporation was excluded [62]. If a microbubble is fixed to a membrane the fluid streaming around the oscillating bubbles creates enough shear to rupture the membrane [63]. Here again, separate release mechanisms should then ensure localised delivery. Finally, it has been speculated that lipid-encapsulated microbubbles, in compressed phase, translate through cell membranes or channels in the cell membrane such as the receptor. In case of therapeutic loading, the load would be delivered directly into the target cell. The main advantage of the latter mechanism is that microbubble translation by means of ultrasonic radiation forces requires very low acoustic pressures. Hence, potential damaging bioeffects due to inertial cavitation can be ruled out.

Materials and methods

Sonoporation configuration

In previous studies, increased gene uptake was demonstrated at $MI < 0.3$ [64, 65]. Similar sonoporation configuration was used for these experiments. An overview of the experimental setup is shown in Figure 21. A signal consisting of 50 cycles with a centre frequency of 6.6 MHz and a pulse repetition frequency of 10 kHz, i.e., a duty cycle of 7.5%, was generated by an AFG3102, dual channel arbitrary function generator (Tektronix, Inc., Beaverton, OR), amplified by a 150A250 radio-frequency (RF) amplifier (Amplifier Research, Souderton, PA) set to maximum gain, and fed to a custom-built 6.6-MHz ultrasound transducer with a hexagonal Y-36° lithium niobate element with a maximum diameter of 25 mm [66].

The peak-negative acoustic pressure was measured to be 0.5 MPa in a separate tank and in the sonication chamber itself. This corresponds to an MI of 0.2.

The transducer was placed in a custom-built, $260 \times 160 \times 150$ (mm)³ Perspex sonication chamber, in which an OptiCell® cell culture chamber (Nunc GmbH & Co. KG, Langenselbold, Germany) was placed. One side of the cell culture chamber contained a monolayer of 1.6×10^6 HeLa cells that had been cultured in MEM with Earl's salts medium (PAA Laboratories GmbH, Pasching, Austria) supplemented with 10% v/v heat-inactivated foetal calf serum, GlutaMAX™ (Life Technologies Gibco, Paisley, Renfeshire, UK), 1% v/v of non-essential amino-acids (PAA), penicillin ($100 \text{ units ml}^{-1}$) and streptomycin ($100 \text{ } \mu\text{g ml}^{-1}$) (PAA), at 37°C in a humidified atmosphere containing

5% CO₂. The cells were used when there was 60–80% confluency. Ultrasound contrast agent was injected into the cell culturing chamber before each experiment. Several lipid-shelled ultrasound contrast agents were tested in this study. In this chapter, results of a 3.33% dilution of MicroMarker® (VisualSonics B.V., Amsterdam, Netherlands), a lipid-shelled agent with a mean diameter of 2.5 µm are presented. A customised BXF-M-F microscope unit with an LCAch N 20×/0.40 NA PhC (Olympus Deutschland GmbH, Hamburg, Germany) and a LUMPlanFL 60×/0.90 NA water-immersion objective (Olympus) was placed on top of the sonication chamber with the objective lens immersed in the water. The colour charge coupled device (CCD) of a PHOTRON FastCam MC-2.1 high-speed camera (VKT Video Kommunikation GmbH, Pfullingen, Germany) was connected to the microscope. The sensor was rotated to make sure that in all recorded movies, the ultrasound is directed from the left to the right of the frame.

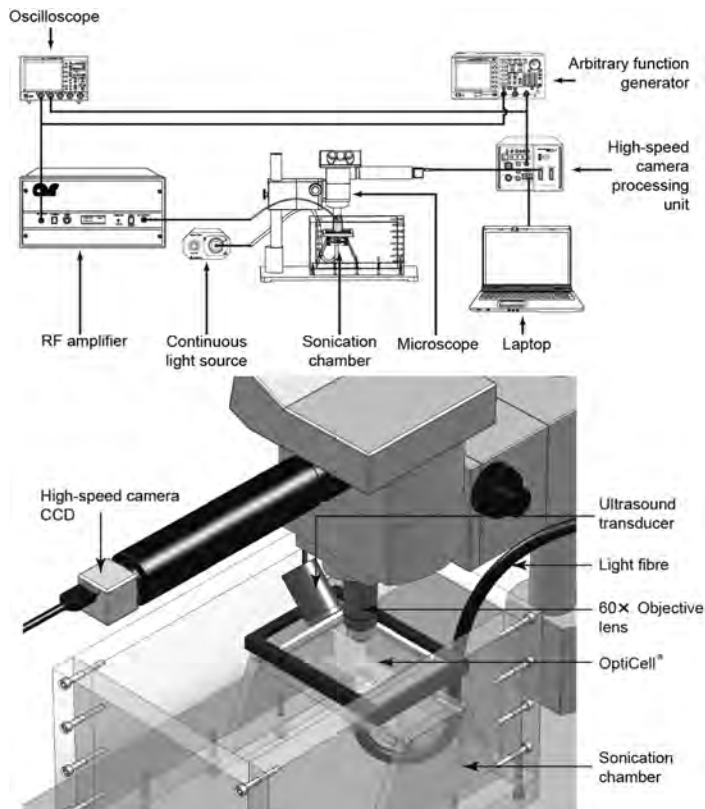


Figure 21 – Experimental setup (*top*) and a close-up of the sonoporation configuration (*bottom*).

Fluorescence configuration

An overview of the setup used for the fluorescence experiments is shown in Fig 22. It is almost identical to the setup described in the previous section. However, here, the signal consisted of 40 cycles with a centre frequency of 6.6MHz and a pulse repetition frequency of 10 kHz, *i.e.*, a duty cycle of 6.1%, was amplified using a 2100L, 50-dB RF amplifier (Electronics & Innovation Ltd., Rochester, NY) and fed to a custom-built 6.6-MHz ultrasound transducer [66]. In this configuration the ultrasound propagated from the bottom-right, to the top-left of the frame.

Prior to injection in the OptiCell®, the MicroMarker® contrast agent was labeled using a DiD (DiI_{C₁₈(5)}) lipophilic fluorescent probe (Vybrant™ Molecular probes, Invitrogen, San Diego, CA). A ratio of 1 µl of DiD to 40 µl MicroMarker® was homogenised by pipetting and incubating for 5 minutes at room temperature.

Figure 23 shows how the DiD fluorescent probe bonded to the phospholipid [67]. Emitted fluorescence ($\lambda = 649\text{--}703\text{ nm}$) was localised on the microbubble shell when exciting at $\lambda = 633\text{ nm}$.

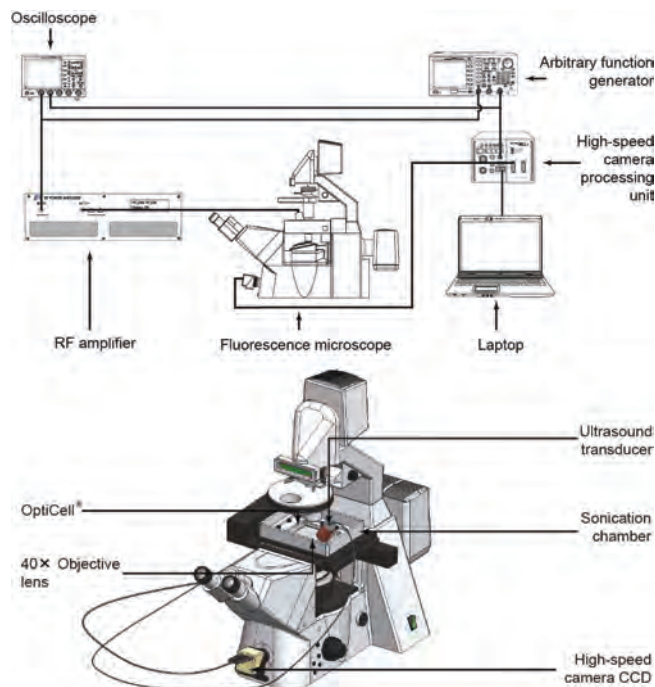


Figure 22 – Experimental setup (top) and a close-up of the fluorescence configuration (bottom).

A custom-made aluminium sonication chamber with internal dimensions of $130 \times 170 \times 35\text{ (mm)}^3$ was locked into to the $x - y$ -stage of a 200M inverted confocal microscope (Carl Zeiss AG, Oberkochen, Germany) coupled with a LSM Axiovert 510 laser scanning

device (Carl Zeiss), using an EC Plan-Neofluar 40×/1.30 NA Oil DIC M27 objective (Carl Zeiss AG), with automated *z* –stack functionality. The peak-negative acoustic pressure was measured at the objective’s field of view and corresponded to MI=0.2.

To evaluate the possible electrostatic attraction between microbubbles and cells, 30 μl MicroMarker[®] was diluted into 700 μl of distilled water and tested for electrophoretic mobility (ζ -potential) using a Zetasizer 3000 (Malvern Instruments, Malvern, Worcestershire, United Kingdom).

To measure the thickness of the cultured cells 10⁵ HeLa cells were seeded into an OptiCell[®]. The cell plasma membrane was labelled with DiD lipophilic fluorescent probe (Vybrant[™] Molecular probes) according to the manufacturer’s protocol. The membrane fluorescence was measured using a 200M confocal microscope (Carl Zeiss). Cell thickness was calculated from the difference between the upper and lower slices where fluorescence was seen. In all fluorescence recordings, the slice thickness was set to <1 μm .

Twenty-three movies under 6.6-MHz sonication at frame rates between 500 and 2000 frames per second, representing 15 minutes of real-time exposure were recorded. Of these, 11 movies were recorded using fluorescence. In addition 10 control movies were recorded, with a total duration of 22 minutes.

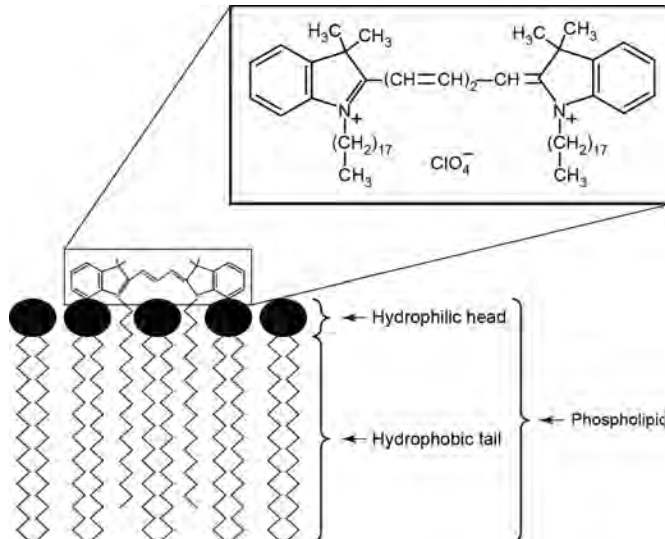


Figure 23 - Schematic representation of DiD [DiIC₁₈(5)] lipophilic fluorescent probe bonding to phospholipid.

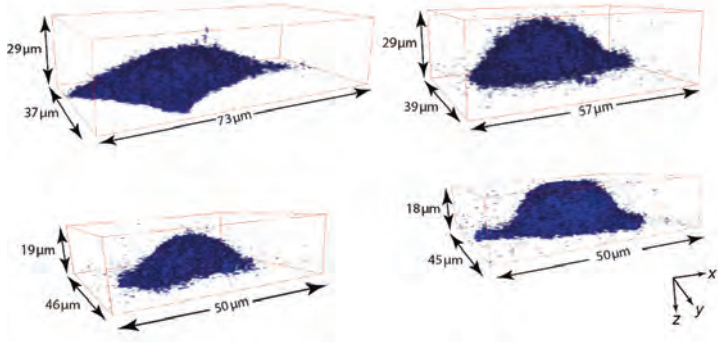


Figure 24 - z -stacks of fluorescence emitted by the DiD dye attached to the membranes of four typical HeLa cells, representing the cell geometry.

Results and discussion

Throughout this section, the optical z -axis is defined from distal-to-focus (negative) to proximal-to-focus (positive), with $z = 0$ as the focal plane.

Figure 24 shows z -stacks of fluorescence emitted by the DiD dye attached to the membranes of four typical HeLa cells, representing the cell geometry. In total, the thicknesses of 42 cells were measured. The cultured cells were found to be $13 \pm 2 \mu\text{m}$ thick. Clearly, these cells had thicknesses much greater than ultrasound contrast agent microbubble oscillations amplitudes at $MI=0.2$.

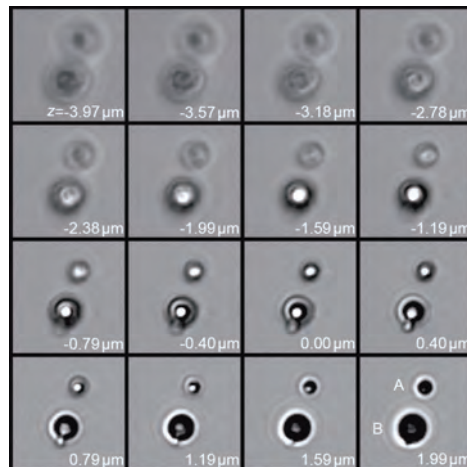


Figure 25 - z -stack of two ultrasound contrast agents microbubbles. Proximal-to-focus Airy disks can be seen around the bubbles, whereas distal-to-focus the bubble boundaries are blurred.

Microbubble “A” has a diameter of 2 μm , whereas microbubble “B” has a diameter of 3 μm . Each frame corresponds to a $11 \times 11 (\mu\text{m})^2$ area.

The optical system was analysed and the results were compared to bubbles and cells that were slightly out of focus, to rule out that the movement of the bubble takes place in a plane different from that of the cell. Figure 25 shows a z –stack of two ultrasound contrast agent microbubbles, similar to Figure 10 of Postema *et al* [68]. Proximal-to-focus Airy disks can be seen around the bubbles, whereas distal-to-focus the bubble boundaries are blurred. Note that the boundary contrast is maximal just proximal-to-focus [68].

At a centre frequency of 6.6 MHz, 17 events of microbubbles entering HeLa cells were recorded. After entering, the microbubbles were observed to quickly dissolve. As an example, Figure 26 shows an event resampled at 3.4 Hz and 40 Hz, respectively, here two bubbles were pushed to a cell during 11 s of sonication.

A microbubble “A” of 4- μm diameter entered the cell and dissolved, whereas a microbubble “B” of 2- μm diameter stuck to the cell membrane.

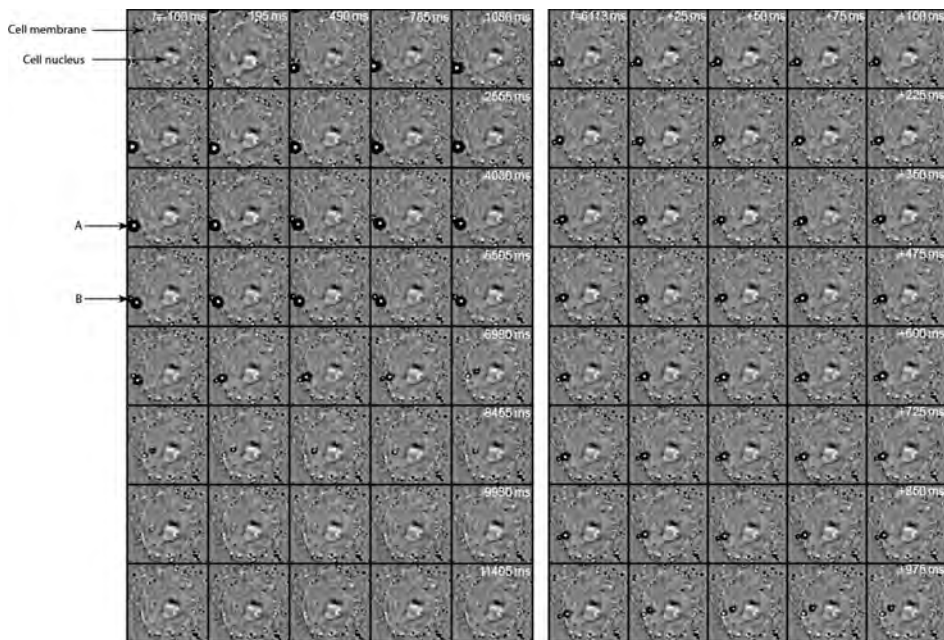


Figure 26 - A sonoporation event including microbubble dissolution during 11 s of sonication (*left*) and selected frames of the microbubble entering a cell (*right*). Microbubble “A” entered the cell and dissolved, whereas microbubble “B” stuck to the cell membrane. Each frame corresponds to a $23 \times 23 (\mu\text{m})^2$ area.

Figures 27 and 28 show two similar events, where fluorescence-coated microbubbles were used. The left panels show a microbubble apparently penetrating through the cell membrane in optical focus. Approximately 70ms after the ultrasound is switched on a microbubble is seen to penetrate through the cell membrane in Figure 27. In Figure 28 the microbubble is seen to penetrate through the cell membrane approximately 24 ms after the ultrasound has been switched on. The right panels show a z –stack through the entire cell, to record whether the apparent microbubble entry is actually into the cell. For both events, Figure 29 shows average fluorescent intensities in two regions of interest, one inside the cell, and one control region. In both events, most fluorescence from apparent microbubble entry can be observed within 5 μm proximal to optical focus, thus well within the cells themselves.

Figure 30 shows frames in optical focus from the events in Figures 27 and 28, before sonication and approximately 8 minutes after sonication. Clearly, fluorescence has transferred into the cells and remained inside the cells long after sonication. At these low acoustic amplitudes, inertial cavitation, fragmentation, and jetting should not occur. Hence, as a mechanism in sonoporation at low MI, these phenomena might justifiably be neglected.

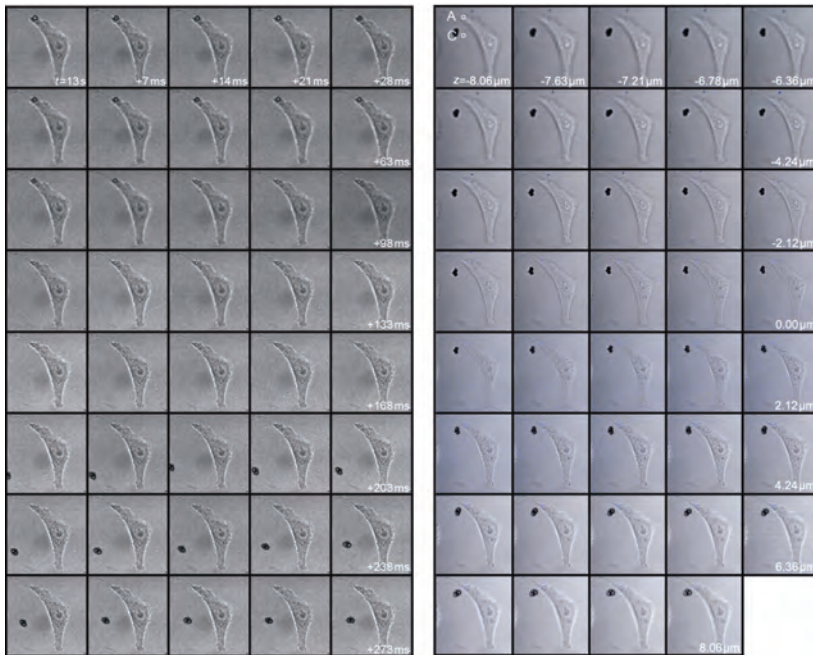


Figure 27 - Microbubble of 5- μm diameter apparently penetrating through the cell membrane in optical focus (*left*); z –stack through the entire cell, to record whether the apparent microbubble entry is actually into the cell (*right*). Areas “A” and “C” are regions of interest inside and outside the cell, respectively. Each frame corresponds to a $76 \times 76 (\mu\text{m})^2$ area.

Our observations do not explain why some microbubbles enter a cell and others don't. The quick dissolution after entering suggests that the microbubble loses (part of) its shell whilst entering.

The ζ potential measurements showed that the microbubble shells had a charge of -43.9 ± 2.4 mV. As cells have a natural negative charge [69, 70], the ultrasound contrast agent should be repelled by the cells. In all recordings it was seen that once the ultrasound was turned on, the microbubbles were attracted to the closest cell, independent of the direction of the sound field. This supports the recent finding that cell membranes can be acoustically active [71], and therefore interact with microbubbles.

Other cell types than HeLa cells must be used in follow-up studies, to investigate differences in bubble–cell interaction.

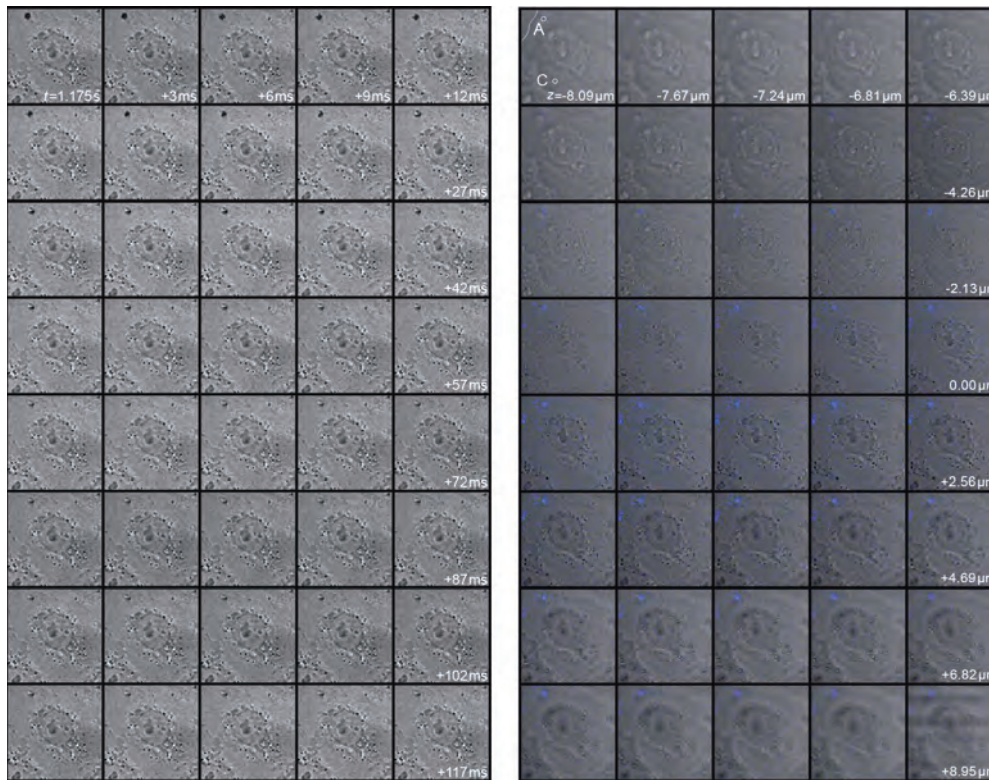


Figure 28 – Microbubble of 4- μm diameter apparently penetrating through the cell membrane in optical focus (*left*); z -stack through the entire cell, to record whether the apparent microbubble entry is actually into the cell (*right*). Areas “A” and “C” are regions of interest of high fluorescence and low fluorescence, respectively. The white dotted line in the upper left frame of the right panel indicated the cell membrane. Each frame corresponds to a 52×52 (μm)² area.

Conclusions

It has been demonstrated that lipid-shelled microbubbles can be forced to enter cells at a low MI. Hence, if a therapeutic load is added to the bubble, ultrasound-guided delivery could be facilitated at diagnostic settings. In addition, these results may have implications for the safety regulations on the use of ultrasound contrast agents for diagnostic imaging.

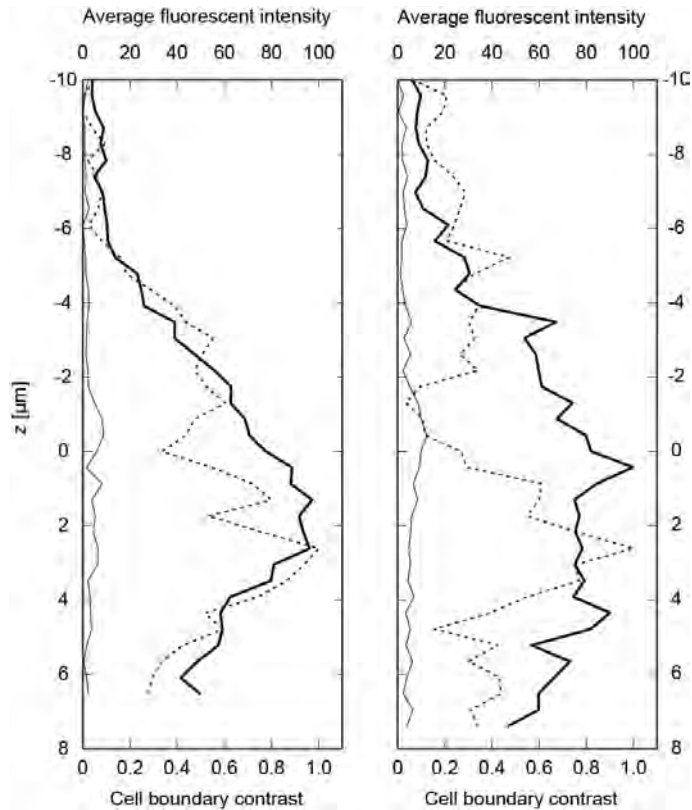


Figure 29 - Average fluorescent intensities in the regions of interest (ROI) of Figures 27 (*left*) and 28 (*right*). Bold lines represent the ROI "A" inside the cells, whereas hairlines represent ROI "C" the control regions. The dotted line represents the cell boundary contrast. Note that the cell boundary is maximal just proximal-to-focus.

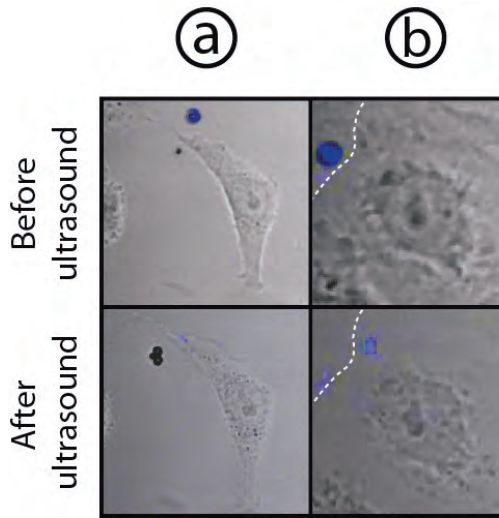


Figure 30 – Columns (a) and (b) represent frames in optical focus from the events in Figures 27 and 28, respectively, before sonication and approximately 8 minutes after sonication. The white dotted line in the right frame indicates the cell boundary. The left frames correspond to $76 \times 76 \text{ } (\mu\text{m})^2$ areas, whereas the right frames correspond to $45 \times 45 \text{ } (\mu\text{m})^2$ areas.

References

1. Unger, E.C. et al., *Therapeutic applications of microbubbles*. Eur. J. Radiol., 2002. 42: p. 160-168.
2. Stewart, I., P.J. Schluter, and G.R. Shaw, *Cyanobacterial lipopolysaccharides and human health: a review*. Environ. Health, 2006. 5(7): p. 1-23.
3. Fleming, L.E. et al., *Blue green algal (cyanobacterial) toxins, surface drinking water, and liver cancer in Florida*. Harmful Algae, 2002. 1(2): p. 157-168.
4. Bury, N., *The toxicity of cyanobacteria (blue-green algae) to freshwater fish*. Comp. Biochem. Physiol. A, 2007. 146(4): p. S92-S93.
5. San Diego-McGlone, M.L. et al., *Eutrophic waters, algal bloom and fish kill in fish farming areas in Bolinao, Pangasinan, Philippines*. Mar. Poll. Bull., 2008. 57(6--12): p. 295-301.
6. Hylland, K. et al., *Interactions between Eutrophication and Contaminants. IV. Effects on Sediment-dwelling Organisms*. Mar. Poll. Bull., 1996. 33(1--6): p. 90-99.
7. Allen, M.B. and D.I. Arnon, *Studies on Nitrogen-Fixing Blue-Green Algae. I. Growth and Nitrogen Fixation by Anabaena Cylindrica Lemm*. Plant Physiol., 1955. 30(4): p. 366-372.
8. Dauta, A. et al., *Growth rate of four freshwater algae in relation to light and temperature*. Hydrobiologia, 1990. 207(1): p. 221-226.
9. Lang, N., J. Krupp, and A. Koller, *Morphological and Ultrastructural Changes in Vegetative Cells and Heterocysts of Anabaena Variabilis Grown with Fructose*. J. Bacteriol., 1987. 169(2): p. 920-923.
10. Postema, M. et al., *Ultrasound-induced gas release from contrast agent microbubbles*. IEEE Trans. Ultrason. Ferroelectr. Freq. Control, 2005. 52(6): p. 1035-1041.
11. Ferrier, M.D. et al., *The effects of barley straw (Hordeum vulgare) on the growth of freshwater algae*. Biores. Tech., 2005. 96(16): p. 1788-1795.
12. Hao, H. et al., *Cavitation mechanism in cyanobacterial growth inhibition by ultrasonic irradiation*. Colloids Surf. B, 2004. 33(3--4): p. 151-156.
13. Ma, B. et al., *Influence of ultrasonic field on Microcystins produced by bloom-forming algae*. Colloids Surf. B, 2005. 41(2--3): p. 197-201.
14. Tang, J. et al., *Growth inhibition of the cyanobacterium Spirulina (Arthrospira) platensis by 1.7MHz ultrasonic irradiation*. J. Appl. Phycol., 2003. 15(1): p. 37-43.
15. Zhang, G., P. Zhang, and M. Fan, *Ultrasound-enhanced coagulation for Microcystis Aeruginosa removal*. Ultrason. Sonochem., 2009. 16(3): p. 334-338.
16. Zhang, G. et al., *Ultrasonic damages on cyanobacterial photosynthesis*. Ultrason. Sonochem., 2006. 13(6): p. 501-505.
17. Zhang, G. et al., *Ultrasonic frequency effects on the removal of Microcystis Aeruginosa*. Ultrason. Sonochem., 2006. 13(5): p. 446-450.
18. Chen, B. et al., *Ultrasound effects on the antioxidative defense systems of Porphyridium cruentum*. Colloids Surf. B, 2008. 61(1): p. 88-92.
19. Postema, M., *Onderzoek naar de veilige toepassing van ultrageluid gebruikt om blauwalg te bestrijden*, 2007, The University of Hull.
20. NATO Undersea Research Centre, *Human Diver and Marine Mammal Risk Mitigation Rules and Procedures*, 2006, NURC-SP-2006-008.
21. Culture Collection of Algae and Protozoa, *Media Recipes*. Vol. EG:JM. 2007.
22. Postema, M. and G. Schmitz, *Ultrasonic bubbles in medicine: influence of the shell*. Ultrason. Sonochem., 2007. 14(4): p. 438-444.
23. Postema, M. et al., *Ultrasound-induced encapsulated microbubble phenomena*. Ultrasound Med. Biol., 2004. 30(6): p. 827-840.
24. Postema, M. and G. Schmitz, *Bubble dynamics involved in ultrasonic imaging*. Expert Rev. Mol. Diagn., 2006. 6(3): p. 493-502.
25. Gorce, J.-M., M. Arditi, and M. Schneider, *Influence of bubble size distribution on the echogenicity of ultrasound contrast agents: a study of SonoVue™*. Invest. Radiol., 2000. 35(11): p. 661-671.

26. Sboros, V., *Response of contrast agent to ultrasound*. Adv. Drug Deliv. Rev., 2008. 60: p. 1117-1136.
27. Kudo, N. et al., *Study of the mechanism of fragmentation of a microbubble exposed to ultrasound using a high-speed observation system*. J. Acoust. Soc. Am., 2000. 108(5Pt2): p. 2547.
28. Lindner, J.R. and S. Kaul, *Delivery of drugs with ultrasound*. Echocardiography, 2001. 18(4): p. 329-337.
29. Postema, M. and O.H. Gilja, *Ultrasound-directed drug delivery*. Curr. Pharm. Biotechnol., 2007. 8(6): p. 355-361.
30. Dayton, P.A., J.S. Allen, and K.W. Ferrara, *The magnitude of radiation force on ultrasound contrast agents*. J. Acoust. Soc. Am., 2002. 112(5): p. 2183-2192.
31. Dayton, P.A. et al., *A preliminary evaluation of the effects of primary and secondary radiation forces on acoustic contrast agents*. IEEE Trans. Ultrason. Ferroelectr. Freq. Control, 1997. 44(6): p. 1264-1277.
32. Crum, L.A., *Bjerknes forces on bubbles in a stationary sound field*. J. Acoust. Soc. Am., 1975. 57(6): p. 1363-1370.
33. Tortoli, P. et al., *On the interaction between ultrasound and contrast agents during Doppler investigations*. Ultrasound Med. Biol., 2001. 27(9): p. 1265-1273.
34. Medwin, H., *Counting bubbles acoustically: a review*. Ultrasonics, 1977. 15: p. 7-13.
35. Di Marco, P., W. Grassi, and G. Memoli, *Experimental study on rising velocity of nitrogen bubbles in FC-72*. Int. J. Therm. Sci., 2003. 42: p. 435-446.
36. Leighton, T.G., *The Acoustic Bubble* 1994, London: Academic Press.
37. de Jong, N., R. Cornet, and C.T. Lancée, *Higher harmonics of vibrating gas-filled microspheres. Part one: simulations*. Ultrasonics, 1994. 32(6): p. 447-453.
38. Duineveld, P.C., *Bouncing and coalescence phenomena of two bubbles in water*, in *Bubble Dynamics and Interface Phenomena*, J.R. Blake, J.M. Boulton-Stone, and N.H. Thomas, Editors. 1994, Kluwer Academic Publishers: Dordrecht. p. 447-456.
39. Postema, M. et al., *Ultrasound-induced microbubble coalescence*. Ultrasound Med. Biol., 2004. 30(10): p. 1337-1344.
40. Postema, M., M. Mleczko, and G. Schmitz, *Mutual attraction of oscillating microbubbles*, in *Advances in Medical Engineering*, T.M. Buzug et al., Editors. 2007, Springer: Berlin. p. 75-80.
41. Postema, M. et al., *High-speed photography during ultrasound illustrates potential therapeutic applications of microbubbles*. Med. Phys., 2005. 32(12): p. 3707-3711.
42. Prentice, P. et al., *Membrane disruption by optically controlled microbubble cavitation*. Nature Phys., 2005. 1: p. 107-110.
43. Bao, S., B.D. Thrall, and D.L. Miller, *Transfection of a reporter plasmid into cultured cells by sonoporation in vitro*. Ultrasound Med. Biol., 1997. 23: p. 953-959.
44. Chen, S. et al., *Optimization of ultrasound parameters for cardiac gene delivery of adenoviral or plasmid deoxyribonucleic acid by ultrasound-targeted microbubble destruction*. J. Am. Coll. Cardiol., 2003. 42(2): p. 301-308.
45. Greenleaf, W.J. et al., *Artificial cavitation nuclei significantly enhance acoustically induced cell transfection*. Ultrasound Med. Biol., 1998. 24(4): p. 587-595.
46. Kondo, I. et al., *Treatment of acute myocardial infarction by hepatocyte growth factor gene transfer: the first demonstration of myocardial transfer of a "functional" gene using ultrasonic microbubble destruction*. J. Am. Coll. Cardiol., 2004. 44(3): p. 644-653.
47. Kudo, N., K. Okada, and K. Yamamoto, *Sonoporation by single-shot pulsed ultrasound with microbubbles adjacent to cells*. Biophys. J., 2009. 96(12): p. 4866-4876.
48. Tachibana, K. et al., *Induction of cell-membrane porosity by ultrasound*. Lancet, 1999. 353: p. 1409.
49. Tinkov, S. et al., *Microbubbles as ultrasound triggered drug carriers*. J. Pharm. Sci., 2009. 98(6): p. 1935-1961.
50. Deng, C.X. and F.L. Lizzi, *A review of physical phenomena associated with ultrasonic contrast agents and illustrative clinical applications*. Ultrasound Med. Biol., 2002. 28(3): p. 277-286.

51. Klibanov, A.L., *Targeted delivery of gas-filled microspheres, contrast agents for ultrasound imaging*. Adv. Drug Deliv. Rev., 1999. 37: p. 139-157.
52. Postema, M. et al., *Nitric oxide delivery by ultrasonic cracking: some limitations*. Ultrasonics, 2006. 44(S1): p. e109-e113.
53. Shortencarier, M.J. et al., *A method for radiation-force localized drug delivery using gas-filled lipospheres*. IEEE Trans. Ultrason. Ferroelectr. Freq. Control, 2004. 51(7): p. 822-831.
54. Postema, M. et al., *Generation of a droplet inside a microbubble with the aid of an ultrasound contrast agent: first result*. Lett. Drug Des. Discov., 2007. 4(1): p. 74-77.
55. Voigt, J.-U., *Ultrasound molecular imaging*. Methods, 2009. 48: p. 92-97.
56. Philipp, A. and W. Lauterborn, *Cavitation erosion by single laser-produced bubbles*. J. Fluid Mech., 1998. 361: p. 75-116.
57. Kodama, T. and K. Takayama, *Dynamic behavior of bubbles during extracorporeal shock-wave lithotripsy*. Ultrasound Med. Biol., 1998. 24(5): p. 723-738.
58. Caskey, C.F. et al., *Microbubble tunneling in gel phantoms*. J. Acoust. Soc. Am., 2009. 125(5): p. EL183-EL189.
59. Kotopoulis, S. and M. Postema, *Microfoam formation in a capillary*. Ultrasonics, 2010. 50: p. 260-268.
60. Postema, M., O.H. Gilja, and A. van Wamel, *CEUS and sonoporation*, in *Fundamentals of Medical Ultrasonics*, M. Postema, Editor 2011, Spon press: London. p. 205-217.
61. van Wamel, A. et al., *Vibrating microbubbles poking individual cells: drug transfer into cells via sonoporation*. J. Control. Release, 2006. 112(2): p. 149-155.
62. Postema, M. and O.H. Gilja, *Jetting does not cause sonoporation*. Biomed. Eng., 2010. 55: p. S19-S20.
63. Marmottant, P. and S. Hilgenfeldt, *Controlled vesicle deformation and lysis by single oscillating bubbles*. Nature, 2003. 423: p. 153-156.
64. Delalande, A. et al., *Ultrasound-assisted microbubbles gene transfer in tendons for gene therapy*. Ultrasonics, 2009. 50: p. 269-272.
65. Kaddur, K. et al., *Transient transmembrane release of green fluorescent proteins with sonoporation*. IEEE Trans. Ultrason. Ferroelectr. Freq. Control, 2010. 57(7): p. 1558-1567.
66. Kotopoulis, S. et al., *Lithium niobate ultrasound transducers for MRI-guided ultrasonic microsurgery*. IEEE Trans. Ultrason. Ferroelectr. Freq. Control, 2011. 58(8): p. 1570-1576.
67. Livanec, P.W. and R.C. Dunn, *Single-molecule probes of lipid membrane structure*. Langmuir, 2008. 24(24): p. 14066-14073.
68. Postema, M. et al., *Simulations and measurements of optical images of insonified ultrasound contrast microbubbles*. IEEE Trans. Ultrason. Ferroelectr. Freq. Control, 2003. 50(5): p. 523-536.
69. Ehrenberg, B. et al., *Membrane potential can be determined in individual cells from the nernstain distribution of cationic dyes*. Biophys. J., 1988. 53: p. 785-794.
70. Takahashi, A., H. Yamaguchi, and H. Miyamoto, *Change in K⁺ current of HeLa cells with progression of the cell cycle studied by patch-clamp technique*. Am. J. Physiol., 1993. 265(2): p. C328-C336.
71. Krasovitski, B. et al., *Subcellular sonophores: ultrasound induced intramembrane cavitation*. Proc. Nat. Acad. Sci., 2011. 108(8): p. 3258-3263.

* Based on: Kotopoulis S, Schommartz A, Postema M. Sonic cracking of blue-green algae. Appl Acoust 2009 70(10):1306–1312; and Kotopoulis S, Schommartz A, Postema M. Safety radius for algae eradication at 200 kHz–2.5MHz. Proc IEEE Ultrason Symp 2008 1706–1709; and Kotopoulis S, Postema M. Microfoam formation in a capillary. Ultrasonics 2010 50(2):260–268; and Kotopoulis S, Postema M. Forming morphing microfoam. Proc Int Congr Acoust 2010 #25; and Delalande A, Kotopoulis S, Rovers T, Pichon C, Postema M. Sonoporation at a low mechanical index. Bub Sci Eng Tech 2011 3(1):3-11.

Micro-acoustics in marine
and medical research

Saliev *et al.* – Influence of ultrasonic waveforms upon
microbubble suspensions

8

Influence of ultrasonic waveforms upon microbubble suspensions

Timur Saliev¹, Loreto Feril², Katsuro Tachibana²
Paul Campbell¹

¹Carnegie Physics Laboratory & Div. Molecular Medicine, Dundee University, UK

²Department of Anatomy, Fukuoka University School of Medicine, Japan

Abstract

Ultrasound appears to hold some promise as a therapeutic modality. Whilst the mechanical action of the wave itself can elicit biological response within cells and tissues, such effects may be enhanced if microscopic bubbles are also present during insonation. This can result in uptake of exogenous species, and/or enhanced bioeffect in terms of lysis and apoptosis, which underscores the clinical potential of the approach. In the present study we looked at the effect of ultrasound waveform on microbubble populations and cell suspensions, addressing such considerations as the role of *standing* versus *travelling* waveforms on both populations, as well as the utility of non-simple harmonic waveforms such as rectangular pulse-trains as opposed to their simple harmonic [sinusoidal] counterparts. The salient observational evidence arising supports emerging evidence from the literature on the important role of standing waves for *in-vitro* sonoporation studies, and highlights for the first time, that judicious choice of waveform offers enhanced control over resultant bioeffects.

Introduction

Our present understanding of ultrasound activated microbubbles owes much to several elegant and quantitative reports that have demonstrated how the bioeffects arising can be correlated with such factors as: rate and extent of microbubble reduction during insonation [1]; cavitation effects, as inferred from attendant sonoluminescent output [2] and free radical activity [3]; as well as directly measured broadband cavitation (noise) [4]. Moreover, an overarching physical model has also been proposed by Nyborg [5] that independently accounts for many salient literature trends and findings, effectively drawing these earlier reports into a cogent theory that also boasts significant predictive power.

Whilst all of the above reports assess the behaviour of contrast agent *en masse*, that is, as clouds of many thousands of microbubbles in suspension, it should be noted that interesting observations on the behaviour of [ultrasound activated] individual bubbles, have also been achieved for *in vitro* [6], and recently, under more clinically relevant scenarios [7]. These latter reports have also served to deepen our understanding of the possible interactions that can arise between suspensions of microbubbles and cells. In general, low level exposure regimes (mechanical indices (MI) < 0.1) lead to a linear response, which, whilst appearing relatively mild in extent, can lead to bubble oscillations that are often sufficient to facilitate the development of micro-streaming in the local fluid [8], shear flow from which may be enough to disrupt the delicate cell membranes of any proximal cells. In more aggressive ultrasound environments, (MI>0.5) bubble cavitation becomes extremely non-linear, although still well described by a suitable Rayleigh Plesset type equation. In such regimes a range of interesting and hugely energetic phenomena can occur, such as sonic cracking [6, 9] and microjetting [6], not to mention the formation and accumulation of sonochemical by-product [10] that may also mediate [often deleterious] bioeffects including membrane disruption. Such uncontrolled sonoporation effects may have markedly different outcomes, such as direct cell lysis, downstream apoptosis, and reparable sonoporation [11-15].

Having thus established the importance of ultrasound activated microbubbles in the context of biomedicine, we turn now to the explicit purpose for this present study, which was to characterise the effect of ultrasound on lipid microbubble population numbers [in our custom-developed insonation chamber], and moreover, to undertake that process by a non-destructive, real time procedure. In pursuit of this, we assessed the utility of a spectrophotometer for this task, calibrating initially to measure the turbidity [i.e. that property of a medium arising due to the presence of suspended particles which may scatter light of a defined wavelength] of several solutions with known microbubble concentrations. We then sought to exploit that calibration for instantaneous measurements on turbidity after insonation of the bubble population. This process differs [advantageously] from previous modes of bubble population assessment, where aliquots needed to be removed in order to measure with either flow cytometry or standalone Coulter counting - the transfer of which takes several minutes during which time the bubble population may be physically changing). In this sense we use the

spectrophotometer as a non-invasive optical alternative to acoustic scattering [1]. The strategy was then to exploit this data, identifying any correlations between population dynamics [number of bubbles that had disappeared] with any biological effects arising [16].

Methodology

Spectrophotometer calibration: Two different lipid-based ultrasound contrast agents (SonoVue[®], Bracco Diagnostics, Inc. and Sonazoid[™], GE HealthCare) were assessed. In the former case, the 'MiniSpike' transfer system was used for the preparation of SonoVue[®] solution (according to the manufacturer's instructions) whereupon freshly prepared solution was shaken vigorously in the original vial and from this stock solution, micro-bubbles with an initial concentration of 100 $\mu\text{l/ml}$ were used to make up standard solutions for calibration purposes, and also for the experiments themselves. The spectrophotometer [ImmunoMini NJ-2300], which operated with a monochromatic light source at 450 nm, was calibrated for each specific type of contrast agent tested via a linear fit to the absorbance as a function of bubble concentration (taken across six different microbubble concentrations each replicated 4 times) and for which each solution of bubbles had been carefully pre-formulated just prior to measurement. The solutions were also gently agitated immediately beforehand, so that buoyancy effects could be discounted.

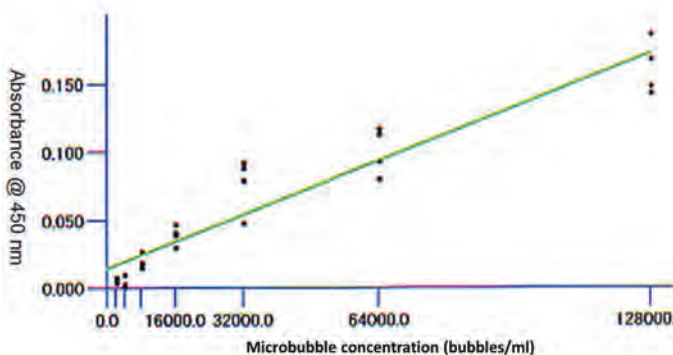


Figure 1 - Calibration plot showing the absorbance (y-axis) versus microbubble concentration (x-axis), with each datum replicated 4 times and a linear plot of best fit established (with correlation coefficient = 0.973).

Exposure apparatus: The insonation rig here consisted of a KTAC-4000 Signal Generator/Amplifier (Sonidel Ltd, Dublin, Eire) producing waveforms at a frequency of 1.011 MHz and a user-selectable (sine and rectangular) waveform option, with variable duty cycle and burst rate. The driving signal was applied to multiple 2 cm diameter plane- faceted ultrasound transducers (KP S20 for KTAC-4000) each arranged in a 2 x

2 array (Fig. 2c) and directly coupled through a water based gel, to the membrane base within a multi-well plate (Lumox Multiwell 24, Grenier-Bio). All experiments were carried out at room temperature with each microbubble/PBS solution distributed in each of the 24 wells. Using the full 2 x 2 array, 4 wells could be sonicated simultaneously and with the same protocol/pulse characteristics, in order to achieve supporting statistics. The 2 x 2 array was then sequentially displaced to cover and expose the next four wells, and so on, as described within Fig. 2, whereupon automated analysis of the 24 well plate was undertaken.

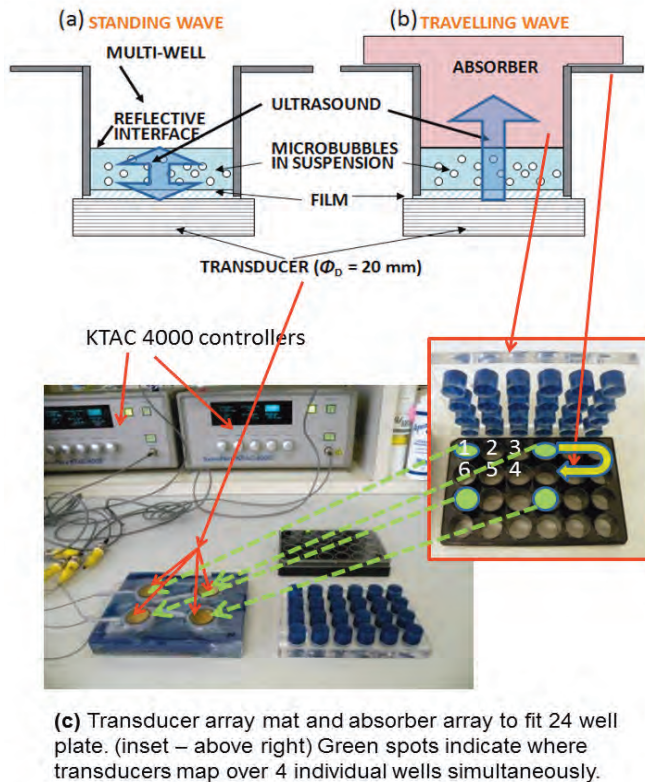


Figure 2 - (a) & (b) Schematic illustrations of the transducer well interface in cross-section for the respective cases used in the experiments. (a) Standing waves (arising through reflection from free-surface) and (b) travelling wave (including absorber material to encourage energy flow across the interface and away from the chamber). (c) Photo of the physical apparatus. Transducers are controlled from the KTAC4000 system and are arranged as a 2 x 2 array, set geometrically to correspond with coverage to 4 individual wells at a time. After each well is exposed, the insonation characteristics can be altered and the transducer array shifted to position 2 (inset) to expose 4 further wells. This is continued by following the yellow U turn arrow (inset) to expose all 24 wells after repositioning of the top left transducer from point 1 through 6 (as shown on inset) in sequence.

Acoustic absorbing material was used to control the standing-/travelling-wave nature of environment. The absorber, which was cut to a snug fit within the 24 well plates (Fig. 2c) was made from polyurethane rubber material (EUA101A (HAM A), Eastek Corporation, Tokyo, Japan) with a density of 1.01 g/cm^3 ; thickness of tile: 14 mm; dimensions: 250 mm by 200 mm. The material has a high transmission loss $> 30 \text{ dB/cm/MHz}$; high echo-reduction $> 42 \text{ dB}$ at 1 MHz degrading to 35 dB at 10 MHz; for frequency range 1-15 MHz; and operating with powers up to 20W. These characteristics allow practical absorbance of any incident ultrasound energy, thus greatly reducing the reflection signal and effectively nullifying the possibility for standing waves. Furthermore, by placing the absorber in direct contact with the cell solution, the possibility of an air/water reflective layer arising was also nullified. The output from the 20mm diameter KP-S20 transducers was characterised with a fibre optic hydrophone (Precision Acoustics) for the two cases of standing and travelling waves, further details of which can be found elsewhere [16].

Cell culture: U937 cells (Human leukemic monocyte lymphoma cell) were employed for the present study, which are non-adherent so that all insonations exposed suspensions of cells (and/or microbubbles). U937 have been extensively utilised for *in vitro* investigations, especially in the context of microbubble enhanced sonoporation and associated bioeffects, such as cell lysis and apoptosis. The cells, which were obtained from the Human Sciences Research Resources Bank, Japan Human Sciences Foundation, Tokyo, Japan, were maintained in RPMI 1640 medium supplemented with 10% heat-inactivated foetal bovine serum (FBS) (Gibco, Carlsbad, CA) at 37.0°C with 5% CO_2 .

In the first instance we wished to ascertain the stability of each ultrasound contrast agent (UCA) under passive conditions. Fresh stock solutions were transferred to the spectrophotometer and measurements taken as a function of time, again with gentle agitation to negate the effects of buoyancy upon each measurement. Measurements were typically repeated in triplicate, the results for which are shown in Fig. 3. Evidently, the turbidity of both agents drops by circa 50% at around 11 minutes after reconstitution. Notably however, Sonovue[®] is retained at a plateau phase for prolonged periods, supporting previous suggestions that it can be used for up to 4 hours after reconstitution [17]. Sonazoid[™] on the other hand is not so long-lived and is seen to decay to 25% of initial population levels within 30 minutes. This again tallies with prescriptions for its recommended usage period being limited to within 2 hours after reconstitution [18].

As far as their use as model contrast agents is concerned, we draw attention to measurements undertaken on both bubble types, where those taken instantaneously upon reconstitution will be most error-prone as the rate of change of population numbers is most rapid at this time, whereas for Sonovue[®] at least, after a 30 minute period of passive suspension then the most resilient microbubbles appear to be all that remain and the rate of change of the population has stabilised somewhat. The former situation demands fast real-time measurements (as here) whereas the latter situation,

once calibrated, would appear more suitable for those experiments subject to implicit delays in the relocation of the suspension.

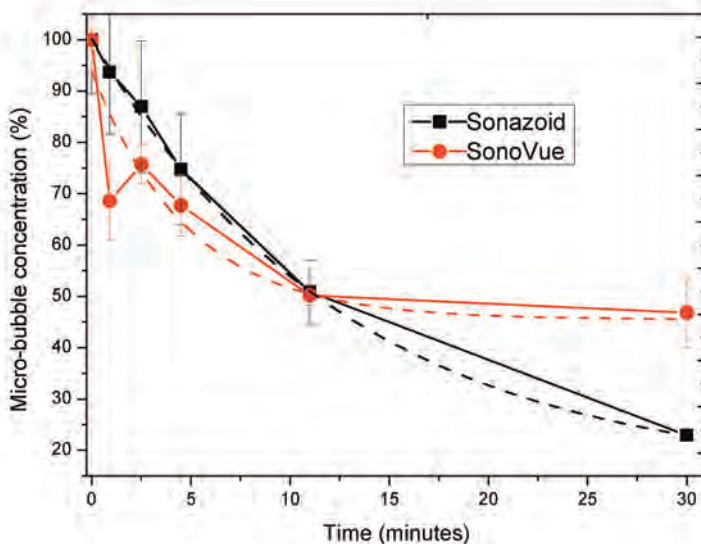


Figure 3 - Concentration of two UCAs as a function of time in quiescent state, as measured by the spectrophotometer. Exponential decay curves (dashed) are fitted to each for comparison. Solutions were gently agitated before each measurement in order to counter any effects of buoyancy.

Flow cytometry: Quantification of any ultrasound-induced biological effects (realized with an appropriate fluorescent stain) was conducted with a commercial flow cytometer (Cell Lab Quanta™ SC system (Beckman Coulter)). This system has a three-color set-up, which provides the additional sizing parameter of electronic volume (EV), and the granularity differentiating parameter of side scatter.

We now focus on the measurements obtained with Sonovue® when subjected to a range of ultrasonic waveforms and environments. The KTAC-4000 sonoporation apparatus described above was used, in association with a 24 well plate and the 2 x 2 array of SP-20 transducers (Fig. 2) to insonate populations of U937 cells. Each sample of U937 cells were divided into two* groups:

(i) those treated with the acoustical absorber in place [therefore in a travelling wave set-up] and in the presence of Sonovue®; and,

(ii) those exposed to ultrasound field in a hard walled vessel without absorber [and thus in a standing wave environment] also in the presence of Sonovue®.

*It should be noted that control groups insonated without microbubbles in solution had no significant difference in characteristics compared with sham non-isonated controls.

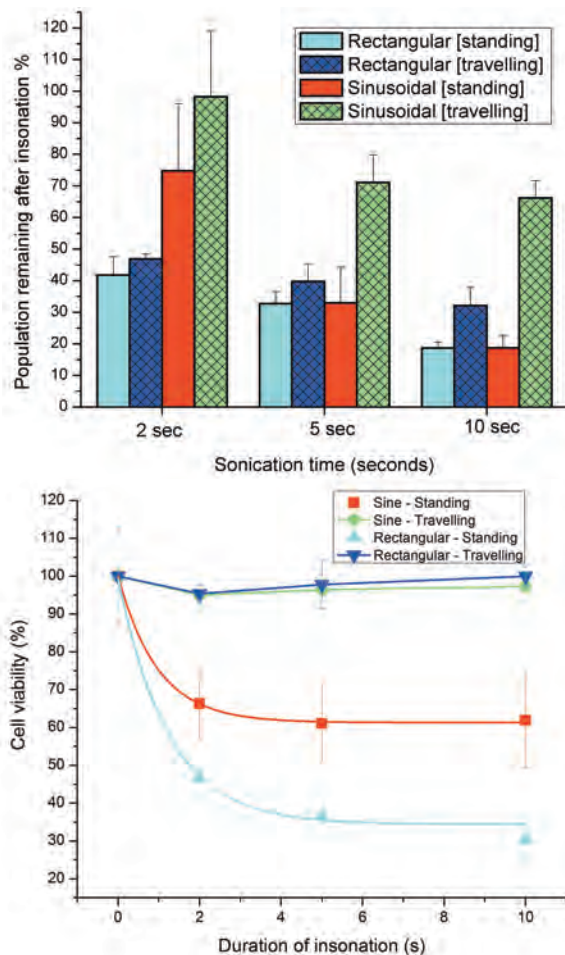


Figure 4 – (above) Response of Sonovue® microbubble populations to insonation with either sine or rectangular waveforms, under either travelling or standing wave conditions and for 3 separate exposure durations. (below) Viability assays (Trypan blue test) of U937 cells subjected to identical insonation conditions. The colour schemes are identical in both upper and lower graphs in accordance with the insets, and exponential fits have been applied to both standing wave data in the lower plot.

The U937 cells were suspended in final concentrations of 2×10^5 cells/ml before insonation by ultrasound pulsing with parameters: frequency 1.011 MHz, intensity 0.45 W/cm^2 , duty cycle 25%, burst rate 0.5 Hz. Both sine and rectangular waves were employed, as will be detailed in direct association with their respective data downstream. The period for insonation varied over 2, 5 and 10 seconds. Sonovue[®] was added just before sonication in a final concentration of $10 \text{ }\mu\text{l/ml}$ [= 2 million bubbles per ml] whereupon the solution was gently agitated. A control group of cells were maintained at 37.0°C and monitored throughout to assist with correct renormalization of the insonated populations.

Results

The suspensions of microbubbles alone (Fig. 4 top), and also cells-plus-microbubbles (Fig. 4 bottom) were subjected to identical sonication protocols as detailed above. Figure 4 (top) shows a combined plot containing data on the normalized degradation of each predefined population of Sonovue[®] subjected to the pulsing regime stipulated above and for durations of 2, 5 and 10 s. Two points become evident from this graph, namely that the non-simple-harmonic rectangular wavefield is much more effective at degrading Sonovue[®] microbubbles than the sinusoidal field for (nominally) identical pressure amplitudes. Also, standing wave-fields, be they in sinusoidal or rectangular form, are more effective at degrading the UCA population than their travelling wave counterparts.

To check whether these outcomes correlated with biological effect in the presence of cells, a preliminary data set was collected on sonicated cells for comparison with any trends arising from the results described in the previous paragraph. Upon analysis of insonated cells, assayed by trypan blue staining and flow cytometry to ascertain viability, it was clear that the level of viable cells remaining for the case of simple harmonic [sinusoidal] standing wave exposure plateaued at $61.9 \pm 12.7 \%$ at 10 seconds), whereas those cells subjected to non-simple harmonic (rectangular) standing waves experienced significantly greater cell death, with a measured viability of $30.3 \pm 5.3 \%$ at 10 seconds. Interestingly, those samples exposed to travelling waves formed from either sinusoidal or rectangular parent waves remained, to all intents and purposes, intact at close to their initial viabilities, as can be clearly observed in Fig. 4 (bottom).

Discussion

Whilst it may be somewhat self-evident that the experimental conditions of any acoustic exposure have a direct impact on any subsequent status of the microbubble population, it serves our purpose here to underline the fact that the architecture of the apparatus is absolutely critical in dictating the outcome [19]. Perhaps the one aspect to experimental design in sonoporation trials that has been overlooked more than any other involves characterization of standing waves within the cell containing medium,

however several recent reports [20-22] have begun to address this deficiency in our understanding.

Clearly, the amplitude associated with a standing wave is larger than that of its travelling wave counterpart, and this is drawn out from our experimental data taken when characterising the KP-S20 transducers (data not shown but further details available in reference [16]). Briefly, we found that bioeffects are limited with travelling waves but pronounced within standing wave environments, where our evidence for this is based on our ability to reliably control reflection levels in the exposure chamber (Fig. 2). On a qualitative level then, we can understand why standing waves lead to such aggressive effects on the bubble population: the energy densities are more pronounced and the intrinsic fragility of lipid bubbles are less likely to withstand that environment. Interestingly however, Ter Haar has suggested that with any non-continuous mode of insonation, then the possibility for establishing standing waves is unlikely [23]. Explicitly for 'tone-burst pulsing on millisecond timescales – standing waves appear negligible whereas cavitation, radiation pressure, and microstreaming effects are all possible. When the insonation regime is adjusted to even shorter pulse trains [as in our own case] then it became even more difficult to ascribe dominant effects, but certainly, standing waves were found unlikely to occur. Physical size in the reaction vessels may be critical - with typical insonation chamber dimensions on the order of centimetres for our own apparatus, then reflections can be established within a few microseconds – thus pulse trains lasting longer than this can theoretically develop into standing wave regimes. It therefore appears that all is not quite so straightforward as it might outwardly appear, and further investigation is certainly warranted to clarify the situation.

Finally, we noticed that bubble populations subjected to standing waves undergo an exponential decay, and similarly, cell viability also exhibits exponential decay when bubbles are present in solution (Fig. 4). This behaviour tallies with the physical model developed by Nyborg and supports the suggestion that bioeffect can be related to the events that lead to bubble disappearance. We are presently developing an observational route to ascertain directly whether this hypothesis is correct and to quantify the magnitude of the exponents involved.

Conclusions

The objectives for this study were three-fold. In the first instance we wished to ascertain whether light-scattering based turbidity measurements on commercial lipid microbubbles offered any advantage over alternative, indeed, complementary methods for quantifying microbubble population dynamics such as flow based cytometric techniques. In the event microbubble populations were able to be measured quickly and non-invasively in situ by the optical technique. A second strand to the study was to ascertain whether exposure to standing waves or travelling waves led to significantly different outcomes: here, we observed that standing waves led to exponential decay of bubble populations, and also led to exponential decay in cell viability, leading us to concur with the suggestions previously put forth by Nyborg [5]. Finally, we explored

whether simple harmonic (sinusoidal) waveforms led to different population and bioeffect outcomes when compared to their non-simple harmonic (rectangular) waveform counterparts. In the event it transpired that non-simple harmonic waves appear to degrade microbubble populations more readily, and led to more aggressive immediate bioeffect in terms of viability studies. Here, whilst the same driving amplitude was used in each case (for sine and rectangular cases) the obvious fact that the rectangular waveform has the larger average *power* for that same *amplitude* amongst the waveforms tested maybe sufficient explanation for its more aggressive outcomes. We are currently testing this aspect over a more substantial parameter space and will report that extended study later in 2012.

Acknowledgements

This work was supported through a Royal Society International Project Award (to KT & PC) and also through a Japan Society for the Promotion of Science (JSPS) Award to PC. PC also acknowledges the EPSRC for a Basic Technology 5 Award [EP/D048958] which provided the infrastructure at Dundee, and half-funded a studentship for TS. PC's present position is funded via a Royal Society Industry Fellowship. We also thank the Northern Research Partnership (SFC) for matched funding on the studentship to TS.

References

1. Kamaev, P.P. et al., *Quantification of Optison bubble size and lifetime during sonication dominant role of secondary cavitation bubbles causing acoustic bioeffects*. Journal of the Acoustical Society of America, 2004. **115**(4): p.1818- 1825.
2. Cochran, S. A. and Prausnitz M.R., *Sonoluminescence as an indicator of cell membrane disruption by acoustic cavitation*." Ultrasound Med Biol, 2001. **27**(6): p. 841-850.
3. Kondo, T. et al., *Free-Radical Formation Induced by Ultrasound and Its Effects on Strand Breaks in DNA of Cultured Fm3a Cells*. Free Radical Research Communications, 1993. **19**: p. S193-S200.
4. Hallow, D.M. et al., *Measurement and correlation of acoustic cavitation with cellular bioeffects*. Ultrasound Med Biol, 2006. **32**(7): p. 1111-1122.
5. Nyborg, W.L., *Ultrasound, contrast agents and biological cells; A simplified model for their interaction during in vitro experiments*. Ultrasound Med Biol, 2006. **32**(10): p. 1557-1568.
6. Prentice, P. et al., *Membrane disruption by optically controlled microbubble cavitation*. Nature Physics, 2005. **1**(2): p. 107-110.
7. Chen H. et al., *Observations of Translation and Jetting of Ultrasound- Activated Microbubbles in Mesenteric Microvessels*. Ultrasound Med Biol, 2012. **37**(12): p. 2139-2148.
8. Marmottant, P., and Hilgenfeldt, S., *Controlled vesicle deformation and lysis by single oscillating bubbles*. Nature, 2003. **423** (6936): p. 153-156.
9. Postema, M. et al., *Ultrasound-induced encapsulated microbubble phenomena*." Ultrasound Med Biol, 2004. **30** (6): 827-840.
10. Hassan M.A. et al., *Evaluation and comparison of three novel microbubbles: enhancement of ultrasound induced cell death and free radicals production*. Ultrasonics Sonochemistry Ultrasonics Sonochemistry, 2009. **16** (3): p. 372-378.
11. Ward, M. et al., *Ultrasound-induced cell lysis and sonoporation enhanced by contrast agents*. Journal of the Acoustical Society of America, 1999. **105**(5): p. 2951-2957.
12. Brujan, E.A. et al., *Jet formation and shock wave emission during collapse of ultrasound-induced cavitation bubbles and their role in the therapeutic applications of high-intensity focused ultrasound*. Phys Med Biol, 2005. **50**(20): p. 4797-809.
13. Kodama, T. et al., *Transfection effect of microbubbles on cells in superposed ultrasound waves and behavior of cavitation bubble*. Ultrasound Med Biol, 2006. **32**(6): p. 905-14.
14. Ohl, C.D. et al., *Sonoporation from jetting cavitation bubbles*." Biophys J, 2006. **91**(11): p. 4285-95.
15. Karshafian, R. et al., *Sonoporation by Ultrasound-Activated Microbubble Contrast Agents: Effect of Acoustic Exposure Parameters on Cell Membrane Permeability and Cell Viability*. Ultrasound Med Biol, 2009. **35**(5): p. 847-860.
16. Saliev, T., PhD Thesis, 2012, University of Dundee.
17. Schneider, M., *SonoVue, a new ultrasound contrast agent*. European Radiology, 1999. **9**: p. S347-S348.

18. Sontum, P.C., *Physicochemical characteristics of Sonazoid (TM), a new contrast agent for ultrasound imaging*. Ultrasound Med Biol, 2008. **34** (5): p. 824-833.
19. Miller, M.W., *Influence of in vitro design*. Ultrasound Med Biol, 1986. **12** p. 682.
20. Khanna, S. et al., *Fluorescein isothiocyanate-dextran uptake by chinese hamster ovary cells in a 1.5 MHz ultrasonic standing wave in the presence of contrast agent*. Ultrasound Med Biol, 2006. **32**(2): p. 289-295.
21. Kinoshita, M. and K. Hynynen, *Key factors that affect sonoporation efficiency in in vitro settings: The importance of standing wave in sonoporation*. Biochemical and Biophysical Research Communications, 2007. **359**(4): p. 860- 865.
22. Hassan, MA. et al., *Modulation control over ultrasound-mediated gene delivery: evaluating the importance of standing waves*. J. Controlled Release, 2010. **141**(1): p. 70-76.
23. Ter Haar, G (1988). "Biological Effects of Acoustic Cavitation." Chap. 8 in_ Ultrasound: Chemical, Physical, and Biological Effects, ed. by K. Suslick, VCH Publishers, Inc., New York, 305.

9

Ultrasound and microbubble-assisted gene delivery: insights for intracellular mechanism

Anthony Delalande^{1,2}, Spiros Kotopoulos^{3,2}, Patrick
Midoux⁴, Michiel Postema², Chantal Pichon⁴

¹Department of Haematology, Haukeland hospital, Bergen, Norway

²Department of Physics and Technology, University of Bergen, Bergen, Norway

³Department of Gastroenterology, Haukeland hospital, Bergen, Norway

⁴Centre de Biophysique Moléculaire, CNRS, Orléans, France

Abstract

Microbubbles are capable to oscillate under specific ultrasound settings that can lead to a permeabilisation of surrounding cells and this phenomenon is called sonoporation. The sonoporation technique has been used to deliver drugs *in vitro* and *in vivo* for gene or chemotherapeutic drug delivery applications. However, the biological and physical mechanisms of sonoporation are still not fully understood. We have used a luciferase reporter plasmid to identify the optimal parameters for an efficient gene delivery in human cancer HeLa cells. The optimal parameters found at 1 MHz were 150 kPa, 40% duty cycle, 60 sec sonication time using 0.3% of microbubbles. The interactions between microbubbles and cells were investigated by high-speed imaging during sonoporation. Specifically at 150 kPa, microbubbles entry into cells has been observed during sonoporation. These results strongly suggest that the microbubble entry could be closely correlated to the plasmid DNA entry into the cell. The intracellular kinetic of the plasmid delivery was followed by confocal microscopy using fluorescent molecules and specific cell markers for late endosomes and nuclear envelope. Most of plasmids

were located in late endosomes 3 hours after sonoporation and some could reach the nucleus 3 hours later. The gene transfer efficiency was almost totally inhibited when depleting the cell ATP and in presence of chlorpromazine suggesting that plasmid uptake after sonoporation was an active mechanism mostly involving the clathrin-mediated pathway.

Introduction

Gene delivery by non-viral methods is still a major challenge nowadays. It offers a great promise for gene therapy because of its safety compared to their viral counterparts. However, a major limiting factor for efficient non-viral gene therapy remains the lack of a suitable and efficient vector for gene delivery. Fifteen years ago, a new drug delivery method based on ultrasound stimulation coupled to gaseous microbubbles has been proposed. Upon ultrasound exposure, microbubbles can be expanded, moved and even destroyed [1] and can modify the cell membrane permeability by a process known as sonoporation [2-4]. These properties offer the opportunity of site-specific local delivery of drug or gene. Although the mechanism of membrane permeabilization has not been clearly elucidated, the main hypothesis assumes the formation of transient pores in the plasma membrane as a consequence of interaction of oscillating microbubbles with the cell membrane [3-5]. Transient pores formed at the plasma membrane are supposed to be responsible for the intracellular delivery of molecules but also the outward transport of intracellular molecules [6]. Recently, two studies have shown that endocytosis process could also be involved in the sonoporation mechanism for large molecules [7, 8]. In the field of gene transfer, several studies have reported an improvement of gene delivery efficiency by sonoporation [9]. Numerous studies on sonoporation *in vitro* and *in vivo* and its exploitation for gene transfer have been reported [5, 10, 11]. However, the mechanisms of gene transfer from microbubble stimulation to protein expression are not well understood. Previous studies have shown that pore membrane formation could occur during sonoporation [5]. This study is focused on optimal ultrasound parameters determination for efficient gene transfer *in vitro*, microbubbles and cell interactions observation during sonoporation and plasmid DNA and microbubbles intracellular trafficking following sonoporation.

Materials and Methods

Cell culture

HeLa cells are adherent human epithelial cells from a fatal cervical carcinoma (ATCC, Rockville, MD). They were grown in MEM with Earl's salts medium (PAA Laboratories GmbH, Pasing, Austria) supplemented with 10% v/v of FCS and 1% of non essential aminoacids (PAA), penicillin (100 U/ml) and streptomycin (100 µg/ml) at 37°C in a humidified atmosphere containing 5% CO₂. HeLa cells stably expressing the fusion protein Rab7-GFP and Nup153-GFP were developed to localise the fluorescent-labelled plasmid DNA into specific cellular structures.

Plasmid preparation and labelling

A 7.5 kb homemade reporter plasmid that encoded the firefly luciferase gene (pLuc) under the control of the strong cytomegalovirus promoter was used. Five consecutive NF κ B motifs that recognized the NF κ B transcription factor were inserted upstream of the promoter [12]. All plasmids were propagated from *Escherichia coli* DH5 α cultures. Supercoiled plasmid was isolated from bacteria by the standard alkaline lysis method, and purification was carried out with the Qiagen Mega Kit (Qiagen, Courtabœuf, France) according to the manufacturer's instructions. Each plasmid DNA was labelled with the Label IT nucleic acid labelling kit (Mirus, Madison, WI, USA) at 1:2 reagent/pDNA weight ratio according to manufacturer's instructions. Plasmids were labelled with cyanine 3 (λ_{ex} = 543 nm, λ_{em} = 570 nm) and DNA was purified by ethanol precipitation. The labelling densities determined by absorbance according to the manufacturer's protocol were 1 cyanine 3 per 80 bp. We have verified that this type of plasmid labelling did not affect the gene expression.

Ultrasound exposure system for gene transfer

US were generated from a 0.5-inch diameter, IBMF-014 transducer with a centre frequency of 1 MHz (Sofranel, Sartrouville, France). The transducer was placed in a custom made polystyrene tank filled with degassed pure water. A signal consisting of 1.0 MHz centre frequency, 40% duty cycle and a pulse repetition frequency of 10 kHz was generated by a 33220A arbitrary function generator (Agilent technologies, Les Ulis, France) and amplified by a RF power amplifier (ADECE, Artannes sur Indre, France) was used as the input for the transducer. Peak negative pressure of 150 kPa was used corresponding to an MI of 0.15. Ultrasound stimulation time was set to 60 seconds. The transducer was calibrated in a Perspex container using an HGL-200 PVDF bullet type hydrophone (Onda, Sunnyvale, CA) placed at 3 cm, the natural focal distance of the transducer. The transducer was positioned in front of the sonoporation cuvette (Sarstedt AG & Co, Nümbrecht, Germany). The attenuation of the cuvette walls was measured separately and found to be negligible (less than 10%). 10^5 cells were grown on a resized Opticell[®] membrane (10×15 mm) (Nunc GmbH & Co. KG, Langenselbold, Germany). The Opticell[®] membranes were transferred into polystyrene cuvettes (Sarstedt, Nümbrecht, Germany) containing 1.5 ml of OptiMEM medium (Invitrogen, Carlsbad, CA, USA) supplemented with 1% FCS. During sonoporation the cell medium was placed under gentle agitation using a magnetic stirrer. After sonoporation the membrane was placed in a 12-well cell culture plate.

Ultrasound exposure system for high-speed imaging

For fast camera imaging experiments, the transducer was placed in a custom-made aluminum sonication chamber with internal dimensions of 130×170×35 (mm)³ was locked into to the xy-stage of a 200M inverted microscope (Carl Zeiss AG, Oberkochen, Germany) coupled with a LSM Axiovert 510 confocal scanning device (Carl Zeiss), using an EC Plan-Neofluar 40×/1.30. Oil DIC M27 objective (Carl Zeiss AG), with automated z-stack functionality. The colour charge coupled device (CCD) of a Photron FastCam MC-2.1 high-speed camera (VKT Video Kommunikation GmbH, Pfullingen, Germany) was connected to the microscope. The sensor was rotated to make sure that in all recorded movies, the ultrasound is directed from the left to the right of the frame.

The peak-negative acoustic pressures were measured in the insonation tank at the objective's field of view and corresponded to MI of 0.1, 0.15 or 0.2. The day before the experiment 1.6×10^6 cells were seed in an Opticell® chamber. Ultrasound contrast agents were injected into the cell culture chamber before each experiment.

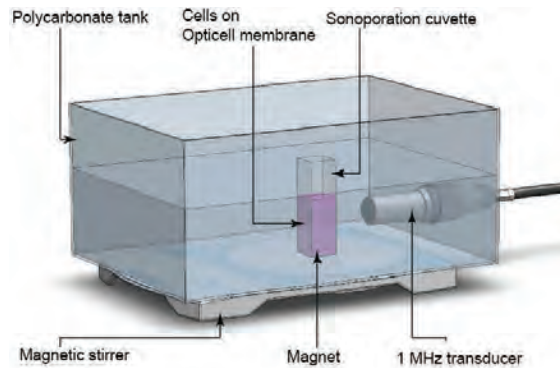


Figure 1 - *In vitro* sonoporation set-up used for gene transfer experiments.

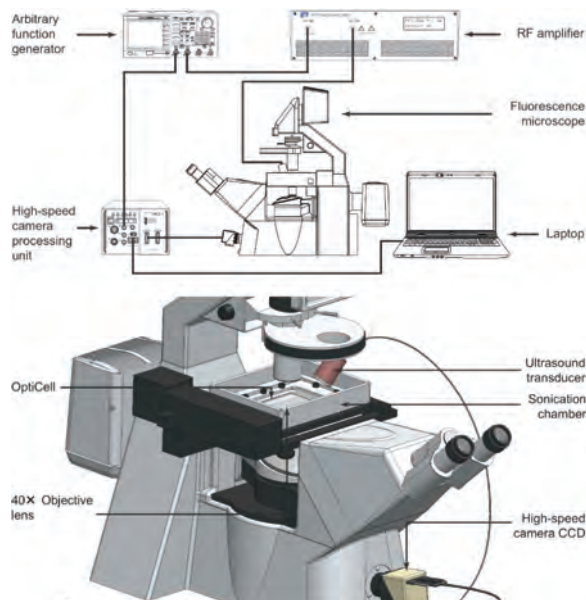


Figure 2 - *In vitro* set-up used for high-speed imaging experiments.

Ultrasound contrast agent

In this study, Micromarker[®] (VisualSonics, La Frette S/seine, France) microbubbles were used. Micromarker[®] contrast agents contain a perfluorobutane (C₄F₁₀) gas encapsulated by a phospholipid shell and have a median diameter of 2.3 to 2.9 μm . Microbubbles were prepared according to manufacturer's protocol, Micromarker[®] suspension contained approximately 2×10^9 MB/ml.

Luciferase activity assay

The efficiency of sonoporation to deliver gene was determined by measuring the luciferase activity 24 h after sonoporation of HeLa cells in the presence of a plasmid encoding the luciferase reporter gene. Cells were harvested, lysed and the luciferase activity was measured using a luminometer (Lumat LB9507, Berthold, Wildbach, Germany) after adding 100 μl of luciferase substrate (1 mM luciferin containing ATP) to 60 μl of cell lysate. The values were expressed as RLU (Relative Luciferase Unit), this level was reported to the protein concentration in RLU/mg proteins. The protein concentration was measured by the bicinchoninic acid assay.

Cell viability assay

The cell viability was determined 24h after sonoporation using the MTT colorimetric assay. Cells were incubated during 4 h at 37°C, 5% CO₂ in presence of 3-(4,5-dimethylthiazol-2-yl)-2,5-diphenyltetrazolium bromide (Sigma-Aldrich, St. Louis, USA) at 500 $\mu\text{g/ml}$. Cells were washed and incubated in a lysis and resuspension buffer consisting of acidified isopropanol containing 3% of SDS (Sigma-Aldrich). Quantification was made measuring the optic density at 560 nm.

Inhibition of endocytosis during sonoporation

To evaluate if the gene uptake by sonoporation was an active mechanism, cells were ATP depleted by incubation in presence of ATP depletion buffer (50 mM 2-deoxy-ATP, 50 mM sodium azide, 1.8 mM CaCl₂ in PBS pH 7.4) 30 minutes before the sonoporation. To study the involvement of the endocytosis pathways on the gene delivery mediated by sonoporation, cells were pre-treated for 30 minutes with either chlorpromazin (2.5 to 20 $\mu\text{g/ml}$; Sigma-Aldrich) an inhibitor of clathrin-mediated endocytosis pathway or filipin III (1 to 4 $\mu\text{g/ml}$; Sigma-Aldrich) or an inhibitor of caveolin-mediated endocytosis pathway. Then, sonoporation was performed in presence of indicated inhibitor and the cell medium was replaced two hours after sonoporation to maintain the inhibition effect.

Microbubble fluorescent labelling

In order to detect the microbubbles location after sonoporation, the envelope of Micromarker[®] microbubbles was stained with the fluorescent lipophilic probe DiD (λ_{ex} = 633 nm, λ_{em} = 643-670 nm) (Vybrant[™], Molecular Probes[®], Invitrogen, San Diego, CA, USA). A ratio of 1 μl of DiD to 40 μl MicroMarker[®] was used. The solution was homogenised by pipetting and it was used after 5 min incubation at room temperature.

Results and discussion

Optimal acoustic parameters determination for efficient gene transfer.

The optimal acoustic parameters that give the maximal gene transfer have been first determined on adherent HeLa cells using the set-up described previously. Four parameters were tested: the sound pressure (kPa), time (sec), the duty cycle (%) and the concentration of microbubbles (%). We tested different values of acoustic pressure in having fixed the other parameters tested (60 sec, 40% DC, 0.3% microbubbles). Figure 3A shows the effect of this the acoustic pressure on the gene transfer efficiency from 100 to 200 kPa. Indeed, increasing the acoustic pressure from 100 to 160 kPa caused a linear increase in the efficiency of gene transfer (from 3.2×10^4 to 2×10^6 RLU/mg prot, increase of about 100 times). The maximum efficiency was obtained at 160 kPa. Beyond 160 kPa, the efficiency of gene transfer was low and at 200 kPa, it reached a value of 1.9×10^5 RLU/mg prot which consists of a reduction by about 10 times compared to the highest value. These values were in the same range as that obtained in the study of Duvshani *et al.* performed on mouse prostate adenocarcinoma cells although these experiments have been conducted with Optison™ [13]. In a similar study performed on HeLa cells using SonoVue®, these authors have found that a maximum efficiency of gene transfer was obtained for an ultrasonic stimulation of 240 kPa for 7 minutes with a duty cycle of 60%. However, a high toxicity was measured (30% cell viability) [14]. In our study, the cell viability reached a value of 90% in the optimal condition. The ultrasound exposure time tested was ranged from 10 to 300 seconds. Figure 3B shows that gene transfer efficiency was positively correlated with ultrasound insonation time between 10 and 60 seconds corresponding to an increase from 2.1×10^4 to 5.4×10^5 RLU/mg prot. A plateau was observed between 60 and 300 seconds. However, it should be noted that a high variability was observed for long stimulation time. This can be explained by an increase in the toxicity induced by sonoporation with time of stimulation. Indeed, we observed a cell toxicity ranging from 30 to 60% for the respective ultrasound stimulation time of 10 and 300 seconds.

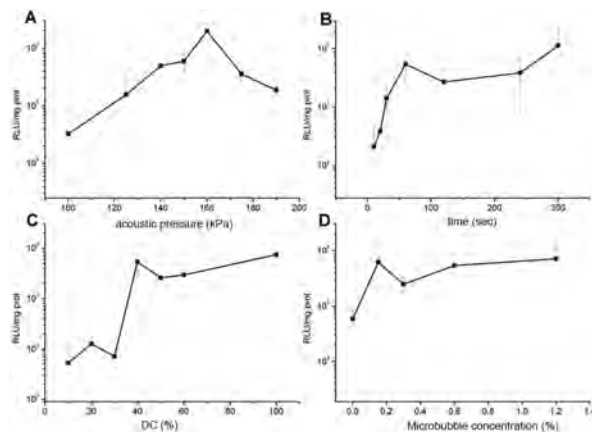


Figure 3 - Optimal sonoporation parameters determination. (A) Influence of the acoustic pressure (parameters: 0.3% MB, 60 sec, 40% DC, 2.5 μ g pDNA). (B) Influence of the time of insonation (parameters: 150 kPa, 0.3% MB, 40% DC, 2.5 μ g pDNA). (C) Influence of the duty cycle (DC) (parameters: 150 kPa, 60 sec, 0.3% MB, 2.5 μ g pDNA). (D) Influence of the concentration in microbubbles (parameters: 150 kPa, 60 sec, 40% DC, 2.5 μ g pDNA). Values shown represent means of 3 experiments done in duplicates.

Regarding the duty cycle (Figure 3C), a threshold value of 40% duty cycle was required for an efficient gene transfer. Between 10 and 30% duty cycle, a very low expression level of luciferase was obtained (around 10^4 RLU/mg prot). At 40% duty cycle, an increase of 75 times of gene transfer efficiency was obtained. Then a plateau was reached between 40 and 60% duty cycle. However, it should be noted that the experiments conducted at 60% duty cycle led to a high toxicity (60%). This was consistent with our previous results on HeLa cells in suspension in the presence of microbubbles BR14 [15]. In this study, a plateau was reached at 40% duty cycle.

The importance of the amount of microbubbles was also evaluated. Figure 3D showed that the presence of a certain concentration of microbubbles (0.15%) to get a gene delivery. Above this concentration, the transfection efficiency was very dependent on the quantity of microbubbles used. This observation was similar to that we previously obtained on HeLa cells in suspension in the presence of microbubbles BR14 [15] and the study of Rahim *et al.* performed on CHO cells adherent in the presence of SonoVue® [16].

Taken together, the above results reflect the importance of the parameters used in ultrasound effectiveness for gene transfer mediated by sonoporation. Depending on the settings used, the microbubble-cell interactions could be changed. Therefore, we established a sonoporation device coupled to a high-speed camera to observe these interactions in real time.

Microbubble behaviour during sonoporation

The behaviour of microbubbles during sonoporation was studied by high-speed imaging methods. We performed real-time visualisation of sonoporation event by high-speed imaging to investigate how microbubbles behave towards cells as a function of the acoustic pressure. Possible interactions between microbubbles and cells were investigated using the optimal acoustic parameters (1 MHz, 40% DC, 100 μ s period, 100 to 200 kPa, 0.3% microbubbles concentration). Figure 4 shows different types of microbubble-cell interactions as a function of sound pressure. Three acoustic pressures were tested (100, 150 and 200 kPa). At 100 kPa, the main observed phenomenon was as a cellular massage. The arrow shows an activated microbubbles by ultrasound remaining in contact with the cell membrane during the whole stimulation (Figure 4A). At this acoustic pressure, a low gene transfer was obtained as seen on Figure 3A. At 150 kPa, an additional phenomenon consisting of the microbubble entry into cells was seen (figure 4B). In the event presented in this sequence, the microbubble enters the cell after 600ms ultrasonic stimulation. Note that at this acoustic pressure range, the optimal efficiency of gene transfer was obtained (Figure 3A). For a sound pressure of 200 kPa, two phenomena were identified: either the microbubbles were driven from the field of view due to excessive radiation force or a violent interaction of microbubbles with the cell was observed. The latter induced a detachment of some cells from their support. It is important to note that at 200 kPa the gene transfer efficiency is ten times lower than at 150 kPa. The results obtained from our real time sonoporation indicate that three events types could be recorded: microbubbles stuck on cell membrane during the insonation corresponding to the cellular massage, microbubbles entering into

cells (translation), microbubbles having a violent interaction with cells. It is tempting to correlate the entry of microbubbles phenomenon and efficiency of gene transfer meaning that the entry of the microbubble could promote the delivery of the plasmid into the cell. Our set up analysis was checked to rule out that the motion of microbubbles takes place in a plane different from that of the cell. This was also validated by fluorescence confocal microscopy analysis. When DiD-labelled microbubbles were used, our observations indicated that microbubbles were inside the cell just below the plasma membrane.

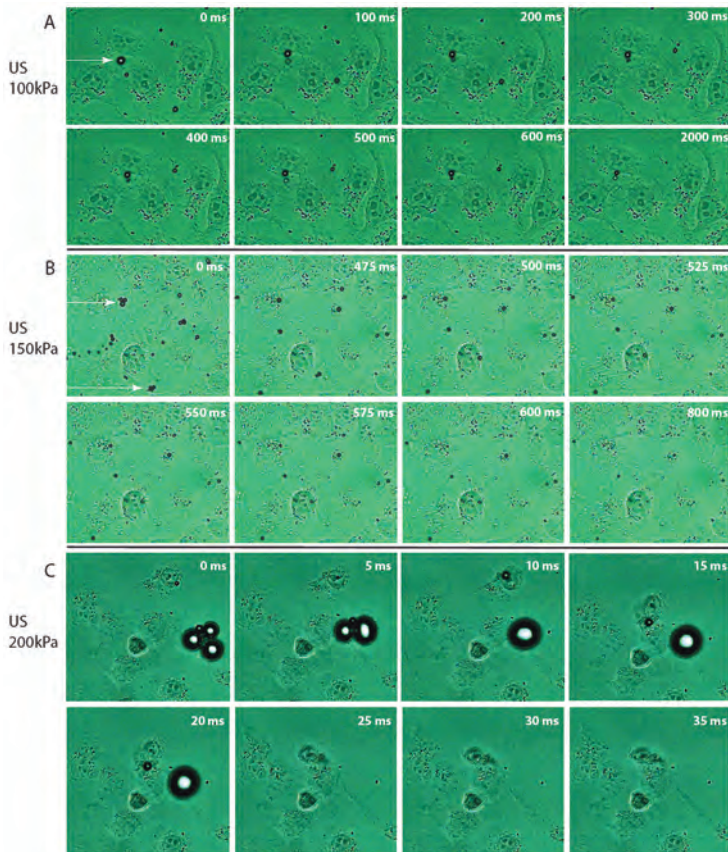


Figure 4 - Sequences of images of HeLa cells in the presence of microbubbles; (A) images taken during an ultrasound stimulation at 100 kPa, the microbubble surrounded interacts with the plasma membrane by cellular "massage"; (B) images taken during an ultrasound stimulation at 150 kPa, the microbubble surrounded enters the cell after 552 ms; (C) images taken during an ultrasound stimulation at 200 kPa, a microbubble interact with a cell and detaches it from its support. The arrows show the microbubbles to observe over time. The time displayed corresponds to the value after the start of the ultrasound stimulation.

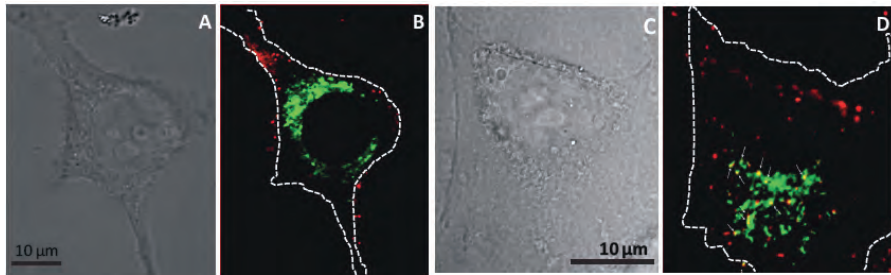


Figure 5 - Localisation of pDNA relative to late endosomes. HeLa Rab7-eGFP cells were sonoporated at optimal acoustic parameters in presence of 2.5 µg of Cy3-tagged pDNA and microbubble. Green and red staining correspond to Rab7-eGFP positive late endosomes and pDNA-Cy3, respectively. Yellow colour corresponds to a co-localisation of pDNA and Rab7 (arrows). Confocal microscopy observations were made either immediately after sonoporation (A, B) or 3 hours post-sonoporation (C, D). A and C: phase contrast images; B and D: merge of green (Rab7-eGFP) and red (pDNA-Cy3) fluorescence images. White dotted lines in the right frames indicate the cell plasma membrane boundary.

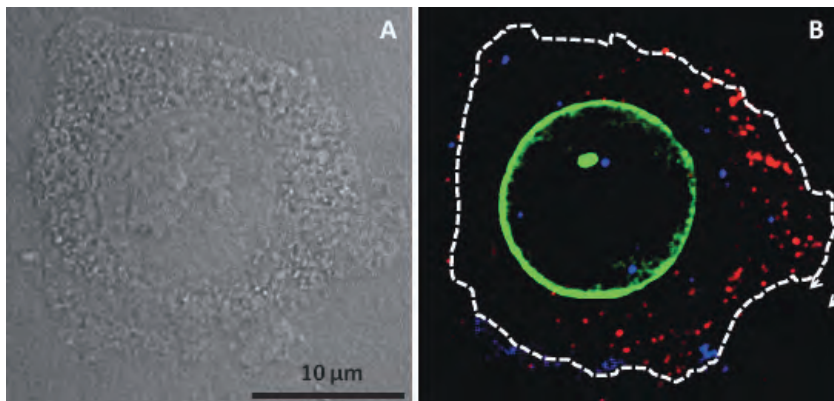


Figure 6 - Localisation of pDNA relative to the nucleus 6h post-sonoporation. HeLaNup153-eGFP cells were sonoporated at optimal acoustic parameters in presence of 2.5 µg of Cy3-tagged pDNA and DiD labelled microbubbles (blue). The green staining corresponds to Nup153-eGFP which delimits the cell nucleus. Some plasmids were found close to the nucleus 6 hours after sonoporation. Microbubbles were found in the cytoplasm and even in the nucleus 6 hours after sonoporation. A: phase contrast image, B: merge of green (Nup153-eGFP), red (pDNA-Cy3) and blue (MB-DiD) fluorescence images.

Plasmid and microbubble intracellular trafficking after sonoporation

A key to success of this technique lies in understanding mechanism governing microbubble and cell interactions. Real time confocal microscopy investigations were performed on adherent cells using plasmid DNA (pDNA) and microbubbles labelled

respectively with Cy3 (red) and DiD (blue) lipophilic tracer, respectively. The first experiments were done on HeLa cells using pDNA-tagged with Cy3 fluorophore. It was mainly localised as red spots at plasma membrane straightaway following sonoporation. At later time, these spots progressively moved inside cells (not shown). The structures could correspond either to vesicles (endosome) or aggregates like structures upon sonoporation. To distinguish between these two possibilities, kinetic experiments were performed in HeLa cells to investigate if pDNA and microbubbles reached some endocytic organelles upon sonoporation. Data presented in figure 5 were obtained with HeLa cells expressing Rab7-eGFP, the late endosomes marker (green). Late endosomes are, intracellular compartments in which end up internalised molecules before being delivered into lysosomes for degradation. Upon sonoporation, pDNA was localised mainly at the plasma membrane and without co-localisation with Rab7-eGFP (Fig. 5A and 5B). Observations made 3 h post-sonoporation indicated that some of pDNA ended up into late endosomes as demonstrated by the yellow colour (merge of green and red spots) indicating their localisation in Rab7 positive organelles (Fig. 5C and 5D). The presence of punctuate red staining corresponding to pDNA could correspond to pDNA that were either free (present inside the cytosol upon sonoporation) or routed in another intracellular compartments different to late endosomes. Microbubbles labelled with DiD were used to follow their fate in HeLa cells expressing Nup153-eGFP that delimit the cell nucleus. The representative analysis shown in figure 6 was acquired 6 h post-sonoporation. Our observations indicated also that pDNA were not efficiently delivered into the nucleus. However, it is worth noticing that some spots were close to the nucleus as indicated by their localisation in the vicinity of nuclear envelope delimited by Nup153-eGFP. The presence of microbubbles and pDNA inside cells raises the question of their intracellular entry pathway. It must be noted that the amount of pDNA found close to or inside the nucleus was not abundant compared to the pDNA entered into the cell suggesting that many pDNA have been degraded or excreted. The sonoporation efficiency could be improved at this step.

Endocytosis involvement during sonoporation

To validate the involvement of endocytosis in the process of gene transfer by sonoporation, we tested the effect of depletion of cellular ATP and inhibitors of endocytosis pathways on the sonoporation gene transfer efficiency. The figure 7 presents that the depletion of ATP reduced by 28 times the efficiency of gene transfer by sonoporation, which demonstrates that this process is active. Inhibition by chlorpromazine was dose-dependent decreasing the gene transfer by 3, 5 and 140 times using concentrations of 7.5, 10 and 20 µg/ml. This decrease corresponded to an inhibition of 70, 82 and 99% of the luciferase activity obtained in untreated cells. In contrast using a concentration of 5 µg/ml no significant inhibition was observed. It is to note that a significant toxicity of chlorpromazine at 20 µg/ml was obtained (approximately 30% cell viability). However, a caveolae pathway inhibitor Filipin III had no significant effect on gene transfer by sonoporation. We validated the effectiveness of the endocytosis inhibition protocol by testing the effect on the internalisation of transferrin, a positive control of the clathrin-dependent endocytosis pathway (data not shown). The conditions used allow an inhibition of transferrin in the presence of

chlorpromazine, while little effect was obtained with cells incubated in the presence of Filipin III. The results obtained with chlorpromazine are in the same direction as those obtained by Meijering *et al.*, they observed a 50% inhibition of the transfer of dextran 500 kDa in endothelial cells [7]. In contrast to our results, these authors have observed an inhibition with the Filipin III, this difference could be due to the size of the molecule transferred which was smaller (500 kDa versus 3 MDa) or to the difference in cell type used.

Conclusion

We have found the optimal ultrasound parameters in our set-up for an efficient gene delivery on HeLa adherent cells. This study showed the cell-microbubbles interactions and the intracellular fate of microbubbles and pDNA during and after the sonoporation process. A set-up combining high speed camera coupled with confocal fluorescence microscopy has allowed us to observe that depending on the acoustic pressure used, some microbubble were forced to enter the cell during sonoporation whilst other were stuck at the plasma membrane. The microbubbles were found to enter in cells only in the best conditions of transfection suggesting that the microbubble entry could be closely correlated to the plasmid DNA entry into the cell. By combining fluorescent pDNA with cellular tools exhibiting fluorescent intracellular compartments, confocal microscopy observations indicated that the pDNA reached the endocytosis pathway as confirmed by their localisation inside late endosomes and the effect of the inhibitors. The next step of our study will be the development of original microbubbles that could both target and deliver efficiently pDNA in a specific site. As long-term perspective, we intend to exploit ultrasound and microbubbles for theranostic purpose by exploiting their combined ability for molecular imaging and drug/gene delivery.

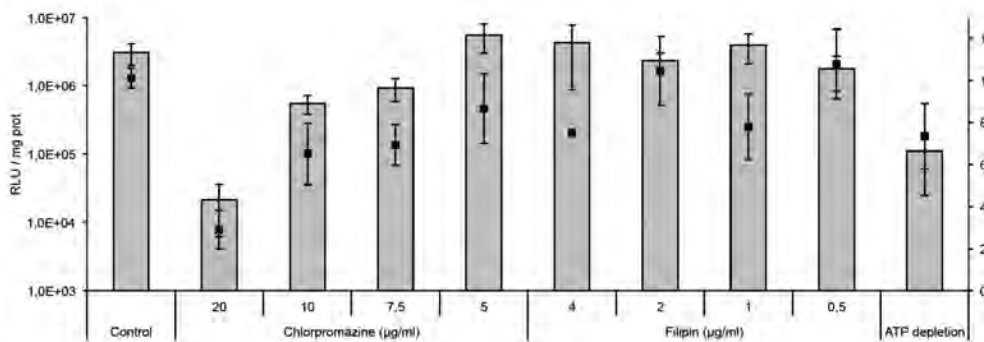


Figure 7 - Effect of endocytosis inhibitors and cellular ATP depletion on the efficiency of gene transfer by sonoporation. Parameters used: 1 MHz, 60 sec, 150 kPa, 40% DC, 0.3% microbubbles, 10 µg pDNA. The efficacy of gene transfer and the cell viability were determined 24 hours post-sonoporation.

References

1. Postema, M. and O.H. Gilja, *Ultrasound-directed drug delivery*. Curr Pharm Biotechnol, 2007. **8**(6): p. 355-61.
2. Bao, S., B.D. Thrall, and D.L. Miller, *Transfection of a reporter plasmid into cultured cells by sonoporation in vitro*. Ultrasound Med Biol, 1997. **23**(6): p. 953-9.
3. Miller, D.L., S. Bao, and J.E. Morris, *Sonoporation of cultured cells in the rotating tube exposure system*. Ultrasound Med Biol, 1999. **25**(1): p. 143-9.
4. Taniyama, Y. et al., *Local delivery of plasmid DNA into rat carotid artery using ultrasound*. Circulation, 2002. **105**(10): p. 1233-9.
5. Mehier-Humbert, S. et al., *Plasma membrane poration induced by ultrasound exposure: implication for drug delivery*. J Control Release, 2005. **104**(1): p. 213-22.
6. Kaddur, K. et al., *Transient transmembrane release of green fluorescent proteins with sonoporation*. IEEE Trans Ultrason Ferroelectr Freq Control. **57**(7): p. 1558-67.
7. Meijering, B.D. et al., *Ultrasound and microbubble-targeted delivery of macromolecules is regulated by induction of endocytosis and pore formation*. Circ Res, 2009. **104**(5): p. 679-87.
8. Paula, D.M. et al., *Therapeutic ultrasound promotes plasmid DNA uptake by clathrin-mediated endocytosis*. J Gene Med, 2011. **13**(7-8): p. 392-401.
9. Wang, X. et al., *Gene transfer with microbubble ultrasound and plasmid DNA into skeletal muscle of mice: comparison between commercially available microbubble contrast agents*. Radiology, 2005. **237**(1): p. 224-9.
10. Pichon, C. et al., *Recent advances in gene delivery with ultrasound and microbubbles*. Journal of Experimental Nanoscience, 2008. **3**(1): p. 17-40.
11. Delalande, A. et al., *Ultrasound and microbubbles assisted gene delivery in Achilles tendons: long lasting gene expression and restoration of fibromodulin KO phenotype*. J Control Release, 2011.
12. Suwalski, A. et al., *Accelerated Achilles tendon healing by PDGF gene delivery with mesoporous silica nanoparticles*. Biomaterials, 2009. **31**(19): p. 5237-45.
13. Duvshani-Eshet, M. and M. Machluf, *Efficient transfection of tumors facilitated by long-term therapeutic ultrasound in combination with contrast agent: from in vitro to in vivo setting*. Cancer Gene Ther, 2007. **14**(3): p. 306-15.
14. Li, Y.S. et al., *Optimising ultrasound-mediated gene transfer (sonoporation) in vitro and prolonged expression of a transgene in vivo: potential applications for gene therapy of cancer*. Cancer letters, 2009. **273**(1): p. 62-9.
15. Kaddur, K. et al., *Transient transmembrane release of green fluorescent proteins with sonoporation*. IEEE Trans Ultrason Ferroelectr Freq Control, 2010. **57**(7): p. 1558-67.
16. Rahim, A. et al., *Physical parameters affecting ultrasound/microbubble-mediated gene delivery efficiency in vitro*. Ultrasound Med Biol, 2006. **32**(8): p. 1269-79.

10

The effect of low intensity ultrasound on adhesion molecules, actin monomers and membrane permeability in endothelial cells

Chen Geffen and Eitan Kimmel

Biomedical Engineering Department, Technion, Israel Institute of technology, Haifa, Israel

Abstract

Biological effects of low intensity ultrasound (US) on cultured endothelial cells (ECs) *in vitro* have been traditionally attributed to streaming, microstreaming and shear stress. Lately, a novel concept of intra-membrane cavitation was suggested as a leading mechanism for the influence of US on ECs. In our experimental setup a US beam is aimed from underneath a horizontal cell culture dish, which is coated with ECs monolayer at the bottom. Acoustic pressure amplitudes in the range between 50 and 300 kPa were tested in 1 MHz frequency (20% duty cycle) for 5 min. Sometimes coated microbubbles (ultrasound contrast agent) were added to the experiment. A tracer spreading in the plate under US was studied and provided evidence that in our system, the streaming is rather weak and microstreaming is negligible in the medium surrounding the cells. We examine three elements in the ECs that are known to be affected by mechanical forces: i) membrane permeability – the membrane is a key factor in the new model for US induced bioeffects; ii) $\alpha V\beta 3$ integrin clustering - a transmembrane protein, a major factor in cell adhesion that connect between the inside of the cell to the extracellular matrix; iii) β -actin monomers – the rapid reorganization of the cytoskeleton can happen in response to an external signal. Under US exposure we observed EC detachment from the surface and reorganization of the cells on the culture dish in a repeatable pattern. We demonstrate that US increase significantly membrane permeability of ECs; and increase significantly integrin clustering in 200 kPa. US do not

increase the amount of β -actin monomers, even with the addition of microbubbles. We speculate that exposure of ECs to the US induces two opposing mechanisms that occur simultaneously: membrane permeability and cell rupture, and mechanical loading - all increase with US pressure amplitude.

Introduction

Our long-term goal is to utilize therapeutic ultrasound (US) for stimulus of biological processes such as vascular regeneration in a controlled manner, by studying the influence of US on endothelial cells (ECs). Very few systematic studies have undertaken to determine threshold levels for observed effects of US. Nearly all of the reports in the literature have tended to be phenomenological in nature, without evidence from further investigations to determine the underlying mechanisms of action. Furthermore, most reports have not yet been confirmed by more than one laboratory (many effects concerning discoveries about US are summarized in the reviews of Dalecki and Kimmel [1, 2]). Some studies have been performed using longer exposure times than would normally be encountered in the clinical situation and this has made the evaluation of health risks from exposure to US extremely difficult. Therefore, there is an urgent need for more carefully coordinated, systematic research in this critical area [3].

In this study we focus on biological elements in ECs that are known to be affected by mechanical loading, and then translate it to biological change. In addition, our motivation is to get a clue about the mechanisms by which US induces the cell mechanical stress. It makes sense that some mechanical forces can act in a manner similar to chemical ligands to stimulate ECs through the activation of mechanosensors, some of which may be through the receptors that respond to ligands. Such mechanotransduction leads to modulations of protein expression and cellular functions [4].

Endothelial Cells

ECs form a single cell layer that lines all blood vessels and regulates exchanges between the bloodstream and the surrounding tissues. ECs originate from the mesoderm and are very flat, about 1-2 μm thick and 10-20 μm in diameter. They have a remarkable capacity to adjust their number and arrangement to suit local requirements, and their signals organize the growth and development of connective tissue cells that form the surrounding layers of the blood-vessel wall. In addition, ECs have mechanoreceptors that allow them to sense the flow of blood over their surface, and by signalling this information to the surrounding cells, they enable the blood vessel to adapt its diameter and wall thickness to suit the blood flow [5].

Using ECs for *in vitro* experiments in the lab is usually done with a monolayer cell culture. These cells are ideal for such analyses for a number of reasons. For example, they assume a flattened morphology when plated onto glass coverslips and assemble large focal contact activity [6].

Physiological blood flow subjects the blood vessel wall to a force system consisting of two mutually orthogonal components: viscose friction and distension. The frictional force per unit area acts tangentially to the wall and is known as the wall shear stress. The shear stress in ascending aorta (2.3-4.5 cm² diameter) is between 2-10 dyne/cm² [7]. The distending force per unit area – the fluid pressure – acts perpendicular to the wall. The wall of the vessel is exposed also to cyclic strain that acts circumferential to the wall. As aforesaid, ECs in vivo are constantly exposed to these hemodynamic forces resulting from the flow of the blood and indeed fluid shear stress caused by blood flow is a major determinant of remodelling of arteries, regulation of arterial tone and atherosclerosis [8]. In the linear part of the arteries, the cells are elongated and aligned in the direction of the flow. In regions of bifurcations, endothelial morphology varies from tightly packed cubical cells in areas with high shear stress to polygonal cells with no obvious orientation in the regions of disturbed non-laminar shear stress. These observations suggest that endothelium is a sensitive “sensor” of local fluid mechanical forces. ECs, as a result of shear stress, mediate many physiological and pathological processes (e.g. adhesion) by synthesis of different proteins and factors.

The bilayer membrane

Biological membranes consist of a continuous double layer of amphipathic phospholipid molecules (hydrophilic at one hand and hydrophobic at the other) in which membrane proteins are embedded. This lipid bilayer is fluid, with individual lipid molecules able to diffuse rapidly within their own monolayer. The thickness of the bilayer membrane is about 5 nm. The role of the bilayer membrane is to separate between the inside of the cell to the outside, where the extracellular matrix (ECM) is. As mentioned, many proteins are embedded inside the membrane, for instance ion channels, receptors and other transmembranal proteins as integrins. In addition, lipid rafts (about 70 nm in diameter) float in the hydrophobic space of the membrane. The head groups of some phospholipids form docking sites for specific cytosolic proteins. The phospholipids have a spontaneous quality (even if they are artificially placed in water) to assemble into bilayers, which form sealed compartments that reseal if torn [5].

Integrins

The interaction of cells with the ECM plays a critical role in development and during periods of tissue remodelling by regulating tissue architecture and function. In many cell types, the molecules involved in cell-matrix adhesion are called integrins. These proteins (about 140 kDa) are heterodimers; the α and β subunits are held together by noncovalent bonds. The globular head of the integrin projects more than 20 nm from the lipid bilayer and the integrins usually present at about tenfold to a hundredfold higher concentration on the cell surface.

The integrins function as transmembrane linkers between the ECM ligands on the outside of the cell (including collagens, fibronectins and laminins) and the actin cytoskeleton (via anchor proteins like talin) inside the cytoplasm [8].

The integrins are found concentrated in specific morphological entities called focal contacts (FCs) or focal adhesions (FAs). These specialized ECM attachment organelles and signalling centres are called FCs when they are still nascent and in the process of

forming, or FAs when they have matured into larger complexes [6]. Within each FC, cell surface receptors of the integrin family cluster together due to mechanical stress and become activated. Understanding their dynamics in ECs has implications for blood vessel physiology *in vivo* because blood vessel development during tissue remodelling and pathological conditions, such as cancer, involves ECs migration in their matrix adhesion sites [9]. The integrins make weak adhesions with the matrix, thus enable the cell to perform migration. This phenomenon is called “The Velcro principle” [5]. When cell loses contact with the ECM, it can undergo a programmed cell death (apoptosis). This dependence on adherence to the ECM for survival and proliferation may help ensure that the cells survive and proliferate only when they are in their appropriate location, which may protect animals against the spread of cancer cells. Integrins also function as signal transducers, activating various intracellular signalling pathways when activated by matrix binding. Integrins and conventional signalling receptors often cooperate to promote cell growth, survival and proliferation [10, 11]. We chose to study $\alpha V\beta 3$ integrin due to its great role with the above. It has already been established that flow induces an enhanced adhesion of ECs to matrix via their $\alpha V\beta 3$ integrins [12, 13].

The actin cytoskeleton

Actin filaments undergo constant remodelling of the assembly and disassembly of their subunits, thus influence the cytoskeleton and processes such as cell division [5]. Actin filaments are hard to stretch but easy to break. There are 6 kinds of actin monomers, and in this study β -actin monomer was used. The importance of β -actin is in reshaping of the cell and formation of cell branches, which are the cell adherence points to surfaces. During the shift of the biological signal, that can happen for example due to integrin activation, a remodelling of the cell shape occurs; actin fibres fragment to monomers and new fibres are created instead. The fibre reconstructing is a very dynamic process that can happen rapidly. In addition, it is known from the literature that cells can quickly express new β -actin monomers: the mRNA was examined and it was estimated that cells can create about 30,000 monomers in a minute if necessary [5, 14].

Ultrasound

Ultrasound (US) is a pressure wave having a frequency above the range of human hearing (typically above 20 kHz), which unlike electromagnetic radiation, requires a medium through which it propagates [15]. The transmission through the medium depends to a great extent on the US frequency and the state of the medium, i.e., gas, liquid, or solid [3].

US propagates in the form of longitudinal waves formed by alternate medium regions of compression and rarefaction. The vibrating particles cause to propagating disturbance [15]. The distance between two consecutive points of maximum compression or rarefaction is called the wavelength (λ) [3]. The speed of sound (c) is a constant that depends on the physical properties of the medium, therefore it is a characteristic of a specific medium:

$$c^2 = \frac{1}{\beta * \rho}, \quad (1.1)$$

where ρ = density and β = the adiabatic compressibility [16].

The frequency of a sound wave (f) determines the rate of compressions and rarefactions. The speed together with the frequency of the US determines the magnitude of the wavelength λ that propagates:

$$\lambda = \frac{c}{f} \quad (1.2)$$

For example, the propagation velocity of the acoustic wave in most human soft tissues ranges from approximately 1450 to 1660 m/sec, so that frequency of 1 MHz corresponds to a wavelength in the range of 1.4 to 1.7 mm respectively.

In many applications, US is usually generated by applying a high frequency voltage across a piezo-electric transducer [17].

Acoustic pressure

The passage of a sound wave through a medium can be characterized by several variables associated with the movement of particles inside the medium. These include: acoustic pressure (p), particle displacement (x_i), particle velocity (v) and particle acceleration (a). Under idealized conditions (harmonic waves), each of these quantities varies sinusoidally with space and time.

The acoustic pressure p is the change in the total pressure at a given point in the medium at a given time. The acoustic pressure oscillates between "positive" (compression) pressure, *i.e.* greater than atmospheric pressure, and "negative" (rarefaction) pressure, *i.e.* lower than atmospheric pressure values, resulting in compression where p is positive, and expansion where p is negative.

The displacement x_i is the difference between the mean position of a particle in the medium and its position at any given instant in time t . The particle velocity v is the instantaneous velocity of a vibrating particle at a given point in the medium. This should not be confused with the speed of sound c from equation 1.1. The latter is the speed with which the wave propagates through the medium, even though the individual particles of the medium vibrate only about their mean position with no bulk movement of matter. Generally in a certain bulk, v is dependent in c .

As a result of the sinusoidal variation in particle velocity (v), each particle experiences an acceleration (a) which also varies with time and position; it has positive values when v increases, and negative values when v decreases [3].

In a medium with attenuation coefficient around zero, the pressure is:

$$p = p_0 \sin(\omega t - kz) \quad (1.3)$$

where p_0 =maximum pressure amplitude; ω =angular frequency= $2\pi f$; t =time; k =wavenumber= $2\pi/\lambda$; and z =wave displacement [15].

Acoustic intensity

Acoustic waves possess and transport both kinetic and potential energy, the former being related to the mean velocity of the substantial molecules while the later stems from the material resistance to compression [18]. The intensity (I) of a sound wave is the amount of energy which is carried by the wave through a unit area perpendicular to the direction of sound propagation per unit time [3]. If the wave is continuous and sinusoidal, I is usually given as the time-averaged intensity [15]:

$$I = \frac{p_0^2}{2\rho c} \quad (1.4)$$

where the acoustic impedance (Z): $Z = \rho c$, describes the resistance of a medium to the passage of a sound wave, thus:

$$I = \frac{p_0^2}{2Z} \quad (1.5)$$

The extent to which ultrasonic energy is transmitted or reflected at an interface separating two continuous isotropic media is determined by the ratio of the characteristic acoustic impedances of the media. The closer this impedance ratio is to 1 the more energy is transmitted into the second medium and the less is reflected from the interface. At an interface between human tissue and air, only about 0.01% of the incident energy through the air is transmitted to the tissue; the remainder is reflected backward. This illustrates the importance of using a coupling medium between the transducer and the human tissue for both therapeutic and diagnostic US applications [3 19].

The ultrasonic field

The ultrasonic transducer which generates the acoustic field is built from many small simple transducers that are placed on the surface of the transducer and radiate energy uniformly in all directions. Calculation of the total contribution of each of the simple transducers to the field can be analyzed (Huygen's principle) using superposition while taking into consideration the phase and amplitude. In general, the direction of the beam is determined by diffraction in the same way a beam of light is affected by an aperture: the higher the frequency of US produced for a given transducer size, the more directional is the beam. The application of Huygen's principle is often rather complicated but for a steady state condition (continuous wave, CW), the beam is constructed of two distinct regions: the near field and the far field (Fr  snel and Fraunhofer zones).

The near field is a zone where the overall beam size remains relatively constant, though there are many variations of intensity within the zone itself, both across and along the beam axis. For a given radius, the near zone increases with decreasing wavelength (higher frequency).

The calculation of the exact field is very complicated and the shape of distribution can be achieved more easily by direct measurement. In the far field zone (or Fraunhofer region), the beam is more uniform and the mathematics analysis is much easier. In

addition, acoustic intensity becomes proportional to the square root of the acoustic pressure (as in equation 1.5). The maximum intensity along the main axis is considered as the spatial intensity [3].

For a circular piston source of diameter d that radiates sound of wavelength λ , the Fresnel zone extends from the transducer to a distance (L) equal to:

$$L = \frac{d^2}{4\lambda}, \quad (1.6)$$

(when $d \gg \lambda$) and beyond this distance is the Fraunhofer zone of the transducer [3].

Furthermore, if the frequency is held constant but the diameter aperture is reduced, the beam divergence increases. Equation 1.7 is the formula for convenient determination of the divergence angle θ in the far field [19] :

$$\sin \theta = 1.22 \frac{\lambda}{d} \quad (1.7)$$

Acoustic radiation force and acoustic streaming

A steady, time-averaged force called the acoustic radiation force typically acts upon an object in an acoustic field. This force results from a transfer of momentum from the sound field to the object. As the acoustic field propagates in a fluid medium, it can give rise to a bulk fluid flow termed "acoustic streaming". Streaming phenomena is a result of attenuation property of the medium, which causes to a gradient of radiation pressure. The streaming velocity is the result of non-linear terms in the wave equation and it depends on factors that include the absorption coefficient, speed of sound, kinematic viscosity, intensity, and beam geometry. If there are particles in the fluid, an "Advection" mechanism can occur where there is particle transportation in the flow direction.

An example for radiation force action is the blood flow stasis phenomenon reported by Dyson *et al.* (1971), where red blood cells in the blood vessels of chick embryos exposed to an ultrasonic standing-wave field, collected into parallel bands spaced at half wavelength intervals [20]. This was also shown in mammalian vessels [21]. Another example is a displacement of US contrast agents to the wall of blood vessels in laboratory animals, achieved by radiation force [22].

Mechanical index

The prediction of the probability for tissue damage occurrence in an acoustic field is determined by a parameter called "Mechanical Index" (MI):

$$MI = \frac{P_{\text{Negative}}}{\sqrt{f}} \quad (1.8)$$

where P_{Negative} is the maximum value of the transmitted negative pressure amplitude in MPa, and f is the frequency in MHz. According to the FDA, the approved MI for ultrasonic devices should not be higher than 0.23 for ophthalmic applications, nor higher than 1.9 for the other applications (such as peripheral vessel, cardiac and fetal imaging applications) [23]. As opposed to *in vivo* uses, in *in vitro* implementations, the MI in the acoustic set up is usually up to 0.6-0.8.

Cavitation

Concerning non-thermal mechanisms of US for producing effects in biological tissues, the great majority of studies have dealt with cavitation. This phenomenon, termed "cavitation", may require pre-existing stabilized nuclei, i.e., little gas bodies of a diameter of μm or less, that are stabilized in holes or crevices in the medium [3]. The number and size distribution of gas nuclei within the medium are particularly important for the occurrence of cavitation. Unfortunately, these quantities are not easily measured. The number of available nuclei within a fluid medium greatly increases when the medium is stirred or mechanically disturbed [24]. Several models exist to explain the stabilization of gas nuclei in fluids [25]. The maximum response of a bubble to an acoustic field occurs when it is exposed to its resonance frequency.

The resonance frequency is dependent on the initial size of the bubble. One of the accepted models that can be used to predict the resonance frequency for bubble pulsation is "Minnaert resonance frequency" equation [25]:

$$f = \frac{1}{2\pi R_0} \left(\frac{3\gamma P_0}{\rho} \right)^{0.5}, \quad (1.9)$$

where P_0 = hydrostatic liquid pressure outside the bubble, γ = polytropic coefficient of the gas inside the bubble (a ratio of specific heat of gas at constant pressure to that at constant volume) and R_0 = the equilibrium radius of the bubble. In the case for air bubbles in water, under 1 atmosphere where surface tension and heat conduction are negligible, together with the assumption that kinetic energy resides solely in the motion of the water – the "Minnaert resonance frequency" equation reduces to form:

$$f \approx \frac{3}{R_0}, \quad (1.10)$$

When a bubble expands and contracts during the US pressure cycle, the surrounding medium flows inwards and outwards with higher velocity than if the gas bubble was absent. As a rough guide, the resonant diameter of a cavitation bubble in water at 1 MHz is about 3.5 μm . Alternatively, gaseous nuclei may exist in the medium which are initially smaller than resonance size but can grow to that size in an applied sound field through the process of rectified diffusion [3]. The US sets the irradiated bubble and surrounding medium into motion, which produces forces that attract particles from the surrounding medium. Rectified diffusion describes the slow growth of an oscillating bubble owing to a net flow of gas into the bubble over many acoustic cycles. The

maximum expansion of a stable cavity typically does not exceed twice the equilibrium radius.

When a gas bubble pulsates, its motion is not usually spherical, either because of distortion by an adjoining boundary or because of surface waves set up by the US field. Asymmetric or non-uniform oscillation of the air-liquid interface, at the surface of an air pocket or bubble, causes a steady eddying motion to be generated in the immediately adjoining liquid, often called “microstreaming”, in which the velocity gradients may be high.

Thus, during the pulsation of gas bubbles when the movement of the surface is not uniform, the interface swirls that cause microstreaming with high velocity gradient can cause to shear stress, as described by Kimmel *et al.* [2, 26]. If biopolymer molecules or small biological cells are suspended in liquid near a pulsating bubble, they may be swept into a region of high velocity gradient. Such a situation can also occur if a small bubble pulsates near a cell membrane causing the membrane to vibrate, producing streaming motions within the cell. The biological system will then be subjected to shearing action and damage may occur, such as fragmentation of macromolecules and membranes. Nyborg *et al.* (1977) estimated that a bubble of 3 μm radius in blood plasma, which started to pulsate at an intensity of 1 mW/cm^2 with a frequency of about 1 MHz (to which the bubble is resonant), would generate a microstreaming field in which the maximum viscous stress would greatly exceed 100 N/m^2 [27].

Two different types of cavitation are mentioned in the literature: stable cavities and transient cavities. Stable cavitation describes a repetitive oscillation of a bubble over many acoustic cycles. It occurs when the cavity size is of the right order to get into resonance in the ultrasonic field - the bubbles oscillate with large amplitude, expand and contract with the same periods of the ultrasonic field. These oscillations cause magnification of the medium amplitude around the bubbles, allowing the medium particles to move faster and the diffusion of gas to the bubble is accelerated. The response of the bubble can be nonlinear and is dependent on some variables including the acoustic pressure amplitude, exposure frequency and bubble size. A variety of physical phenomena can be associated with stable cavitation, for example the microstreaming phenomenon mentioned above [28].

In contrast to stable cavitation, transient (or collapse) cavitation is more violent and occurs at higher US intensity levels. These changes may cause volume increment of the nuclei, raising the possibility for violent collapse. In the final stage of collapse, kinetic energy given to a relatively large volume of liquid has to be dissipated in an extremely small volume, thus the result is high temperature and pressure [3]. The unstable cavities can cause a lot of damage because of the high energy that bursts from them. The damage can be physical, like over-heating and tissue destruction, or chemical like free radicals and hydroxyl-ions which can react with biological macromolecules and change them (*i.e.* causing mutations).

The response of an inertial cavity to an acoustic field is highly nonlinear, such that a small increase in the acoustic pressure amplitude can change the bubble response

from a stable cavity to a transient cavity. The acoustic pressure at which the transition occurs is often called the threshold for transient cavitation [28].

The higher the frequency is, the higher the intensity that is needed to create the cavities (according to the MI). Higher temperature and larger irradiated volume lower the threshold for cavitation. However, the most important factor is the number of nuclei and the rate of acquiring new nuclei which is higher in a mechanically disturbed medium. Moreover, rectified diffusion hastens the presence of the transient cavitation. In the appropriate exposure conditions, even a single US pulse in duration of 1 μ sec can cause a bubble to expand rapidly and collapse violently [29]. Bubbles that undergo transient cavitation near solid boundaries can collapse asymmetrically, and that can result in the formation of high-speed, fluid microjets that impinge on the boundary. Microjets can cause to cell detachment and membrane rupture [30].

Ultrasound contrast agents

The contrast materials that are used today in US are usually built from micro gas bubbles (e.g. gas Fluor) wrapped with a polymer (Poly-Ethylene-Glycol for example) or a biological material like a lipid or a glycoprotein (albumin or galactose for instance). The most common use of the contrast agents in medical is for cardiovascular imaging. The gas is characterized by acoustic impedance which is almost zero regarding the blood and tissues. This fact causes almost full reflection of the sound waves when they hit the gas bubbles. Therefore, one way to use the contrast agents is to inject them to the vein and follow after the perfusion in the tissue according to the reflection magnitude. In an ischemic tissue, the reflection magnitude of the sound wave will be lower compared to normal tissue because there are less blood vessels in that area, so less bubbles can pass through it.

The role of the bubble shell is to conserve the gas long enough (usually between minutes to dozens of minutes) in the blood in order to achieve full and reliable measurements. For frequencies relevant to diagnostic US, the size of resonant bubbles is of a few micrometers in radius. This small size of the bubbles is also important in order to enable the bubbles pass in the lung cycle. The reflection that was referred to before originates from a bubble clouds, so there is also a minimum concentration of bubbles that enables a good reflection of the sound wave. The resistance of the gas bubbles to the acoustical radiation can be described by the MI that was mentioned earlier. A widespread assumption is that $MI > 0.8$ causes cavitation of contrast agents in tissues. In addition, the resonance frequency for a coated bubble is different than the resonance frequency based on equation 1.10. In this research, the contrast agents were used for raising the acoustical pressure, as will be described later (see *Materials and Methods* section).

The bilayer sonophore

Recently, Prof. Eitan Kimmel has been developing a revolutionary model for the effects of US on living cells and tissues. Those effects, he claims, are induced on the cell through a direct influence on cell membranes, in and around the cell. For simplicity, imagine the lipid bilayer membrane as comprised of two flat, parallel, monolayer leaflets with a thin intra-membrane hydrophobic space between them, bound together by a

circular ring of transmembrane proteins. Water surrounds the membrane from the external hydrophilic side, and gas (air) molecules that are dissolved in the water can diffuse through the leaflets into the intra-membrane hydrophobic space. At equilibrium, no force is acting between the leaflets and the atmospheric pressure in the water is balanced by the pressure of the gas molecules entrapped between the hydrophobic tails. At negative US pressure (lower than 1 atmosphere – based on modelling and experimental measurements), the leaflets are pulled apart symmetrically, by overcoming the molecular attraction forces between the leaflets, the tension that develops in the curved and stretched leaflet, as well as inertial forces of accelerating the water in close proximity, and viscous forces. This process is reversed during positive acoustic pressure, and the entire cyclic motion of the leaflets is determined by a dynamics force (pressure) balance equation for a pulsating bubble and a diffusion equation determining the rate of transport of dissolved gas into and out of the hydrophobic space from the surrounding water. In addition, the periodically pulling the leaflets away from each other is also involved with overcoming on the elastic and viscous resistance against stretching and deformation of the tissue attached to the leaflets.

At the same time, pockets of dissolved gas accumulate in the hydrophobic space located between the leaflets. Prof. Eitan Kimmel suggests calling it “the bilayer sonophore” (BLS) - as it is capable of absorbing millimetre wavelength acoustic energy and transforming it to periodic subcellular-level forces. This predicted behaviour is supported by experimental observations of widened cavities coinciding with membranes in (=the two membranes that enclose the nucleus, the mitochondria and the endoplasmic reticulum) and around cells, when we exposed a multi-layered epithelium to US in-vivo [31].

The preliminary BLS model predicts that the bilayer membrane is the origin of many, if not most of the bioeffects induced by US in living cells. In this framework, the cyclic expansion and contraction of the BLS stimulates cycles of stretch and release in the cell membranes and in the cytoskeleton, which in turn can activate mechano-sensitive proteins and increase membrane permeability. The different bioeffects induced by US could thus potentially be interpreted in light of the BLS model as progressive stages along a graded scale of induced phenomena that differ in maximum area strain of the leaflets due to different US exposure parameters, mechanical tissue properties, proximity to a free surface or the presence of extracellular gas bubbles.

With increasing maximum area strain of the leaflets we can expect to encounter: 1) delicate and reversible bioeffects induced by leaflet stretching or bending in excitable cells or cells that have mechano-sensitive membrane proteins; 2) damage to membrane proteins and/or cytoskeletal fibres as they become dislodged, denatured or fragmented; 3) membrane perforation, pore formation and rupture, potentially facilitating the uptake of drugs and genes, inducing sonophoresis and enhancement of tissue permeability; 4) Complete membrane disruptions and irreversible cellular damage, e.g., capillary haemorrhage, which is generally attributed to the rupture of ECs.

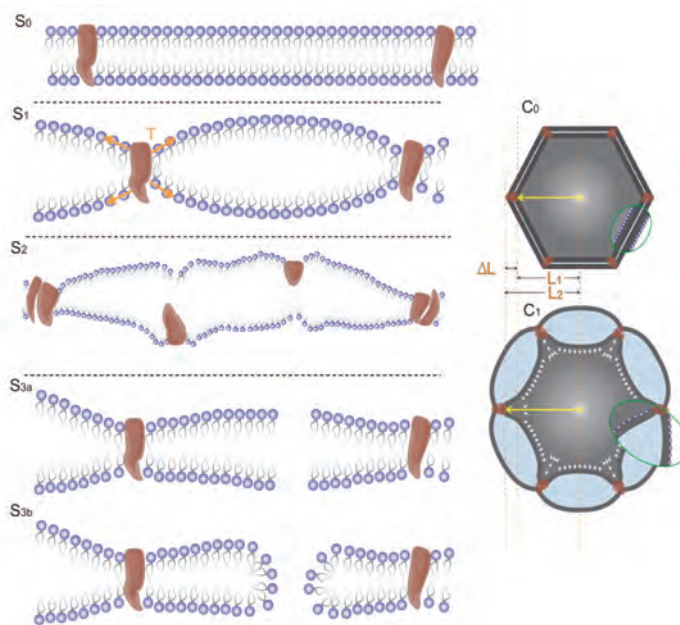


Figure 1 - Different stages in the interaction of a BLS and an US field can induce different bioeffects on the cell membrane and the cytoskeleton. As tension increases gradually in the leaflets around a pulsating BLS, from the reference stage (S_0), the slightly stretched leaflets might at first activate mechano-sensitive proteins (S_1); growing tension in the leaflets might damage membrane proteins (S_2), and then might induce pore formation (S_{3a} , S_{3b}) or cause membrane rupture at high levels of stretching. Pulsations of the BLSs that surround a cell initially at (C_0), might induce from reversible mild stretching of cytoskeleton fibres to irreversible rupture (C_1) [31].

Mechanosensitivity of Endothelial Cells

Mechanical forces are known to play a key role in many physiological processes, but how cells perceive mechanical stimuli and convert them into biochemical signalling pathways is not yet well understood. Shear stress, the tangential component of hemodynamic forces acting on the vessel wall, is an important modulator of vascular cell functions in normal and patho-physiological conditions, e.g., endothelial wound healing, atherosclerosis and reperfusion injury [32].

In vitro experiments using ECs cultured in flow channels have proved that the structure and function of ECs are modulated by physiological-like shear stress [12]. Note that it was found that oscillatory shear stress caused EC apoptosis whilst laminar shear stress did not [33]. In addition, the activation of mechanosensors by shear stress led to the triggering of phosphorylation cascades of signalling molecules [34].

Besides the physiological shear stress, therapeutic US is another mechanical stimulus to ECs and has been studied by e.g. Raz *et al.* who found that transient reorganization of actin stress fibres in ECs followed by some recovery, but mostly demonstrated the damage induced to stress fibres due to US sonication for 15 min. The experiments were performed with 0.5, 1 and 3 MHz transducers at maximum intensity of 2.2 W/cm² [35]. Damage to microtubules and focal adhesions was demonstrated too. Since the total amount of vinculin in the cells did not change, it was concluded that the focal adhesions were physically disassembled rather than subjected to biochemical lysis. The last outcome may imply that direct mechanical effect was involved.

Barzelai *et al.* have demonstrated that serial low intensity US irradiation induced angiogenesis and improved tissue perfusion of moderate and severe limb ischemia in rats (2 MHz, 0.05 W/cm²) [36]. Dyson and Young found that Wounds in rat skin were exposed to US for 5 min daily at 0.1 W/cm² at frequencies of either 0.75 or 3 MHz. 5 days after injury there were more blood vessels in equivalent regions of the injured tissue of the US treated wounds than in the control wounds [37].

In our laboratory, Mizrahi *et al.* found that US induced EC proliferation, migration and sprouting in PEG fibrinogen gel. An expression of angiogenic receptors phenotype was also observed [38].

Hypothesis

Our hypothesis is that low intensity US with pressure amplitudes of about 50-300 kPa affects three elements in the cell that are interconnected mechanically and that are known to be affected by mechanical forces: membrane permeability, integrin activation and expression of β -actin monomers. US intensity and frequency (see MI definition) determine whether the influence on the cells is delicate and the alterations are reversible in low intensity US or whether cell lysis happens due to application of higher intensity US. It is already known that following US, the membrane permeability of ECs increases and US-enhanced gene and drug delivery is currently under extensive research. Integrins might also respond to US because they serve as transmembranal proteins and connect between the inside and outside of the cell. It was reported that physiological shear stress enhanced $\alpha V\beta 3$ integrin clustering in ECs. US was documented to influence actin filaments and therefore it is assumed that US affects β -actin monomer expression.

Materials and Methods

Cell Culture

Bovine Aortic Endothelial cell line (BAECs) catalogue number BW-6001 was purchased from "Cambrex Bio Science Walkersville". These primary cells were grown in Dulbecco's modified Eagle's medium (DMEM) with low glucose supplemented with 10% foetal bovine serum (FBS), 1% L-Glutamine, 1% Penicillin Streptomycin and 1% Sodium Pyruvate (Biological Industries, Kibutz Beit Haemek, Israel). Cells were cultured at 37°C in an atmosphere containing 5% CO₂ and high humidity and were grown to passage 9 until reached 80-90% confluent monolayer.

Experimental Setup

An experimental low-intensity US system was used to apply US irradiation to monolayer BAEC cultures (Fig. 2).

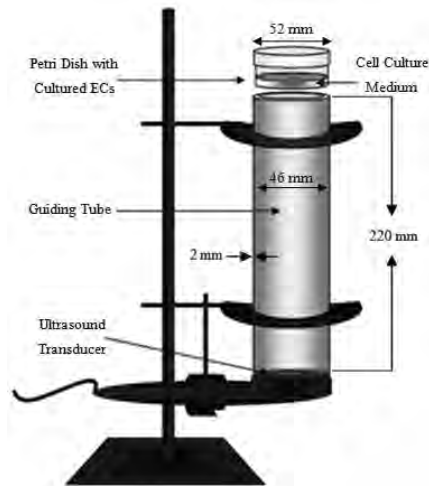


Figure 2 - Schematic illustration of the experimental setup for EC sonication [40].

As one can see from the scheme, the US system was composed from a flat circular unfocused US transducer "Sonicator 740" (Mettler Electronics) and a hollow tube guide (PVC) that was put on the transducer and filled with acoustic propagating medium (distilled water that were de-gassed using a vacuum chamber and a water pump). The tube length was adjusted to the far field calculation, allowing uniform acoustic radiation. A 60 mm- diameter cell culture dish (Corning) was placed on top of the tube where a nitrile glove and an acoustic gel (Ultra-gel Aquarius 101) were also placed enabling no air penetration that can interfere with the transmission. The sonication was perpendicular to the culture plate surface using a pulsed signal with 20% duty cycle (D.C). The pulse length was 2 msec and the total pulse repetition frequency (PRF) was 10 msec. In 5 min duration of transmission in 1 MHz frequency, $6 \cdot 10^7$ cycles were applied. Due to a lateral reduction of the averaged acoustic intensity, the cells next to the dish wall were not examined.

Calibration of the ultrasonic system

In order to use Sonicator 740 as the US transmitter, a calibration of the system has been made. Our aim was to probe what would be the pressure amplitude of the sound wave where the cell monolayer was placed. According to the theoretical calculations, no great attenuation of the sound wave should exist in distilled water with the assumption that we deal with harmonic waves.

The pressure amplitude of the ultrasonic signal was measured using a HNR-500 needle hydrophone (ONDA) put at the bottom of the cell culture plate which was placed on the upper part of the tube guide (Fig. 3). TDS 224 scope (Tektronix) was used to convert the electrical signals of the hydrophone to wave amplitudes on a screen. The hydrophone measured the peak-to-peak voltage, thus, the mean pressure amplitude was calculated. The sinus wave oscillated around zero.

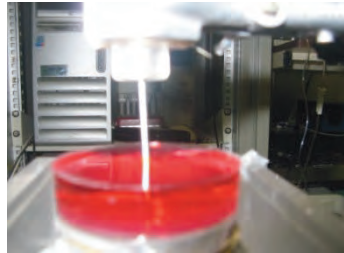


Figure 3 - Calibration of the ultrasonic system. The setup of the HNR-500 hydrophone in the cell culture dish full with DMEM medium.

The calibration was made at average intensity of 0.1-0.6 W/cm² in 5 min duration, 1 MHz and 20% D.C. Following equation 1.5: $P \propto \sqrt{I}$, therefore, the linear formula of the graph can characterize a propagating wave: $P = \sqrt{2\rho c} \cdot 100 \cdot \sqrt{I}$. It was possible to make an extrapolation from the graph and conclude about higher intensities (Fig. 4). Later, we evaluated any temperature changes in the plates following treatment, as those can have an effect on both cell viability and micromechanical measurements. That was done at room temperature using a HH23 JKT microprobe thermometer (OMEGA, USA). Temperature changes in the cell culture medium during and following the US treatment were measured for 200 and 300 kPa. In order to determine the contribution of the US irradiation alone to possible temperature rise in the medium, all temperature measurements were done relatively to an untreated medium. Maximum temperature increase was 0.3°C at the higher-pressure amplitude (300 kPa).

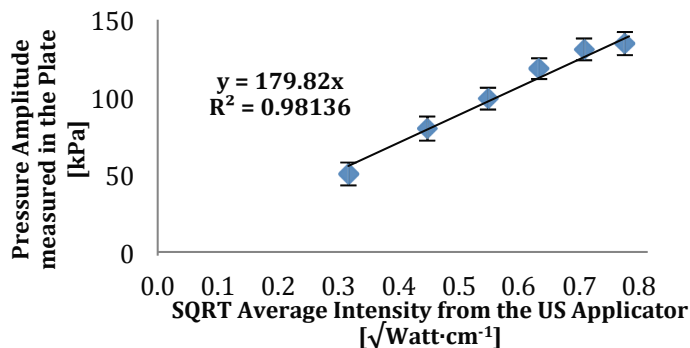


Figure 4 - SQRT average intensity from the US applicator vs. pressure amplitude.

Identification of the US induced flow in our experimental system

Given that we investigated the influence of low-intensity US on BAECs, our interest was to determine the existing streaming field in the EC artificial surroundings after implementing US irradiation. Due to that, 50-300 kPa acoustic pressure amplitudes were transmitted for 5 min on 0.1 g/ml coffee solution that was put in the middle of a culture dish full with 5 ml distilled water (Fig. 5).

The expansion of the coffee dye was monitored using continuous video tracking (25 fps) that was analysed with computerized programs (Power Point and Windows Media Player 11). The pictures were taken from above with a digital camera (Canon FS20) that was aiming at the upper surface of the water from a constant height of about 20 cm and the lighting conditions were kept constant as well. The stain slowly became wider and the measurements were calculated up to the first minute. Only at 300 kPa the stain expanded quickly and the dye faded and was untraceable.

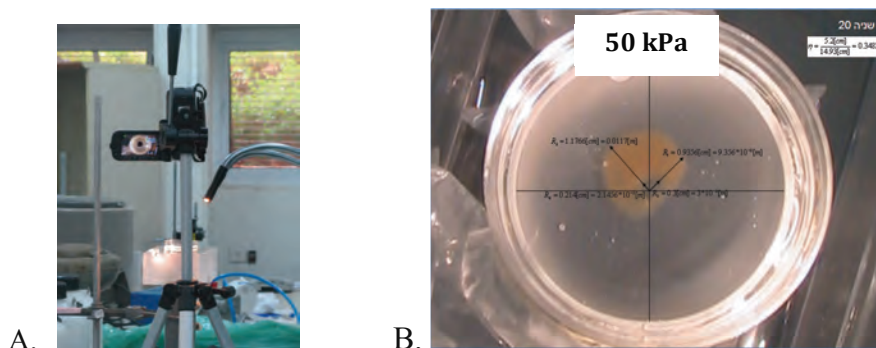


Figure 5 - Evaluating streaming and microstreaming in the plate above the cells. A) The apparatus that was used to estimate the generated streaming field in the US system; B) An example for the coffee stain dimensions.

Two parameters were set for the streaming field estimation using the simplified equations below (Equations 2.1 and 2.2 and figure 6 where r =radius and t =time): U , the advection index was evaluated by the spreading of the stain front. The horizontal streaming is the component that causes shear stress; D , the stain spreading parameter was developed according to the diffusion equation (Fick's second law). If there would be an increase in D following US irradiation (as opposed to control), it might imply on enhanced transport of the dye particles, hence occurrence of microstreaming in the plate. In order to calculate the parameters from our data, some simplifying assumptions were made:

1. The advection index and the stain spreading parameter stay constant at a given radius.
2. Changes in temperature were insignificant in the various pressure amplitudes.

$$D \approx \frac{(\Delta r_2 - \Delta r_1)^2}{\Delta t} \quad (2.1)$$

$$U \approx \frac{r_2 - r_1}{\Delta t} \quad (2.2)$$

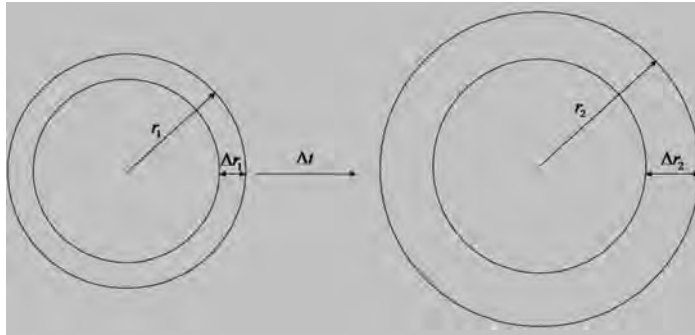


Figure 6 - Illustration of the dye spreading and approximated calculation of the parameters.

Membrane permeability measurement

BAECs passage 9 were exposed to low intensity US irradiation of 50-300 kPa pressure amplitudes for 5 min in 1 MHz, 20% D.C in the setup described above. Immediately afterwards normal and membrane damaged cells were counted under light microscope (Nikon) with 0.4% Trypan Blue solution (Sigma) measurement using a haemocytometer (Marienfeld, Germany) according to the manufacturer instructions. The Trypan Blue reagent dyes the cells in blue as a result of cell damage and increase in their membrane permeability. During 6 experiments, 17 samples were collected for quantification.

Integrin activation measurement

BAECs passage 9 were seeded on 22×22 mm² sterile coverslips (Menzel-Gläser, Germany) placed in standard 60 mm diameter culture plates (Corning). Once the cells reached 90% confluence they were put under various pressure amplitudes of low intensity US for 5 min in 1 MHz, 20% D.C. Immediately after the treatment the cells were taken for fixation. For cell fixation, the medium was aspirated and the coverslips were washed with PBS. After aspirating the PBS, the cells became permeable during soakage for 5 min in 4% Paraformaldehyde (PFA, Electron Microscopy Sciences, Hatfield, PA) in PBS containing 0.5% Triton X-100 (A.R., Bio Lab, Israel). Next the cells were washed twice in PBS for 2 min each time and 4% PFA was added for 25 min. The PFA was then aspirated and the coverslips were rinsed with PBS for 3 times. LM609 antibody (5 µg/ml Chemicon) was used to stain αVβ3 integrins of fixed cells. The procedure of the staining was applied on a parafilm sheet. The coverslips were gently tapped to remove any excess moisture, and placed cell-face down onto the drops (70

μl). The coverslips were placed in a humid, dark chamber, and incubated for 1 hr at room temperature. Next, the coverslips were washed twice in PBS for 2 min each time in a covered dipping chamber (Thomas). Meanwhile, 4'-6-diamidino-2-phenylindole (DAPI, Sigma) for staining cell nuclei was diluted in PBS to a final concentration of 2.5 μg/ml. Drops (70 μl) of the diluted DAPI together with the secondary antibody cy3-labeled goat anti-mouse IgG (115-166-072, 14 μg/ml, Jackson ImmunoResearch, West Grove, PA) were prepared, and the coverslips were incubated again for half an hour. Finally, the coverslips were washed twice in PBS for 2 min each time in the covered dipping chamber, and then mounted face-down onto blank slides with Fluoromount G (Southern Biotech, Birmingham, AL). The slides were left to dry in a slide box and were prepared the next day for microscope imaging. The cells were assayed with an inverted fluorescent microscope (Nikon) in 100× magnification using two different wavelength filters for recording the two fluorescent labels in a single sample. Pictures of the samples were taken blindly using a digital camera (Lumenera). Negative control with IgG1 Isotype Control antibody (14-4714, eBioscience) was preformed as well in order to deny non specific staining of αVβ3 integrins.

Following that stage, the pictures were analysed using software for quantification (Axio Vision Rel. 4.6). The integrin clustering was expressed by a parameter defined as "Integrin Activation":

$$I.A. = \frac{\sum(A_i \bar{I}_i)}{N} \quad (2.3)$$

Where I.A. = integrin activation; N= number of nuclei in the picture; A_i = stain area; \bar{I}_i = averaged stain brightness. The quantification program automatically calculated stain areas and the averaged grey level (=brightness) for each stain, which describes a cluster of integrins in the picture. The number of nuclei was counted manually. It is important to mention that the cells in the experiment were equally seeded therefore it was not important to determine the cell boundaries. Then it can be said that the value of integrin activation would be higher if there was more lighting of integrins surrounding one cell. It is hypothesized that as far as the integrin activation grows, the adhesion and cell signalling processes will become more dominant in the cell. We assumed that without US the integrin activation level would have been lower. The pixels that were counted had a grey level in between 20-60 where the whole range is 0-255. This was done in order to omit background signal or noise. In 6 repetitions of 50-135 kPa, 37 samples (N=37) were examined, whereas in 3 repetitions of 200-300 kPa treatments, only 7 samples (N=7) could have been examined (see results).

Cell lysis, SDS-PAGE and immunoblot analysis

In order to evaluate the amount of β-actin monomers in BAECs, cell extracts were prepared right after US irradiation using a lysis buffer containing 50 mM Tris-HCl pH 7.6 150 mM NaCl, 6 mM EDTA and 1% Triton X-100, supplemented with protease inhibitors: 1 mM PMSF, 21 μM Leupeptin, 0.5 M Na orthovanadate and 0.5% Aprotinin (Sigma). Protein concentration was determined by Bradford reagent (Bio-Rad, Hercules CA) and samples were resolved by SDS-PAGE under reducing conditions using 8%

polyacrylamide gel. Equal amounts of lysate samples were then subjected to immunoblotting with anti- β -actin (5.8 μ g/ml, A5441 Sigma) and anti-GAPDH (0.4 μ g/ml, sc-47724 Santa Cruz, CA) monoclonal antibodies. After electrophoresis, proteins were transferred to polyvinylidene difluoride membrane (PVDF, Bio-Rad) which was activated by methanol. The membrane was probed with the appropriate antibody followed by HRP-conjugated goat-anti-mouse secondary antibody (Jackson Immunoresearch Laboratories), and protein bands were visualized by an ECL fluorescent detection with an EZ-ECL kit (Biological Industries) according to the manufacturer instructions. Quantification of each protein was performed by densitometric analysis (Multi Gauge ver. 3.0 software; FujiFilm, Tokyo, Japan). GAPDH was chosen as the housekeeping gene, but unfortunately the amount of GAPDH was not kept stable under the influence of US. Therefore, the amount of actin monomers was normalized according to the amount of monomers in the control sample (without US). The experiment was repeated for 5 times (N=5).

Microbubbles addition

It is known from the literature that microbubbles (ultrasound contrast agents) increase low intensity US bioeffects [39]. The US contrast agent Definity™ (Bristol-Myers Squibb Medical Imaging, N. Billerica, MA, USA) comprises from octafluoropropane gas (OFP, C3F8 empirical formula) coated with a flexible lipid shell. OFP is a stable gas that is not metabolized. The phospholipid components of the microsphere are thought to be metabolized to free fatty acids. The encapsulated microbubbles are stable in MI below 0.8 *in vivo*, and in our *in vitro* experiments the MI was no higher than 0.3. According to the manufacturer's description, the mean diameter range of Definity™ microbubbles is 1.1-3.3 μ m, with only 2% of bubbles larger than 10 μ m. Kimmel *et al.* have discovered that a frequency of about 2.7 MHz may be considered as the resonance frequency of the Definity™ cloud [42]. In this research we used 1 MHz frequency because of the transducer features. The microbubble vials were activated by a shaker (VIALMIX Activation Device, USA) and were gently shaken before each trial to assure their even distribution in the liquid before the injection into the cell culture medium. The injection of the microbubbles to the medium was always performed in proximity to the start of the US transmission and the microbubble concentration that was used throughout the experiments was calculated to be about $5 \cdot 10^6$ microspheres/ml. Besides the presence of Definity™, all other setup parameters remained unchanged. The experiment was repeated for 3 times.

Real time phase contrast microscopy of live BAECs under US - A preliminary study

Our goal was to explore the membrane distortions in living cells while assuming that different light refraction happened, hence, change in the illumination of the parts that were subjected to the membrane deformation. Two subsequent experiments were performed. BAECs passage 9 were grown to 60% confluence on 30 mm diameter cover slips (Menzel-Gläser, Germany). In this experiment a different US setup was used which allowed to conduct energy while the cells were under a microscope and image them simultaneously. The cover slips were placed in a polycarbonate chamber that held the cover slip in place and was connected to an US transducer via a water-filled

perspex hose-shaped waveguide (designed by Naila Inataev). The US pulses were sinusoidal waves generated by a Tabor 8024 signal generator and amplified by a 50 dB power amplifier (Fig. 7).

The synchronized triggering of the signal generator and the camera (Lumenera Infinity) was done by an NI acquisition device (USB 6211), which operated according to trigger signals created in a Matlab environment GUI (designed by Omer Naor). The electronic components combined with the chamber and waveguide were calibrated using a HNR-1000 needle hydrophone (ONDA) in order to estimate the pressure amplitude applied to the cells.

Experiment #1: In this experiment, the transducer used was a 3.8 cm diameter, single element transducer with 0.5 MHz central frequency manufactured by Imasonic. The imaging was performed on an inverted microscope (Nikon) using an objective lens with 60X magnification and NA of 0.7 (Fig. 7).

The cells were stimulated with 100 μ sec pulses (amplitudes of 50, 100, 200 and 300 kPa) that were turned on manually every 1 min. The images were manually captured and were analysed using Matlab codes that were written by Michael Plaksin. Binary (black and white) images were produced according to a threshold value and a subtraction of consequent US stimulus images with no-US images was performed. The first experiment purpose was to find out about the pattern of the pixel change and to decide how to efficiently analyse the data.

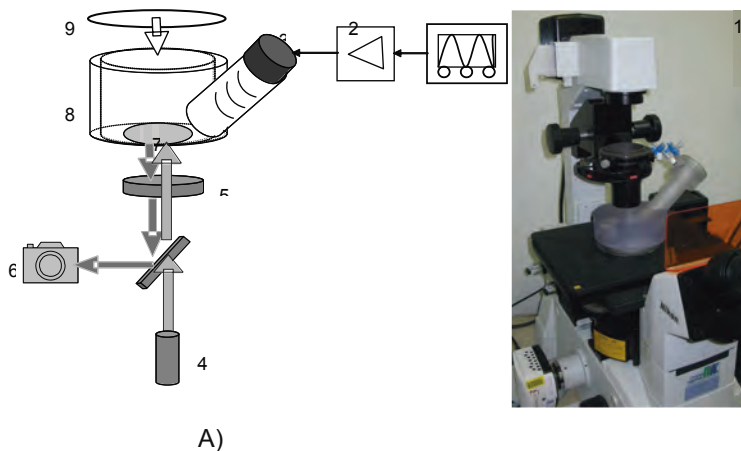


Figure 7 - A schematic diagram of the setup: 1-function generator, 2-power amplifier, 3-US transducer, 4- monochromatic light source, 5-microscope objective, 6-camera recording synchronized with US transmission, 7- irradiated cell monolayer on a cover slip, 8-cell-culture chamber, 9- condenser for white illumination; B) photograph of the cell culture chamber placed on the inverted fluorescent microscope, connected to a CCD camera.

Experiment #2: The cultures and setup were identical to the first experiment, with the exceptions of:

Fluorescent staining: before the placement inside the polycarbonate chamber the cultures were stained with Dil colour (5 µg/ml, Invitrogen) diluted in serum free DMEM medium for half an hour incubation followed by 3 washes with medium for 10 min duration each time in 37°C.

Ultrasound transducer: A more suitable transducer was available (also a single element transducer (Imasonic) of identical diameter and shape) operating at a central frequency of 1 MHz.

After capturing a single fluorescent image of a cell, the illumination was manually switched to white illumination and a sequence of 30 images was automatically captured over 10 seconds. The first 15 images were captured without US transmission (OFF mode), while the last 15 images were captured in synchronization with 100 µsec pulse stimuli (100 cycles in one pulse), with a certain pressure amplitude (ON mode). In this way, transmission of US bursts with amplitudes of 50, 100, 200 and 300 kPa was performed in series, during which images of the same cell were captured.

We were able to calculate the grey level change in each pixel after the US pulse. Briefly the Matlab program took the average of 15 images at each mode (ON or OFF) for reduction of the random noise in each picture. The OFF-mode mean was subtracted from the ON-mode mean yielding the pixel-wise differences between modes, while same-mode means were subtracted from each other as a control. In addition, binary images were produced according to a threshold value (that was easy to be defined due to the fluorescent image), and a subtraction of consequent US stimulus images with no-US images was performed. The later image processing was carried out in order to find whether there was a translocation of the cells or not. The underlying postulation was that if in a certain pixel a change was observed, which was not attributed to a cell movement; it can be attributed to a light refraction change that was caused by membrane deformation.

Statistical analysis

Statistics were performed using Bartlett's test for equal variances. In the case of unequal variances, as was found in our experiments, a Kruskal-Wallis non-parametric test was applied to determine whether there was a significant difference between the values of 3 or more independent groups. If a significant change was found using Kruskal-Wallis test, the Dunn-Sidak multicompare method was used as a post-hoc test to evaluate where the significant differences lie. When the parameters were dependent, a Friedman's test was applied instead of Kruskal-Wallis test. Values are expressed as mean \pm standard error. In all cases, a *p*-value of less than 0.05 was considered statistically significant. All statistical analysis was performed using MATLAB 2007b.

Results

Identification of the US induced flow in our experimental system

Most studies have interpreted the mechanism of low intensity US by the eventuation of streaming and microstreaming, and consequently formation of shear stress in the fluid

above a cell monolayer. In brief, the streaming phenomenon can be described by a steady flow field that carries particles, thus is characterized by advection and streaming velocity; Microstreaming is commonly depicted by tiny whirlpools in the fluid induced by pulsating bubbles (especially next to a wall) under US. If enhanced transport happens, microstreaming may be created. On the assumption that superposition of advection and microstreaming occurs, we performed an analysis where a tracer spreading in the plate under low intensity US was studied in order to calculate the advection index and the stain spreading parameter. It was found that our system was stable and no visual turbulence streaming occurred there. The tracer stain was confined in the water and varied gradually. Note that the stain concentrated mostly at the bottom of the dish, where the ECs were attached. Intriguingly, the advection index in the dish irradiated by US was found to be about $10^{-4} \pm 10^{-6}$ m/s, therefore, the streaming was rather weak in the medium surrounding the cells (Fig. 8). The stain spreading parameter in our system was no higher compared to control ($10^{-7} \pm 10^{-8}$ m²/s, Fig. 9), but it was hard to conclude from this result about enhanced transport due to the crude measurement way. In both graphs, the standard error measurements imply on another interesting phenomenon that might happen in the 100 kPa pressure amplitude. Moreover, earlier set of experiments was conducted with ink solution and the results were very much the same in the sense of a confined stain that expands slowly, although the physical properties of the ink are different from those of the coffee solution (data not shown).

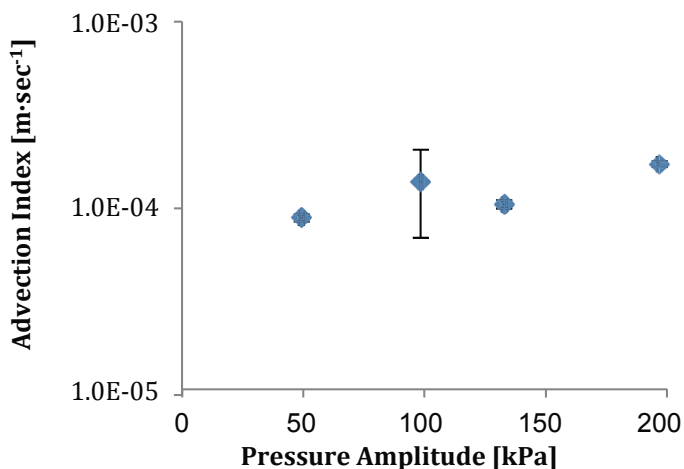


Figure 8 – Advection index vs. various pressure amplitudes.

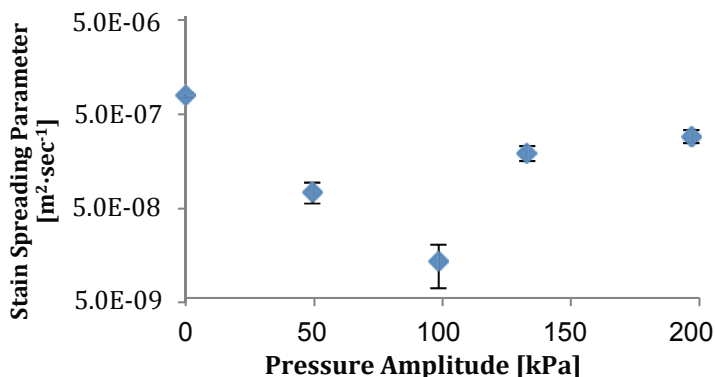


Figure 9 – Stain spreading parameter vs. various pressure amplitudes.

Membrane permeability measurement

The influence of US on membrane integrity in BAECs was examined after the streaming field evaluation was done in the culture dish plate. The cells that adhered to the plate went through a Trypan Blue measurement according to the manufacturer's protocol. The graph below describes the influence of various pressure amplitudes on the percentage of permeable cells that were attached to the plate (Fig. 10).

It can be seen that as the acoustic pressure amplitudes around the cells intensify, the percentage of the permeable cells increases. Following Kruskal-Wallis non-parametric test and Dunn-Sidak multicompare it was found that there was a significant difference (p -value < 0.05) in the percentage of the permeable cells between the 200 and 300 kPa groups to the control, 50 and 100 kPa groups. The 135 kPa group was not significantly different from any group.

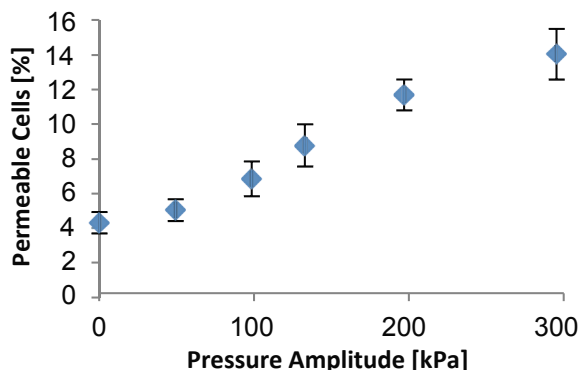


Figure 10 - The percentage of permeable cells vs. various pressure amplitudes.

The results guided us to perform some experiments regarding phenomena that involve the cell membrane, as adhesion and cytoskeleton changes mediated by membrane modification.

The influence of US on integrin activation

Chein *et al.* have discovered that shear stress causes integrin clustering in BAECs [15]. Therefore, it was our attempt to find out if US induces similar mechanical impact on cell adhesion while using the integrin molecules.

In figure 11 in the previous page, the nuclei of the ECs are coloured in blue and the integrin clusters appear as red stains. The pressure amplitudes were between 50-135 kPa.

As described in "*Materials and Methods*" section, we refer to the biological effect of integrin clustering as "integrin activation" and analyse it. Following Kruskal-Wallis non-parametric test, no significant change (p -value < 0.05) was found between the integrin activation of the control group without US, to the US-irradiated groups at 50-135 kPa (Fig 12).

Note that actin fibres were also stained using Phalloidin (Sigma), but due to inadequate staining we did not make a similar analysis on them (data not shown).

Concerning the results at 50-135 kPa pressure amplitudes, and after detection of peculiar staining pattern that appeared at 200 kPa, another set of integrin activation experiments was performed at 200-300 kPa. It is important to mention that it was harder to perform the second set of experiments because in higher pressure amplitudes it was very difficult to find cells in 100× magnification. In fact, we were unable to collect any data at 300 kPa in 100× magnification. As a result, out of 3 experiments that were made, we were able to collect data only on 7 samples at the 250 kPa group.

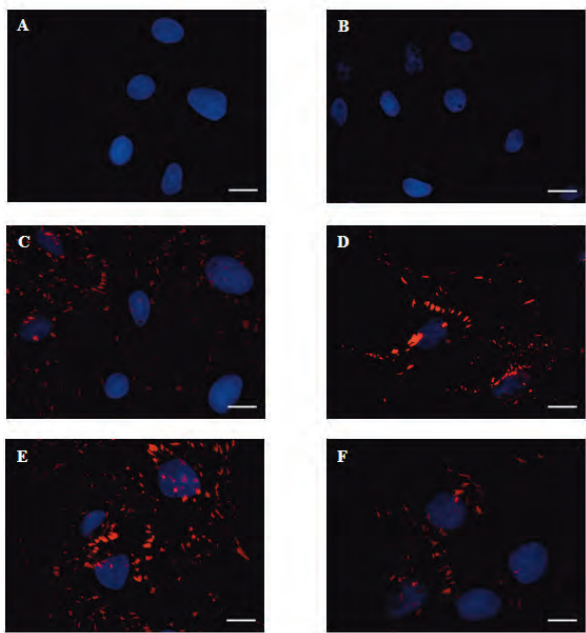


Figure 11 - The influence of US integrin clustering in BAECs at 50-135 kPa pressure amplitudes. A) IgG Control without US; B) IgG Control w US - 50 kPa; C) No US; D) 50 kPa; E) 100 kPa; F) 135 kPa; (X100). The nuclei are coloured in blue (DAPI), and the integrins are stained in red (LM6 antibody). The scale is 10 μ m.

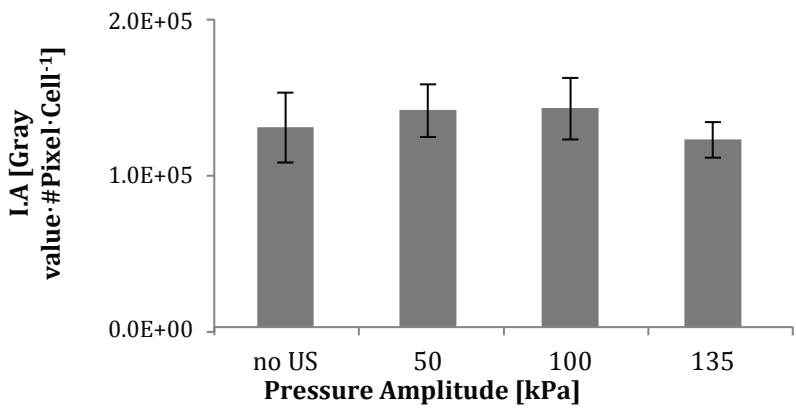


Figure 12 - Integrin activation vs. pressure amplitudes (50-135 kPa).

In the next figure you can see the typical integrin and nuclei staining pattern of BAECs without US treatment. The cell boundaries are outlined in white where it was possible to draw them.

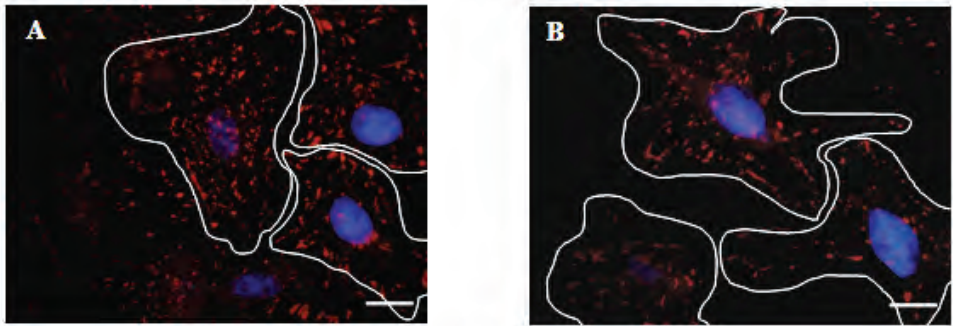


Figure 13 - The influence of no-US treatment on integrin clustering, A-B. The nuclei are coloured in blue (DAPI), and the integrins are stained in red (LM609 antibody). The cell boundaries are marked in white where it was possible to draw them. The scale is 10 μ m.

The figure which describes the 200 kPa treatment is characterized with a unique staining pattern (Fig. 14, A-C), such as smeared stains and less cluster-like stains besides the regular pattern (as in Fig. 14D) that still appeared. Moreover, it was possible to observe places where no integrins were in proximity to the nuclei.

At 250 kPa treatment one can clearly notice the difference in staining as opposed to the control figures: the staining pattern is unusual and even the shape of the nuclei is different. The nuclei were spread uniformly before the US treatment, and after the irradiation there were piles of nuclei and no other nuclei around them (Fig. 15 A-C).

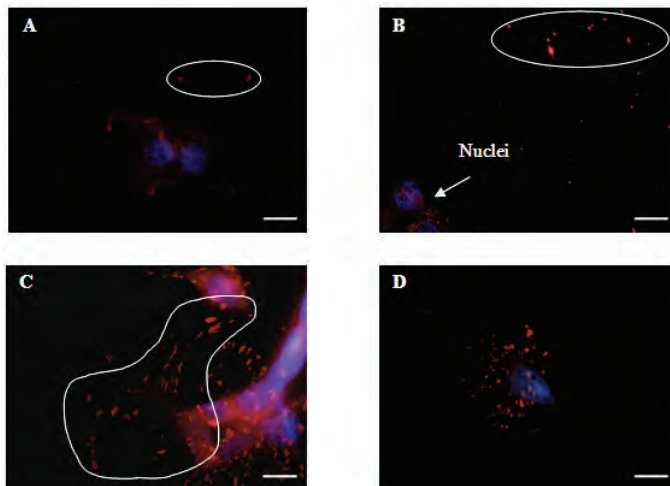


Figure 14 - The influence of 200 kPa pressure amplitude treatment on integrin clustering, A-D. The nuclei are coloured in blue (DAPI), and the integrins are stained in red (LM609 antibody). The scale is 10 μ m. Note that in pictures A-C there are stains of integrins in places where there are no nuclei. The white delineations point to clusters of integrins far from the nuclei.

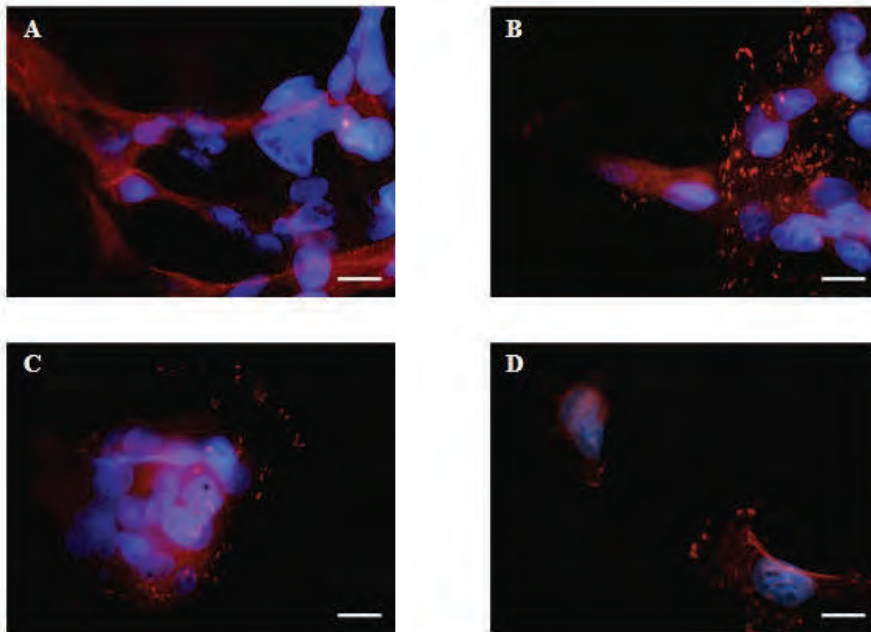


Figure 15 - The influence of 250 kPa pressure amplitude treatment on integrin clustering, A-D. In Fig A there is a smearing of the coloured clustering. Fig B seems to describe an intermediate state – stains and smearing together. In figure C the cells are very condensed while around them there are no cells at all, and it is clear that some of the integrins are not within the cell boundaries. The nuclei are coloured in blue (DAPI), and the integrins are stained in red (LM609 antibody). The scale is 10 μm .

The piles of the nuclei suggest that not only the cells might be pushed because of the US, but also imply on cells that are no longer alive. Apparently, our results indicate that more aggressive effect has happened to the cells in these pressure amplitudes. It is important to mention that the smearing of the $\alpha\text{V}\beta 3$ integrin immunostaining is not a consequence of a background colour and that there were no other nuclei in a different focus level. To explore the effect of US at 300 kPa we had to lower the microscope magnification because cells were not found in 100 \times magnification. Thus, all the samples were rechecked in lower magnification. In the pictures without US there was an equal distribution of the nuclei (Fig. 16). Figure 17 describes the unique pattern of spreading of nuclei that can appear following US treatment. This topic will be discussed at length in the “*Discussion*” section.

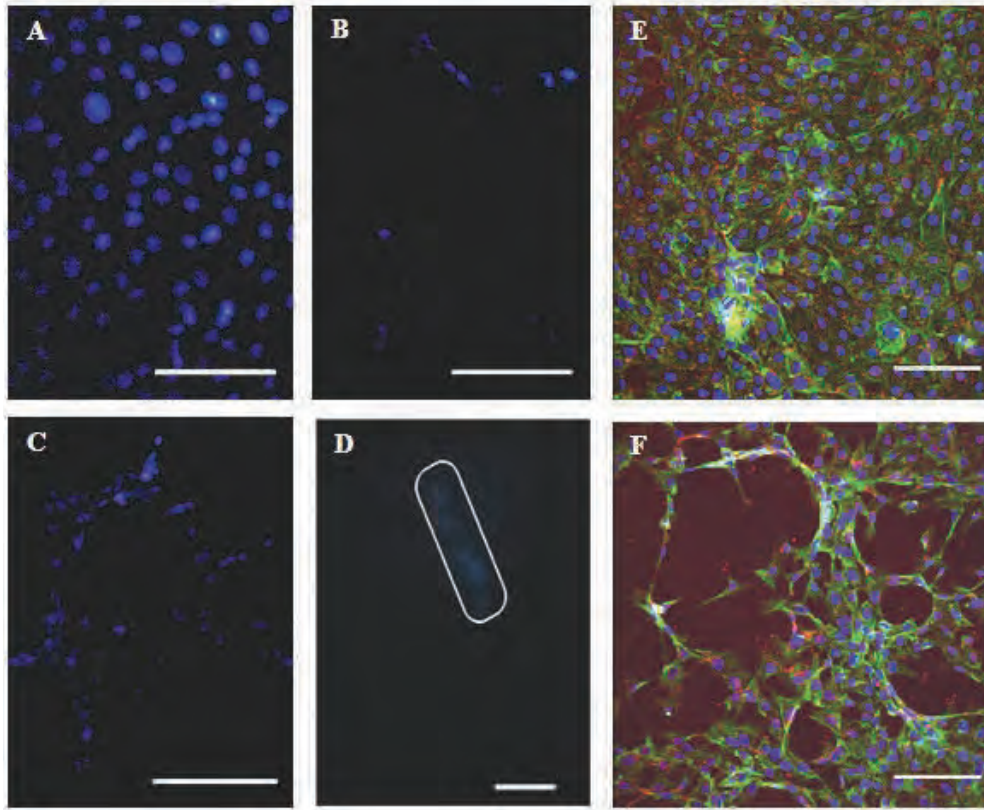


Figure 16 - Different US pressure amplitudes influence on spreading of nuclei (lower magnification pictures). The nuclei are coloured in blue (DAPI), integrin clusters appear as red dots (LM609 antibody) and actin fibres are in green (Phalloidin). A) nuclei in un-treated cells; B) 200 kPa; C) 250 kPa (20 \times); D) 300 kPa (10 \times). In picture D there is a barely-noticed blue smear which indicates on nuclei, with no other nuclei around it. In addition, this picture was taken in a higher exposure rate. E) nuclei in un-treated cells; F) 50 kPa (Confocal figures, 25 \times). The scale is 100 μ m.

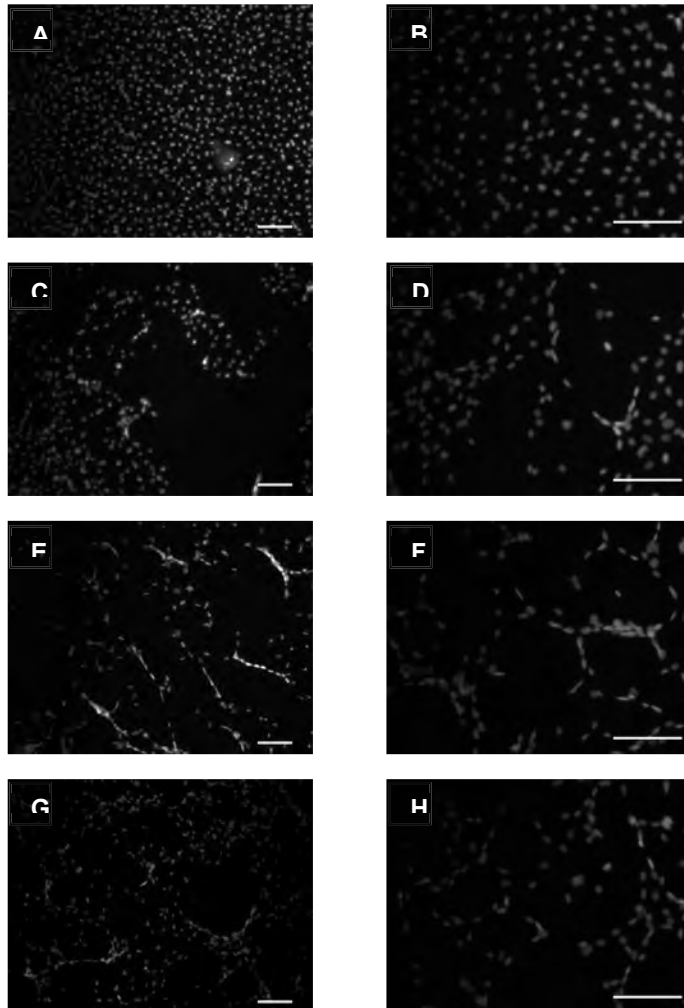


Figure 17 - Different textures of spreading of nuclei following US treatments. A-B) nuclei in untreated cells; C-D) 50 kPa; E-F) 100 kPa; G-H) 135 kPa. Pictures A,C,E,G are in 10× magnification and pictures B,D,F,H are in 20× magnification. The scale is 100 μ m.

The new results from the 200-300 kPa treatments illuminate in a different way the results from the integrin clustering experiment after acoustic irradiation of 50-135 kPa. Even though the cells were spread equally on the cover slips before the US irradiation, they were no longer found in equal distribution on the cover slips after the treatment with higher intensities. Possibly many cells were torn off at 200 and 250 kPa. At 300 kPa you can barely see a blue smearing of DNA in 10× magnification and in a higher exposure rate in the microscope. Following that, another test was performed in which it

was discovered that under 300 kPa, the detaching percentage of the cells was 70% (significance was found from 8 repetitions, p -value < 0.05 , data not shown). The results of integrin activation at 200-250 kPa were quantified as before. It came out that there was a significant difference (p -value < 0.05 in a non parametric Kruskal-Wallis test followed by Dunn-Sidak multicompare) between the 200 kPa treatment and the control group, and also between 200 and 250 kPa groups. There was no significant difference between the 250 kPa treatment and the control group without US (Fig. 18). However, the cell pulling out shows that the measurement way of integrin activation is inappropriate in this case as will be explained later.

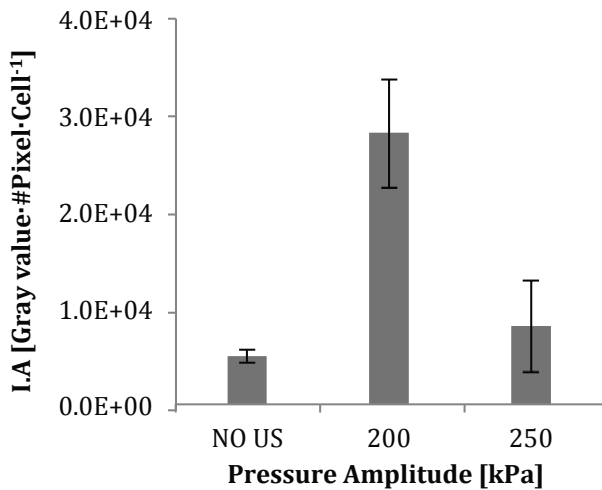


Figure 18 - Integrin activation vs. pressure amplitudes (200-250 kPa).

The influence of US on the expression of β -actin monomers

If indeed the cells reorganized the cytoskeleton and strengthened the actin fibres at the focal adhesion points in response to US irradiation, it should result in more expression of β -actin monomers; but according to Friedman non-parametric test, no significant change (p -value < 0.05) was found in the quantitative measurements between the amount of β -actin monomers in the control group without US, to the US-irradiated groups at 50 and 200 kPa (Fig. 19).

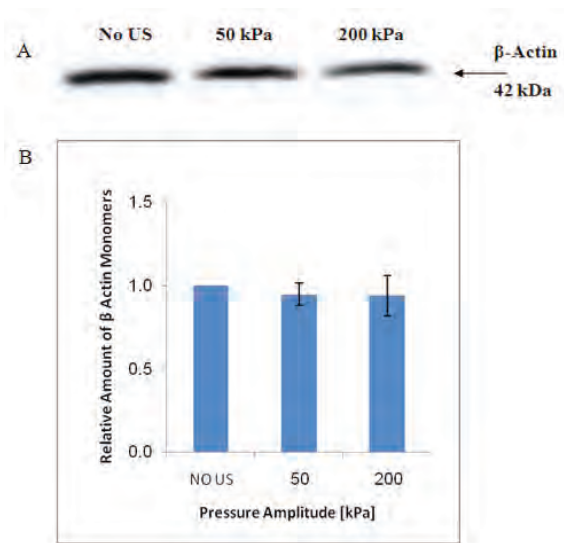


Figure 19 - Expression of β -actin monomers. A) BAECs were irradiated at 50 and 200 kPa and lysate samples were subjected to immunoblotting with anti- β -actin antibody. B) The amount of actin monomers was normalized according to the amount of monomers in the control sample (without US).

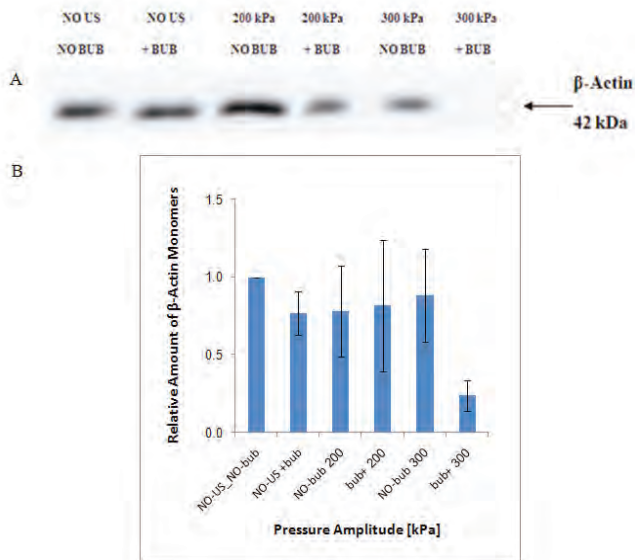


Figure 20 - Expression of β -actin monomers with US contrast agents. A) BAECs were irradiated under 200 and 300 kPa with or without microbubbles (US contrast agents), and lysate samples were subjected to immunoblotting with anti- β -actin antibody. B) The amount of actin monomers was normalized according to the amount of monomers in the control sample (without US).

The influence of US on the expression of β -Actin monomers - higher-pressure amplitudes

Since we did not notice any clear influence of US on the amount of β -actin monomers in lower pressure amplitudes, we made the western experiments in higher-pressure amplitudes in order to observe an obvious impact. Consequently, US contrast agents were added to the medium to amplify the US effect, and their independent influence, without the US, was also studied on the cells in our system.

Following Friedman non-parametric test, no significant difference (p -value < 0.05) was found in the amount of β -actin monomers due to the US treatments (Fig. 20).

Any independent influence of the US contrast agents on the β -actin monomers was not shown. Moreover, there was a great dispersion of the results that might derive from several biological phenomena that happen in the cells (see "Discussion").

Real time phase contrast microscopy of live BAECs under US – A preliminary study

Next, we examined the membrane deformation of BAECs by tracing after light refraction changes in the pictures as a result of the US pulses that the cells received.

Figure 21 describes the results from the first experiment (as described in the "Materials and Methods" section). One can see from the figures below that the control images (Fig 21, A-B) show similar pattern of random noise ("flickering dots"). In figure 21C, on the other hand, there is an obvious different pattern – there are more clusters of black and white pixels, implying that some cell translocation changes occurred after US transmission (according to the image processing: white colour implies where there was a cell and black colour implies where there is a cell now). The non-automatic way of capturing images that we used at the first stage did not allow us to average the images, therefore there was more noise. Also, it was impossible to know the cell contour. An improved experiment was performed after significant drawing conclusions. On the second and improved experiment, membrane deformation was evaluated by the automated switch between OFF and ON modes, combined with the increased frame rate, allowed a short recording period during which cell movement was rarely observed and images could be averaged. Thus, a major problem that arose in the previous experiment was eliminated. The fluorescent labelling enabled to determine the threshold value, in order to get a clearer description of the cell contour (see Fig. 22B), again successfully solving a main challenge from the previous experiment. Unfortunately, a clearer pattern was not observed after the mean images' subtraction, but rather a random pattern which did not lend itself to a straight-forward interpretation.

Discussion

The present study concerns with effect of low intensity US *in vitro* on mechanical related processes in the cell such as membrane permeability enhancement, functioning of adhesion molecules, expression of actin and cytoskeleton organization, and cell detachment from a surface. In the long run, the idea is to identify those processes in

order to allow controlled mechanical loading of US on cells and tissues for therapeutic use.

Identification of the US induced flow in our experimental system

No significant difference was found between the value of the advection index (U) and the stain spreading parameter (D) in the various pressure amplitudes of US versus the control. The advection index is indicative of the organized velocity field of the liquid while the stain spreading parameter is indicative of random mixing streams. The small magnitude of both parameters (D and U) indicates that the motion of the fluid in the plate is very slow (Figs. 8 and 9). The fact that the stain spreading parameter did not increase due to the US irradiation might suggest that the vortex velocities did not increase. Nonetheless, we cannot ignore the high calculation errors arising from the crude way of measurement. Even if we have noticed the appearance of some surface waves and jets that were formed in acoustic pressure amplitude of 200 kPa in the interface, the bulk of the water stayed almost static. A crude estimation of the shear stress that acts on the plate as a result of the measured streaming velocity, assuming linear velocity profile in the boundary layer is about 10^{-4} Pa. Regarding streaming, note that the reflection from the air-water interface generates standing waves that may reduce the streaming velocity. This result points that at the bottom of the plate, where the ECs are located in our experimental system, there is a zone of almost "standing" water and that US does not induce on the ECs any considerable shear stress compared to the flow related shear-stress that is typical in the range of 0.01 to 1 Pa, that can be found in the cardiovascular system [32]. If shear stress related streaming does not explain the observed bioeffects on the ECs in our experimental setup, what are the other mechanisms by which US influences ECs in our system? Cavitation is well known to be associated with ultrasonic energy, and to play a major role in many of the biological changes that have been induced by US applied *in vitro*.

Direct measurement of cavitation was not performed in our system, however, it can be said that the indirect measurements of microstreaming showed that at up to 300 kPa there was no mixing and probably no significant influence of cavitation. The answer to this question may rely on the new theory that has been developed in our lab recently – the "BLS" theory [31]. Our proposed model describes the cell membrane as an oscillating bubble that vibrates due to the sound wave. The bubble expands as a result of pressure below 1 atmosphere (negative pressure) and expands again with pressure acceleration. Under negative pressure, a critical tension is reached where various phenomena can occur: from membrane reversibly wounding, to broadening the two phospholipid layers in a way that irreversibly damage proteins and perforate the cell membrane. As the theory been developed, the results of this thesis were explained according to it.

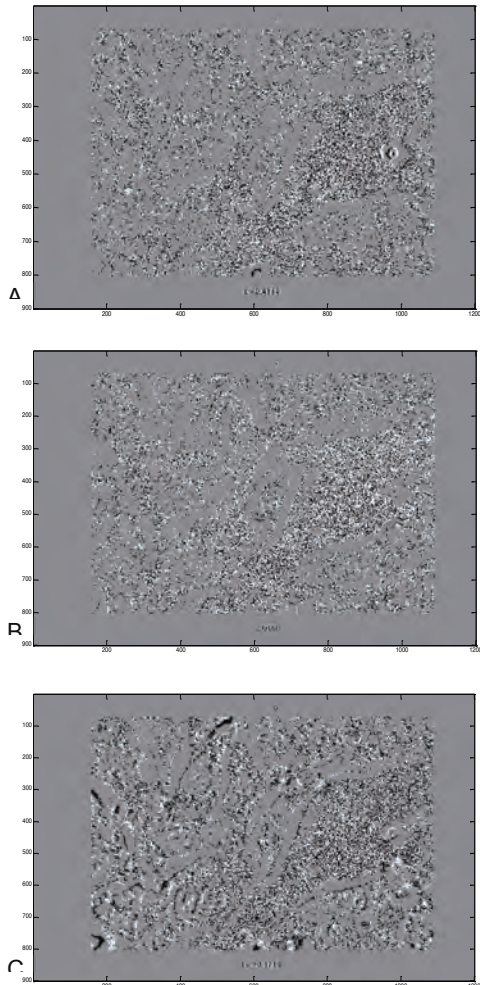


Figure 21 - Real-time microscopy – first experiment. Subtraction of consequent A) no-US images; B) US stimulus images; C) US stimulus image with no-US image. White colour implies where there was a cell; Black colour implies where there is a cell now; and grey colour implies where there was no change in cell movement.

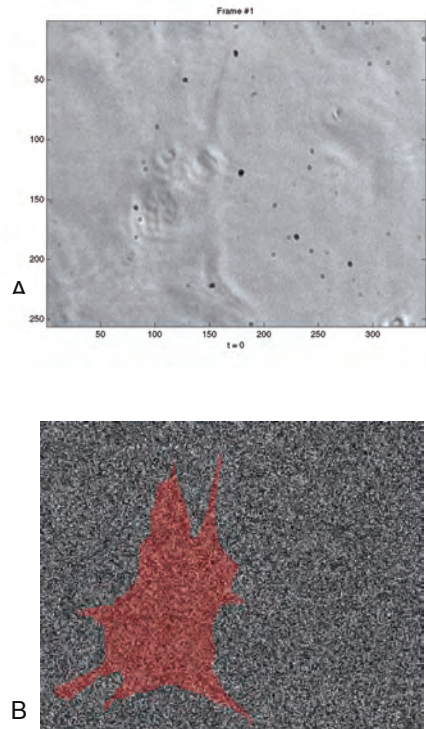


Figure 22 - Real-time microscopy – second experiment. An image of a cell (about $10 \mu\text{m}$ length) that received a pulse of 50 kPa pressure amplitude; B) Merging of a fluorescent image of the cell from picture A with a processed image of the illumination changes after applying the US pulse ("processed" = where a subtraction of two mean bright-field pictures was made).

US significantly increases membrane permeability of ECs

The results reveal that after 200 kPa treatment there is a significant increase in the percentage of the Trypan Blue permeable cells that are attached to the plate, which imply on increase in the permeability of the cell membrane (Fig. 10). This outcome suggests that the effect of US irradiation on ECs involves an influence on the cell membrane, and supports the notion that US might affect the membrane according to the "BLS" theory.

The influence of US on integrin activation

Little is known about how cells perceive mechanical forces and convert them into biochemical responses [4]. Since many signal-transducing molecules concentrate in the FA complex that interconnects the cytoskeleton to integrins and ECM, it is very likely that integrins and the FAs may represent a major site of integration of mechanotransduction processes [41, 42]. Indeed, it has already been discovered that shear stress can activate integrin clustering [12]. During the effort to resolve and study whether US also urges clustering of integrins, and following that urges their activation in ECs or not, it was found that the cells were torn off from the surface plate at pressure amplitudes of 50-300 kPa. Unexpectedly, the effect of US on ECs monolayer was quite drastic, contrary to previous knowledge that the cells should not get hurt after US irradiation in the mentioned pressure amplitudes of our system. The inconsistency arose because vitality examinations, such as proliferation and apoptosis, that were held before (also in our lab) [35, 38], did not diagnose any severe cell damage. The difference in the results came from the fact that in the previous studies, the vitality tests were carried out 24-48 hours after the cell irradiation and not right after the treatment (as in this study). Apparently, the cells that were not torn off the surface, continued to proliferate as before. The integrins are the cell surface linkers (= adhesion molecules), so it is possible that even though the cell loses its function or is completely exploded, the integrins can still attach to the surface, thus they were shown in the immunostaining pictures and were considered in the counting. Clusters of nuclei stayed adhered to the cover slips too. Nevertheless, it appears that due to membrane damage and accelerated death at US pressure amplitudes above 200 kPa, there was some protein damage which appeared as integrin immunostaining different from control (even though they stayed attached to surface). It is therefore implied that we might have overestimated integrin activation by counting integrins that were attached to the cover slip without actually belong to a cell. On the other hand, we might have overestimated the number of cells by counting also dead cells and thereby reducing the number of integrins per cell. Another source of error could be that not only clear stains of integrin clusters were counted but also stains of smeared integrin contents were measured. Therefore, it was erroneously found that at 200 kPa US induces integrin activation. The results indicate that the assessment of integrin activation was inadequate, even for the lower pressure amplitudes (the same effect might happened there too, only in a small magnitude). In the conditions which the experiment was taken care of, apparently it was hard to separate between examination of the integrin activation and the cell rupture by US. Thus, at the moment, there is a problem to conclude about the influence of US on cell adhesion, and in future experiments the cells should be kept attached to the plate

the entire experiment. The results integrate with a new research that has been published recently by researches from Atlanta [43]. The researches performed a flow cytometry experiment where a large distribution of biological phenomena was discovered in cells right after they went through an US treatment: about 1/6 of cells had reversible membrane wounding shown by calcein uptake, about 1/3 was apparently unaffected and about 1/2 was nonviable. The results of this article further support our assumption that two processes occurred at the same time: on one hand, the mechanical effect of membrane oscillations (as a bubble) because the acoustic pressure, and change in membrane tension which translate the mechanical signal to movement of integrins on the membrane and their activation (the integrins can also be stretched). The integrin cluster activation then leads to cell signalling processes that occur together with cytoskeleton change. On the other hand, the bilayer membrane of the cells and the nuclei is perforated in such a severe way that the cell content (DNA and cytoplasm) is spilt outside the cells. This harsh effect of rupturing can also cause damage to the membrane proteins (such as integrins) and affect their functioning.

The influence of US on the expression of β -actin monomers

Enhanced expression of β -actin was not observed in US treated BAECs. Supplementation of US contrast agents to intensify the supposed effect did not contribute to its appearance either. A large distribution of the results appeared because of several biological phenomena that happened together: in agreement with the integrin experiment conclusions, even if there was a reorganization and strengthening of the cytoskeleton following integrin activation and more actin monomers were created [14], which should cause to increase in the expression of β -actin monomers, since the actin is soluble in water it can easily leak outside the damaged cell membrane and then the amount of actin would decrease. If indeed a discrepancy of the results appeared in the pressure amplitudes that were used, lower pressure amplitudes should be used for next experiments.

Real time phase contrast microscopy of live BAECs under US – A preliminary study

This preliminary study was held in order to get a clue about the type of *in vitro* experiments that should be done in order to prove the novel BLS theory, by examining the membrane contour on the assumption that any change that occurred was not a result of spontaneous cell movement, but because of membrane swelling that changed the light refraction in the picture. During the experiment planning we encountered few obstacles such as:

1. The membrane change phenomenon was expected to be smaller than the optical resolution: the change should be smaller than 100 nm while the resolution (Δl)

is $\Delta l = 0.61 \frac{\lambda}{NA}$ at best (according to the “Rayleigh” criterion). Given that the shortest

wavelength of visible light is blue ($\lambda=450$ nm), the resolution limit of a light microscope using visible light is about 400 nm, so it was impossible to visualize the distance between the membrane layers.

2. The optical magnification size was limited to 60× because of the setup restrictions. Together with the digital resolution of the camera, the result was that one pixel equals a $430 \times 430 \text{ nm}^2$. Thus, the scale of the anticipated phenomenon was much smaller than the size of a single pixel, further worsening the situation.

3. The random noise in a single picture hampers the image processing, while the alternative possibility of averaging several images resulted in smeared images.

The increase in measurement efficiency in the second stage of the experiment showed that Fig. 21C was actually misleading, as only random changes were observed between images of stimulated or un-stimulated cells (see Fig. 22B). It is possible that the change that was observed in Fig. 21C was a result of the slower image capturing (1 fps instead of 3 fps in the second experiment).

We expected to see some sort of ordered pattern of change in the pixels, but observed only a random difference pattern, which does not exclude the possibility that a change in the membrane geometry occurred. It is mentioned in the literature that the averaged distance between two proteins in the bilayer membrane is about 53 nm [44], so we can assume that this can be the diameter of the swelling "hill" that develops due to the acoustic oscillations. If the pixel length is about 400 nm, we can easily assume that entire membrane curvature can be in one pixel. Nothing can guaranty that in two neighbouring pixels the light refraction caused by the hills they contain would be the same. It is also possible that every pixel includes several hills or parts of them that refract the light differently, causing a sort of random pattern as in figure 22B.

Collectively, our results indicate that the imaging concept in this experiment could not help us differentiate between membrane deformation that was caused by radiation pressure or because of membrane oscillations according to the BLS theory. We could not prove that something happened at all after a single pulse of US. It is possible that after a few US pulses there is no accumulated effect in the cell, and we need at least a couple of cells next to each other (maybe the interaction between the cells can preserve the effect a little longer), under longer acoustic irradiation duration to observe the effect with our equipment.

As this research has progressed, it was clarified that there is still a long way in proving the mechanism of US in the "nano level", yet, it can be negate in a more confident way the identical influence of shear stress and low intensity US on ECs. US induces tension membrane that may be higher than physiological values. Under negative pressure, the membrane oscillates, curves and stretched, which causes eventually to higher tension that develops, and when the membrane reaches to maximum area strain – an irreversible damage occurs.

All in all, we suggest based on the BLS model that US, like shear stress, increases the tension in the bilayer membrane. However, the US intensities that were tested by us caused more damage to the tested ECs compared to the effects induced by physiological shear stress. In an earlier study that was done in the lab (Mizrahi *et al.*), the acoustic pressure was about 10 kPa while our lowest acoustic pressure was 50 kPa

It is important to note that the effect of elapsed time is not clear at all. The BLS model is about periodic loading of the membrane and the cell in the US frequency. To the best of our knowledge, no study exists for periodic mechanical loading of biological substance in such high frequencies. Different fatigue and plastic responses are expected if we implement different treatment durations with US. Perhaps in a shorter treatment we would not pass the membrane tension threshold, even in the same frequency and intensity. In addition, based on the BLS model we speculate that the cells themselves may be envisioned from outside as gas bubbles, whereas a gas bilayer encloses a fluid core. Under acoustic pressure the cells tend to cluster like bubbles do (many studies demonstrated the interconnections between bubbles [45]), and this may explain the clusters of nuclei in figures 16 and 17.

As pulsating bubbles, the cell outer leaflets of the bilayer membrane expand under US and push the neighbouring cells when in a packed confluence. This expansion and "pushing", and the subsequent stretching and moving of the neighbouring cells occur when the cells are loosely connected to the surface. We expect that the weakly connected cells will be the first to respond. They will move, turn and stretched at an intermediate stage and then finally will detach from the surface, leaving the cells that are still attached to the surface stretched around. Figure 17 shows this phenomenon: so the cells try to resist the pulling out forces that have been developed in their near environment; They activate their adhesion mechanism, but some of the cells might lose their grip in the surface due to membrane oscillations, and that can lead to cell detachment. On top of that, while some of the cells are half loosened, they can push other cells that are still attached to the surface but are compliant and pressed against each other. Their shape changes – they become more stretched. Then the loosened cells completely detach, and that what explains the nuclei pictures after US irradiation in 20X magnification! There was no accumulated effect in the membrane itself, but we have discovered that there is a clue for an accumulated effect in the cell monolayer.

Conclusions

Application of US as a targeted therapeutic tool requires a greater understanding of the mechanisms by which US interacts with tissues. The aim of this project was to evaluate the influence of low intensity US (50-300 kPa, 1 MHz) on cultured ECs whereas both cavitation and heating effects are negligible. In absence of streaming related shear stress on the ECs' surface, it seems that the results can be explained only by the effects of the acoustic pressure pulse on the bilayer membrane expansion and increase in tension as described in the BLS theory. All in all, we intended to study in this research the effect of low intensity US on ECs adhered to a plastic dish. However, it turned out that in order to avoid detachment of the cells from the surface and rupture of the adhesion molecules one has to apply much lower US intensities. We therefore recommend using US pressure amplitude of less than 50 kPa for further study of cultured ECs in a similar setup. Perhaps the unique organization and spontaneous response to the artificial mechanical loading of US irradiation is typical to ECs that have become loosely connected to the surface, and will be different in other kinds of cells. Synthetic liposomes in a suspension can be examined as well, where there are no integrins, but strain on the wall can be found.

In addition, it seems that valuable data can be derived from a different setup where the cells are either adhered to a much more flexible surface or grown within viscoelastic scaffold. Cells in living tissues might preserve the periodic US effects through irreversible/plastic response. Using TEM microscopy e.g. in this case may allow characterize phenomena in the nanometric range.

References

1. Dalecki, D., *Mechanical bioeffects of ultrasound*. Annu Rev Biomed Eng, 2004. **6**: p. 229-48.
2. Kimmel, E., *Cavitation bioeffects*. Crit Rev Biomed Eng, 2006. **34**(2): p. 105-61.
3. Wells, P.N.T., *Biomedical Ultrasonics*. London: Academic Press, 1977.
4. Chien, S., *Mechanotransduction and endothelial cell homeostasis: the wisdom of the cell*. Am J Physiol Heart Circ Physiol, 2007. **292**(3): p. H1209-24.
5. Alberts, B., *Molecular biology of the cell*. 4th ed. Garland Science, 2002.
6. Tsuruta, D. et al., *Microfilament-dependent movement of the beta3 integrin subunit within focal contacts of endothelial cells*. Faseb J, 2002. **16**(8): p. 866-8.
7. Goldsmith, H.L. and V.T. Turitto, *Rheological aspects of thrombosis and haemostasis: basic principles and applications. ICTH-Report--Subcommittee on Rheology of the International Committee on Thrombosis and Haemostasis*. Thromb Haemost, 1986. **55**(3): p. 415-35.
8. Tsuruta, D. and J.C. Jones, *The vimentin cytoskeleton regulates focal contact size and adhesion of endothelial cells subjected to shear stress*. J Cell Sci, 2003. **116**(Pt 24): p. 4977-84.
9. Brakebusch, C. and R. Fassler, *The integrin-actin connection, an eternal love affair*. Embo J, 2003. **22**(10): p. 2324-33.
10. Hynes, R.O., *A reevaluation of integrins as regulators of angiogenesis*. Nat Med, 2002. **8**(9): p. 918-21.
11. Mitra, S.K., D.A. Hanson, and D.D. Schlaepfer, *Focal adhesion kinase: in command and control of cell motility*. Nat Rev Mol Cell Biol, 2005. **6**(1): p. 56-68.
12. Wang, Y. et al., *Interplay between integrins and FLK-1 in shear stress-induced signaling*. Am J Physiol Cell Physiol, 2002. **283**(5): p. C1540-7.
13. Jalali, S. et al., *Integrin-mediated mechanotransduction requires its dynamic interaction with specific extracellular matrix (ECM) ligands*. Proc Natl Acad Sci U S A, 2001. **98**(3): p. 1042-6.
14. Bassell, G.J. et al., *Sorting of beta-actin mRNA and protein to neurites and growth cones in culture*. J Neurosci, 1998. **18**(1): p. 251-65.
15. Nyborg W. L., C.P.L., Miller M.W., Dunn F., Ziskin M.C., Miller D.L., Carstenen E.L., Thopson H.E., *Biological effects of ultrasound: Mechanics and clinical application*. NCRP Report, 1983. **74**.
16. Davidovits, D., *Physics in biology and medicine*. Englewood Cliffs, New Jersey: Prentice-Hall Inc, 1975.
17. ter Haar, G. and J.W. Hand, *Heating techniques in hyperthermia. III. Ultrasound*. Br J Radiol, 1981. **54**(642): p. 459-66.
18. Fahy, F., *Foundations of engineering acoustics*. San Diego, Calif.: Academic Press, 2001.
19. L. E. Kinsler, A.R.F., *Fundamentals of acoustics*. 2nd ed. New York: John Wiley & Sons, Inc, 1962.
20. Dyson, M., B. Woodward, and J.B. Pond, *Flow of red blood cells stopped by ultrasound*. Nature, 1971. **232**(5312): p. 572-3.
21. ter Haar, G., M. Dyson, and S.P. Smith, *Ultrastructural changes in the mouse uterus brought about by ultrasonic irradiation at therapeutic intensities in standing wave fields*. Ultrasound Med Biol, 1979. **5**(2): p. 167-79.
22. Dayton, P. et al., *Acoustic radiation force in vivo: a mechanism to assist targeting of microbubbles*. Ultrasound Med Biol, 1999. **25**(8): p. 1195-201.

23. Robert Phillips, G.H., *Guidance for industry and FDA staff - Information for manufacturers seeking marketing clearance of diagnostic ultrasound systems and transducers*, F.U.F.A.D. Administration, Editor. 2008.
24. Williams, A.R., *Absence of meaningful thresholds for bioeffect studies on cell suspensions in vitro*. Br J Cancer Suppl, 1982. **5**: p. 192-5.
25. Leighton, T.G., *The Acoustic Bubble*. Academic Press, 1994.
26. Krasovitski, B. and E. Kimmel, *Shear stress induced by a gas bubble pulsating in an ultrasonic field near a wall*. IEEE Trans Ultrason Ferroelectr Freq Control, 2004. **51**(8): p. 973-9.
27. Nyborg, W.L., *Physical mechanisms for biological effects of ultrasound*. Washington DC: US DHEW, 1977. 78-8062.
28. Marmottant, P. and S. Hilgenfeldt, *Controlled vesicle deformation and lysis by single oscillating bubbles*. Nature, 2003. **423**(6936): p. 153-6.
29. Flynn, H.G., *Generation of transient cavities in liquids by microsecond pulses of ultrasound*. J Acoust Soc Am, 1982. **72**(6): p. 1926-1932.
30. Vogel, A. et al., *Mechanism of action, scope of the damage and reduction of side effects in intraocular Nd:YAG laser surgery*. Fortschr Ophthalmol, 1990. **87**(6): p. 675-87.
31. Krasovitski, B. et al., *Intramembrane cavitation as a unifying mechanism for ultrasound-induced bioeffects*. Proceedings of the National Academy of Sciences of the United States of America, 2011. **108**(8): 3258-3263.
32. VanBavel, E., *Effects of shear stress on endothelial cells: possible relevance for ultrasound applications*. Prog Biophys Mol Biol, 2007. **93**(1-3): p. 374-83.
33. Harrison, D.G. et al., *Endothelial mechanotransduction, nitric oxide and vascular inflammation*. J Intern Med, 2006. **259**(4): p. 351-63.
34. Fisher, A.B. et al., *Endothelial cellular response to altered shear stress*. Am J Physiol Lung Cell Mol Physiol, 2001. **281**(3): p. L529-33.
35. Raz D., Z.U., Einav S., Elad D., *Cellular alterations in cultured endothelial cells under therapeutic ultrasound irradiation*, in *ISMBE conference*. 2004.
36. Barzelai, S. et al., *Low-intensity ultrasound induces angiogenesis in rat hind-limb ischemia*. Ultrasound Med Biol, 2006. **32**(1): p. 139-45.
37. Young, S.R. and M. Dyson, *The effect of therapeutic ultrasound on angiogenesis*. Ultrasound Med Biol, 1990. **16**(3): p. 261-9.
38. Mizrahi, N., D. Seliktar, and E. Kimmel, *Ultrasound-induced angiogenic response in endothelial cells*. Ultrasound Med Biol, 2007. **33**(11): p. 1818-29.
39. Duvshani-Eshet, M. et al., *Therapeutic ultrasound-mediated DNA to cell and nucleus: bioeffects revealed by confocal and atomic force microscopy*. Gene Ther, 2006. **13**(2): p. 163-72.
40. Kimmel, E. et al., *Subharmonic response of encapsulated microbubbles: conditions for existence and amplification*. Ultrasound Med Biol, 2007. **33**(11): p. 1767-76.
41. Ingber, D.E., *Tensegrity: the architectural basis of cellular mechanotransduction*. Annu Rev Physiol, 1997. **59**: p. 575-99.
42. Radcliff, C. and V. Rizzo, *Integrin mechanotransduction stimulates caveolin-1 phosphorylation and recruitment of Csk to mediate actin reorganization*. Am J Physiol Heart Circ Physiol, 2005. **288**(2): p. H936-45.
43. Schlicher, R.K. et al., *Changes in cell morphology due to plasma membrane wounding by acoustic cavitation*. Ultrasound Med Biol. **36**(4): p. 677-92.
44. Pralle, A., *Physical properties of the plasma membrane studied by local probe techniques*, in *Dissertation an der Fakultät für Physik*. 1999, Ludwig-Maximilians-Universität: München. p. 138.
45. Xiaoyu Zheng, R.E.A., *Acoustic interaction forces between two fluid spheres in an acoustic field*. J. Acoust. Soc. Am., 1995. **97**(4): 2218-2226.

11

Flow cytometric characterization and sorting of ultrasound contrast agents

Maja Mujić¹, Spiros Kotopoulos^{2,3},
Anthony Delalande^{1,3}, Marianne Enger¹,
Odd Helge Gilja^{1,2}, Emmet Mc Cormack¹,
Michiel Postema³, Bjørn Tore Gjertsen^{1,4}

¹Institute of Medicine, Hematology Section, University of Bergen, Bergen, Norway,

²National Centre for Ultrasound in Gastroenterology, Haukeland University Hospital,
Bergen, Norway,

³Department of Physics and Technology, University of Bergen, Norway,

⁴Department of Internal Medicine, Hematology Section, Haukeland University Hospital,
Bergen, Norway

Abstract

Ultrasound contrast agents consist of microscopically small gas bubbles encapsulated by elastic shells, and are regularly employed in ultrasound blood pool perfusion diagnostics and currently explored as drug delivery vehicles. Successful development of functional ultrasound contrast imaging demands precise and effective microbubble evaluation techniques. We have examined flow cytometry as a method for *in vitro* quantification, optical characterization and sorting of microbubbles with flexible lipid shell or albumin shell. Flow cytometry provided reproducible side and forward scatter analysis and quantification of gas filled microbubbles enumeration, at various pressure levels and fluid flow speeds. Quantification allowed determination of the static microbubble stability, indicating increased stability at 4°C compared with storage at ambient temperature. Flow cytometry allowed detection of microbubbles in mixture with cell lines or whole blood *ex vivo*. Furthermore, flow cytometry analysis permitted microbubble sorting by size or fluorescence, allowing evaluation of isolated

microbubble populations. We anticipate that flow cytometry will be a reliable technology for analysis of novel modified microbubbles for use in clinical ultrasonography.

Introduction

Ultrasonography is a cost-effective and safe clinical imaging modality [1]. Blood perfusion imaging is desirable in human diagnostics, but blood is a poor ultrasonic scatterer. Hence, ultrasound contrast agents have been added to the blood pool to increase the signal-to-noise ratio [2,3]. These ultrasound contrast agents consist of liquids containing encapsulated microbubbles. Upon sonication these microbubbles undergo volumetric oscillations [4] resulting in a detectable acoustic signal. Potential therapeutic applications of ultrasound contrast agents include ultrasound guided sonothrombolysis [5], molecular imaging [6,7], and drug and gene delivery [8-14].

The microbubble oscillations create a transient permeabilization of cell membranes enhancing drug uptake [15]. This microbubble-induced permeabilization may be the consequence of pore formation in the cell membrane [16-19], thus leading to targeted delivery of therapeutic agents [11,20].

Recently we have found that fluorescence-labelled microbubbles can be forced/pushed into cancerous cells using clinical diagnostic settings allowing the delivery of a therapeutic payload [19]. This delivery is primarily dependant on the acoustic conditions the microbubble size distribution and shell composition. Thus, using microbubbles loaded with specific agents could enhance the release of the therapeutic agent at a desired location.

In all applications of clinical ultrasound it is critical to select microbubbles with specific sizes or composition [21]. Current sizing methods include Coulter counting, zeta sizing and optical microscopy, although none of these methods allow for microbubble sorting. Current size sorting methods include filtration and using microfluidics chambers, whilst atomic force microscopy can be used to characterize the microbubble shell properties [22]. None of these methods allow for real time multi-parameter sizing and sorting, and have limitations for use in medium or high throughput chemical screens of microbubble shell modification. For further development of therapeutic and diagnostic ultrasound contrast agents, there is a need for a reliable methodology to size, select and sort microbubbles. Here, we present data that suggest that both low threshold and state-of-the-art flow cytometry instrumentation represent versatile and simple technology platforms for future development of ultrasound contrast agents.

Flow cytometry is a well-established method used in clinical practice and biomedical research to characterize cells [23,24]. We hypothesize that flow cytometry can be used to non-destructively size, select and sort ultrasound contrast agent microbubbles in real-time.

Materials and methods

Cell lines and whole blood

Human acute myeloid leukaemia cell lines NB4 and HL-60 were purchased from Deutsche Sammlung von Mikroorganismen und Zellkulturen GmbH (Braunschweig, Germany). MOLM-13 and MV4-11 cell lines were purchased from ATCC subsidiary LGC Standards AB (Borås, Sweden). NB5, HL-60 and MOLM-13 were cultured in RPMI-1640 medium (Sigma, St. Louis, MO) with 10% FBS, 2 mM L-glutamine and Penicillin (50 U mL⁻¹)/Streptomycin (50 U mL⁻¹) (Gibco, Grand Island, NY). The MV4-11 cell line cultured in IMDM (BioWhittaker, Cambrex Bio Science, Verviers, Belgium) with 10% FBS, L-glutamine and Penicillin/Streptomycin. Human whole blood samples were collected from healthy volunteers.

Microscopy

A TE2000 fluorescence microscope (Nikon Corporation, Tokyo, Japan) was used with Hoffman modulation contrast for microscopy of microbubbles. The microbubbles were placed on an object slide and imaged at room temperature using a 40×/0.55 HMC LWD air objective. For detection of DiI fluorescence a Leica TCS SP2 AOBS inverted confocal microscope (Leica Microsystems, Heidelberg, Germany), with a 63×/1.40 HCX PL Apo oil objective and a Helium/Neon I, 1-mW / 543-nm laser was used. A Zeiss LSM 510 META (Carl Zeiss Microscopy AG, Oberkochen, Germany) with a 63×/1.40 Plan-Apochromat oil objective and a Helium/Neon II, 5-mW / 633-nm laser was used to detect DiD fluorescence.

Flow cytometry

Five different flow cytometers were used to analyse the SonoVue® ultrasound contrast agent (Bracco Diagnostics Inc., Milano, Italy): a FACSCalibur using a 12-60 µL/min flow rate at 31 kPa, a FACS Aria cell sorter (Becton Dickinson Immunocytometry Systems, San Jose, CA) using a 12-48 µL/min flow rate at 138 kPa, a Cytomics FC 500 (Beckman Coulter Inc., Fullerton, CA) using a 12-60 µL/min flow rate at 207 kPa, an Accuri (Accuri Cytometers, Inc., Ann Arbor, MI) using a 14-66 µL/min flow rate and a non-pressurized system, and a Guava® easyCyte™ 6-2L Base System (Merck Millipore Billerica, MA) using a 60 µL/min flow rate at 55 kPa. In our experiments 2×10⁴ microbubbles were analysed for each measurement. FlowJo software version 8.8.6 and 7.6.3 (Tree Star Inc., Ashland, OR) were used to analyze the flow cytometry data.

Microbubble static stability determination

The microbubble static stability was determined by measuring the microbubble concentration using flow cytometry. To determine the microbubble concentration 100 µL of a size and concentration standard (10µm diameter, 1×10⁶ fluorospheres/mL) (Flow-Count fluorospheres, Beckman Coulter Inc., Fullerton, CA) were added to 25 µL of each microbubble sample. The concentration of microbubbles was determined using:

$$MC = (\Sigma_{MB}/\Sigma_{FS}) \times FC, \quad (1)$$

where MC is the microbubble concentration, Σ_{MB} is the sum of microbubbles counted, Σ_{FS} is the sum of fluorospheres counted and FC is the fluorospheres concentration. Before flow cytometric analysis, microbubbles were counted using a Bürker cell counting chamber (Hawksley, Lancing, United Kingdom). The microbubble stability was measured at stepped time intervals during storage at room temperature (20°C) or at 4°C for 96 hours.

Detection of microbubbles in cell lines and whole blood

A volume of 0.5, 1, 10 or 50 μL of microbubbles at a concentration of 0.3×10^6 microbubbles/ μL was added to 50 μL of either HL-60, NB4, MOLM-13 or MV4-11 cells ($5 \times 10^6/\text{mL}$) and analyzed using the FACSCalibur flow cytometer. In addition 0.1–50 μL of microbubbles (0.3×10^6 microbubbles/ μL) were added to 500 μL whole blood and analyzed by FACSCalibur.

Flow cytometric analysis of SonoVue® and Quantison™ ultrasound contrast agents

The Accuri flow cytometer was used to analyse SonoVue® (Bracco Diagnostics Inc) and Quantison™ (Upperton Limited, Nottingham, UK) ultrasound contrast agents; both individually and in mixture. In addition to the 10- μm size standard a drop of 5.1 μm (5.0–5.9 μm) SPHERO™ COMPTrol Goat anti-Mouse Ig blank (Spherotec Inc., Lake Forest, Illinois) standard particles were used to evaluate the size of SonoVue®.

Fluorescent labeling of microbubbles

To create fluorescent microbubbles, the lipophilic probes DiI ($\lambda_{\text{ex}}=549 \text{ nm}$, $\lambda_{\text{em}}=565 \text{ nm}$) and DiD ($\lambda_{\text{ex}}=644 \text{ nm}$, $\lambda_{\text{em}}=665 \text{ nm}$) (Vybrant™ Molecular Probes, Invitrogen, San Diego CA) were added at different concentrations (0.2–12.5 μM) to microbubbles. The same concentrations of DiI were added to NaCl in control experiments.

Fluorescence-activated cell sorting and isolation of microbubbles

The FACS Aria cell sorter was used to sort two populations of microbubbles based on their size and fluorescence. For size sorting small and large microbubbles were gated on the FSC-SSC plot. For fluorescence measurements the microbubbles were labelled with DiI or DiD. The system was kept at 4°C at all times to increase the stability of microbubbles. After sorting, both populations were analysed by microscopy and flow cytometry to evaluate the microbubbles presence, the size of the sorted microbubbles, and their fluorescence. Before sorting, microbubble labelling was confirmed by confocal microscopy. A final concentration of 6.25 μM of DiI or DiD was added to microbubbles and sorted using the FACS Aria flow cytometer. The fluorescent positive and negative populations were collected after sorting. BD FACSDiva™ software (Becton Dickinson Immunocytometry Systems) was used to draw gates for sorting of microbubbles.

Size distribution, acoustic activity and stability of sorted microbubbles

To measure the microbubble size distribution and to verify if the SonoVue® microbubbles were still acoustically active after sorting, the sorted microbubbles were inserted into an OptiCell® cell culture chamber (Nunc GmbH & Co. KG, Langenselbold,

Germany) filled with 10 mL of 0.9% saline solution. The OptiCell® was placed in the xy stage of a TS100 Eclipse inverted microscope (Nikon Corporation, Shinjuku, Tokyo, Japan) and the microbubbles were observed through a 20×/0.40 and 40×/0.55 (Nikon Corporation) objectives. The color charge coupled device (CCD) of a Photron FastCam MC-2.1 high-speed camera (VKT Video Kommunikation GmbH, Pfullingen, Germany) was connected to the microscope via the c-mount and used to capture still images of the sorted microbubbles. The captured images were size calibrated using a Bürker haemocytometer. The acoustic activity and stability of the microbubbles under sonication was checked before and after sorting inside an OptiCell®. To check if the microbubbles were acoustically active a VScan clinical ultrasound scanner (General Electric Healthcare, Fairfield, CT) was used as the ultrasound source. Eco Supergel ultrasound gel (Ceracarta, Forli, Italy) was used to create an acoustic path from the transducer to the OptiCell®. The scanner pointed at the microscope objective and was placed at an elevation angle of 45° and an azimuth of 90°. In all recordings the direction of the sound field is from far right to far left of the frame. The scanner was set at a Mechanical Index of 1.2 and a Thermal Index of 0.4 with colour Doppler activated to allow for the highest possible duty cycle. The acoustic microbubble attraction was monitored using the high-speed camera at 1000 frames per second (25). To measure the size distribution a total of 1328 microbubbles were measured using ImageJ v1.440 (National Institutes of Health, Bethesda, MD).

Statistical analysis

In all figures values are presented as mean \pm SEM. Data was compared using an unpaired, two-tailed Student *t*-test. The difference between two samples was considered statistically significant when *p*-value was lower than 0.05. Analyses were performed using GraphPad® Prism 5.0 (GraphPad Software, La Jolla, CA).

Results

Flow cytometry analysis of gas filled microbubbles

To investigate if gas filled microbubbles could be detected by flow cytometry, microbubbles were analysed on multiple flow cytometers of various specifications. Optical microscopy showed microbubble size distribution within the expected size range of 1-10 μm (Fig. 1A). The flow cytometry data showed a specific serpentine pattern on five different flow cytometers when examined for forward and side light scatter (Fig. 1B–F). The serpentine distribution was reproducible independent of the flow cytometer, the fluidic pressure and flow rate (Fig. 1 B–F).

Temperature dependent microbubble stability

The microbubble concentration is proportional to the stability (Fig. 2), thus minimal decay in concentration indicates higher stability. The microbubbles showed equal stability over two hours independent of storage conditions. From 6 to 96 hours when storing at room temperature, the microbubble concentration decreased by a factor of 7 (from 1.84×10^8 microbubbles/mL to 2.7×10^7 microbubbles/mL). In contrast, when

storing at 4°C, the microbubble concentration was much more stable for up to 48 hours, and a slow decay was seen up to 96 hours (from 2.15×10^8 microbubbles/mL after 6 hours to 1.39×10^8 microbubbles/mL after 96 hours). The microbubble stability at 4°C was statistically significantly higher when compared to that at room temperature from 24 hours onwards (2.06×10^8 microbubbles/mL versus 1.18×10^8 microbubbles/mL, p -value: 0.032).

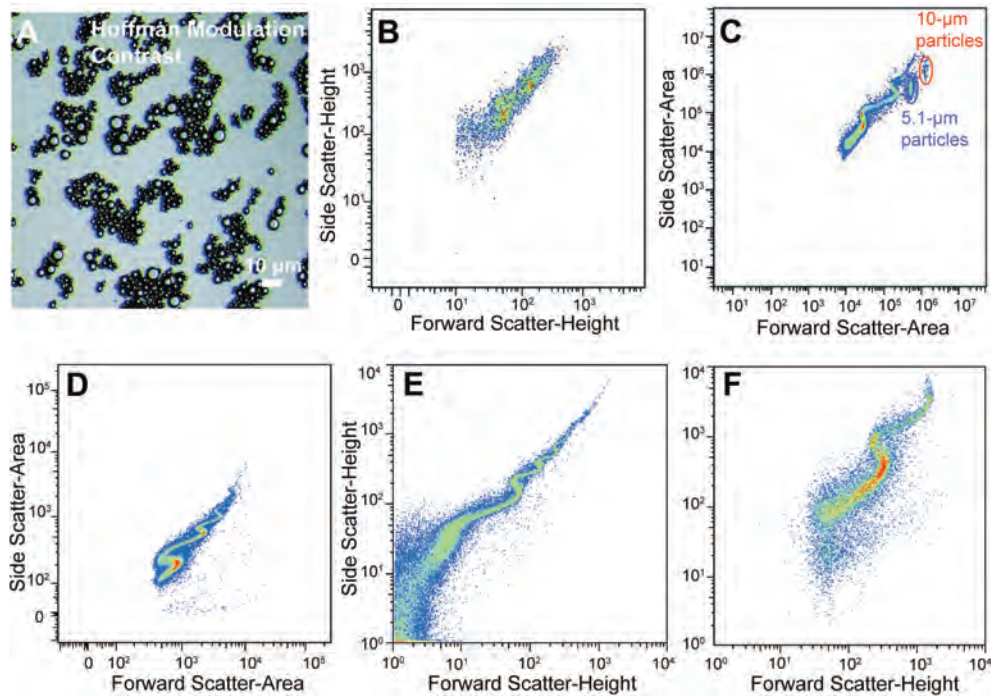


Figure 1 - Micrographs and flow cytometric plots of gas filled soft shell microbubbles. (A) Hoffman Modulation contrast (40x HMC LWD air objective) was used for microscopy of microbubbles. Microbubbles (SonoVue®) vary in size between 1-10 µm. Scale bar, 10 µm. (B) Flow cytometric analysis of microbubbles using a low-pressure fluidic system, Guava, n=1. (C) Flow cytometric analysis of microbubbles with a 10 µm and 5.1 µm standard using a flow cytometers with a low-pressure fluidic system (Accuri), n=10. (D) Flow cytometric analysis of microbubbles using a pressurized system, FACS Aria cell sorter, n=10; (E) FACS Calibur, n=10; (F) Cytomics FC 500, n=2.

Comparing flow cytometry and haemocytometer based concentration measurements of microbubbles, the flow cytometer measured 7% less microbubbles/mL than optical microscopy (3.03×10^8 microbubbles/mL versus 3.28×10^8 microbubbles/mL respectively).

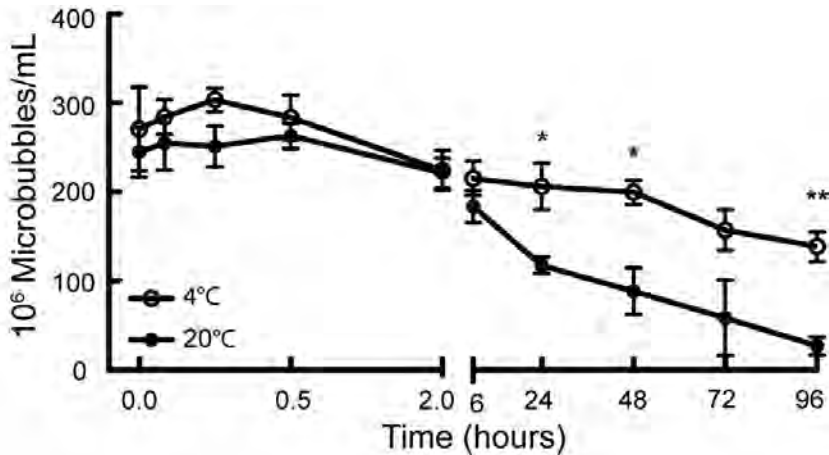


Figure 2- Temperature dependent stability of gas filled microbubbles. The number of microbubbles was determined using the 10 μm size and concentration bead standard. Analyses were done using FACSCalibur. The effect of the two storage conditions; room temperature and 4 °C was determined at selected time points up to 96 hours, $n=3$. The p value at 24 hours is $p=0.0323$, at 48 hours is $p=0.0197$, at 96 hours is $p=0.0045$. Data are compared using an unpaired, two-tailed Student t test.

Detection of microbubbles in cell lines and whole blood

Differentiating microbubbles within a cell mixture could help validate microbubble cell interactions. This could help improve ultrasound-guided drug delivery. We were able to detect microbubbles in mixture with four different human cell lines, illustrated here by HL-60 acute myeloid leukaemia cells (Fig. 3A). The serpentine shape did not change when microbubbles were mixed with cells. The microbubbles and the cells could be clearly distinguished. Furthermore, we tested if microbubbles were distinguishable in whole blood (Figs. 3B and 3C), a much more complex fluid with multiple cell populations. It was possible to detect the microbubbles at concentrations down to 1:1000 microbubbles to whole blood. The microbubble were stable for up to 60 min in whole blood independent of concentration (Fig. 3D).

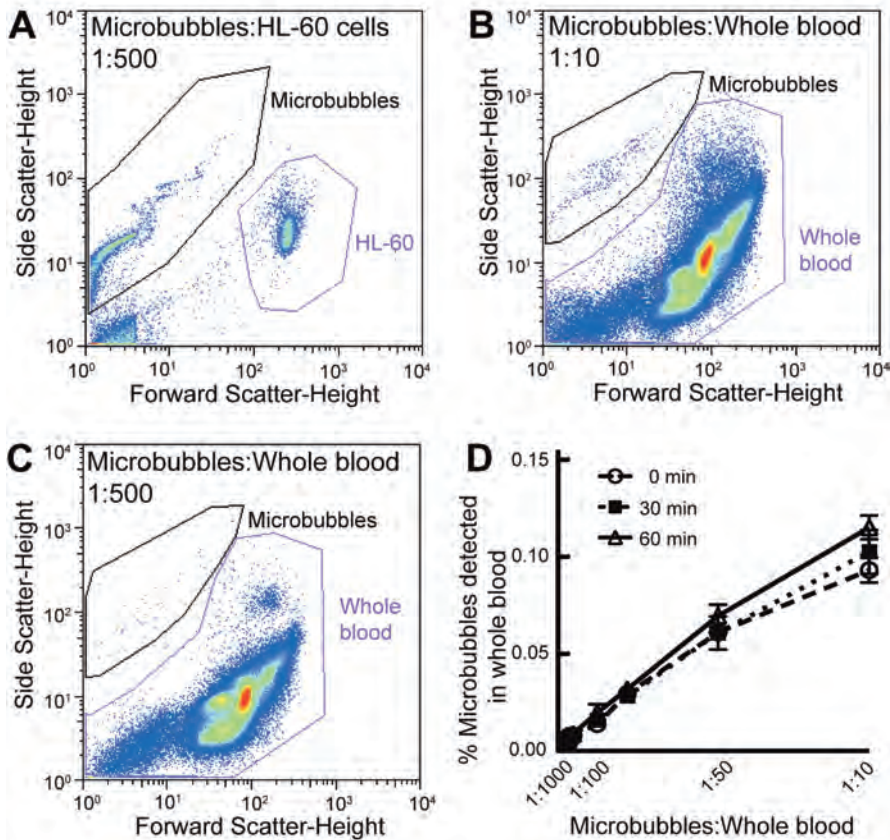


Figure 3 - Discrimination of Microbubbles from mixtures in human cell lines and whole blood. (A) Flow cytometric analysis showing microbubbles and the HL-60 leukemic cell line. Similar data was obtained with other human cell lines (microbubble volume : cells volume, 1 : 500, n=3). (B) Flow cytometric analysis of microbubbles and whole blood, microbubble volume : whole blood volume - 1 : 10, n=3; (C) 1 : 500, n=3. (D) Per cent (%) detectable microbubbles in whole blood is indicated at 0, 30 and 60 min, n=3.

Flow cytometric comparison of lipid-shelled (SonoVue®) and albumin-shelled (Quantison™) ultrasound contrast agents

Flow cytometry analysis of the albumin-shelled microbubbles was also possible under the same parameters (Fig. 4A). The scatter pattern was different compared to lipid-shelled ultrasound contrast agent (SonoVue®). The characteristic serpentine shape observed in the lipid-shelled microbubbles was not found in the albumin-shelled microbubbles. In a mixture containing both ultrasound contrast agents, we were able to

distinguish the respective agents (Fig. 4B). This indicates that microbubbles with different shell materials and thus properties could be characterized using flow cytometry

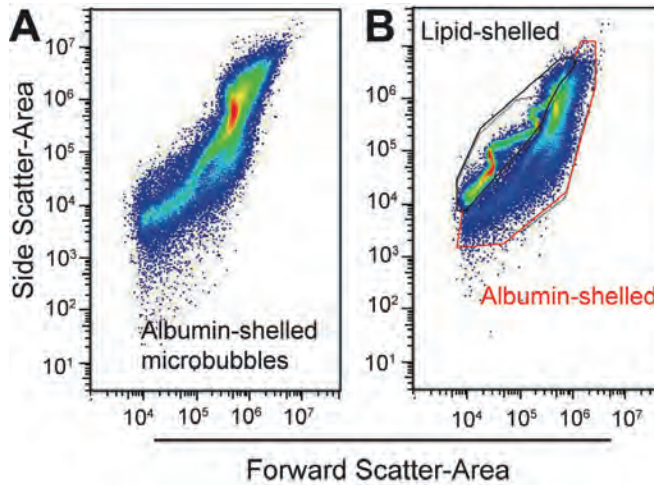


Figure 4 - Flow cytometric analysis of gas filled lipid and albumin microbubbles. (A) Flow cytometric analysis of albumin (Quantison™) microbubbles. (B) Flow cytometry analysis of combined lipid microbubbles and albumin microbubbles.

Fluorescence-activated cell sorting and isolation of intact microbubbles

Sorting of microbubbles based on size is useful as small diameter microbubbles with a narrow size distribution have the ability to pass through small capillaries [27], and be used to improve harmonic imaging [21,26]. The unsorted microbubbles showed a Gaussian type distribution with a mean diameter of $3.49 \pm 2.05 \mu\text{m}$ (Fig. 5A). The small-sorted microbubbles also showed a Gaussian distribution with a mean diameter of $2.82 \pm 0.77 \mu\text{m}$ (Fig. 5B). The mean diameter of the large-sorted microbubbles was $5.96 \pm 2.54 \mu\text{m}$, the histogram indicated two peaks, one at $8.3 \mu\text{m}$ containing large microbubbles, and one at $3.0 \mu\text{m}$ containing smaller microbubbles (Fig. 5C). The size distribution parameters of the three populations clearly demonstrate that smaller bubbles had a narrow size distribution and could be easily separated whilst the larger population contained a large amount of smaller bubble contaminants (Fig. 5D). Both populations were seen to still be acoustically active after sorting. The physical properties of intact microbubbles were tested after sorting by acoustic attraction (Fig. 5E). The sorted microbubbles were attracted to each other and coalesce (fuse into one entity) after 235 milliseconds of low energy ultrasound indicating they are still acoustically active and oscillating in phase, similarly to unsorted microbubbles prepared freshly (data not shown). Confocal microscopy confirmed DiI and DiD labelling on the lipid shell of the microbubbles (Fig. 6A and 6C respectively). An increase in mean fluorescence intensity was observed with increasing concentration of the fluorescent

dye as illustrated by DiI (Fig. 6B). The highest fluorescence intensity was obtained at an optimal dye concentration of 6.25 μM , with only a small difference in fluorescence compared to 12.5 μM . Additionally, the mean fluorescence intensity increased over time and incubation of microbubbles with DiI for 90 min resulted in the highest mean fluorescence intensity for the various concentrations of the dye. Fluorescence-based sorting could be used to select labelled microbubbles for use in ultrasound-assisted drug delivery or in molecular imaging. Sorting of microbubbles resulted in a significant increase in the amount of fluorescently labelled microbubbles after sorting (Fig. 6D; from 9.9% before to 65.6% after). The population that was sorted for non-fluorescent microbubbles contained only 5.3% DiD positive microbubbles confirming successful sorting of fluorescence-labelled microbubbles.

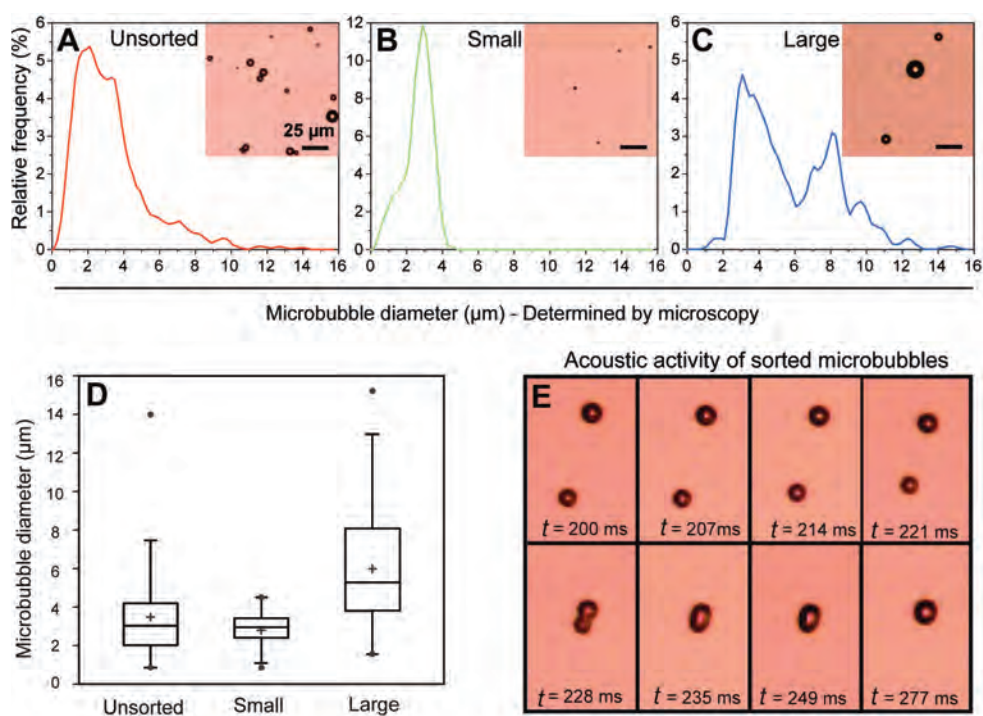


Figure 5 - Flow cytometry assisted particle sorting of microbubbles based on size and fluorescence. (a) Two populations of microbubbles were discriminated based on size and sorted using FACSaria cell sorter. (A) Bright field micrograph and a 5-step average smoothed histogram for the sorted microbubbles before sorting; (B) Small microbubbles after sorting; (C) Large microbubbles after sorting. (D) Box plot describing microbubble size distribution before and after size sorting. Cross: mean, Box centre line: median, Box bottom line: 1st quartile, Box top line: 3rd quartile, Bottom and top whiskers: 5th-95th percentiles, Dots: minimum and maximum values. (E) Image sequence of large sorted microbubbles under sonication at MI=1.2. Inter-frame time is 7 ms.

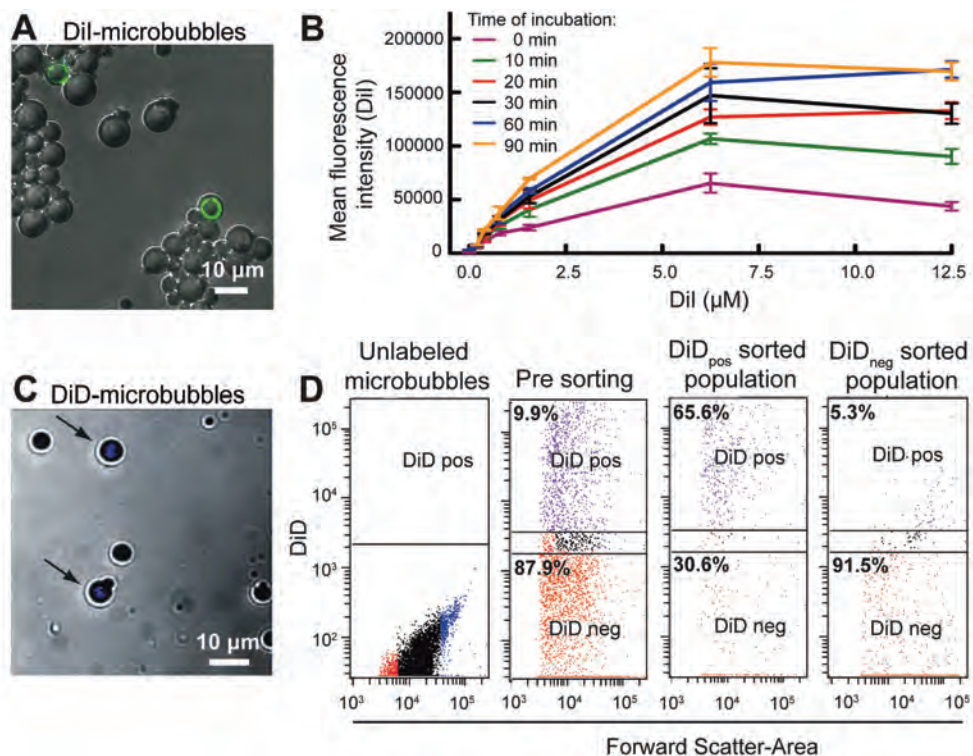


Figure 6 - Screening of fluorescent microbubbles. (A) Confocal microscopy (63 x 1.4 oil) of microbubbles illustrating binding of Dil in the lipid membrane of the microbubbles. Scale bar, 10 μm . (B) Graph of Dil mean fluorescence intensity illustrating various Dil concentrations stained at different time points (0-90 min). (C) Confocal micrograph of DiD labelled microbubbles before sorting (E) Flow cytometric analysis of unlabelled microbubbles; DiD labelled microbubbles before sorting; DiD labelled microbubbles sorted for DiD fluorescence; Sorted for no DiD fluorescence.

Discussion

After testing the lipid-shelled microbubbles in multiple flow cytometers with different flow rates and pressures, we observed a similar serpentine scatter pattern indicating that these parameters do not affect the microbubble analysis. This serpentine pattern was not observed in the albumin-shelled microbubbles (Fig. 4), and allowed a clear distinction between the two types of microbubbles. This could be due to the different shell properties, e.g. heterogeneity in shell composition from microbubble to microbubble. This scatter pattern may correlate to different shell stiffness thus be used to evaluate and optimize custom microbubbles. We conclude that microbubble analysis can be performed using a large variety of flow cytometers.

The characteristic serpentine shape and repeatable relative forward/side scatter location of the microbubbles also allowed for distinction of microbubbles in mixture with cell lines or whole blood (Fig. 3). Flow cytometry enabled rapid and accurate measurements of microbubble concentrations. These were in agreement with other concentration measurement methods. The stability of the microbubbles was greatly improved when storing at 4°C. This could be explained by the lower gas diffusion rate at a lower temperature.

Small microbubbles with a narrow size distribution have the ability to pass capillaries and could be used to improve harmonic imaging [21,26] and to reduce the risk of microbubbles blocking lung capillaries respectively [27]. Particle sorting was used to isolate microbubbles based on particle size or fluorescence emission (Figs. 5 and 6). After sorting, it was seen that the stability of the microbubbles during sonication was decreased indicating that fluorescence-activated sorting alters the microbubble shell. In the control samples microbubbles demonstrated stability for several minutes of sonication, in contrast to sorted microbubbles, which dissolved following less than 10 seconds sonication. The sorted microbubbles demonstrated a higher likelihood of coalescing, indicating a thinner shell that is more susceptible to film drainage [28]. Also, sorting of microbubbles appeared more effective for small bubbles, demonstrating a more uniform size distribution and absence of contamination with large bubbles (Fig. 5 B and C). This contamination may be a consequence of the sorter sensitivity allowing multiple microbubbles per droplet. The droplet formation by the vibrating nozzle could fragment microbubbles. Furthermore the microbubble concentration after sorting was decreased thereby possibly limiting the use of flow cytometry in large scale microbubble sorting. Sorting by size is beneficial as it allows a narrower size distribution at required resonance frequencies.

Fluorescence-based sorting allowed a concentration enhancement of fluorescent microbubbles. Potential uses of this application could be to sort fluorescent drug loaded microbubbles for use in ultrasound-assisted drug delivery and fluorescently labelled functional antibodies attached to microbubbles for use in molecular imaging.

Microbubbles have revolutionized clinical analysis of vascularity and perfusion, and are currently tested as vehicles for drug delivery [12,13]. Our results indicated that flow cytometry is a relatively non-destructive analysis method that can be used to evaluate gas-filled microbubbles. Flow cytometry is an existing technique widely available in research and clinical laboratories and could easily be implemented in current development of functionalized microbubbles for clinical use. We anticipate that flow cytometry can be an important tool to optimize microbubble fabrication for improved contrast-enhanced ultrasonography and microbubble facilitated drug delivery.

Acknowledgments

This study has been supported by the Norwegian Cancer Society, Bergen Research Foundation and the DFG Emmy Noether Programme (grant no. 38355133). The study was supported by MedViz (<http://medviz.uib.no/>), an interdisciplinary research cluster from Haukeland University Hospital, University of Bergen and Christian Michelsen Research AS. We appreciate the expert assistance from Molecular Imaging Centre (MIC) and the core facility for Flow cytometry, University of Bergen.

References

1. *Basic and New Aspects of Gastrointestinal Ultrasonography*, ed. Ødegaard S, Gilja OH, and G. H. Vol. 3. 2005, Singapore: World Scientific. 502.
2. Postema, M. and O.H. Gilja, *Contrast-enhanced and targeted ultrasound*. World J Gastroenterol, 2011. **17**(1): p. 28-41.
3. Postema, M. and O.H. Gilja, *Ultrasound-directed drug delivery*. Curr Pharm Biotechnol, 2007. **8**(6): p. 355-61.
4. Postema, M., *Fundamentals of Medical Ultrasonics* 2011, London: Spon Press.
5. Alexandrov, A.V. et al., *Ultrasound-enhanced systemic thrombolysis for acute ischemic stroke*. N Engl J Med, 2004. **351**(21): p. 2170-8.
6. Klivanov, A.L. et al., *Targeted ultrasound contrast agent for molecular imaging of inflammation in high-shear flow*. Contrast Media Mol Imaging, 2006. **1**(6): p. 259-66.
7. Pysz, M.A. et al., *Antiangiogenic cancer therapy: monitoring with molecular US and a clinically translatable contrast agent (BR55)*. Radiology, 2010. **256**(2): p. 519-27.
8. Dijkmans, P.A. et al., *Microbubbles and ultrasound: from diagnosis to therapy*. Eur J Echocardiogr, 2004. **5**(4): p. 245-56.
9. van Wamel, A. et al., *Vibrating microbubbles poking individual cells: drug transfer into cells via sonoporation*. J Control Release, 2006. **112**(2): p. 149-55.
10. Schneider, M., *Molecular imaging and ultrasound-assisted drug delivery*. J Endourol, 2008. **22**(4): p. 795-802.
11. Klivanov, A.L., *Microbubble contrast agents: targeted ultrasound imaging and ultrasound-assisted drug-delivery applications*. Invest Radiol, 2006. **41**(3): p. 354-62.
12. Bull, J.L., *The application of microbubbles for targeted drug delivery*. Expert Opin Drug Deliv, 2007. **4**(5): p. 475-93.
13. Mitragotri, S., *Healing sound: the use of ultrasound in drug delivery and other therapeutic applications*. Nat Rev Drug Discov, 2005. **4**(3): p. 255-60.
14. Delalande, A. et al., *Ultrasound and microbubble-assisted gene delivery in Achilles tendons: Long lasting gene expression and restoration of fibromodulin KO phenotype*. J Control Release, 2011. **156**(2): p. 223-230.
15. Bao, S., B.D. Thrall, and D.L. Miller, *Transfection of a reporter plasmid into cultured cells by sonoporation in vitro*. Ultrasound Med Biol, 1997. **23**(6): p. 953-9.
16. Prentice P, C.A., Dholakia K, Prausnitz M and Campbell P, *Membrane disruption by optically controlled microbubble cavitation*. Nature Physics, 2005. **1**: p. 107 - 110.
17. Stringham, S.B. et al., *Over-pressure suppresses ultrasonic-induced drug uptake*. Ultrasound Med Biol, 2009. **35**(3): p. 409-15.
18. Schlicher, R.K. et al., *Mechanism of intracellular delivery by acoustic cavitation*. Ultrasound Med Biol, 2006. **32**(6): p. 915-24.

19. Delalande, A. et al., *Sonoporation at a low mechanical index*. Bubble Science, Engineering and Technology, 2011. **3**(1): p. 3-11.
20. Ferrara, K., R. Pollard, and M. Borden, *Ultrasound microbubble contrast agents: fundamentals and application to gene and drug delivery*. Annu Rev Biomed Eng, 2007. **9**: p. 415-47.
21. Gorce, J.M., M. Arditi, and M. Schneider, *Influence of bubble size distribution on the echogenicity of ultrasound contrast agents: a study of SonoVue*. Invest Radiol, 2000. **35**(11): p. 661-71.
22. Sboros, V. et al., *Nanomechanical probing of microbubbles using the atomic force microscope*. Ultrasonics, 2007. **46**(4): p. 349-54.
23. Mittag, A. and A. Tarnok, *Recent advances in cytometry applications: preclinical, clinical, and cell biology*. Methods Cell Biol, 2011. **103**: p. 1-20.
24. Ibrahim, S.F. and G. van den Engh, *Flow cytometry and cell sorting*. Adv Biochem Eng Biotechnol, 2007. **106**: p. 19-39.
25. Kotopoulos, S. and M. Postema, *Microfoam formation in a capillary*. Ultrasonics, 2010. **50**: p. 260-268.
26. Meltzer, R.S. et al., *Pulmonary wedge injections yielding left-sided echocardiographic contrast*. Br Heart J, 1980. **44**(4): p. 390-4.
27. Tranquart, F. et al., *Clinical use of ultrasound tissue harmonic imaging*. Ultrasound Med Biol, 1999. **25**(6): p. 889-94.
28. Postema, M. et al., *Ultrasound-induced microbubble coalescence*. Ultrasound Med Biol, 2004. **30**(10): p. 1337-44.

12

Funding your research from the European Framework Programs for Research and Innovation

Anja Hegen

Adviser for externally financed research, University of Bergen, Anja.Hegen@adm.uib.no

Tips and Links

Where to look in FP7 if you are :

-an **individual** looking for a **thematically open** project:

Marie Curie individual fellowships (IEF, IOF)¹, ERC Starting and Advanced Grants²

-a **group** looking for **thematically open** projects:

Marie Curie Initial Training Network (ITN¹, PhD education), Marie Curie IRSES¹ Staff exchange (with countries outside of Europe), Marie Curie Industry-Academia partnerships and pathways (IAPP)¹, ERC synergy grant², FET open (only in the areas of Information and Communication Technologies³ and Energy (please consult the latest work program) in FP7)

-a **group** with a **research focus**:

Thematical programs in the **cooperation⁴ program**, for example Nanotechnologies (NMP) or Health. Click on the link above and chose your program of interest from the menu on the right hand side.

Please be aware that the LAST round of FP7 calls will be published in July 2012 with deadlines in autumn 2012/winter/spring 2013. The budget will be the highest ever.

Useful links:

The FP 7 Cordis⁵ site will bring you to a description of the different programs, allow you to do a search for projects⁶ and register as an expert

¹ http://cordis.europa.eu/fp7/mariecurieactions/home_en.html

² <http://erc.europa.eu/funding-and-grants>

³ http://cordis.europa.eu/fp7/ict/fet-open/home_en.html

⁴ http://cordis.europa.eu/fp7/cooperation/home_en.html

⁵ http://cordis.europa.eu/fp7/home_en.html

⁶ http://cordis.europa.eu/fp7/projects_en.html

FP7 participant portal⁷: will bring you to the calls and their documents and allow you to negotiate and report on projects

European Research Area ERA⁸

Outlook Horizon 2020 (FP8) 2014-2020:

The ERC and Marie Curie programs will continue (although maybe in a modified form), FET will most likely expand into other areas as well, thematical programs will be reorganised but continue. Link⁹ to Horizon 2020 (FP8) official site.

Where to get more information:

At your Universities/Research Institutes EU office

UK Research Office (UKRO)¹⁰: well-structured information on the ERC and Marie Curie programs, accessible for everyone.

KoWi (German FP7 info-site) offers news in English¹¹. You can choose your topics of interest.

Swiss Core: sends an easy to read newsletter (Swiss Core synopsis¹²) on the newest developments in Brussels.

⁷ <http://ec.europa.eu/research/participants/portal/page/home>

⁸ http://ec.europa.eu/research/era/index_en.htm

⁹ http://ec.europa.eu/research/horizon2020/index_en.cfm

¹⁰ <http://www.ukro.ac.uk/Pages/UKRO.aspx>

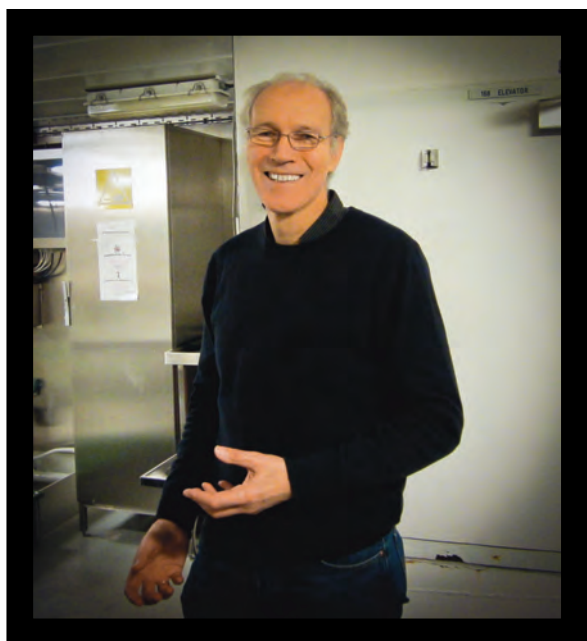
¹¹ <http://www.kowi.de/en/desktopdefault.aspx/tabid-111/>

¹² <http://www.swisscore.org/E/newsletter/Pages/synopsis.aspx>

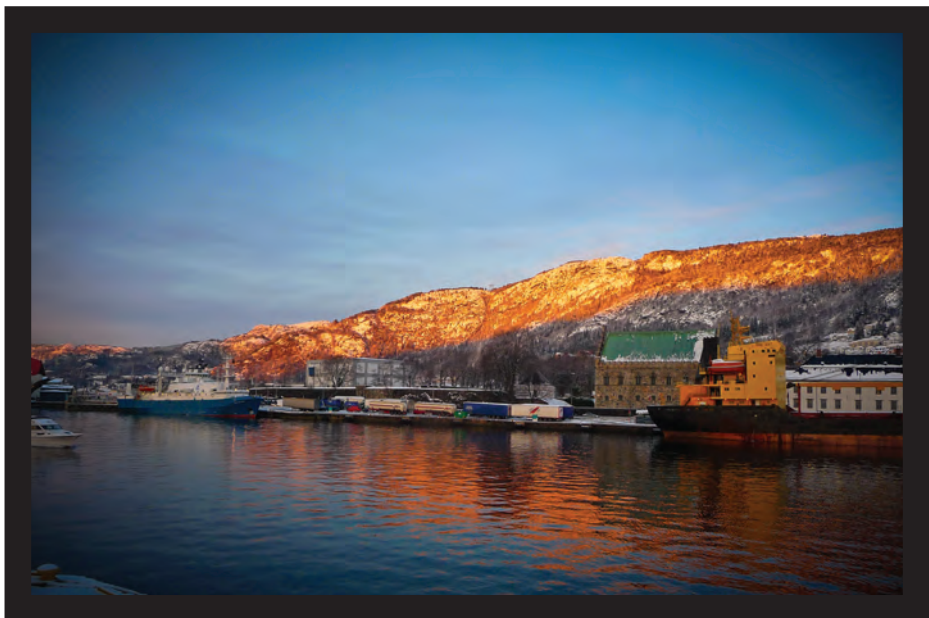
Micro-acoustics in marine
and medical research

Hegen – Research Funding opportunities

Photographs from the workshop









Micro-acoustics in marine
and medical research

Author	<i>page</i>
Calise, Lucio	7–14
Campbell, Paul	107–117
Cochran, Sandy	29–39, 41–50, 51–60
Mc Cormack, Emmet	171–183
Démoré, Christine	29–39
Enger, Marianne	171–183
Feril, Loreto	107–117
Fiabane, Joe	41–50
Geffen, Chen	131–170
Gerold, Bjoern	51–60
Gilja, Odd Helge	171–183
Gjertsen, Bjørn Tore	171–183
Hegen, Anja	185–187
Kimmel, Eitan	131–170
Kotopoulos, Spiros	51–60, 67–105, 119–130, 171–183
Kubilius, Rokas	7–14
Malik, Ritu	41–50
Midoux, Patrick	119–130
Mujić, Maja	171–183
Ona, Egil	7–14
Pancholi, Ketan	41–50
Pichon, Chantal	67–105, 119–130
Postema, Michiel	51–60, 67–105, 119–130, 171–183
Prentice, Paul	51–60
Qiu, Yongqiang	29–39
Saliev, Timur	107–117
Steel, John	41–50
Tachibana, Katsuro	107–117
Torkelsen, Terje	15–28
van Wamel, Annemieke	61–66